CARRIER TRANSPORT IN DIRAC-BAND MATERIALS AND THEIR DEVICE PHYSICS

GAURAV GUPTA

NATIONAL UNIVERSITY OF SINGAPORE

2015

CARRIER TRANSPORT IN

DIRAC-BAND MATERIALS

AND THEIR DEVICE PHYSICS

GAURAV GUPTA
(B.E. (First Class, Hons.), Delhi College of Engineering, India)

A THESIS SUBMITTED

FOR THE DEGREE OF DOCTOR OF PHILOSOPHY

DEPARTMENT OF ELECTRICAL AND COMPUTER ENGINEERING

NATIONAL UNIVERSITY OF SINGAPORE

2015

DECLARATION

I hereby declare that this thesis is my original work and it has been written by me in its entirety. I have duly acknowledged all the sources of information which have been used in the thesis.

This thesis has also not been submitted for any degree in any university previously

Gaurav Gupta

27 July 2015

Acknowledgements

I would like to express my sincere gratitude to my PhD supervisor, Assoc. Prof. Gengchiau Liang, for his intellectual mentorship and psychological support throughout my graduate career. This journey would not have been possible without his patience, constant encouragement, specifically technical and wise insights on life in general, regular critical comments on my work, and the freedom to explore the beautiful world of nanoscale devices. I am especially indebted to him. Next, I would like to thank my co-supervisor Assoc. Prof. Mansoor Bin Abdul Jalil for the intellectually stimulating discussions over the course on my research work. This work has greatly benefited from his expertise in spintronics and magnetic materials. I would also take this opportunity to thank our collaborators Prof. Arun Bansil from North Eastern University and Dr. Hsin Lin from NUS.

I thank all my friends in Computational Nanoelectronics and Nanodevices lab for their help during my PhD candidature. Among them, foremost I thank Dr. Lam Kai Tak for mentoring me on the quantum transport. This work greatly benefited from discussions and friendly support from Dr. Argo Nurbawono, Dr. Eduardo Cuansing, Dr. Huang Wen, Dr. Minggang Zeng, Kain Lu Low, Qian You, Siu Zhuo Bin, Dr. Tony Low, Dr. S Bala Kumar, Mohammad Abdullah Sadi, Guo Yan and Praveen Deorani.

I thank my friend Varun Arora for lending his patient ear through the ups and downs of this course. Lastly, the support and love of my parents and sister throughout my life is beyond any thanks. Especially, my mom has been a key pillar of support and motivation in all the positive endeavors in life and thus this thesis is dedicated to her.

Table of Contents

Acknowledgements 4

Abstract 8

List of Tables 11

List of Figures 12

1. Introduction 23
1.1 Dirac-Band Materials 26
1.2 Objectives of Research 29
1.3 Organization of Thesis 30

2. Methodology 34
2.1. Hamiltonian 35
2.1.1. Electronic Structure of Group-IV Monolayer 35
2.1.2. Electronic Structure of Bi_2Se_3 Three-Dimensional Topological Insulator 38
2.2. Non-Equilibrium Green's Function Formalism 42
2.3. Real-Space Modeling on GPGPUs 47

3. Performance Evaluation of Electro-Optic Effect based Graphene Transistors 49
3.1. Introduction 49
3.2. Computational Setup 53
3.3. Results and Discussion 55
3.4. Conclusion 64

4. Y-Shape Spin-Separator for two-dimensional Group-IV Nanoribbons based on Quantum Spin Hall Effect 66
4.1. Introduction 66
4.2. Computational Setup 68
4.3. Results and Discussion 69
4.4. Conclusion 76

5. Effect of Phase Transition on Quantum Transport in Group-IV Two-Dimensional U-shape Device 78
5.1. Introduction 78
5.2. Computational Setup 82
5.3. Results and Discussion 83
5.4. Conclusion 95

6. Carrier Transport in Bi_2Se_3 Topological Insulator Slab ……. 96
6.1. Introduction ……. 96
6.2. Simulation Approach ……... 99
6.3. Deformation Potential for Acoustic Phonon Scattering ……..…. 101
6.4. Ballistic Transport ……..……..…. 103
6.4.1. Source to Drain Bias (V_{DS}) …….. 103
6.4.2. Temperature ……. 106
6.4.3. Effects of Slab Thickness and Fermi-Level ……... 107
6.5. Acoustic Phonon Scattering ……..……. 109
6.5.1. Effect of Channel Length ……...…. 110
6.5.2. Effect of Temperature ……. 114
6.6. Validation of Model against Experimental Data ……..……. 116
6.7. Electronically Detecting Topological Surface ……..…. 122
6.8. Conclusion ……. 123

7. Contact Effects in thin 3D-Topological Insulators: How does the current flow? ……..…….. 127
7.1. Introduction ……..……. 127
7.2. Simulation Setup ……..……..……. 131
7.3. Results and Discussion ……..……. 132
7.4. Conclusion ……. 148

8. Evaluation of mobility in thin Bi_2Se_3 Topological Insulator for prospects of Local Electrical Interconnects ……..……. 150
8.1. Introduction ……..……. 150
8.2. Computational Setup ……...…. 153
8.3. Results ……..……. 155
8.3.1 Defect Scattering ……. 155
8.3.2 Phonon Scattering ……..……. 157
8.4. Discussion ……...……. 158
8.5. Conclusion ……..…. 164

9. Effect of Band-Alignment Operation on Carrier Transport in Bi_2Se_3 Topological Insulator ……. 166
9.1. Introduction ……..……. 166
9.2. Results and Discussion ……. 169
9.2.1 Band-Alignment for Lateral Transport ……...……. 170
9.2.2 Band-Alignment for Vertical Transport …….. 175
9.3. Conclusion ……...…. 182

10. Conclusion and Future Works ……...……. 184
10.1. Conclusions ……..……. 184
10.2. Future Works ……. 187
10.2.1. Valley-Valve effect in 2D Group-IV monolayers ……. 187
10.2.2. Threshold of Scattering Angle on the Topological Surface ….…. 188
10.2.3. Obtain Real-Space spin-texture on Topological Surface ….……. 189
10.2.4. Effect of Strain ……...……..……. 189

Appendix ……. 191

A. Derivation of Gate-Voltage for I_{OFF} in Chapter 3 ……. 191

B. Supplementary for Chapter 4 ……. 194
B.1. Local Density of States Distribution for 14 cell wide Y-shaped Device …. 194
B.2. Transmission in Equilibrium Condition ……. 196
B.3. Spin Distribution for 14 cell wide Y-shaped Device ……. 200

C. Spin-Polarization of Current for Arm-R for the Spin-Filter Operation in Chapter 5 ……. 202

D. Supplementary for Chapter 7 ……. 203
D.1. Effect of Top-Contacts on on Short-Channel Device ……. 203
D.2. Layer-Dependence for Short-Channel Device with FM Contacts ……. 204
D.3. Enlarged Figure 7.5(a) ……. 206

E. Supplementary for Chapter 8 ……. 207
E.1. Transport through defect-free Bi_2Se_3 TI-Nanowire ……. 207
E.2. Transport through Bi_2Se_3 TI-Nanowire with defects ……. 210
E.3. Non-Equilibrium Transport through Bi_2Se_3 TI-Slab with Acoustic Phonons ……. 216

F. Supplementary for Chapter 9 ……. 218
F.1. Effect of Mode Mismatch at Contact ……. 218
F.2. Effect of Gate Potential on Transport through Dirac-Band ……. 218
F.3. Effect of Channel-Bias V_{DS} ……. 220

G. List of Publications and Awards ……. 222

Bibliography ……. 224

Abstract

Dirac-band materials have recently become one of the most promising materials under research for the prospects of designing low-power high-speed computing devices for future applications, an objective which can no longer be sustained via scaling down of silicon channel in transistors. The Dirac-band materials, at least the ones studied in this work (Group-IV monolayer elements and Bi_2Se_3 topological insulator), generally have very high drift velocity, good thermal properties to avoid hot-spots in the devices, and have spin-polarized bands either intrinsically or can be easily made so by magnetic dopants or just electric field, which make them especially attractive for engineering pure or hybrid spintronic applications. The device design with Dirac-band materials mandates the understanding of the carrier transport in these materials. The understanding of charge and spin flow in Dirac-band materials is critical for this purpose. The nanoscale dimensions of these materials exhibit strong quantum mechanical characteristics which warrant a quantum transport simulator. Non-equilibrium green function (NEGF) formalism is one such quantum algorithm for studying carrier transport in complex mesoscopic systems in both ballistic and diffusive regime, provided it is computationally feasible. This thesis, therefore, computationally investigates the carrier (charge and spin) transport in Dirac-band materials and some of their prospective devices generally via NEGF based on tight-binding Hamiltonian.

Firstly, graphene (first Group-IV element) which is one of the most important Dirac-band materials, because of its high-mobility and thermal conductivity, is studied for non-conventional switching scheme based on electro-optic phenomenon with two different device architectures. The ray-optic based simulation shows large

current-switching ratio along with sub-60 mV/decade subthreshold slope. It is observed that over a gamut of design criteria, both of the architectures have certain merits over one another. Therefore, the circuit design engineers should select the designs as per the system constraints.

Next, the carrier transport through next four Group-IV elements (Si, Ge, Sn and Pb), which have larger spin-orbit coupling (SOC) leading to intrinsically spin-polarized bands in electronically accessible energy regime, is investigated for three-terminal spin-separator and spin-filter devices. The zigzag (and anti-zigzag) nanoribbons of these materials are intrinsically in quantum spin-hall phase near the Dirac-points and this region functions as a two-dimensional topological insulator (2D-TI). Despite of injecting unpolarized current at source terminal in these devices, strongly polarized current with opposite polarities is obtained at its two drain terminals. The effect of phase transition in these devices is furthermore investigated to provide a comprehensive understanding of carrier transport in these materials and its influence on device operation.

After investigating 2D-TI, the focus of this thesis moves to three-dimensional (3D) TI. Bi_2Se_3 is chosen as an exemplar material because of relative large bulk bandgap among extant 3D-TIs and hence provides greatest isolation from bulk bands to operate device in spin-polarized surface bands. The carrier transport investigation in this material helps in comprehensive understanding of complex transport physics in 3D-TI, expounds on lot of conceptual points and explains the anomalous observations in experiments. The effect of different type of contacts and various electronic and geometrical parameters in presence of various scattering mechanisms like acoustic phonons, defects, vacancies and edge roughness has been investigated to develop this understanding. The transport results have been applied to evaluate the feasibility of

3D-TI based devices like local interconnects for replacing Cu in the chips and resonant devices for analog oscillators and multipliers.

Therefore, this thesis should help in understanding the carrier transport in Dirac-band materials and their prospective devices which should assist in developing next generation of low-power computing systems.

List of Tables

2.1 Model parameters for Hamiltonian in eq. (2.1) ……..... 37

3.1 Comparing behaviour of Design-A with Design-B …….…..…… 64

6.1 Estimated surface carrier density at 100K for $v_f = 4.1 \times 10^7$ cm/s and $\lambda = 0.25$ for different values of the Fermi energy (E_f)……..... 101

List of Figures

1.1 Expected power dissipation in microprocessors targeted for high-end markets like servers and mobile devices and for ultra-power segment for energy harvesting and medical applications. Re-adapted with permission from "Challenges & Enablers of LOGIC CMOS SCALING IN THE NEXT 10 YEARS" presentation by Aaron Thean at imec 2013 and Ref. [4]. 23

1.2 Illustration of some of the benefits of non-volatile computing. Non-volatile electronics is expected to directly benefit in industries like aerospace, health-care, servers, mobile devices (like Internet of Things) and sensors because of the ability to retain data in case of power disruption which may be intentional or otherwise. 24

1.3 Overview of the flow of a new discovery in semiconductor physics to a product in the market. Observe that the physics-based accurate simulations mark the transition of concept from investigating physics to design and optimization for the computing or memory chips. 28

1.4 Organization of the thesis illustrating the flow of the investigation for the carrier-transport in the Dirac-band materials and the devices ……..…..... 30

2.1 (a) Zigzag-Nanoribbon (ZNR) of monolayer Group-IV material. The device lies in the *x-y* plane. The red (type-A) atoms are out-of-plane from the blue atoms (type-B) by Δ_C along the *z-axis* because of the buckling in the material. Energy Bands for 14 rings wide (166.46 Å) zigzag-Germanene Nanoribbon (GeNR) in unbuckled state (b), Quantum-Spin Hall (QSH) phase (c) and band-insulator (BI) phase (d). In (e-i) a small λ_V (~ 0.005 λ_{SO}) is applied is life band degeneracy to distinguish the bands computationally. (e-h) spin-polarization (along z-axis) of the first two conduction and valence bands (CB and VB). (i-l) $|\psi^*\psi|$ distribution across momentum-vector and atom-position (see discussion) shows edge-localized characteristic of Dirac-bands which extend from approximately $+\lambda_{SO}$ to $-\lambda_{SO}$ energy range in (b). The red region in (i, k) corresponds to n=29 i.e. on bottom-edge (type-B blue atoms) while for (j, l) n=56 i.e. on top-edge (type-A red atoms). ……..... 35

2.2 (a) Energy bands for a 13-QL slab of Bi_2Se_3 obtained from our model Hamiltonian, exhibiting the Dirac-cone surface states centered at the *Γ-point* (red bands). (b) Layer-dependent charge density of the surface states (bottom surface, blue solid line; top surface, red dashed line) around the *Γ-point* [75]. Also, note the major contribution (60%) of helical states from surface layers and their significant penetration into bulk layers [68]. In-plane spin texture of topological surface states in the conduction band around the *Γ* point for top (c) and bottom (d) surfaces illustrates left-handed and right-handed chirality. (e) and (f) Energy dispersions on the side surfaces for 200 and 50 nm wide slabs (infinitely thick along the z-axis) respectively, for kz = 0/Å. Side surface Dirac bands, therefore, require the sample to be both sufficiently thick (z-axis) and wide (y-axis). The anisotropic behaviour [76] in Bi_2Se_3, however, allows the observation of Dirac bands on the top and bottom surfaces for a relatively much smaller thickness (>6 QLs) [77] but wide samples. ……..... 41

2.3 (a) Energy Bands for 10 QL thick (z-axis) – 60 nm wide (y-axis) Bi_2Se_3 TI nanowire. Small energy bandgap opens due to confinement along y-axis. (b) Local Density of States (LDOS) (ψ^2) distribution across layers (QLs) of the wire for the first conduction band at the k-point marked ($k_x a \sim 0.5$) with red line in (a). Top and Bottom surfaces can be clearly distinguished from ($\psi 2$) distribution which shows localization on the surface layers in accordance with the topological properties. A representative Bi_2Se_3 3D-TI wire of 10 QL thickness – 60 nm width – 80 nm length has been chosen in this chapter unless specified otherwise. ……..... 42

3.1 Device structure of analyzed proposals for four terminal Graphene Electro-Optic Transistor (GEOT). Both induce bandgap by blocking certain energies by emulating 2-D ray optics. Graphene channel, in x-y plane, rests over substrate/dielectric. Both have two back gates, which electrostatically segment the channel into region 1 (n-side) and 2 (p-side), under V_{G1} and V_{G2} respectively, with relative refractive index η_{21} and critical angle θ_C (sin-1 η_{21}). a) Ref. [96] Electron stream (circular wavefront) from point electron injection source is blocked by insulating barrier placed in the centre of the channel. Junction is formed in y-direction along the barrier. In addition, electron incident at junction with angle (θi) greater than θ_C is blocked. θ_B is barrier subtended at source for symmetrically placed barrier i.e. for Upper Barrier Angle (*UBA*)=Lower Barrier Angle (*LBA*). b) Ref. [98, 99] Electron injected from source (planar wavefront) is blocked from traversing from region 1 to region 2, if the critical angle of its wavefront is less than gate inclination angle (δ). 51

3.2 Effect of moving insulation barrier of fixed dimensions along the y-axis in design-A and polarity of gate inclination for design-B. a) minimum I_{OFF} is achieved for symmetrically placed barrier i.e. when *UBA=LBA* (20o in our case) (blue line). Drain current remains same for barrier positions mirrored about x axis along the barrier's y-axis (black overlapping with red line). Black line stands for intermediate barrier position i.e. *UBA=2 LBA*. b) Gate inclination (δ) in design-B begets similar transfer characteristics in Graphene channel as θ_B in design-A. Moreover, black ($\delta = +20^o$) overlap with red ($\delta = -20^o$) lines predicts functional independence of device of polarity of δ. Green trend corresponds to absence of barrier for both a) and b). 55

3.3 Impact of half-barrier angle (Design-A) and gate inclination (Design-B) for V_{G1} = 1 V at 300 K. For designs A and B, width along y-axis of symmetrically placed insulation barrier subtending θ_B at source and gate junction inclination (δ) w.r.t y-axis is swept respectively. Both I_{ON} and I_{OFF} decrease with increase in θ_B (δ), but I_{ON}/I_{OFF} improves continuously due to steeper fall in I_{OFF}. SS < 60 mV/dec can be achieved for nn-config for wide range (b, e) of θB (δ) which gives flexibility in selection of I_{ON} and I_{ON}/I_{OFF} (c, f) for circuit design. ……..... 56

3.4 Impact of Temperature for V_{G1} = 1 V at θ_B (δ) = 20°. (a, d): I_{OFF}, which corresponds to leakage current in circuits, decreases with temperature, but V_{G2} corresponding to I_{OFF} remains constant. (b, e): Subthreshold Slope (SS) degrades with increase in temperature for both np and nn config. (c, f) I_{ON} fractionally increases and decreases with increase in temperature for np and nn configurations, respectively..... 58

3.5 Impact of Gate Voltage over Segment 1 (V_{G1}) for $\theta_B(\delta)$ = 200 at 300 K. Note the independence of device behavior of polarity of V_{G1}. (a, d) Drain current decreases

with increase in V_{G1} because of emulation of smaller critical angle leading to blockage of wider energy spectrum for injected electrons. (b, e) SS declines with increasing magnitude of V_{G1} to fall below 60 mV/dec benchmark and finally becomes relatively constant for $V_{G1} > V_{G2max}$ because of Density of States (DOS) factor in current equation (Eq. (A.3)) which we have crudely taken to be lesser of the two segments (Eq. (1) of Ref. [116]) because segment with smaller DOS acts as stronger impediment in current flow. (c, f) I_{ON} peaks for full swing voltage of *VG2* in either polarity, because of competing effect of DOS for electron transport and total internal reflection on source side. 60

3.6 Impact of chemical doping or Top Gate on V_{G2} translation at 300 K and V_{G1} = 1 V. Graphene channel is doped to equivalent of V_{dope} eV or top gate is used to materialize the effect. Main objective is to attain zero V_{G2} for I_{OFF} to match with switch-off for contemporary logic levels. V_{dope} is a function of θ_B (or δ), *VG1* and gate transfer capacitance factor (β) if top gate is used for tuning. Refer Appendix for derivation. As per Eq. (A.8), for both designs, V_{dope} = 0.1345 eV (red). 62

4.1 Y-shaped device with three contacts A, B and C. 4 atoms in dotted black line are referred as one cell in discussion. Orange and blue atoms do not lie in a plane for a low buckled system and are referred to as type-A and type-B, respectively. N-cells along the width form a super-cell..... 68

4.2 Conductance (a, c, e) and Spin Polarization (SP) (b, d, f) of current in Arm-B for the Y-shaped device made of zigzag low-buckled nanoribbon of Silicon (Si; blue square), Germanium (Ge; red circle), Tin (Sn; black diamond) and Lead (Pb; magenta triangle). Arm-C has same conductance but opposite spin polarity. (a, b) Both conductance and SP increase with device width and eventually saturate because of weakening inter-edge coupling. E_f = 1 meV, V_{BA} (V_{CA}) = 1 mV. (c, d) Conductance and SP roll-off as the Fermi-level (E_f) moves out of the energy range governed by the spin-polarized edge states [48] due to intrinsic (λ_{SO}) spin-orbit coupling (SOC). Conductance again picks up due to the bulk states (see Fig 4.3), but SP still declines owing to lack of polarization. V_{BA} (V_{CA}) = 1 mV. (e, f) Larger bias allows for larger energy range of electrons to sweep across the spin-polarized edge and unpolarized bulk (>λ_{SO} eV) states, which results in a local maxima for Si and Ge. Sn and Pb have much larger λ_{SO}, values given on top of the figure have been taken from Table I of Ref. [65]. E_f = 5 meV. Refer to Fig. B.2 and Fig. B.3 for local density of states (LDOS) distribution for some exemplar cases to develop an intuitive understanding of the Y-device..... 70

4.3 Effect of buckling field (λ_V) (a,b,e,f) and magnetic (H_Z) (c,d,g,h) field on Conductance (a, c, e, g) and Spin-Polarization (SP) (b, d, f, h) (broken y-axis) of current through Arm-B (blue triangle) and Arm-C (red star) of Germanene device. (a-d) fields are applied in Arm-A (see Fig 4.1(a)). (e-h) fields are applied in central region. E_f = 5 meV, V_{BA} (V_{CA}) = 4 mV. Refer to Fig. B.7 for LDOS distribution and Fig. B.9 and B.10 for spin distribution plots for exemplar cases. 72

5.1 A three-terminal U-shape device. Arm-P is connected to a source, and Arm-Q and Arm-R are connected to the drain terminals. The device lies in the *x-y* plane. The red (type-A) atoms are out-of-plane from the blue atoms (type-B) by Δ_C along the *z-axis* because of the buckling in the material. Four-atom unit-cell is labeled as a cell and

one chain of cells along the transverse axis is labeled as super-cell. These are used to earmark device dimensions along *y* and *x-axis* respectively. 81

5.2 Effect of the channel width at zero λ_V on the conductance (a) and the spin-polarization (SP) of the current (b) at Arm-Q for Si (black rectangle), Ge (red circle), Sn (blue triangle), and Pb (cyan triangle). Transmission in the equilibrium condition for a Si-device with Arm-P width of 14-cells (c) and 5-cells (d). 83

5.3 Effect of λ_V on Arm-P of the silicene ((a) and (c)) and germanene ((b) and (d)) device. Observe a local maximum in the conductance at Arm-Q (Arm-R) as the device transitions from the QSH to the BI phase for a positive (negative) λ_V. The peak-conductance (G_{max}) for the Si-device is observed to be larger than that of the Ge-device (see text for the details). For the Sn and Pb devices the local maximum is absent (not shown). (c, d) Spin-polarization for both the arms degrades for the increasing magnitude of λ_V, albeit at different rates that switch with the polarity of λ_V. 85

5.4 Energy-dispersion of 14-cell wide zigzag germanene nanoribbon in (a) QSH phase (λ_V = 5 meV) and (b) BI phase (λ_V = 13 eV). The forward moving channel in the conduction band changes from B↓ to A↓ after the phase-transition, along with the opening of the bandgap. (c) The critical λV (λC) at which phase-transition occurs is plotted against the width of the Ge nanoribbon. (d) Charge distribution on the bottom-edge of Arm-Q, for a Ge-device with λV = 7 meV applied on Arm-P, implying a current flow through the bottom-edge of Arm-Q. (e, f) The tunneling phenomenon in a 14-cell wide Ge U-shape device in the BI phase is illustrated by plotting the transmission from Arm-P to Arm-Q for (e) different lengths of Arm-P at λ_V = 13 meV and (f) different bandgaps (computed for nanoribbon) with λ_V applied only over Arm-P. 87

5.5 Effect of λ_V on the conductance at Arm-Q for a Ge device. (a) λ_V applied on Arm-P of lengths 14 (black line), 20 (blue line), 28 (Cyan line) and 42 (red line) super-cells shows that the G_{max} for Arm-Q increases in magnitude and shifts to larger λ_V for longer Arm-P. (b) Effect of λ_V applied throughout the device with each of the arm lengths set to 14 super-cells (red line), 20 super-cells (blue line), and 28 super-cells (cyan line). The trend lines saturate when the entire energy window for the transport lies in the bandgap. 90

5.6 Spin-filter realized by applying λ_V on one of the drain-arms (Arm-R) of a Ge-device with P, Q, and R arm-lengths of 6, 60, and 60 super-cells respectively at E_F = 1 meV and V_{DS} = 1 mV. (a) Arm-R conductance is effectively blocked at high λ_V whereas Arm-Q transporting ↑ spin has a saturating conductance of nearly 2 q^2/h. (b) Spin-polarization for the Arm-Q decays from unity to yet an acceptable value of 0.45 at λ_V = 15 meV. The spin-filter filters out of the oppositely-polarized current through the other drain-arm. (c, d) Spin-charge distribution, computed via Trace(σz.Gn) and integrated over entire energy range, for λV = 0 meV (c) and λ_V = 15 meV (d) insinuates that for λ_V = 15 meV B↓ current from the bottom-edge of the source-arm is partly re-routed along the inner-edge of Arm-Q which counters the A↑ on the outer-edge, in contrast to the zero-field case in which ↑ and ↓ current completely flow along the outer-edges of the two drain-arms. The zoomed insets suggest the SP decay of B↓ current on migrating from Arm-P to Arm-Q. 93

6.1 Schematic for modeling acoustic phonon scattering in quantum transport [82]. 101

6.2 (a) Atomic structure of Bi_2Se_3. (b) Semi-infinite slab of Bi_2Se_3 with finite thickness along the z-axis and an infinite width along the y-axis. Electron transport is along the x-axis. Gate voltage shifts the Fermi-level (E_f) uniformly in the entire slab. E_f is defined to be zero at the Dirac point. (c) Illustration of potential distribution through the energy bands along the transport direction. 103

6.3 (a) Ballistic I-V characteristics of 13 QL thick Bi_2Se_3 slab at 100 K for Fermi-level (E_f) at Dirac point. Red square is at V_{DS} = 40 meV, where the simulations in panels (b)-(f) in this figure have been carried out. (b) Drain current through various layers for four different values (see legend) of V_{DS}. (c) Percentage contribution of various layers to the total drain current for four different values of V_{DS}. Small differences as a function of V_{DS} are not visible in the main plot, and are blown up for layers 1 and 7 in the insets. (d) Surface (bottom layer) and middle (7th layer) layer contribution to the total drain current as a function of for V_{DS}. (e, f) Contribution to the total current from electrons of various energies in different layers (in μA/μm) for V_{DS} = 0.04 V (e) and 0.16 V (f). 104

6.4 (a) Ballistic current as a function of temperature for the 13 QL thick Bi_2Se_3 slab for Fermi-level (E_f) at the Dirac point (V_{DS} = 0.04 V). The inset gives an Arrhenius plot of resistance. (b) Drain current through various layers at four different temperatures. (c) Percentage contribution to the total current from various layers at four different temperatures. Differences as a function of temperature are fairly small in the main plot, and are blown up for layers 1 and 7 in the insets. (d) Surface (Bottom layer) and middle (7^{th} layer) layer contribution to the total drain current. (e, f) Contribution to the total current from electrons of various energies in different layers (in μA/μm) at T = 50K (e) and 300K (f) ……..…… 106

6.5 Variation in ballistic resistance as a function of slab thickness at 100K (V_{DS} = 0.04 V) for four different values of the Fermi-level (E_f), see legend ……..…… 108

6.6 (a-d) Ballistic current through various layers for slabs of four different thicknesses, see legend on right hand side of the figure, at 100K (V_{DS} = 0.04 V) for different values of the Fermi-levels (E_f) shown on the top of the figure. (e-h) Corresponding percentage contribution to the total drain current. 108

6.7 (a-d) Resistance vs. Channel Length (L_x) for ballistic (red squares) and acoustic transport for weak (λ=0.08; green triangles) and strong (λ=0.25; blue star) electron-phonon coupling, for different Fermi-levels at 100 K for 13 QL thick Bi_2Se_3 slab biased at 40mV. …..……...……..…… 111

6.8 Competition between the effects of phonon induced level broadening, thermal activation and in-plane scattering is shown through plots of energy (y-axis) vs transmission, *T(E),* through the slab, density of states, *DOS(E,)* of the bottom surface in the middle of the channel, and the difference in Fermi-distribution, $\Delta f_{SD}(E)$, between the source and drain for various values of the parameters. Values of *T(E)* and $\Delta f_{SD}(E)$ are shown on the top horizontal scale (logarithmic) in magenta, while those of the DOS are given on the bottom horizontal scale (logarithmic). *Top Row*: E_f = 0 at

100 K for channel lengths (L_x) of 15 nm (a), and 50 nm (b). *Bottom Row*: E_f = 0.1 eV, L_x = 30 nm at temperatures of 50 K (c) and 250K (d). For better illustration, the values of $\Delta f_{SD}(E)$ are scaled in different panels by the factors given on the right hand side of each row. *T(E)* and *DOS(E)* are scaled up by 2π in all panels. Note that a finer transverse mode grid in the computations will smooth the high energy serrations seen in some of the curves. Red, green and blue colors represent ballistic, weak-acoustic scattering and strong-acoustic scattering cases respectively. 112

6.9 Resistance vs. temperature for ballistic (red squares) and acoustic transport for weak (λ=0.08; green triangles) and strong (λ=0.25; blue star) electron-phonon coupling for four different values of the Fermi-level at 30nm channel length for 13 QL thick Bi_2Se_3 slab biased at 40 mV ……..… 115

6.10 Same as Fig. 6.8 but for L_x = 30 nm, λ = 0.25 for E_f values of 0.05 eV (a) and 0.1 eV (b). Red, green and blue colors represent temperature of 50 K, 125 K and 200 K respectively. ….. 115

6.11 (a) Experimentally observed resistance of a Bi_2Se_3 nanoribbon taken from fig. 2(a) of Ref. [172] (Readapted with permission). (b) Schematic of the simulated semi-infinite slab of Bi_2Se_3. (c) Schematic of the potential profile (dashed line) through the energy bands for E_f = 0.05 eV. (d) Potential profile for E_f = 0.2 eV (positioned within bulk conduction bands). (e) Computed (resistance×width) vs temperature for different positions of E_f (shown over various curves) for acoustic transport (λ = 0.25). The inset shows an enlargement of the bottom four curves from the main figure with same color scheme but broken (by blue hyphens) with a shifted *y* axis (unchanged scale) to emphasize the features (*x* axis gives temperature from 50 to 250 K) of trend lines. Note the local maximum in the red and purple curves at around 125 and 200 K, respectively. 117

6.12 Contributions from different energy channels and different sets of QLs to the total current for the 13-QL-thick slab for E_f = 0.05 eV. (a)–(c) refer to results at 50 K, while (d)-(f) refer to those at 250 K. Ballistic transport is considered in (a) and (d), weak electron-phonon coupling with λ = 0.08 in (b) and (e), and strong coupling case with λ = 0.25 in (c) and (f). 118

6.13 Contributions from different energy channels and different sets of QLs to the total current for the 13-QL-thick slab for E_f = 0.2 eV. (a)–(c) refer to results at 50 K, while (d)-(f) refer to those at 250 K. Ballistic transport is considered in (a) and (d), weak electron-phonon coupling with λ = 0.08 in (b) and (e), and strong coupling case with λ = 0.25 in (c) and (f). 120

6.14 Energy integrated partial contribution (given as a percentage of the total current) of various layers to the total drain current for ballistic transport (blue circles), weak acoustic scattering (red squares), and strong acoustic scattering (black stars). Insets give absolute drain current (in μA/μm) flowing through various layers for the bottom half of the slab. Cases (a) and (b) refer to energy integrated result of Fig. 6.12, and (c) and (d) of Fig. 6.13. The energy-integrated results reemphasize that the maximum current is carried by the surface layers (1st and 13th layers). The percentage contribution illustrates a large decrease in surface current for strong acoustic scattering. Comparison of the insets in (a) and (c) or (b) and (d), shows that for E_f =

0.2 eV, even under ballistic conditions, the middle layers contribute significantly to the total current, resulting in reduction of the net resistance of the slab compared to the E_f = 0.05 eV case. By comparing the corresponding curves from the insets of (c) and (d), we can also observe a reduction in the surface current due to increased scattering at 250 K. 121

6.15 Percentage decrease in the current in the surface layer as a function of temperature. Acoustic regime (long sample length) for weak (λ = 0.08, solid lines) and strong (λ = 0.25, dashed lines) electron-phonon coupling are compared to the ballistic regime (sample length smaller than mean-free path ~20nm). …..... 123

7.1 (a) Spin-texture in momentum space for conduction bands for top and bottom surface. Blue arrows are spin vectors, red circle is energy contour and black arrows denote momentum vectors. (b) Atomic structure of Bi_2Se_3 (3D-TI). 5 atomic layers constitute one quintuple layer (QL ~ 0.943 nm). (c) Device Structure for quantum transport modeling through Bi_2Se_3 slab. The axis is given over the device along with convention for polar representation of Magnetization vector (M). θ is polar angle and $\emptyset$ is azimuthal angle. Slab dimensions of 10 QL thickness – periodic width (uncoupled mode space) – 65 nm channel length – 10 nm contact on both side of channel, , temperature of 0 K, a potential drop of 35 mV across channel (V_{DS}) and Fermi-level (E_f) = 0.075 eV has been considered as a representative case throughout this chapter unless specified otherwise. (d) Illustration of the potential distribution through the energy bands along the transport direction. μ_S (μ_D) is electrochemical potential at source (drain) end. 129

7.2 FM-TI-exTI system. Spin-Polarization (SP) at Drain end and current through slab over a range of (a) contact-coupling strength (α) for 100 % '$-y$' source magnetization (M_S); (b) '$-y$' M_S for α = 0.6. From here on only α = 0.6 is considered for moderate quality of contact. Current distribution across slab layers for (c) 100 % and (d) 40 % M_S along $\pm y$ axis. Note that current chiefly flows through layer with conducive spin-texture (see Fig. 7.1(a)). Inset shows the symmetric current distribution for 0 % M_S. SP at drain end and current for 100 % M_S along $\pm y$ axis over a range of (e) Fermi-level (E_f) (f) slab thickness. 133

7.3 FM-TI-exTI system. (a) Experimentally observed trend for signature of spin-momentum locking on Bi_2Se_3, taken from Fig. 5(c) of Ref. [203] (Adapted by permission from Macmillan Publishers Ltd: [Nature Nanotechnology] [203], copyright (2014)). (b) Computed spin-polarization at drain end across temperature (without phonons) for $+y$ (100%) M_S contact. $-y$ Magnetization produces same values but with opposite polarity. (c, d) Current distribution across slab layers for ballistic transport at 0 K ($|SP_{Drain}| \sim 34.7\%$) and 300 K ($|SP_{Drain}| \sim 0.43\%$) and with acoustic scattering at 300 K ($|SP_{Drain}| \sim 0.32\%$) for 100 % source magnetization (M_S) along (a) '$+y$' and (b) '$-y$' axis. …..... 136

7.4 Current distribution along transport direction for ($-y$) 100 % M_D FM Drain for normal mode (ky = 0). Source contact-type is stated over each column. Operating condition is as follows: (a-c) $E = \mu_S$, f_S = 0, f_D = 1; (d-f) $E = \mu_D$, f_S = 1, f_D = 0. Refer text for symbols. 138

7.5 (a) Transmission distribution at equilibrium (V_{DS} = 0 V) for normal metal contacts at both ends of the TI channel (see enlarged version of (a) in Appendix D.3 for better visibility) Note that the confinement along the transport *direction* quantizes the bands which cannot be captured in energy-dispersion along transport direction (x-axis). Current distribution across slab layers for (b) three different combinations with normal metal contact, (c) with anti-phase ferromagnetic contacts, and (d) in-phase ferromagnetic contacts. 142

7.6 Energy resolved microscopic examination of current (a), Transmission (b), k_y-*resolved* Transmission spectrum (c), spin-polarization of current through top (d) and bottom surface (e) layers for three sample cases (as stated over each column (1)-(3)) taken from Fig. 7.5. Zoom-in plots are illustrated instead of showing full-information to emphasize on the key features. Square box are drawn to draw attention to dominant modes (see text). Specifically, observe the confinement induced band quantization which limits the current through certain dominant energy and *ky* modes in (c). Also note that the current through surface layers is symmetrical about middle of the slab for NM contacts, but is spin-dependent for FM contacts. The net current integrated over all layers is always positive in above cases. Spin-polarization of certain dominant energy and *ky* modes in (d) and (e) decide the selection of topological surface for transport illustrated in (a). Note that NM contacts strictly comply with spin-texture diagram in Fig. 7.1. In contrast, for FM contacts the net solution atleast depends on magnetization axis of source and drain, sub-band quantization, transverse mode and injection energy. 145

8.1 (a) Atomic structure of Bi_2Se_3 (3D-TI). (b) Device Structure for quantum transport modeling through Bi_2Se_3 nanowire. 152

8.2 Mobility characterization across temperature at different Fermi-Levels (E_f). (a) Ballistic Mobility for a finite width and an infinitely wide wire. Effect of charge impurities (b), vacancies (c), edge roughness (d) and acoustic phonon (e) on mobility. (f) Effect of defects (10% Edge Roughness + 5 x 10^{18} /cm^3 Charge Impurities + 5 x 10^{18} /cm^3 vacancies) and phonons on mobility at 300 K with the scaling of the wire length. Note that for low defect concentration mobility trends follow approximately ballistic results. 158

8.3 Effective mobility in presence of all the defects (Phonons + 10% Edge Roughness + 5 x 10^{18} /cm^3 Charge Impurities + 5 x 10^{18} /cm^3 vacancies) as described by Matthiessen's rule (see Eq. (8.1)) for different Fermi-Levels. 161

8.4 80 nm long – 64 nm wide TI-wire at 300 K. (a) Effect of wire width and (b) thickness on the mobility in presence of all the defects (Phonons + 10% Edge Roughness + 5 x 10^{18} /cm^3 Charge Impurities + 5 x 10^{18} /cm^3 vacancies) for different Fermi-Levels at 300 K. 162

9.1 (a) Device Structure (Design-A) for quantum transport modeling through Bi_2Se_3 slab with shorted top and bottom gates. (b) Potential distribution along the transport direction. μ_S and μ_D are electrochemical potential at the source and drain end respectively. Gate voltage V_{TG} shifts the potential energy in the channel. Δ represents the energy difference between μ_S and the Dirac-point in the source contact and is used as a reference energy scale throughout this chapter. (c, d, e) Schematic of the band

profile along the transport direction (source, channel and drain from left to right) for three different gate voltages, illustrating the mechanism of mode matching. At 0 K transport is within the energy window delineated with blues dot-dashed line. Blue arrows depict ballistic transport along the transport direction with conserved transverse (along y-axis) momentum. Green bands in (d) emphasize the band-aligned condition between source and channel region. 169

9.2 Design-A. (a) Operation for 13 QL thick 3D-TI for three different Fermi-Levels in the surface bands ($V_{DS} = 2\ \Delta$) at 0 K. Observe the resonant peak at $-\Delta$. I_R/I_0 ratio is defined between $V_{TG} = 0$ (I_0) and $V_{TG} = -\Delta$ (I_R) and stated over each trendline with respective color. (b-d) Transmission spectrum (in per μm) for V_{TG} equal to 0 (b), $-\Delta$ (c) and -2Δ (d) at 0 K for $\Delta = 0.04$ eV as a representative case from (a). 172

9.3 Design-A. (a) Current vs gate voltage at 0 K (blue circles), 100 K (red square), 200 K (magenta triangle) and 300 K (black stars) for $\Delta = 0.04$ eV. I_R/I_0 ratio and temperature are stated with respective colors for each trendline. Observe that signature of mode matching is severely weakened due to spread in Fermi-distribution. (b, c) Transmission spectrum (in per μm) for two gate voltages at 300 K. Compare it with Fig. 9.2 to observe the extinction of signature of mode match/mismatch in quantum transport. Dark red region is bulk conduction band. 174

9.4 (a) Device Structure for vertical transport in 3D-TI. Source is coupled to bottom few layers (bottom slab) and drain to top few layers (top slab). As a representative case, bottom and top slabs are 13 QL each, whereas middle region is 4 QL. Electrons injected from the source have to tunnel through the middle slab for operation in the bulk band gap. For Design-B, the top and bottom gate voltages uniformly modulate the doping electronically in the respective slabs. For Design-C, a more practical scenario for 3D-TI is presented with uniformly n-doped sample. (b) Potential distribution in x-z plane for band-aligned condition. Blue arrow depicts vertical transport from Dirac-bands of bottom slab to that of top slab, tunneling through the middle region. For channel bias, all layers of bottom (top) slab are hold at μ_S (μ_D) electro-chemical potential of source (drain), while a linear gradient is considered in the middle. Gradient for gate potential in Design-B is assumed to be only in the middle region, whereas for Design-C it is from bottom to top layer of the device (across all three regions). 175

9.5 Design-B. (a) Current vs top gate voltage at 0 K for $\Delta = 0.02$ eV (red squares) and $\Delta = 0.04$ eV (blue circles). Observe the resonant condition at $V_{TG} = -2\Delta$. (b) Illustration of current flow in the device. Observe that the current mainly flows laterally (along x-axis) on top and bottom surface but is forced to transit vertically (z-axis) at the device boundary. (c-h) Transmission spectrum (in per μm) for V_{TG} equal to 0 (a), $-\Delta$ (b), -1.5Δ, (c) -2Δ (d), -3Δ (e) and -4Δ (f) at 0 K for $\Delta = 0.04$ eV as a representative case from (a). 177

9.6 Design-C. (a) Current vs top gate voltage at 0 K for $\Delta = 0.02$ eV (red squares) and $\Delta = 0.04$ eV (blue circles). Observe the absence of resonance condition at $V_{TG} = -2\Delta$. (b-f) Transmission spectrum (in per μm) for V_{TG} equal to 0 (b), $-\Delta$ (c), -2Δ (d), -3Δ (e) and -4Δ (f) at 0 K for $\Delta = 0.04$ eV as a representative case from (a). 180

B.1 5-cell wide device for the configuration of Figs. 4.2 (a, d), i.e. E_f = 1 meV and V_{BA} (V_{CA}) = 1 mV. Note stronger confinement towards the edges on all three arms, observed from relative distribution of red region in individual plots, as the intrinsic spin orbit coupling (λ_{SO}) strength becomes progressively stronger from (a) to (d). 194

B.2 Ge device corresponding to Fig. 4.2(c, d), i.e. 1 mV bias for two Fermi-levels (E_f). 195

B.3 Ge device corresponding to Fig. 4.2(e, f) i.e. E_f = 5 meV for two bias (V_{DS})... 193

B.4 Ge device corresponding to Fig. 4.3, i.e. E_f = 5 meV and bias = 4 mV..... 196

B.5 Transmission (T) vs Energy (E) for different devices for transport at equilibrium. (a) Two-terminal Ge device (with SOC). Here, T(E) corresponds to the band structure. Absence of SOC just changes the energy value for inflections in T(E) plot (driven by the change in band-structure). (b) Three-terminal Y-shaped Ge device without SOC. (c) Y-shaped Ge device with SOC. (d) Y-shaped Si device with SOC. (e) Y-shaped Sn device with SOC. (f) Y-shaped Pb device with SOC. (a-f) For various systems T(-E) = T(E). Note that SOC creates spin-polarized edge states that drive the T(E) to one in $\pm$ λ_{SO} energy range, around which T(E) declines similar to the case without SOC (b). If device is sufficiently wide to have first bulk band edge at ~ λ_{SO} eV, then T(E) will be roughly flat throughout $\pm$ λ_{SO} energy range. The local minima of Fig. 4.2(b) and local maxima of Fig. 4.2(c) should be absent for such widths. 199

B.6 Spin and charge distribution for the Germanene Device of Fig. 4.3, i.e. E_f = 5 meV and bias = 4 mV, where color scale gives the magnitude of Trace(σ_Z.Gn). Observe that Fig. 4.3(e) shows that SP should increase for Arm-C and decrease for Arm-B on applying λ_V on Arm-A. However, (b) shows a reduced magnitude of color intensity. This is due to reduced current as shown in Fig. 4.3(a). Increase in spin polarization is verified by plotting the normalized spin distribution as shown in Fig. B.7(b). Color scale has units of per eV. 200

B.7 Normalized Spin-Polarization (SP) distribution (color scale) in Germanene Device for Fig. 4-3, i.e. E_f = 5 meV and bias = 4 meV. Note that color information does not convey full information on spin flux through the device because charge may not be flowing through a certain region. Therefore, the results should be studied together with LDOS (Section B.1) and un-normalized spin-polarization (Fig. B.6) for understanding the concepts presented in chapter 4. 201

C.1 The spin-polarization of Arm-R of a Ge-device with P, Q, and R arm-lengths of 6, 60, and 60 super-cells respectively at E_F = 1 meV and V_{PQ} (V_{PR}) = 1 mV when λ_V is applied only on Arm-R for the spin-filter operation. 202

D.1 Transport at 0 K for k_y = 0 (normal mode) for V_{DS} = 30 mV through 230 nm long and 10 QL thick TI channel with normal-metal contacts on the top. 203

D.2 Transport at 0 K for V_{DS} = 35 mV through 65 nm long TI channel with 100 % polarized ferromagnetic contacts at both ends. Source terminal is magnetized along '+y' whereas drain terminal is magnetized along '–*y*' (a-f) and '+y' (b-l). (a, g)

Current distribution across slab layers of different thicknesses. (b-f, h-l) Energy and transverse mode *kya* resolved Transmission corresponding to current distribution in respective columns for thickness stated on right side in each row. 205

E.1 Non-equilibrium current distribution at 0 K across layers for 10 QL – 60 nm wide – 80 nm long defect free Bi_2Se_3. The ballistic transport properties is presented in (a) current distribution (in uA/eV) along the transport direction, (b) energy integrated current (in μA) distribution across layers and along the channel, (c) current distribution (in uA/eV) across layers of the nanowire, (d) current distribution at source and drain end, (e) bottom layer charge distribution (arbitrary units) i.e. $|\psi^*\psi|$ for the given non-equilibrium condition. (f) Density of states across energy, (g) Transmission across electron-energies, and (h) Mobility distribution across energy. …..... 209

E.2 (a) Density of states (DOS) vs. Energy and (b) Transmission vs Energy of a defect-free Bi_2Se_3 TI-wire (10 QL thick – 60 nm wide – 80 nm long). (c) Bottom layer charge distribution (arbitrary units) i.e. $|\psi^*\psi|$ of the same system. (d) Mobility vs Energy. ……...…….. 210

E.3 Near-Equilibrium transport through Bi_2Se_3 TI-wire (10 QL thick – 60 nm Wide – 80 nm Long) with defects (I. Charge Impurities; II. Vacancies; III. Edge Roughness) as stated in the heading for each sets of plots (a-c). (a) Density of States (DOS) vs. Energy. (b) Transmission vs Energy. (c) Bottom Layer Charge Distribution. (d) Standard-deviation (σ) for Mobility vs Energy for four Different Fermi-Levels (E_f). ……... 214

E.4 Non-Equilibrium transport through Bi_2Se_3 TI-wire (10 QL thick – 60 nm Wide – 80 nm Long) with defects stated over each row. (a,c,e,g,i) Current distribution across layers along the direction of transport. Note that in defect-free case current is perfectly symmetric across middle layer and hence the trend lines overlap. (b,d,f,h,j) Bottom Layer Charge Distribution for respective case. 215

E.5 Non-Equilibrium transport through Bi_2Se_3 Slab. (a ,e) Density of States (DOS) vs. Energy. (b, f) Transmission vs Energy. (c, g) Current Density distribution across quintuple layers of the slab. (d, h) Current Density distribution along the transport direction. 217

F.1 Current vs channel bias for $\Delta = 0.04$ eV at 0 K for a fixed V_{TG} of $-\Delta$ for Design-A (a) and -2Δ for Design-B (b) and Design-C (c). The resonant condition is expected at $V_{DS} = 2\Delta$ in each, but instead observe the increase in current with bias voltage. 221

Chapter 1

Introduction

Inventions and innovations in semiconductor electronics have spearheaded the revolutions in field of information technology, consumer electronics, health industry, military applications and space research for over a century now [1]. These breakthroughs have been chiefly driven by understanding and advances in semiconductor material research. Among these materials, Fe (iron), Co (cobalt) and Ni (nickel) compounds have driven magnetic media and storage [2], whereas Si (silicon) has been the dominant material in computing devices like integrated circuits and microprocessors [3].

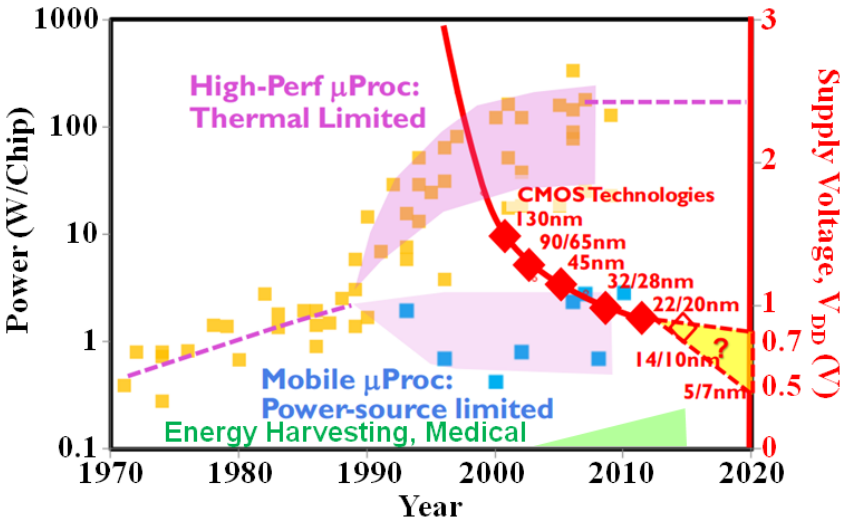

Figure 1.1 Expected power dissipation in microprocessors targeted for high-end markets like servers and mobile devices and for ultra-power segment for energy harvesting and medical applications. Re-adapted with permission from "Challenges & Enablers of LOGIC CMOS SCALING IN THE NEXT 10 YEARS" presentation by Aaron Thean at imec 2013 and Ref. [4].

These computing devices have hitherto exploited the charge based properties of the electron to manipulate and carry information. The exponential down-scaling of the channel length of the transistor, via which this charge flows, for over five decades has driven these innovation trends by packing more functionality per unit die area [5]. With over four billion transistors computing over two billion times per second within

an area of few hundred square millimeters [6], the power density has become a critical issue especially for compute-intensive highly-integrated portable applications operating on battery [7] (see Fig. 1.1). Even for applications drawing power directly from the electrical grid, like for data and network servers, recent worldwide power consumption by these servers has been over a quarter-trillion kilowatt-hour in a year [8, 9].

Figure 1.2 Illustration of some of the benefits of non-volatile computing. Non-volatile electronics is expected to directly benefit in industries like aerospace, health-care, servers, mobile devices (like Internet of Things) and sensors because of the ability to retain data in case of power disruption which may be intentional or otherwise. Image Sources: data centre: https://gcn.com/Articles/2013/03/13/~/media/GIG/GCN/Redesign/Generic/datacenterheat.png; green earth: http://thumbs.dreamstime.com/z/green-earth-19960517.jpg; burning laptop: http://www.laptopmag.com/articles/researchers-burning-hot-notebooks-cause-toasted-skin-syndrome; laptop burn on legs: http://www.gizmodo.com.au/2010/10/what-is-toasted-skin-syndrome/; kid with a laptop: http://thumbs.dreamstime.com/z/child-laptop-26640375.jpg; left pacemaker: https://edmarthey.files.wordpress.com/2011/11/open-heart-surgery.jpg; right pacemaker: http://s3.fortishealthcare.com.s3.amazonaws.com/images/image_popup/MY00276_IM03530_hb7_pacemakerthu_jpg.png.

Hence, devising new low-power computing solutions is an extremely important research area in the field of semiconductors and is expected to benefit in a wide range of applications as schematically illustrated in Fig. 1.2. Another challenge which has emerged with information technology especially internet is the need of tremendous amount of extremely-fast highly-dense storage whose demand is expected

to go over a Zettabyte in this decade [10]. Therefore, devising such storage solutions is also a critical problem in semiconductor research. To sustain the rapid technological innovation, the solution of both the problems has now become apparent in a promising emerging technology called Spintronics [11, 12].

Spintronics maneuvers the spin of the electrons, with or without its charge property, for information processing and storage. It promises new zero standby power computing devices with integrated memory elements to store information in case of power loss which can be unintentional (power failure) or intentional (non-volatile logic NVL), and dense non-volatile memories (NVM) [13]. Additionally, spin based STNOs (spin transfer torque oscillators) operating in GHz range enable new sources of microwave power [14] and spin interaction with light has resulted in creation of new sub-fields like opto-spintronics [15, 16] and spin-plasmonics [17]. Other emerging spin based domains are spin-mechatronics [18] and spin-caloritronics [19, 20] for mechanical and thermoelectric applications.

Spintronics got a major thrust with discovery of GMR (giant-magnetoresistance) [21, 22] and TMR (tunnel-magnetoresistance) [23-25] in magnetic multi-layer system with metallic and insulating intermediate layer for spin-valve and MTJ (magnetic tunneling junction), respectively. This effect has already been deployed in hard disks, and with the recent progress in spin-transfer-torque (STT) devices [26], domain-wall motion (DWM) devices [27], spin field-effect transistors [28] and all-spin logic [29] devices in prototypical computing applications. Initially, driven by success of spintronics in storage industry, the material of choice even for other applications had been ferromagnetic. However, since large spin current [30] is required, in absence of **B**-field (magnetic field), to manipulate the magnetic moment of ferromagnetic material and superparamagnetism makes the spin thermally unstable

[31] for targeted device dimensions, research has advanced through materials [11] like half-metallic oxides (CrO_2, Fe_3O_4, double Perovskites) and III-V and II-VI dilute magnetic semiconductors (DMS) [32, 33].

However, due to problems of inefficient spin-injection [34] from ferromagnetic source terminal into DMS and oxides, loss of spin-based information due to spin dephasing in these channel and small transition temperature (well below room-temperature) for DMS, the materials like InAs that can form 2DEG (two-dimensional electron gas) with spin-orbit coupling (SOC) [35] have been studied as an alternative [36] to generate spin-polarized current that can be manipulated via pure electronic controls. Spin-orbit coupling, which is a relativistic quantum effect, manifests effect of **B**-field on electrons flowing through the channel under electric field (**E**-field) and provides better spin control [37] and possibility of new functional devices.

1.1 Dirac-Band Materials

For compute-intensive applications, besides good spintronic properties for non-volatile functionality to reduce power, it is critical to have high operating speed. This later criteria benefit tremendously from the large velocity of the carriers in the device, and has been one of the key driving force for the emerging trend of III-V material integration with silicon for charge-based computing. The breakthroughs in the last ten years have, however, furnished new set of materials with linear gapless Dirac-bands in bulk (Group-IV monolayers sheets, Cd_3As_2, Na_3Bi) or surface (Bi_2Se_3, Sb_2Te_3, $Pb_xSn_{1-x}Te$) or edge (HgTe, Group-IV monolayers nanoribbons). These materials provide some of the largest drift velocities among extant materials, robustness to scattering and good spin control and transport.

Graphene, the first two-dimensional (2D) material, since its realization in 2004 [38] has spawned new possibilities for physicists and device engineers alike [39]. The relativistic linear Dirac-bands with reported Fermi-velocity up to 2.5×10^6 m/s [40], extremely high mobility of over 200000 $cm^2V^{-1}s^{-1}$ [41] and Klein tunneling in graphene makes it an excellent material for electron transport in THz high-speed [42, 43] and low-power atomically-thin devices [44, 45] of the future. The larger spin-orbit coupling (SOC), than in graphene, in later 2D-materials like Silicene and Germanene [46] provides an additional control over the spin of an electron, which can possibly be used for non-volatile logic and zero-standby power applications [47].

Investigation of SOC in graphene [48] has, however, taken a more prolific research direction with more recent discovery of topological insulating (TI) phase of matter in both 2D [49, 50] and three-dimensional (3D) [51, 52] systems. TI gets its unique advantage from having bulk band gap and SOC engendered spin-momentum locked helical Dirac 2D surface-states (1D edge-states) in 3D (2D) materials with large Fermi-velocity (~ 3-5 x 10^5 m/s in Bi_2Se_3 [53-56]) which are robust to non-magnetic impurities and disorders [57]. The suppression of backscattering in both 2D [58] and 3D [59] TIs and weak electron-phonon coupling [60] enables dissipationless surface (edge) transport. Additionally, the majorana-fermion quasiparticles are expected to exist at 3D TI-superconductor interface [61]. Therefore, topological insulators are posited to have gamut of applications ranging from interconnects [62], spintronics [63], optoelectronics [16] to quantum computing [64], making them one of the most important contemporary material under investigation.

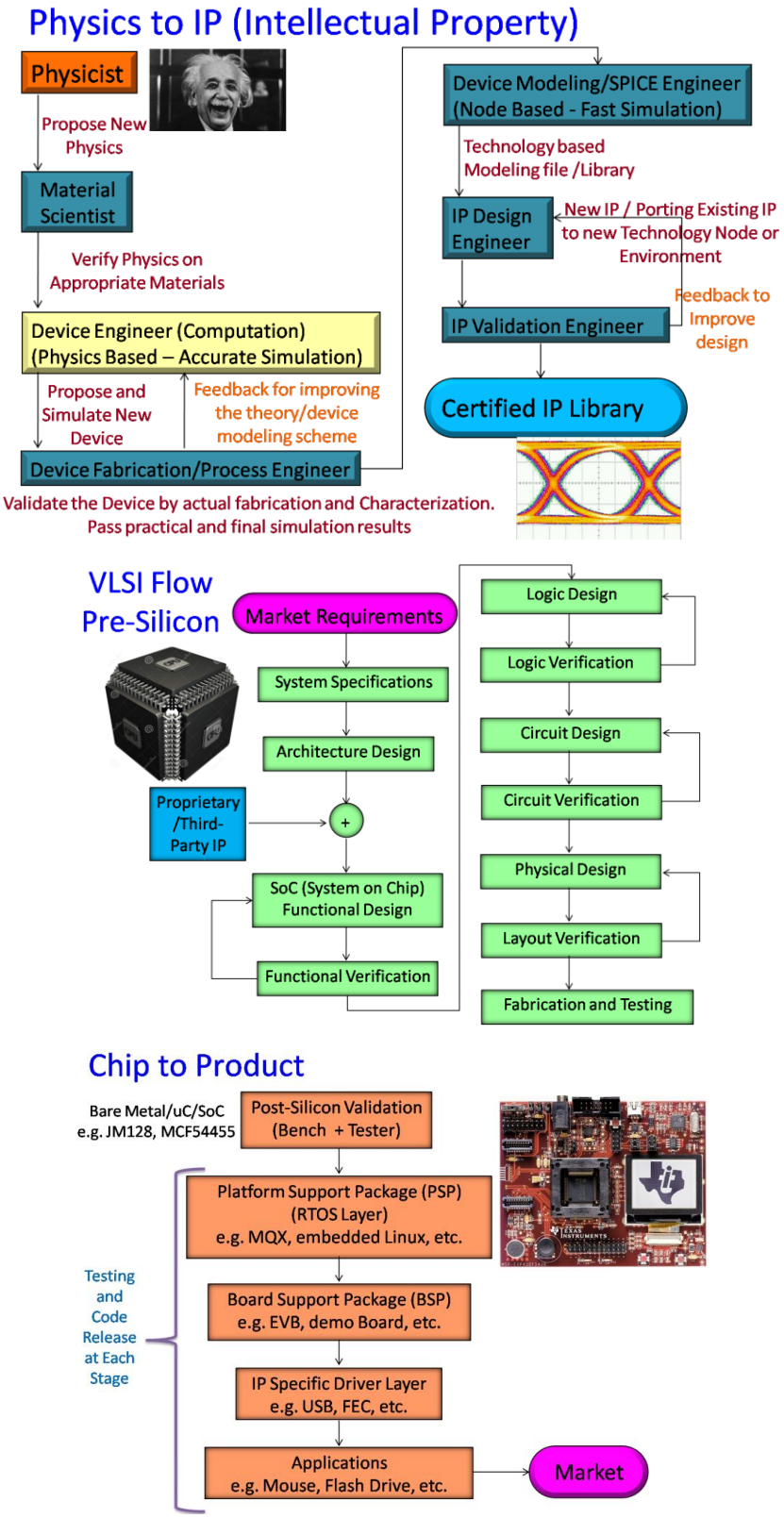

Figure 1.3 Overview of the flow of a new discovery in semiconductor physics to a product in the market. Observe that the physics-based accurate simulations mark the transition of concept from investigating physics to design and optimization for the computing or memory chips. Images Sources: Dr. Albert Einstein: http://www.deism.com/einstein.htm; eye-diagram: http://thenetworksherpa.com/wp-content/uploads/2013/10/s2gx-rollout-6g-eye.jpg; Three black chips: http://thumbs.dreamstime.com/z/three-computer-chip-processor-3d-isolated-27584453.jpg; Texas Instruments board: http://www.newark.com/productimages/nio/standard//4627300.jpg.

1.2 Objectives of Research

Figure 1.3 illustrates the flow of a new physics discovery to a product in the market. The accurate simulation of device physics (yellow block) enables semiconductor community to filter-in only relevant materials and device designs for subsequent costly experimental evaluation for developing the application, and hence carefully guard the future of semiconductor electronics. The key to developing next-generation of device applications via Dirac-band materials is to understand how the current and spin is carried in these materials. For this the quantum transport model and simulator has to be developed for characterizing the device, appraising and predicting the device performance to avoid post-fabrication failures. Therefore, the carrier transport in Dirac-band material based devices must be thoroughly investigated in both absence (ballistic) and presence of different scattering mechanisms like phonons and defects to develop a comprehensive understanding of transport physics in these systems, which serves as the research objective of this thesis. This thesis, accordingly, endeavors to achieve the following objectives:

1. Develop a quantum transport simulator based on non-equilibrium green function formalism (NEGF) for extensively parallelized computing on both traditional computing hardware (CPU cores) and novel General-Purpose Graphic Processing Unit (GPGPU).

2. Use the above simulator to investigate carrier (charge and spin) transport through key Dirac-band materials under various physical and electronic constraints. Group-IV materials with (Silicon, Germanium, Tin, Lead) and without (Carbon) SOC have been chosen for 2D systems, while Bi_2Se_3 as 3D-TI has been chosen as exemplar material.

3. The understanding of transport has then been applied to propose and evaluate new charge and spin-based devices established from the Dirac-band materials. Four

devices i.e. Graphene electro-optic transistor, Group-IV monolayer spin-separator and spin-filter, 3D-TI interconnect, and 3D-TI based band-alignment induced resonance devices have been investigated.

The results of this research on the carrier transport in Dirac-band materials and their device applications should serve to enhance the understanding of these materials for designing new low-power high-speed computing systems.

1.3 Organization of Thesis

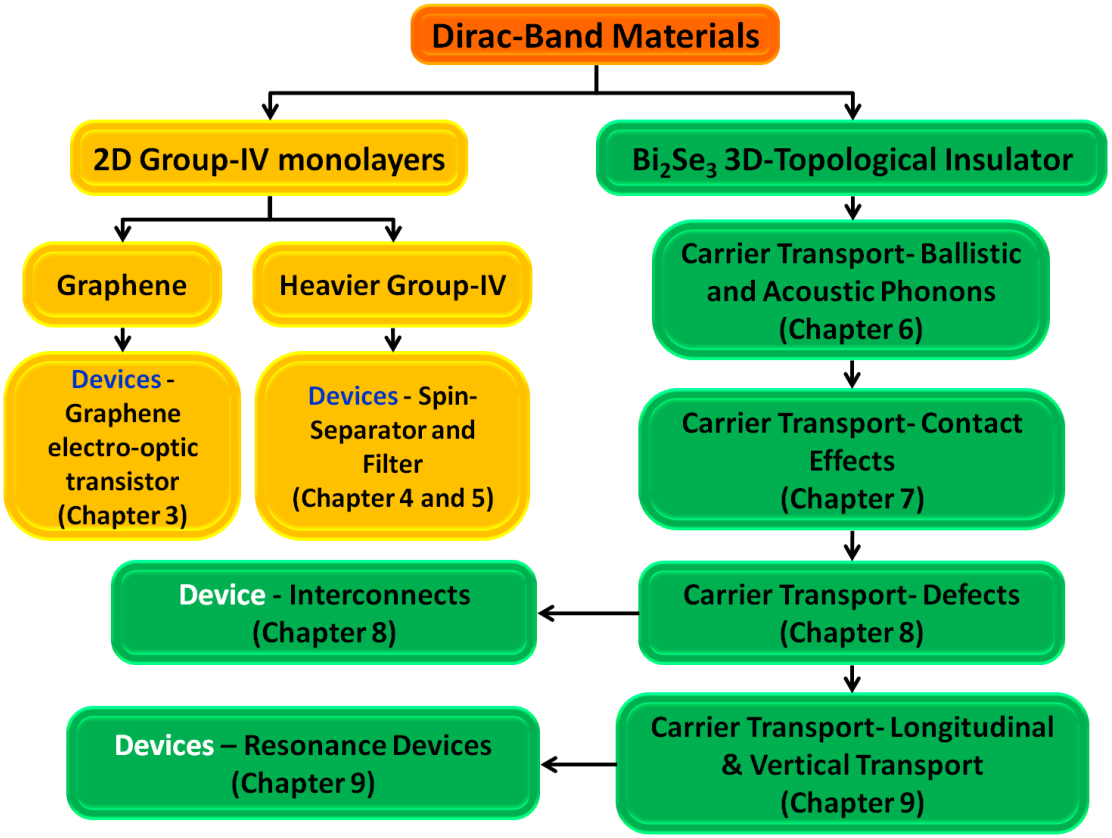

Figure 1.4 Organization of the thesis illustrating the flow of the investigation for the carrier-transport in the Dirac-band materials and the devices.

This thesis is organized as follows:

After the introduction and motivation for the thesis in **Chapter 1,** the electronic structure of materials is investigated in **Chapter 2**. It also summarizes the NEGF formalism for developing the quantum simulator for appraising carrier transport in Dirac-band materials.

Firstly, non-conventional charge-based switching devices in Graphene, the seminal Dirac-band material with one of the weakest scatterings and hence largest mobility, are investigated in **Chapter 3.** This chapter presents a computational comparison of device performance for two proposed Graphene electro-optic transistors by evaluating the device geometry, temperature and voltage conditions, to examine an exotic approach of achieving high current-switching ratio with sub-60 mV/decade subthreshold-slope (at room-temperature) in gapless Dirac-bands without actual bandgap opening.

However, Graphene has extremely weak SOC and may support only charge based devices in pristine form. Magnetic dopants in graphene have not been considered in this thesis because of reduced external control on spin due to fixed magnetization of the magnetic dopants. Nevertheless, going down the periodic-table, although the mobility of Group-IV semiconductors decreases, the SOC becomes stronger and hence these materials (Si, Ge, Sn and Pb) may provide a handle on both charge and spin for realizing more optimal low-power devices.

Hence, then **Chapter 4** presents the investigation of charge and spin transport in 2D Group-IV monolayer materials in quantum spin hall phase and appraise the feasibility of an extremely efficient three-terminal Y-shaped spin-separator device.

This work although shows that an efficient spin-separator can be realized from Group-IV monolayers, it is also observed that the device characteristics are vulnerable to quantum phase transition and more easily for the materials with relatively small SOC like silicene and germanene. Moreover, Y-shape is observed to induce Fano interference and degrade the transport behaviour.

Chapter 5, thence, presents the effect of phase-transition from the quantum-spin-hall to the band-insulator phase in 2D Group-IV monolayer materials on the

transport through a three-terminal U-shape spin-separator device that can be extended to operate as a spin-filter by selectively inducing the phase transition in the channel.

The small bulk-band-gap and hence the feasibility to obtain strongly spin-polarized transport only along the edges of the nanoribbon in the above devices, severely limits the magnitude of the drive current. The three-dimensional (3D) Dirac-band materials like topological insulators (TI) dispense spin-polarized transport on the entire surface and hence much larger currents can be obtained. Furthermore, among the experimentally proven 3D-TIs hitherto, Bi_2Se_3 has the largest bulk band-gap of 0.3 eV which provides relatively large operating energy window for spin-polarized electrons for transport.

However due to poor understanding of transport behaviour in these materials at the time of this work, firstly carrier transport is investigated in Bi_2Se_3 3D-TI. Thus, **Chapter 6** expounds a model for quantum transport in the thermal activation regime in a Bi_2Se_3 3D-TI slab with the inclusion of acoustic phonon scattering to comprehensively appraise their transport physics and explain the anomalous experimental observations in resistance vs temperature trends. It furthermore, suggests an experimental strategy for obtaining a handle on the strength of electron-phonon coupling in topological insulators via temperature-dependent transport measurements.

For the quantum devices, understanding the transport channel is insufficient because of the sizeable influence of the contacts on the device characteristics. Hence, **Chapter 7** subsequently presents the effect of different contact configurations (semi-infinite extended-channel, normal metal and ferromagnetic metal) on quantum transport through thin Bi_2Se_3 3D-TI slab, and applies it to explain another experiment on electrical detection of spin-momentum locking on topological surface. It also suggests a simple mechanism to validate topological insulators via quantum transport experiments.

Then **Chapter 8** examines the first application of 3D-TI in this work i.e. the feasibility of using thin 3D-TI (Bi_2Se_3) wire for the local electrical interconnects, as a replacement of Cu for future chips, in the presence of edge roughness, vacancies, acoustic phonons and charge impurities across temperature and Fermi-level.

For the second application of 3D-TI, **Chapter 9** presents an investigation of band-alignment induced current modulation in Bi_2Se_3 3D-TI slab for three different device designs, one for purely lateral transport and other two with vertical transport, to appraise the possibility of a 3D-TI based resonant device for the pursuit in the future for spintronic oscillators and analog multipliers based on band-alignment induced resonance.

Finally, **Chapter 10** concludes the thesis and suggests future works in this area.

The organization of the thesis is illustrated in Fig. 1.4.

Chapter 2

Methodology

Classical mechanics fails to describe the carrier transport in nanoscale devices required for next-generation of low power high-speed applications. In these devices quantum mechanical phenomenon like energy band quantization, tunneling and wave nature of electrons dominate the transport physics. Such devices have to be investigated and characterized via quantum simulator based on Schrödinger equation. Complexity of solving many-body quantum mechanical equation has been circumvented with the evolution of NEGF formalism with certain acceptable approximations for simulating material properties and devices with contacts and various scattering mechanisms.

One of the key inputs to NEGF is the Hamiltonian that describes the electronic interactions in the system. The formalism can provide spatially resolved the current, charge, spin (for spin-resolved basis) and density of states information for all relevant electron-injection energies. The tight-binding model developed by various schemes like fitting to experimental data, ab-initio approach and discretization of *k.p* model is often used to describe Hamiltonian for device simulations. This chapter elucidates the Hamiltonian for materials investigated in this thesis, followed by a summary of NEGF formalism used for developing quantum simulator. This is followed by a summary and justification for using heavily parallelized non-conventional hardware platform of GPGPUs for computationally intensive full real-space modeling of topological wires.

2.1. Hamiltonian

2.1.1. Electronic Structure of Group-IV Monolayer

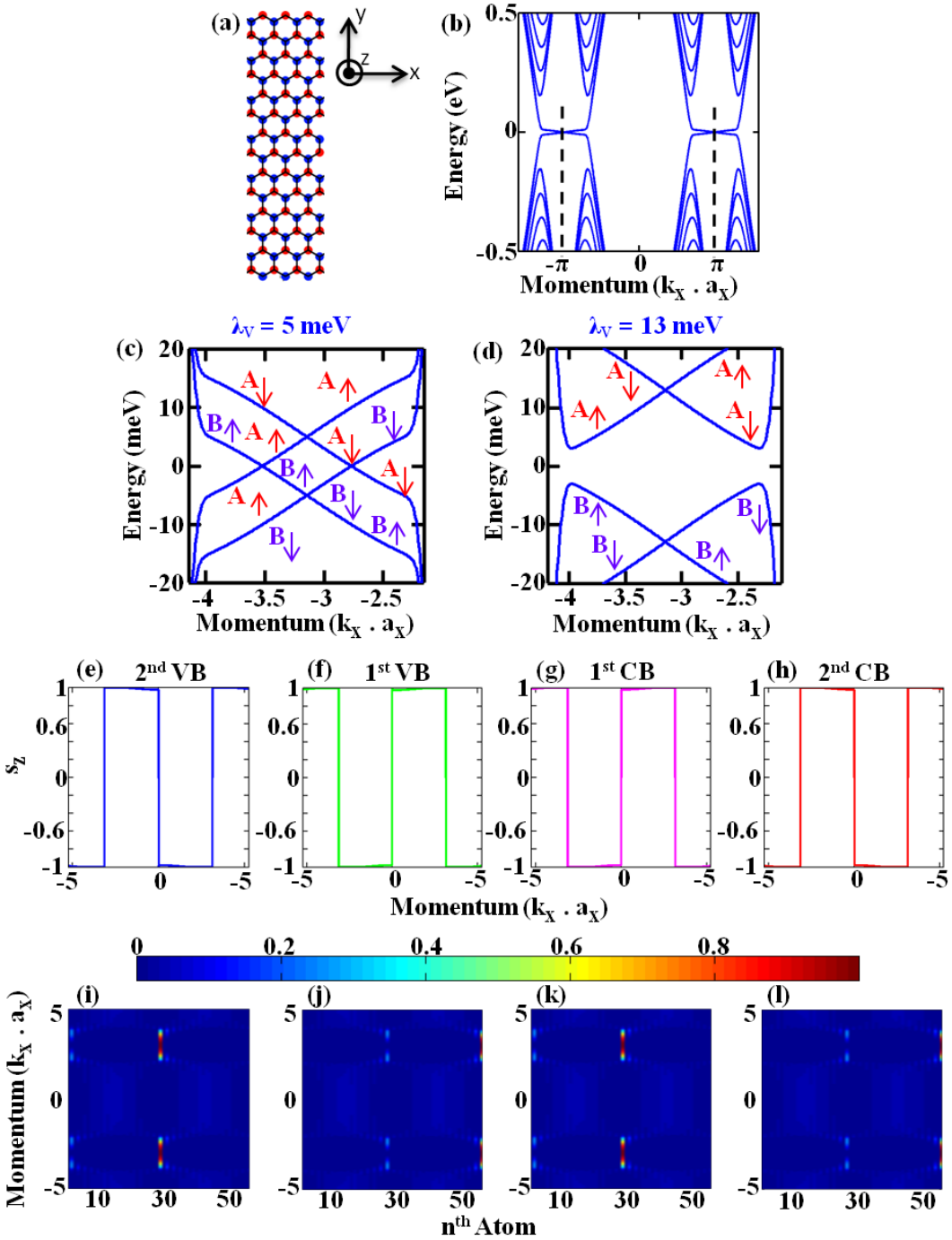

Figure 2.1 (a) Zigzag-Nanoribbon (ZNR) of monolayer Group-IV material. The device lies in the *x-y* plane. The red (type-A) atoms are out-of-plane from the blue atoms (type-B) by Δ_C along the *z*-axis because of the buckling in the material. Energy Bands for 14 rings wide (166.46 Angstroms) zigzag-Germanene Nanoribbon (GeNR) in unbuckled state (b), Quantum-Spin Hall (QSH) phase (c) and band-insulator (BI) phase (d). In (e-i) a small λ_V (~ 0.005 λ_{SO}) is applied is life band degeneracy to distinguish the bands computationally. (e-h) spin-polarization (along z-axis) of the first two conduction and valence bands (CB and VB). (i-l) $|\psi^*\psi|$ distribution across momentum-vector and atom-position (see discussion) shows edge-localized characteristic of Dirac-bands which extend from approximately $+\lambda_{SO}$ to $-\lambda_{SO}$ energy range in (b). The red region in (i, k) corresponds to n=29 i.e. on bottom-edge (type-B blue atoms) while for (j, l) n=56 i.e. on top-edge (type-A red atoms).

Figure 2.1(a) illustrates a schematic of zigzag nanoribbon (ZNR) which embodies the spintronic devices studied in **Chapter 4 and 5**. For identification, the numbering has been assigned to atoms as follows: 1 to bottom left-most atom with an increment towards the top and then to next bottom most atom on the next right column of atoms. Therefore, for 'm' rings along the width, bottom-edge atom is numbered 2m+1 while top edge is at 4m. The four-band tight-binding parameters are employed to model the device Hamiltonian which was extracted in Ref. [65] by fitting tight-binding parameters to the ab-initio calculations. The details of the derivation of the Hamiltonian are available in Ref. [66]. The Hamiltonian H is,

$$H = -t\sum_{<ij>,s} c_{is}^{\dagger}c_{js} + i\frac{\lambda_{SO}}{3\sqrt{3}}\sum_{<<ij>>,ss'} v_{ij}c_{is}^{\dagger}\sigma_{ss'}^{z}c_{js'} + i\frac{2\lambda_R}{3}\sum_{<<ij>>,ss'} \mu_{ij}c_{is}^{\dagger}(\boldsymbol{\sigma}\times\boldsymbol{d}_{\boldsymbol{ij}})_{ss'}^{z}c_{js'}$$
$$+ \lambda_V\sum_{i,s}\xi_i c_{is}^{\dagger}c_{is} + h\sum_{i,ss'} c_{is}^{\dagger}\sigma_{ss'}^{z}c_{is'} \qquad (2.1)$$

where t is the nearest-neighbour hopping term on the honeycomb lattice. $c_{is}^{\dagger}$ and c_{is} are respectively the creation and destruction operators for the spin-polarization s at site i. The intrinsic (λ_{SO}) and Rashba (λ_R) spin-orbit interactions are represented in the second and third terms respectively for the system with the inversion symmetry. But mirror symmetry is violated in the third term, which also involves spin-dependent next nearest-neighbour (NNN) hopping. In the second term, v_{ij} is given by $(\boldsymbol{d_i}\times\boldsymbol{d_j})^z/|\boldsymbol{d_i}\times\boldsymbol{d_j}| = \pm 1$ with two nearest-neighbour bonds, $\boldsymbol{d_i}$ and $\boldsymbol{d_j}$ connecting NNN $\boldsymbol{d_{ij}}$. $\boldsymbol{\sigma}$ are Pauli spin-matrices.

Furthermore, μ_{ij} = 1(–1) for connecting A-A (B-B) sites. The fourth term breaks inversion symmetry via staggered sublattice potential ($\xi_i = \pm 1$), which arises when an external perpendicular differential electric field (λ_v) is applied. The last term reflects the effect of exchange field with strength h. The values of the constants are

summarized in Table I of Ref. [65] (reproduced here as Table 2.1 for the convenience of the reader). Energy-bands are plotted in Fig. 2.1(b, c, d) for Ge-NR as an example for unbuckled system, in QSH and in BI phase respectively.

Table 2.1 Model parameters for Hamiltonian in eq. (2.1).

	a (Angstrom)	Δ_C (Angstrom)	t (eV)	λ_{SO} (meV)	λ_R (meV)	l (e Angstrom)
Si	3.87	0.44	1.04	4.2	8.66	0.035
Ge	4.06	0.68	0.97	11.8	2.81	0.046
Sn	4.67	0.84	0.76	36.0	18.75	0.055
Pb	4.93	0.89	0.72	207.3	0.06	0.143

Lattice constant (a) with buckled structure, buckling distance (Δ_C), transfer energy (t), spin-orbit coupling (λ_{SO}), Rashba spin-orbit coupling (λ_R), and the linear dependence of the applied electric field on λ_V ($l \equiv \lambda_V/E_Z$)

In unbuckled system, bands are degenerate although spins are localized on opposite edges i.e. the system is by default in QSH phase. By applying a small field the degeneracy is lifted to clearly distinguish the spin-polarized bands. However, applying strong field drives the system into BI phase where both the spins are on same type of atoms because bands are re-inverted, as well as, a band-gap opens up in the dispersion. The critical field at which nanoribbon transits from QSH to BI phase is a function of ribbon width and tends to λ_{SO} for 2D sheet. This shall be dealt in more depth in section 5.3 where the transport through these bands and the effect of phase transition is discussed. Next, more detailed distribution of spin and wavefunction across the wave-vectors across the ribbon are illustrated in Fig. 2.1(e-l) for QSH phase. Observe that the bands are strongly spin-polarized (Fig. 2.1(e-h)) and localized on the edges (edge-states) (Fig. 2.1(i-l)).

2.1.2. Electronic Structure of Bi_2Se_3 Three-Dimensional Topological Insulator

In this section, we present the tight-binding model used to simulate transport through Bi_2Se_3 3D-TI. The other common models in literature are 2×2 Dirac Hamiltonian and 4x4 Zhang's Hamiltonian [67] which primarily describe transport only on the surface. In reality, the surface wavefunction actually penetrates into the sub-surface layers [68] and moreover, for thin layer 3D-TI, the opposite surfaces may be coupled. The Dirac model cannot capture this effect, whilst our model allows us to simulate distribution of current and electron flow across layers, and thus mimic the actual 3D-TI.

In order to realistically describe both the surface and the bulk states on the same footing, the model Hamiltonian of Refs. [69, 70] was adapted, including real space hopping parameters normal to the [111] surface of Bi_2Se_3, which is a layered material consisting of stacks of quintuple layers (QLs) [71] . For each QL, the effective Hamiltonian is given by

$$H_p = \begin{bmatrix} k^2/m_1 & d + k^2/m_2 & ivk_x - vk_y & 0 \\ d + k^2/m_2 & k^2/m_1 & 0 & -ivk_x + vk_y \\ -ivk_x - vk_y & 0 & k^2/m_1 & d + k^2/m_2 \\ 0 & ivk_x + vk_y & d + k^2/m_2 & k^2/m_1 \end{bmatrix} \tag{2.2}$$

where v is the velocity parameter, m_1 and m_2 are the orbital masses, and the parameter d is the hopping between the two same-spin orbitals within the QL [69]. This Hamiltonian is constructed by considering the two equivalent Se atoms within the QL where each Se atom has two up and down spin p_z orbitals. This choice of basis set is supported by the related first-principles calculations [71], which show that the most important orbitals around the Fermi level are the Se p_z orbitals.

The hopping between the two adjacent QLs is realized by

$$T = \begin{bmatrix} 0 & 0 & 0 & 0 \\ t_z & 0 & 0 & 0 \\ 0 & 0 & 0 & 0 \\ 0 & 0 & t_z & 0 \end{bmatrix} \tag{2.3}$$

where t_z is the nearest-neighbor hopping parameter. The total Hamiltonian for a Bi_2Se_3 (semi-infinite) slab can thus be written as

$$\overline{H} = \begin{bmatrix} H_1 & T_1 & & & 0 \\ T_1^{\dagger} & H_2 & T_2 & & \\ & T_2^{\dagger} & H_3 & & \\ & & & . & \\ 0 & & & & . \end{bmatrix} \tag{2.4}$$

where H_i=H_p and T_i=T where i denotes the index of QLs. Values of various parameters used in the present computations are: m_1 = 0.125 eV^{-1}-$Å^{-2}$, m_2 = −0.04 eV^{-1}-$Å^{-2}$, d = −0.22 eV, v = 2.5 eV-Å, and t_z = 0.35 eV. In-plane wavevector k is computed as $k^2 = k_x^2 + k_y^2$ where k_x and k_y are wavevectors along x-axis and y-axis, respectively.

In modeling transport, it is important that the underlying dispersions are described properly. For this reason, the preceding model parameters were chosen to fit the experimental dispersion and yield a semiconducting bulk gap ~300 meV. This is more realistic than the use of parameters fitted to first-principles band structures, which typically underestimate the bandgap and Fermi velocity of the surface states. Our model parameters, on the other hand, yield an excellent fit to the experimental ARPES results of Refs. [57, 72] for energies less than 250 meV above the Dirac point and are thus well suited for our low-energy transport computations. Notably, our model has the advantage of allowing simulations for an arbitrary slab thickness, and it captures reasonably both the nontrivial topological surface states and the quantum well states due to real space confinement.

The sample thickness has been chosen to be sufficiently large [73] so that inter-surface coupling effects are negligible [74]. The electronic structure of a 13-QL slab is shown in Fig. 2.2(a). The local charge distribution, see Fig. 2.2(b), was plotted for Dirac bands to quantitatively verify their localization in surface layers. The model is seen to correctly give the left-handed chirality of the spin texture for the upper Dirac cone on the top surface as shown in Fig. 2.2(c). The direction of the spin reverses for the surface states on the bottom surface (Fig. 2.2(d)). The energy-dispersion for side-surfaces is next appraised in Figs. 2.2(e) and 2.2(f) for two different widths (confined along y-axis) but infinitely (periodic boundary condition) thick (z-axis) and long (x-axis). The observation of side surface topological bands further strengthens the confidence in Hamiltonian.

The slab imposes periodic boundary condition along the width and the simulation along this transverse direction is executed in mode-space, as explained in next section. For simulating defects like impurities, vacancies and edge roughness, the transverse direction should be of finite width and thus described in the real-space. The energy bands for 3D-TI wire of finite width for an exemplar case are plotted in Fig. 2-3(a). In Fig. 2.3(a), the confinement along transverse direction quantizes the bands resulting in the opening up a small bandgap. To validate the topological property of the wire, the local density of states (LDOS) across the 3D-TI layers had been plotted as shown in Fig. 2.3(b). It is important to ascertain topological behaviour for a nanowire before evaluating transport because strong confinement (finite-size effect) may destroy topological characteristics [75] along with the corresponding touted conductance properties.

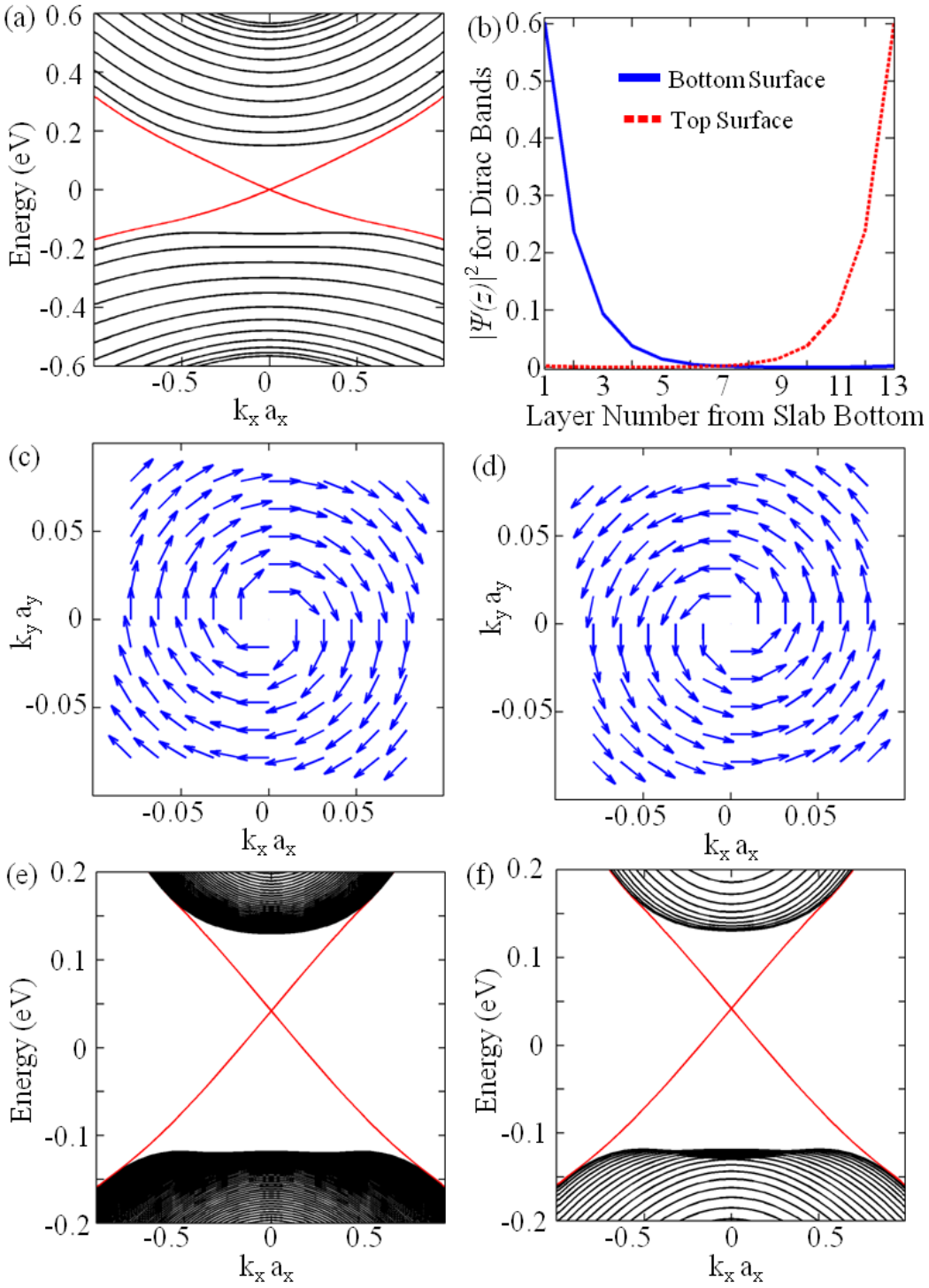

Figure 2.2 (a) Energy bands for a 13-QL slab of Bi_2Se_3 obtained from our model Hamiltonian, exhibiting the Dirac-cone surface states centered at the Γ-point (red bands). (b) Layer-dependent charge density of the surface states (bottom surface, blue solid line; top surface, red dashed line) around the Γ-point [76]. Also, note the major contribution (60%) of helical states from surface layers and their significant penetration into bulk layers [68]. In-plane spin texture of topological surface states in the conduction band around the Γ point for top (c) and bottom (d) surfaces illustrates left-handed and right-handed chirality. (e) and (f) Energy dispersions on the side surfaces for 200 and 50 nm wide slabs (infinitely thick along the z-axis) respectively, for k_z = 0/Å. Side surface Dirac bands, therefore, require the sample to be both sufficiently thick (z-axis) and wide (y-axis). The anisotropic behaviour [77] in Bi_2Se_3, however, allows the observation of Dirac bands on the top and bottom surfaces for a relatively much smaller thickness (>6 QLs) [78] but wide samples.

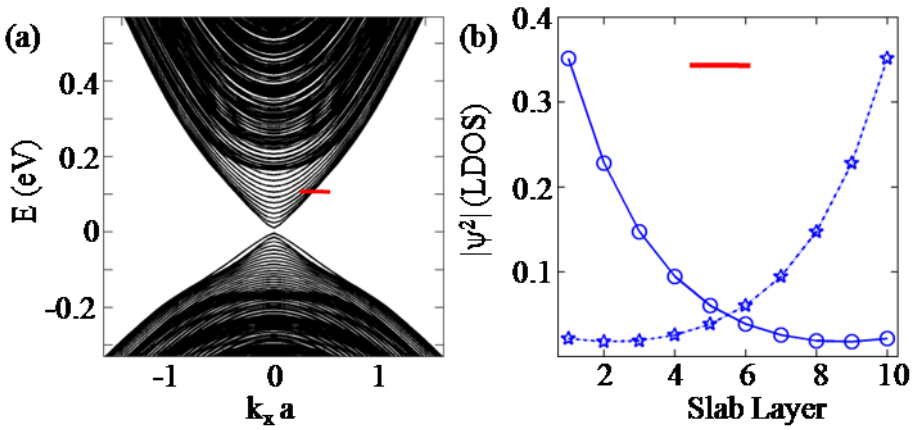

Figure 2.3 (a) Energy Bands for 10 QL thick (z-axis) – 60 nm wide (y-axis) Bi_2Se_3 TI nanowire. Small energy bandgap opens due to confinement along y-axis. (b) Local Density of States (LDOS) (ψ^2) distribution across layers (QLs) of the wire for the first conduction band at the k-point marked ($k_x a \sim 0.5$) with red line in (a). Top and Bottom surfaces can be clearly distinguished from (ψ^2) distribution which shows localization on the surface layers in accordance with the topological properties. A representative Bi_2Se_3 3D-TI wire of 10 QL thickness – 60 nm width – 80 nm length has been chosen in this chapter unless specified otherwise.

We emphasize that 3D TIs do not possess an ideal Dirac cone dispersion and exhibit hexagonal warping effects [69, 70] [72]. Compared to Bi_2Te_3 [79], the warping effect in Bi_2Se_3 is relatively weak. ARPES results on Bi_2Se_3 show approximately isotropic energy contours up to 250 meV above the Dirac point [see Fig. 2(e) of Ref. [72]), while this is not the case in Bi_2Te_3 (see Fig. 1(b) of Ref. [80]). Since, in this thesis, the transport computations on Bi_2Se_3 only access states lying less than 250 meV above the Dirac point, this Hamiltonian is expected to capture the relevant physics reasonably.

2.2. Non-Equilibrium Green's Function Formalism

The quantum transport computations in this thesis have been performed via Non-Equilibrium Green function (NEGF) formalism [81, 82], except in **Chapter 3**. Briefly the quantum transport simulation is described by following steps in sequence:

(i) Extract the Hamiltonian in tight-binding model (TBM) from *k.p* theory or ab-initio simulation. This should provide the matrix elements either as constant interaction terms or as function of wave-vector k_m where 'm' is the basis of the coordinate system.

For transport, k_m is discretized via finite difference method (FDM) by substituting it by $-i\nabla_m$. This operation should be applied at least in the direction of transport with appropriately selected unit-cells to obtain planes orthogonal to the transport direction. If there is a confinement along any or both of the other two-basis of the coordinate system, the discretization should be done with appropriate substitution.

In this work, all TBM parameters for Group-IV monolayers have been extracted from ab-initio calculations in Ref. [65], whereas the in-plane parameters for Bi_2Se_3 3D-TI are in described by ***k.p*** theory. Therefore, for simulating 3D-TI slab (emulating infinite width with periodic potential) of finite thickness only k_x is discretized, whereas for a nanowire k_y is also decomposed to obtain interaction matrix along y-axis, as described in respective chapters.

(ii) The Hamiltonian and the hopping matrices (onsite, forward and backward interaction) should be verified via energy-dispersion plots.

(iii) The transport through the system should be modeled via NEGF equations.

(iv)The equilibrium transmission should then be validated against the energy-dispersion.

(v) Non-equilibrium transport is then executed and appraised for unexpected data which may be a novel result or more probably a bug in the code.

For modeling transport via NEGF, firstly the impulse response to the system is given by retarded Green's function [G^r] as,

$$\left[G^r\right]=\left[(E+i\eta)I-H-U_0-\Sigma_{contacts}-\Sigma_{scattering}\right]^{-1} \tag{2.5}$$

where E is the electron-injection energy, U_0 is the potential profile in the system and $\Sigma_{contacts}$ is the net self-energy of all the terminals, which is obtained by simply adding the self-energy matrices of each terminal 'k'. In this work, for three-terminal devices $\Sigma_{contacts} = \Sigma_{source} + \Sigma_{drain1} + \Sigma_{drain2}$, whereas for two-terminal device it is only source and

drain. $\Sigma_{scattering}$ is net self-energy from scattering mechanism provided they can be modeled in this form.

A particular case of acoustic phonons has been used in this work for investigating carrier transport in 3D-TI. The relevant equations for acoustic phonons are described in **Chapter 6**. η is a very small positive number (~ 10^{-6}) and numerically makes the system causal with a convergent solution, whereas negative value will give advanced Green's function and an unphysical solution. Computationally, it smears the energy levels and connects the battery (contacts) with the channel. For computing surface-Green function, the second-order norm of successive modifications to be less than 10 ppm has been used as the convergence criterion in this work.

Self-energy for each terminal k is computed from the surface-green function g_k^S as,

$$\left[\Sigma_k\right] = \left[\tau_k\right]\left[g_k^S\right]\left[\tau_k\right]^{\dagger} \tag{2.6}$$

where τ_k is the hopping-matrix at the terminal and represents coupling between the contact and the channel. If τ_k is same as hopping matrix of the channel material, Eq. (2.6) models the ideal contacts [83], with perfect transmission at terminals, assuming same material for contacts and channel. For such cases, surface-green function has been computed iteratively by implementing the Sancho-algorithm [84].

For the semi-infinite metallic contacts, g_k^S is phenomenologically calculated [85] assuming constant density of states (DOS_M [86]) (~ 0.008 eV^{-1}) of metal and a contact-coupling coefficient (α), in range of 0 to 1, that describes the quality of contact with channel. The contact self-energy for metallic contacts therefore becomes

$$\left[\Sigma_k\right] = -i\Delta = -i\pi\alpha^2 trace\left(\left[\tau_k\tau_k^{\dagger}\right]\right) DOS_M \left[I_{side}\right] \tag{2.7}$$

where, I_{Side} is identity matrix of size, number of layers × basis size, between metallic contact and channel. Next, the self-energy gives level-broadening matrix Γ_k for the terminal k as,

$$[\Gamma_k] = i\,([\Sigma_k - \Sigma_k^{\dagger}]) \tag{2.8}$$

and spectral function [A] and Density of States (DOS) as,

$$[A] = i\,([G^r - G^{r\dagger}]) = 2\,\pi\,[DOS] \tag{2.9}$$

The correlation matrix G^n is then computed on appropriately weighing Γ_k with Fermi-distribution f_k at each terminal,

$$\left[G^n\right] = \left[G^r\right]\left(\left[\Gamma_k\right] f_k + ...\right)\left[G^r\right]^{\dagger} = \left[G^r\right]\left[\Sigma^{in}\right]\left[G^r\right]^{\dagger} \tag{2.10}$$

where Σ^{in} is the in-scattering function. The transmission T(E) for a given electron-injection energy, through the system from terminal k_1 to k_2 is computed as,

$$T_{k_1 k_2}(E) = Trace\,(\Gamma_{k1}\,G^r\,\Gamma_{k2}\,G^{r\dagger}) \tag{2.11}$$

From the correlation matrix G^n and the forward and backward interactions in the Hamiltonian, the current between two adjacent orthogonal blocks of unit-cell ‘u’ and ‘v’ is calculated for each terminal as,

$$I_{u->v} = \frac{q}{h}\int_{\mu_D - 6K_BT}^{\mu_S + 6K_BT} dE\; Trace(i[H_{uv}G^n_{vu} - G^n_{uv}H_{vu}]) \tag{2.12}$$

and the spin-polarization SP of the current along axis ‘p’ (for instance p may be z-axis in Cartesian coordinates) is calculated from the corresponding Pauli matrix σ_p and G^n by taking an average of the SP computed at each energy point E along the energy-grid,

$$SP_p = \frac{1}{\mu_S - \mu_D + 12K_BT}\int_{\mu_D - 6K_BT}^{\mu_S + 6K_BT} dE\,\frac{Trace(\sigma_p.G^n)}{Trace(G^n)} \tag{2.13}$$

where μ_D and μ_S are electro-chemical potentials at the source and drain terminals, related by the expression $\mu_D = \mu_S - V_{DS}$ for positive bias V_{DS}.

For the negative bias, the role of μ_D and μ_S should be swapped in the limits of the integration in Eq. (2.12) and Eq. (2.13). K_B is the Boltzmann constant in eV-K^{-1}, and in the integration limits it accounts for the spread in Fermi-distribution at a finite temperature T.

For systems with infinite width, since the transverse axis is in mode space ky, the current equation becomes

$$\frac{I_{u->v}}{Width} = \frac{q}{h}\int \frac{dk_y}{2\pi} \int_{\mu_D - 6K_BT}^{\mu_S + 6K_BT} dE\, Trace(i[H_{uv}G^n_{vu} - G^n_{uv}H_{vu}]) \tag{2.14}$$

Note that similar integration over transverse modes should be carrier out for other NEGF parameters if applicable e.g. for transmission.

Since, the retarded Green's function G^r (Eq. (2.5)) is a function of spatial dependence along the channel (x-axis), layers (z-axis) (if applicable), energy (E) and the transverse momentum (k_y) (if applicable), I_{uv} has information on the current flowing across each sampling point for each electron injection energy (and k_y mode). For multi-layer system, the trace taken over the matrix of basis for each layer and integrated over energy (and k_y) gives the current distribution across layers.

Next, for near-equilibrium transport through a channel of length L, the conductance G, linear free-charge density 'n' (in number per unit length) and ballistic mobility 'μ' are computed as,

$$G = \frac{q^2}{h}\int dE \cdot \bar{\mathrm{T}}(\mathrm{E})\left(-\frac{\partial f}{\partial E}\right) \tag{2.15}$$

$$n = \int dE \, \frac{\mathrm{DOS}(\mathrm{E})}{\mathrm{L}} \left(-\frac{\partial f}{\partial E} \right) \tag{2.16}$$

$$\mu = \frac{G \,.\, L}{n \, q} \tag{2.17}$$

2.3. Real-Space Modeling on GPGPUs

A non-conventional computational platform (non-conventional at the time of this work although now it is more widely adopted for heavy computations) was adopted for modeling large 3D-TI wires for the quantum transport. The presented results in this work are for wires up to 13 layers thick, 63 nm wide (64 sampling points) and 84 nm long (85 sampling points). Therefore, for a sampling distance of 1 nm along the x-y plane with 4x4 basis to describe each point, it corresponds to a unit cell (in the y-z plane of wire) matrix of 3328 x 3328 size which takes up ~169 MB of memory and therefore a *single main-diagonal matrix* for the entire device even with RGF algorithm will take up a huge memory of ~ 14 GB. To surmount the computational challenge of dealing with these large matrices, we had thus resorted to a relatively new hardware in the domain of computational nanoelectronics i.e. General Purpose Graphic Processing Unit (GPGPU). Graphic Processing Units (GPUs) had chiefly remained inaccessible beyond their niche market of video games and some computer science research where algorithms were modeled to emulate the rendering of computer graphics [87] using high-level shading languages like DirectX, OpenGL and Cg. However, lately with the advent of Fermi [88] GPU architecture, C enabled software architecture (Compute Unified Device Architecture (CUDA)) and cheap availability of high end Tesla GPUs from Nvidia with hundreds of cores targeted for general purpose scientific computing, GPGPUs have recently been examined for

simulating quantum transport for realistic device dimensions [89]. The promising results had been subsequently reported in all the publications.

In this work, therefore, the transport was modeled on Nvidia GPGPU (Tesla C2070 and M2090) in CUDA 5.0 supported by MAGMA 1.3 (Matrix Algebra on GPU and Multicore Architectures) and LAPACK 3.2.1 (Linear Algebra Package) libraries. Specifically, we had optimized the RGF algorithm for memory and speed by breaking up the computation along the channel length to fit into 6GB GDDR5 RAM of Tesla, and to compute without forming a device diagonal. (The problem would be otherwise virtually unsolvable if full inversion is deployed). The device dimensions used in this work are therefore constrained by the RAM of our computing nodes, but the code is readily scalable to solve much larger devices.

Chapter 3

Performance Evaluation of Electro-Optic Effect based Graphene Transistors

Despite the advantages afforded by the unique electronic properties of graphene, the absence of bandgap has limited its applicability in logic devices. This has led to the study of electro-optic behavior in graphene for novel device operations, beyond the conventional field effect, to meet the requirements of ultra-low power and high-speed logic transistors. Recently, two potential designs have been proposed to leverage on this effect and open a virtual bandgap for ballistic transport in the graphene channel. The first one implements a barrier in the centre of the channel, whereas the second incorporates a tilted gate junction. In this chapter, we computationally evaluate the relative device performance of these two designs, in terms of subthreshold slope (SS) and I_{ON}/I_{OFF} ratio under different temperature and voltage bias, for defect-free graphene channel. Our calculations employ pure optical modeling for low field electron transport under the constraints of device anatomy. The calculated results show that the two designs are functionally similar and are able to provide SS smaller than 60 mV/decade. Both designs show the similar device performance but marginally top one another under different operating constraints. Our results could serve as a guide to circuit designers in selecting the appropriate design as per their system specifications and requirements.

3.1. Introduction

Smaller and faster transistors, dissipating lower power than their contemporaries, are required to truss more functionality in a standard package for

application in high-performance computing and consumer electronics [90]. Specifically, low sub-threshold slope (SS) is required to achieve high "switch-on current" (I_{ON}) for faster charging of load capacitors, and low switch-off current (I_{OFF}) for lower static dissipation within the available gate voltage swing. The optimization of power against speed in CMOS System-on-Chip, limits SS to 60 mV/dec at room temperature [91, 92], owing to traditional MOSFET architecture. Other MOS architectures [92], such as feedback MOSFETs, impact ionization MOSFETs, nano-electromechanical FETs, and tunnel FETs, to overcome the constraints of the conventional Si-MOSFET architecture, these result in trade-offs against other critical device performance metrics, like device reliability, intrinsic area, ideal I-V characteristics, etc. Therefore, as of now, to the best of our knowledge, no ideal solution exists for silicon-based transistors.

Graphene, discovered in 2004 [93], has been touted to replace silicon in electronic nano-devices because of its smaller atomic size, high mobility and long mean free path. However, the absence of a bandgap in graphene results in small I_{ON}/I_{OFF} in conventional graphene field effect transistors (GFETs), thereby restricting their possible applications mainly to RF amplifiers [94, 95]. Although several approaches have been proposed to create a bandgap in graphene-related materials, such as chemical modification and quantum confinement, they usually alter the electronic properties of graphene adversely [96], like reduction in electron mobility. Therefore, non-conventional graphene transistors which exploit new physical phenomenon like pseudospin [97], Klein tunneling [98] and electro-optic effect [96, 99, 100] have been proposed to circumvent the bandgap limitation.

Recently, computational analysis [100-102] of electron transport in graphene channel, which is analogous to optical transmission in fibers, and its experimental

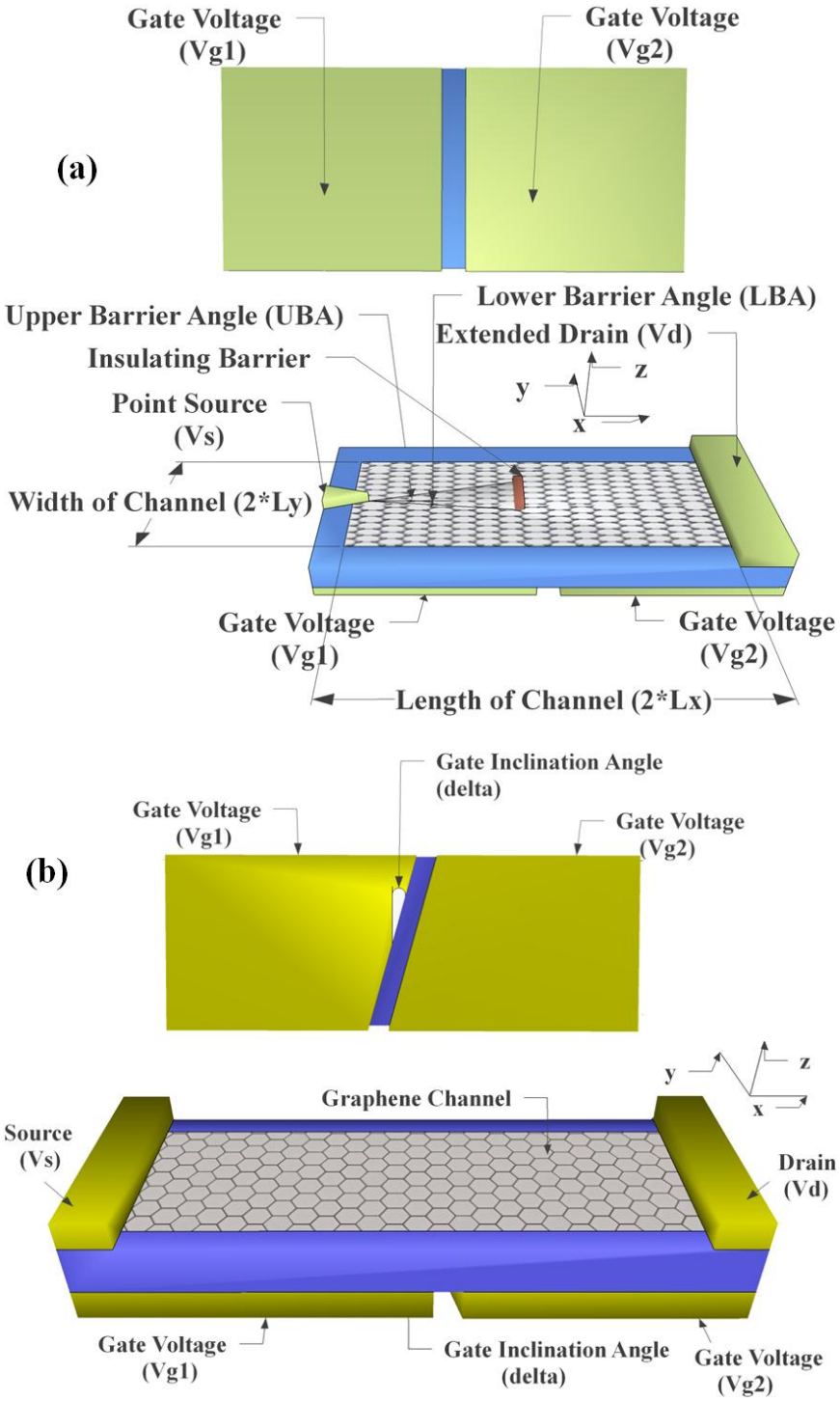

Figure 3.1 Device structure of analyzed proposals for four terminal Graphene Electro-Optic Transistor (GEOT). Both induce bandgap by blocking certain energies by emulating 2-D ray optics. Graphene channel, in x-y plane, rests over substrate/dielectric. Both have two back gates, which electrostatically segment the channel into region 1 (n-side) and 2 (p-side), under V_{G1} and V_{G2} respectively, with relative refractive index η_{21} and critical angle θ_C ($\sin^{-1} \eta_{21}$). a) Ref. [96] Electron stream (circular wavefront) from point electron injection source is blocked by insulating barrier placed in the centre of the channel. Junction is formed in y-direction along the barrier. In addition, electron incident at junction with angle (θ_i) greater than θ_C is blocked. θ_B is barrier subtended at source for symmetrically placed barrier i.e. for Upper Barrier Angle (*UBA*)=Lower Barrier Angle (*LBA*). b) Ref. [98, 99] Electron injected from source (planar wavefront) is blocked from traversing from region 1 to region 2, if the critical angle of its wavefront is less than gate inclination angle (δ).

verification [102] have led to two proposals of graphene electro-optic transistor (GEOT) [96, 98, 99], as shown in Fig. 3.1, where a bandgap is opened artificially by blocking certain electron energies in analogy with 2D-optics. In design-A, electrons are injected from a point source, and are blocked by a barrier placed at the centre of the grapheme channel, while in design-B, a slanted gate is placed across the channel, and electron blockade is effected via total internal reflection. The resulting high I_{ON}/I_{OFF}, small SS and virtual bandgap of both designs make them apt for logic devices. However, detailed analysis is still required to analyze trade-offs in device design and the operational parameters of these proposed devices.

Therefore, this chapter focuses on investigating and comparing the relative device performance of the two GEOT designs, and the influence of device geometry, voltage and temperature. Note that the original proposal of design-B posits its transistor mechanism on the basis of the Klein paradox [98]. However, given the controversial nature of this effect with both proof of its existence [103-109], and repudiation [110-115], we have presented the operation of design-B in terms of its electro-optic behavior, and found it to be similar to design-A. Specific advantages and disadvantages of both designs are highlighted and discussed. Additionally, we also suggested modification in the original design to overcome the limitation of non-zero V_{G2} for I_{OFF} point.

The chapter is organized as follows. This introduction section is followed by elaboration of computation setup required simulating devices illustrated in Fig. 3.1. Next, the performance of both device designs is comprehensively examined in results section, and the key results are then summarized in conclusion section. Appendix A of the thesis serves as a supplementary to this chapter and presents mathematical derivation for some of the more relevant equations.

3.2. Computational Setup

In design-A, two back gates, V_{G1} and V_{G2}, are implemented to control current in the undoped channel. On the other hand, in design-B, the channel is chemically doped in lieu of gate voltages. To investigate physical insights and performance of both designs, we consider ideal (pure 2D) undoped channel with two gates, with abrupt junction and without edge effects. The gate bias under the right and left graphene segments can dope the segments to either n-type or p-type, respectively. If biasing dopes both graphene segments to n-type, it is described as "nn-Config." whereas if segment 1 is n-type and segment 2 is p-type, it is referred as "np-Config.". By utilizing the different doping configurations between graphene segments, one can block electrons within a certain energy range from traversing from source to drain (for instance see Fig. 2 and Fig. 3 of Ref. [96]). This energy range is determined by the conservation of transverse modes from injection side to the receiving segment and dealt in detail in section 3.3. This virtual band-gap (described by Eq. (A.4) of Appendix A) is similar to inducing an actual bandgap in graphene which is more challenging from the fabrication point of view [95]. The device dimensions can be considered to be within limits of ballistic transport for graphene, due to graphene's long mean free path [93]. Within these ballistic limits, electron transport in the graphene channel can be approximated to wave propagation, as was done by Cheianov *et al*. [100]. Therefore, in calculating the transmission T(E) [96] which is required by the current equation (Eq. (A.3)), it is assumed that the point source in design-A generates a circular wavefront, while the extended source in design-B forms a planar wavefront.

In device A, the origin (0, 0) is taken to be the point at the intersection of electrostatically separated graphene segments and normal to the point source, whereas

for design-B, the origin is set at the midpoint of inclined gate junction. In design-A an insulating barrier of finite dimensions is placed in the center of the channel to inhibit normally incident electron waves from the point source up to the angle subtended by barrier at the source, i.e. *UBA* (upper barrier angle) in the +y plane and *LBA* (lower barrier angle) in the –y plane. Additionally, because of different doping profiles, i.e., different V_{G1} and V_{G2} values on the two graphene segments, electron waves from segment 1 to 2 will see the relative refractive index η_{21} and critical angle θ_C ($\sin^{-1} \eta_{21}$), which occludes electrons incident at the junction with an angle (θ_i) greater than θ_C (total internal reflection) [96]. However, for smaller θ_i, electron waves will traverse into segment 2 at a refracted angle $\theta_r = \sin^{-1}((\sin \theta_i)/\eta_{21})$. In the OFF state of the transistor, large fraction of energy spectrum of injected electrons will have its critical angle θ_C smaller than the barrier angle; therefore, irrespective of the incident angle θ_i, the electron wavefront will be blocked. However, in the ON state, only small fractions of energies have θ_C smaller than the barrier angle. Under this condition, only electrons with incident θ_i smaller than the barrier angle, as well as electrons with large incidence angle θ_i exceeding θ_C, are blocked. The rest of the electrons can transmit through, thereby driving the transistor into saturation. Generally, by varying control parameters, one may induce steeper changes in I_{OFF} than I_{ON}.

On the other hand, design-B inclines the gates by angle δ to attain the universal condition of $\theta_i = \delta$ and, thereby, block electrons which have energies such that their $\theta_C < \delta$. In the OFF state, a broad range of electron energies satisfy this criterion as η_{21} (Eq. (A.1)) tends to zero. The OFF (I_{OFF}) and ON (I_{ON}) currents are set as the minimum and maximum source-drain current (I_D) for a given configuration, irrespective of ‘np’ or ‘nn’ configuration. Besides, since θ_C depends on the voltage bias and energy of individual electrons, the transistor-switching action in both designs

is achieved by toggling V_{G2} while keeping V_{G1} fixed. The equations governing the electron transmission in both designs and the gate voltage for switch-off are consolidated in Appendix A.

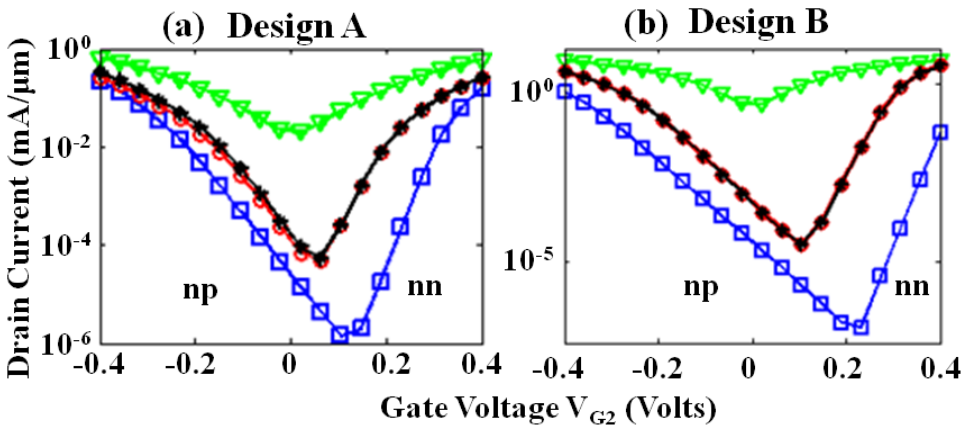

Figure 3.2 Effect of moving insulation barrier of fixed dimensions along the y-axis in design-A and polarity of gate inclination for design-B. a) minimum I_{OFF} is achieved for symmetrically placed barrier i.e. when *UBA=LBA* (20^o in our case) (blue line). Drain current remains same for barrier positions mirrored about x-axis along the barrier's y-axis (black overlapping with red line). Black line stands for intermediate barrier position i.e. *UBA=2 LBA*. b) Gate inclination (δ) in design-B begets similar transfer characteristics in Graphene channel as θ_B in design-A. Moreover, black ($\delta = +20^o$) overlap with red ($\delta = -20^o$) lines predicts functional independence of device of polarity of δ. Green trend corresponds to absence of barrier for both a) and b).

3.3. Results and Discussion

Firstly, we study the effects of barrier position and geometry. In design-A, we investigate the effect of moving the barrier along the y-axis, while for design-B we investigate the influence of the orientation of the gate inclination. As illustrated in Fig. 3.2, it can be observed that designs A and B are symmetrical about the x and y-axis, respectively, as depicted by the overlap of the red and black curves. Thus, if there are two variants, labeled m and n, of design-A (or design-B) such that (UBA_m, LBA_m) = (LBA_n, UBA_n) (or $\delta_m = -\delta_n$), they will have the same transfer characteristics. This agrees with the symmetry of the two devices about their respective axes.

Next, for design-A, the lowest I_{OFF} and the highest I_{ON}/I_{OFF} ratio is achieved when *UBA=LBA* (blue line in Fig. 3.2(a)). Under this condition, the maximum fraction of electron energies is blocked. In the asymmetrical scenario, electrons with

low θ_i and/or energies may be able to pass via either the positive or the negative y-plane, depending on which part of the barrier (upper or lower) which subtends a lower angle to the source, thereby increasing both I_{ON} and I_{OFF} (leakage current). Although, the symmetric barrier configuration lowers I_{ON}, it results in an even steeper decline in I_{OFF}, due to the blocking of a large spectrum of energies, thus improving the I_{ON}/I_{OFF} ratio. Therefore, a symmetric barrier configuration is optimal to the operation of devices based on design-A.

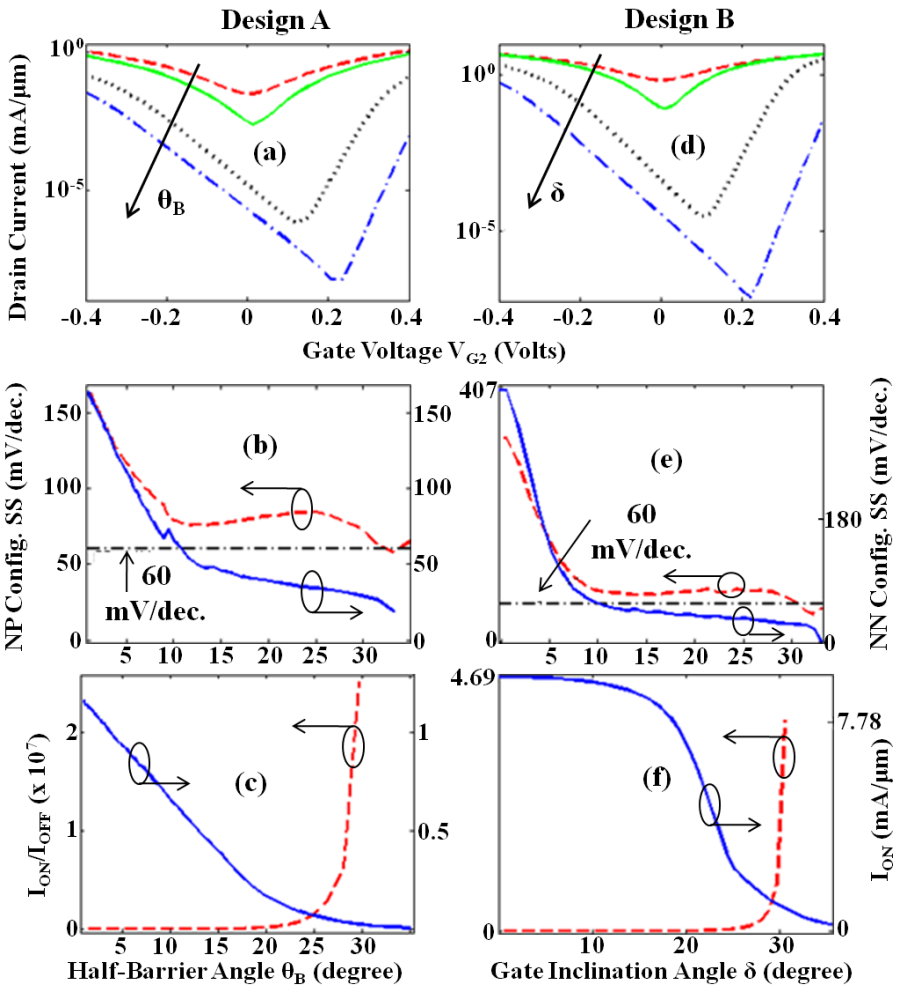

Figure 3.3 Impact of half-barrier angle (Design-A) and gate inclination (Design-B) for V_{G1} = 1 V at 300 K. For designs A and B, width along y-axis of symmetrically placed insulation barrier subtending θ_B at source and gate junction inclination (δ) w.r.t y-axis is swept respectively. Both I_{ON} and I_{OFF} decrease with increase in θ_B (δ), but I_{ON}/I_{OFF} improves continuously due to steeper fall in I_{OFF}. SS < 60 mV/dec can be achieved for nn-config for wide range (b, e) of θ_B (δ) which gives flexibility in selection of I_{ON} and I_{ON}/I_{OFF} (c, f) for circuit design.

Secondly, we investigate the effect of widening the insulating barrier along y-axis, i.e., increasing θ_B subtended at the source ($UBA=LBA=\theta_B$) for design-A, and the

gate inclination angle δ for design-B. As shown in Fig. 3.3, the drain current decreases with increase in θ_B (δ) (Fig. 3.3(a) and 3.3(d)), because a larger θ_B (δ) would exceed the critical angle over a wider range of electron energies. However, for design-A, there is a steeper roll-off in I_{OFF} than I_{ON}, because of blockage of large energy spectrum, thus enhancing the I_{ON}/I_{OFF} ratio and lowering the SS for design-A. The reason can be attributed to the steep declivity of the I_{ON} versus θ_B slope in contrast to design-B. Thus, this indicates that design-A marginally outperforms design-B with respect to the transistor action under the influence of the gate geometry.

Moreover, there is an optimal range for θ_B and δ. When θ_B (δ) > 30-35^o, I_{ON} becomes too small for high frequency applications, whereas when these two angles are smaller than 10^o, I_{OFF} or the leakage current becomes appreciable. For circuit design, the favorable angle ranges from about 17^o to 21^o. However, the final value also depends on selected region of operation. For instance, for a given value of I_{ON}, nn-operation allows for smaller magnitudes of θ_B (δ) than np-operation, although at the cost of smaller I_{ON}/I_{OFF} ratio.

Next, it can be observed that I_{OFF} (OFF-state) corresponds to non-zero V_{G2}. This may lead to significant static dissipation if the circuit is designed with an OFF-state voltage of zero. Furthermore, the 'nn-config' yields SS < 60 mV/dec over a substantial range of θ_B (δ), giving room to tune other parameters, in contrast to the 'np-config'. With increase in θ_B (δ), V_{G2} corresponding to I_{OFF} shifts towards higher positive values, thereby making device asymmetrically bipolar w.r.t 0 V bias point. In fact, for unipolar operation, design-B offers I_{ON} and I_{OFF} for same polarity of V_{G2} up to certain δ (25.2^o in our simulations).

However, if design-A is operated in unipolar mode then I_{ON} and I_{ON}/I_{OFF} are approximately halved. Finally, from circuit and fabrication perspective, symmetry

about both *x* and *y*-axis for design-B, like traditional MOSFET, makes it easier to place in Very-Large Scale Integration (VLSI) environment and fabrication processes giving it an edge over design-A, because transistor layout can be mirrored and interconnects routed easily among them.

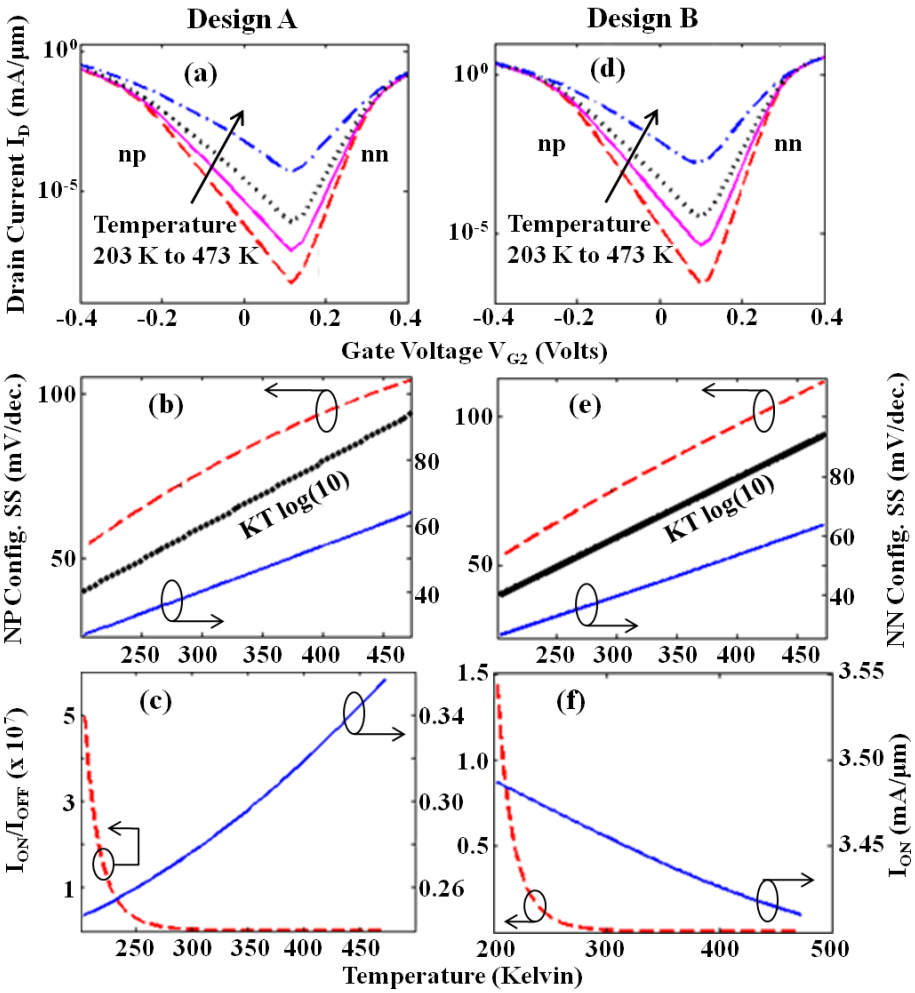

Figure 3.4 Impact of Temperature for V_{G1} = 1 V at θ_B (δ) = 20°. (a, d): I_{OFF}, which corresponds to leakage current in circuits, decreases with temperature, but V_{G2} corresponding to I_{OFF} remains constant. (b, e): Subthreshold Slope (SS) degrades with increase in temperature for both np and nn config. (c, f) I_{ON} fractionally increases and decreases with increase in temperature for np and nn configurations, respectively.

Next, we study effect of temperature on device performance of both designs, to determine the operational temperature range of the GEOT device. As shown in Fig. 3.4, it can be observed that increasing temperature degrades the performance because of higher SS (Fig. 3.4(b) and 3.4(e)) and lower I_{ON}/I_{OFF} (Fig. 3.4(c) and 3.4(f)) for both designs. The reason can be attributed to the aggravated contribution of electron

injection at energies far from equilibrium chemical potential due to the tail of Fermi distribution at higher temperature and therefore, increased leakage current at I_{OFF}. This indicates that, even though the operation principle of these GEOTs is not same as MOSFETs, thermionic currents still play an important role in determining the magnitude of I_{OFF}. However, SS for nn-config still remains lower than MOSFET benchmark of $2.3k_BT$, for entire temperature range, due to the dependence of allowed energies on V_{G2}, as expressed in Eq. (A.4) of the Appendix A (also see Eq. (4) of Ref. [96]).

Furthermore, it is observed that I_{ON} fractionally increases with temperature around saturation point (Fig. 3.4(c) and 3.4(f)) for design-A, whereas the reverse trend is observed for design-B. This is because of the interplay between three competing factors, namely: i) increasing temperature, the magnitude of the difference in the Fermi distribution (Δf) between the quasi-Fermi levels of the source and drain (μ_S and μ_D respectively) gets smaller, ii) Δf increases in energy range about μ_S and μ_D where η_{21} and therefore θ_C is higher (Eq. (A.1)) and iii) fixed θ_i ($=\delta$) for design-B whereas for design-A, $\theta_i \in [-\pi/2, \pi/2]$. However, in design-B, factor i) mentioned above dominates, resulting in negative slope for Fig. 3.4(f)). Moreover, the decay of I_{ON} with temperature for design-B excludes the possibility of thermal runaway thereby making it better than design-A with respect to thermal response.

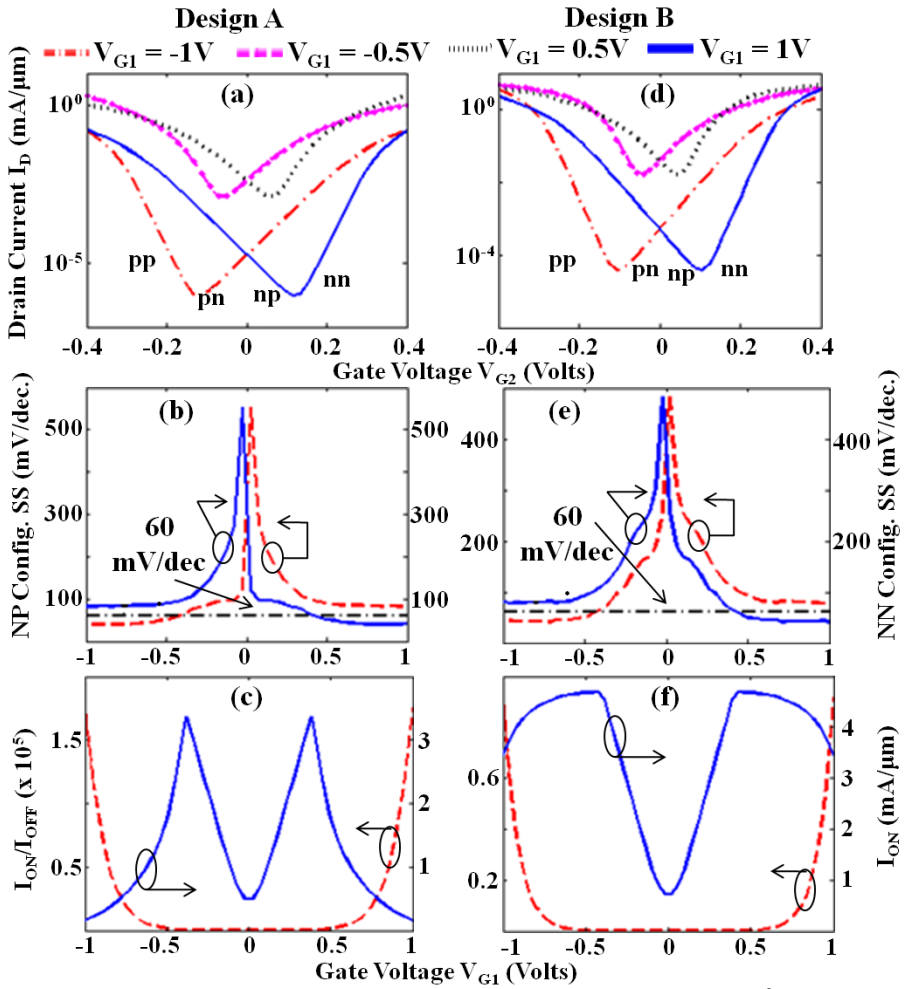

Figure 3.5 Impact of Gate Voltage over Segment 1 (V_{G1}) for θ_B (δ) = 20^0 at 300 K. Note the independence of device behavior of polarity of V_{G1}. (a, d) Drain current decreases with increase in V_{G1} because of emulation of smaller critical angle leading to blockage of wider energy spectrum for injected electrons. (b, e) SS declines with increasing magnitude of V_{G1} to fall below 60 mV/dec benchmark and finally becomes relatively constant for $V_{G1} > V_{G2max}$ because of Density of States (DOS) factor in current equation (Eq. (A.3)) which we have crudely taken to be lesser of the two segments (Eq. (1) of Ref. [116]) because segment with smaller DOS acts as stronger impediment in current flow. (c, f) I_{ON} peaks for full swing voltage of V_{G2} in either polarity, because of competing effect of DOS for electron transport and total internal reflection on source side.

Next, we investigate effect of V_{G1} on device performance with a fixed V_{G2}. Electrostatically, V_{G1} defines the static doping profile of one segment of the device, and range of relative refractive index (η_{21}) (Eq. (A.1)) for optical emulation of device characteristics. An optimum value of V_{dope} (Eq. (A.8)) can also be used to have equivalent chemical doping of entire graphene channel to get rid of V_{G1} [98], thereby reducing one electrical connect per transistor. As shown in Fig. 3.5, both designs have the symmetrical response for bipolar V_{G1} with respect to both drain currents (Fig. 3.5(a) and 3.5(d)) and SS (Fig. 3.5(b) and 3.5(e)) i.e., nn-configuration is equivalent

to pp-configuration. As shown in Fig. 3-5(c) and 3.5(f), I_{ON} has local maxima over the full swing voltage of V_{G2} for either polarity. This is because of the competing effect of density of states (DOS) for electron transport, and total internal reflection on the source side. Based on our approximation, for a full swing of V_{G2} ($\pm$ 0.4 V), the DOS in the current equation (Eq.(A.3)) is determined by its value in graphene under V_{G1} from 0 to V_{G2}, beyond which the DOS in segment 2 becomes the limiting factor and keeps the DOS factor constant in equation. This is a simple approximation for DOS and experimental results should show relatively smooth maxima instead of the sharp peak observed in our simulation. I_{ON} then decays beyond the maximum because the total internal reflection within segment 1 becomes stronger with increasing V_{G1}.

In addition, for higher magnitudes of V_{G1}, I_{OFF} decreases considerably because the relative refractive index is inversely proportional to V_{G1} (Eq. (A.1)). Therefore, it becomes easier to achieve total internal reflection for a given θ_B (δ) leading to lower leakage or OFF-state current. Owing to the steeper decline in $I_{OFF,}$ the I_{ON}/I_{OFF} ratio invariably increases with increasing magnitude of V_{G1}, resulting in lower sub-threshold slopes. In summary, it can be found that a) design-A and B is equivalent w.r.t. V_{G1}, b) bias voltage of either polarity can be used, c) $SS<60$ mV/dec is achieved with for $V_{G1}>0.5$ V, and d) for V_{G1} beyond 0.5 V, the SS is nearly constant; therefore V_{G1} bias is a function of I_{ON} and I_{ON}/I_{OFF}.

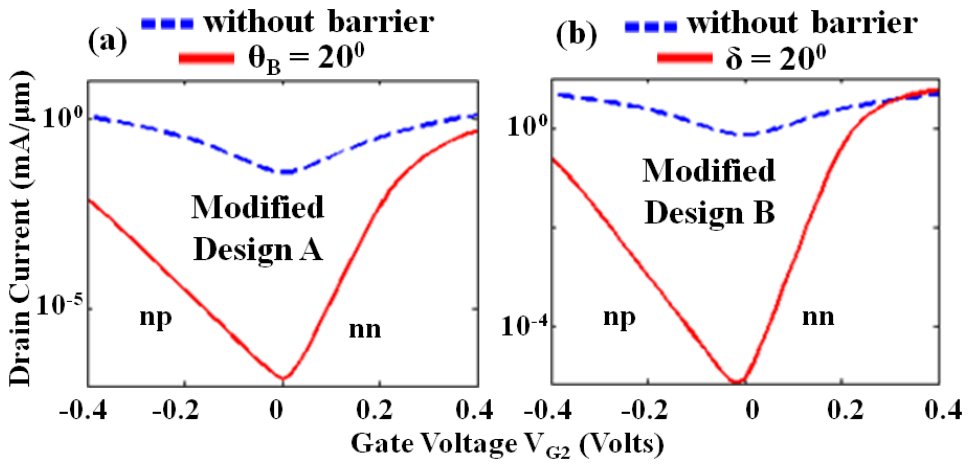

Figure 3.6 Impact of chemical doping or Top Gate on V_{G2} translation at 300 K and V_{G1} = 1 V. Graphene channel is doped to equivalent of V_{dope} eV or top gate is used to materialize the effect. Main objective is to attain zero V_{G2} for I_{OFF} to match with switch-off for contemporary logic levels. V_{dope} is a function of θ_B (or δ), V_{G1} and gate transfer capacitance factor (β) if top gate is used for tuning. Refer Appendix for derivation. As per Eq. (A.8), for both designs, V_{dope} = 0.1345 eV (red).

Finally, a modification, which is applicable to both designs, is proposed to overcome the problem of non-zero V_{G2} see, Fig 3.3. Based on the mathematical analysis of this problem as presented in the Appendix A, it can be found that the problem may be resolved by chemically doping the channel to the equivalent of V_{dope} [98], or by placing a top gate and applying a compensation voltage V_{dope} with capacitance transfer factor 'β'. The latter would electrostatically shift DOS for entire result in an electrostatic shift in the channel by βV_{dope}. Therefore, with careful tuning of doping or gate voltages in both designs, one can have shift the drain current profile so as to achieve zero V_{G2} at the I_{OFF} point, as shown in Fig. 3.6. This would thereby reduce the static power dissipation, although, this improvement comes at the cost of additional terminal or increase in the number of fabrication steps.

Before concluding, we would like to note that in this work, ray-optics based model and ideal graphene channel with abrupt junction without edge effects are assumed. However, for the realistic devices, with finite transition width across p-n junction, the transmission is expected to decrease [116] for both designs because of decreased angular bandwidth ($2\theta_C$ and $2\delta_{\text{effective}}$ for design-A and B, respectively), and

therefore decreased current. However, taking abrupt junction and neglecting self-consistent calculations for charge profile in transition region lead to overestimate of E_{DOS} under the high bias (see Eq. (A.3)) which projects larger currents than the calculations using NEGF for np-config at large biases [116]. Nevertheless, for nn-config., the recommended device operation region for GEOT, the results from two models are comparable [116]. Next, for neglecting edge effects, we have presumed infinitely wide channel for both designs, however, in real device, especially B, some electron transport is expected along the edges [117] that increases the current (counter-effect of finite transition width). Therefore, since capturing these effects is beyond the ray-optic model, for future evaluation, the more sophisticated simulation with self-consistent potential calculations via NEGF should be implemented to simulate accurate device characteristics despite of its high computational resource requirements.

Table 3.1 Comparing behaviour of Design-A with Design-B

Swept Parameter	DESIGN A	DESIGN B
Moving Barrier Position ($\pm\theta_B$) for design-A or Orientation of Gate Inclination ($\pm\delta$) for design-B.	Drain Current same for designs m and n if (UBA_m,LBA_m) = (LBA_n,UBA_n) Lowest I_{OFF} and highest I_{ON}/I_{OFF} for UBA=LBA.	Drain Current same for designs m and n if (δ_m = -δ_n).
Increasing θ_B (δ)	a) Drain Current decreases. b) I_{ON}/I_{OFF} increases. c) SS decreases. d) For I_{ON} >0.1mA/μm and I_{ON}/I_{OFF} > 10^4 : nn region: 14^o-21^o np region: 14^o-26^o e) At θ_B = 19^o : nn region :: I_{ON} ~ 0.15mA/μm; I_{ON}/I_{OFF} ~ 11 x 10^4; SS ~ 40mV/dec np region :: I_{ON} ~ 0.28mA/μm; I_{ON}/I_{OFF} ~ 20 x 10^4; SS ~ 82mV/dec	a) Drain Current decreases. b) I_{ON}/I_{OFF} increases. c) SS decreases. d) For I_{ON} >0.1mA/μm and I_{ON}/I_{OFF} > 10^4 : nn region: 16^o-26^o np region: 16^o-36^o e) At δ = 19^o : nn region :: I_{ON} ~ 3.7mA/μm; I_{ON}/I_{OFF} ~ 6 x 10^4; SS ~ 44mV/dec np region :: I_{ON} ~ 2.5mA/μm; I_{ON}/I_{OFF} ~ 3.5 x 10^4; SS ~ 81mv/dec
Increasing Temperature	I_{ON} slightly increases.	I_{ON} slightly decreases.
Effect of V_{G1} (Equivalent for both designs)	Device Characteristic symmetrical about polarity of V_{G1}.	Device Characteristic symmetrical about polarity of V_{G1}.

3.4. Conclusion

Within the purview of ray-optic model, Table 3.1 summarizes the key findings both qualitatively and quantitatively of these two designs with respect to variation of above stated parameters. We found that firstly both designs have similar response to V_{G2} dynamics and generate best response for symmetrical device geometry for barrier position or gate inclination. Secondly, for θ_B~ δ = 19^o, though SS is almost same, but I_{ON} for design-B is expected to be higher (factor of 24.67 in Table 3.1) whereas

I_{ON}/I_{OFF} for design-A betters B by factor of 2. We have also suggested range for $\theta_B(\delta)$ for fabrication for optimal performance of transistor. Thirdly, we observed opposing thermal response of I_{ON} and glossed over it later in discussion. Fourthly, we have observed that both designs have similar response about the polarity of V_{G1}. Finally, a solution is proposed for the issue of non-zero V_{G2} for I_{OFF} for proposed devices.

In summary, by sweeping V_{G1}, V_{G2}, temperature and device geometry (input parameters), we expect the two design proposals to have similar effect on drain current. Therefore, comparable I_{ON}, I_{OFF}, SS and I_{ON}/I_{OFF} ratio (output parameters) should be achievable for given electrical specifications for transistor with prudent choice of device geometry. Secondly, unipolar operation i.e. 'nn' (V_{G1}, $V_{G2} > 0$) or 'pp' (V_{G1}, $V_{G2} < 0$) is recommended to attain sub SS slope for entire temperature range of interest. Anyhow, suitable device geometry has been suggested in Table 3.1 according to region of operation to aid circuit designers, though we suggest NEGF based calibration for exact modeling and optimization before parameter extraction.

Chapter 4

Y-Shape Spin-Separator for two-dimensional Group-IV Nanoribbons based on Quantum Spin Hall Effect

An efficient spin-separator that operates in quantum spin hall phase has been investigated for two-dimensional Group-IV materials. A three-terminal Y-shaped device has been simulated via Non-Equilibrium Green Function to demonstrate the separation of unpolarized current at source terminal into spin-polarized current of opposite polarity at the two drain terminals. Device controls, i.e. tunable buckling and perpendicular magnetic field have been modeled comprehensively to evaluate the device feasibility and performance. It is shown that these controls can preferentially steer current between the two drains to create a differential charge current with complementary spin polarization, thus enabling a convenient regulation of output signal.

4.1. Introduction

Silicene and Germanene, the two dimensional (2D) honeycomb structural analogs of graphene for silicon and germanium, have recently advanced from the stage of theoretical [118-120] prediction to experimental [121-124] realization. The expected high-mobility [125-127] along with the predicted quantum spin-hall (QSH) state - a topological phase of matter protected by time-reversal symmetry (TRS) [65, 128-130], has resulted in a surge of interest in these and other Group-IV materials for electronic transistors [131] and spintronics applications [65, 126, 127, 132].

In 2D honeycomb structure of Group-IV materials, the ideal sp^2 (in-plane σ-bonds) hybridized orbitals partially overlap with out-of-the-plane π-bonds to form

sp^2-sp^3 hybridization [133] to yield an energetically stable structure. The mixing of σ-π bonds results in an intrinsic spin-orbit coupling [134] (SOC), $\lambda_{SO,}$ that creates the gap of ~ 2 x λ_{SO} at an otherwise gapless Dirac-point. The strength of sp^3 hybridization increases for heavier atoms down the group, buckling the structure and displacing the alternative atoms into two different planes separated by a distance Δ_C. The bandgap can now be tuned electrically [127, 135-137] by applying a perpendicular electric field, which we will refer to as the buckling field (λ_V) to distinguish it from the phenomenological gate potential applied to shift the Fermi-level (E_f).

The buckling field breaks the inversion symmetry and induces spin-polarized states in the presence of SOC. Buckling field and perpendicular magnetic field (Zeeman splitting) have recently been shown to drive Group-IV materials into spin and valley polarized phases [65] that can be engineered for second generation of spintronic devices like spin-filters [11] and spin-based logic gates.

An important stumbling block in spintronics devices is to generate spatially distributed, highly polarized spin-current of both polarities. Spin-Hall effect has been shown to be a promising solution so far [31, 138]. Accordingly, the QSH phase of Group-IV materials has been exploited here to examine an efficient three terminal Y-shaped spin separator whose operation and performance can be controlled in exotic ways. It has also been shown that these controls can provide distinct digital and analog functionalities in spintronic circuits by extracting the differential current signal at the output along with its spin polarization. Appendix B provides information that would help in understanding the results presented in this chapter.

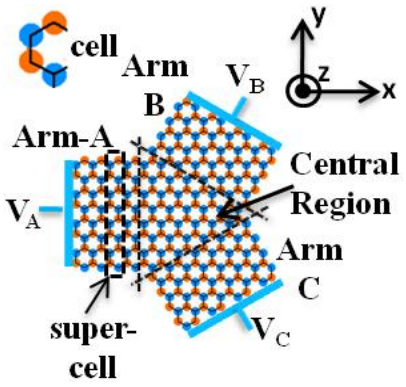

Figure 4.1 Y-shaped device with three contacts A, B and C. 4 atoms in dotted black line are referred as one cell in discussion. Orange and blue atoms do not lie in a plane for a low buckled system and are referred to as type-A and type-B, respectively. N-cells along the width form a super-cell.

4.2. Computational Setup

The quantum transport simulations through Non-Equilibrium Green Function [81] (NEGF) have been carried out for a three-terminal Y-shaped [65] device (see Fig. 4.1(a)) to investigate the feasibility and performance of our spin-separator. Figure 4.1 shows the three-arms of equal width, each of which is a zigzag nanoribbon (NR). The central region whose dimension is governed by the width of the adjacent arms has an armchair interface on all three sides. The buckled atoms in the two planes are at an offset of Δ_C and have been marked by orange and blue colors for clarity. A four-band tight-binding model, that was fitted to ab-initio calculations as described in Ref.[65], has been used to model the Hamiltonian as explained in **Chapter 2**.

The spin-polarized edge-states [48] around the Dirac-points have been verified by plotting local spin/charge distribution probability (LSCDP). The device Green function has been calculated by full inversion, whereas iterative convergence [84] of surface Green function has been done to calculate self-energy for all three contacts. Specifically, Eq. (2.12) and (2.13) has been used to compute the current and its spin-polarization in each of the three-arms. Note that we have considered 2D Silicon (Silicene), Germanium (Germanene), Tin (Stannene) and Lead (Plumbene) but not Carbon (Graphene) sheets because of very weak SOC ($\lambda_{SO} \sim 1$ μeV [134]) in latter,

which in spite of impurities [139] (λ_{SO} ~ 1 meV) is much lower for device applications. We also note that Ge has been chosen as an exemplar material for full device analysis as it has the highest λ_{SO} among graphene, silicene, and germanene, the experimentally realized 2D nanoribbons [123, 124] to date. Here we simulate transport at zero Kelvin because of the small energy range, dictated by $\lambda_{SO,}$ of spin-polarized bands in 2D-Group IV materials that can be fabricated currently. The future technological advances in fabricating 2D devices of high SOC elements like tin [140, 141] and lead may, however, allow room temperature operation of our Y-shaped spin separator at small bias.

4.3. Results and Discussion

For a nanoribbon based device, one of the most important physical parameter is its width because of the spatial confinement in transverse direction that quantizes the 2D bands. This mainly affects the device behavior when Fermi-level is in bulk bands. We, however, observe in Fig. 4.2(a, b) that both conductance and spin polarization (SP) of current wanes as width is scaled down even though the operating energy range for quantum transport (E_f = 1 meV, V_{BA} (V_{CA}) = 1 mV) is far below bulk bands. The reason can be attributed to the wavefunction overlap of the two edges, which in electronics is more commonly referred to as crosstalk. The crosstalk reduces both the conductance and SP on both the edges. For sufficiently weak crosstalk, the increase in width has negligible effect on device and, therefore, trend lines in Fig. 4.2(a) and 4.2(b) saturate. Crosstalk also abates with the increasing strength of SOC for this device because of the stronger confinement of the current at the edges. This is the reason for larger conductance and spin polarization with heavier atoms (see also Fig. B.1 to compare confinement along edges of the device for different materials). We have chosen 14 cell wide (see Fig. 4.1(a)) nanoribbon arms for subsequent

analysis as a representative width for a reasonable load on computational resources, and with the study of effect of width we have established that device performance would improve for larger widths, making it easier for experimentalists to attain 100% SP.

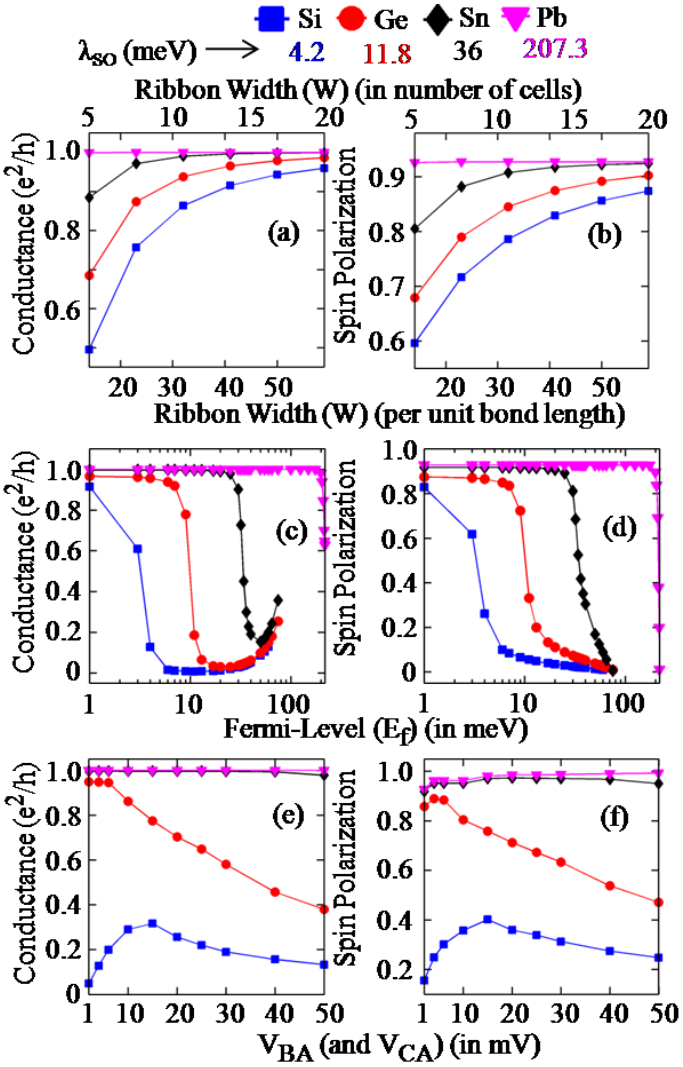

Figure 4.2 Conductance (a, c, e) and Spin Polarization (SP) (b, d, f) of current in Arm-B for the Y-shaped device made of zigzag low-buckled nanoribbon of Silicon (Si; blue square), Germanium (Ge; red circle), Tin (Sn; black diamond) and Lead (Pb; magenta triangle). Arm-C has same conductance but opposite spin polarity. (a, b) Both conductance and SP increase with device width and eventually saturate because of weakening inter-edge coupling. E_f = 1 meV, V_{BA} (V_{CA}) = 1 mV. (c, d) Conductance and SP roll-off as the Fermi-level (E_f) moves out of the energy range governed by the spin-polarized edge states [48] due to intrinsic (λ_{SO}) spin-orbit coupling (SOC). Conductance again picks up due to the bulk states (see Fig 4.3), but SP still declines owing to lack of polarization. V_{BA} (V_{CA}) = 1 mV. (e, f) Larger bias allows for larger energy range of electrons to sweep across the spin-polarized edge and unpolarized bulk (>λ_{SO} eV) states, which results in a local maxima for Si and Ge. Sn and Pb have much larger λ_{SO}, values given on top of the figure have been taken from Table I of Ref. [65]. E_f = 5 meV. Refer to Fig. B.2 and Fig. B.3 for local density of states (LDOS) distribution for some exemplar cases to develop an intuitive understanding of the Y-device.

Next, the Fermi-level is moved away from the Dirac-point, deeper into the conduction bands, in Fig. 4.2(c, d). Fig. 4.2(d) shows that SP degrades as electron energies move out of λ_{SO} energy window which can be expected for quantum spin hall (QSH) insulator phase [48, 65] for a zigzag nanoribbon. However, more interesting physics is embedded in Fig. 4.2(c). To understand this result, the Transmission (T) has been plotted for equilibrium conditions across energy (E) for different structures and materials as shown in Fig. B.5. Appendix section B.2 expounds the reasons and implications of the quantum interference effects observed in Fig. B.5 for various constraints and the discussion in this chapter has been qualified to help reader develop more intuitive understanding of quantum transport in these materials and devices. The local minimum observed in the conductance in Fig. 4.2(c) corresponds to a local minimum in the transmission at λ_{SO} for each material. In Fig. 4.2(e, f), the voltage bias across channel has been swept for a constant Fermi-level. Increasing the bias also increases the range of electron energies moving from source (Arm-A) to drain (Arm-B and Arm-C). Therefore, the net current and SP is just the weighted average of contribution from electrons moving through spin polarized edge state (within $\pm \lambda_{SO}$) and energies beyond λ_{SO} (eV) that are un-polarized and may even have lower transmission (see Fig. B.5), this is also the reason for local maxima observed for Silicene in Figs. 4.2(e) and 4.2(f). Note that local-maxima are not visible for heavier Group-IV materials in Fig. 4.2(e) because of the choice of E_f in this particular case. For Si, it is slightly over corresponding $+\lambda_{SO}$ while for others it is well below this energy-level. Hence, others just exhibit the conductance roll-off while for Si conductance first improves with inclusion of electron-injection for higher transmission energies below $+\lambda_{SO}$ as bias is increased. Next, we delve into the effects of buckling and Zeeman field which shift the spin-polarized bands along energy-grid,

an equivalent of affecting quasi Fermi-level, into different transmission window, induce phase transitions [65] and affect the interference (see section B.2), and thus transmission, in the channel.

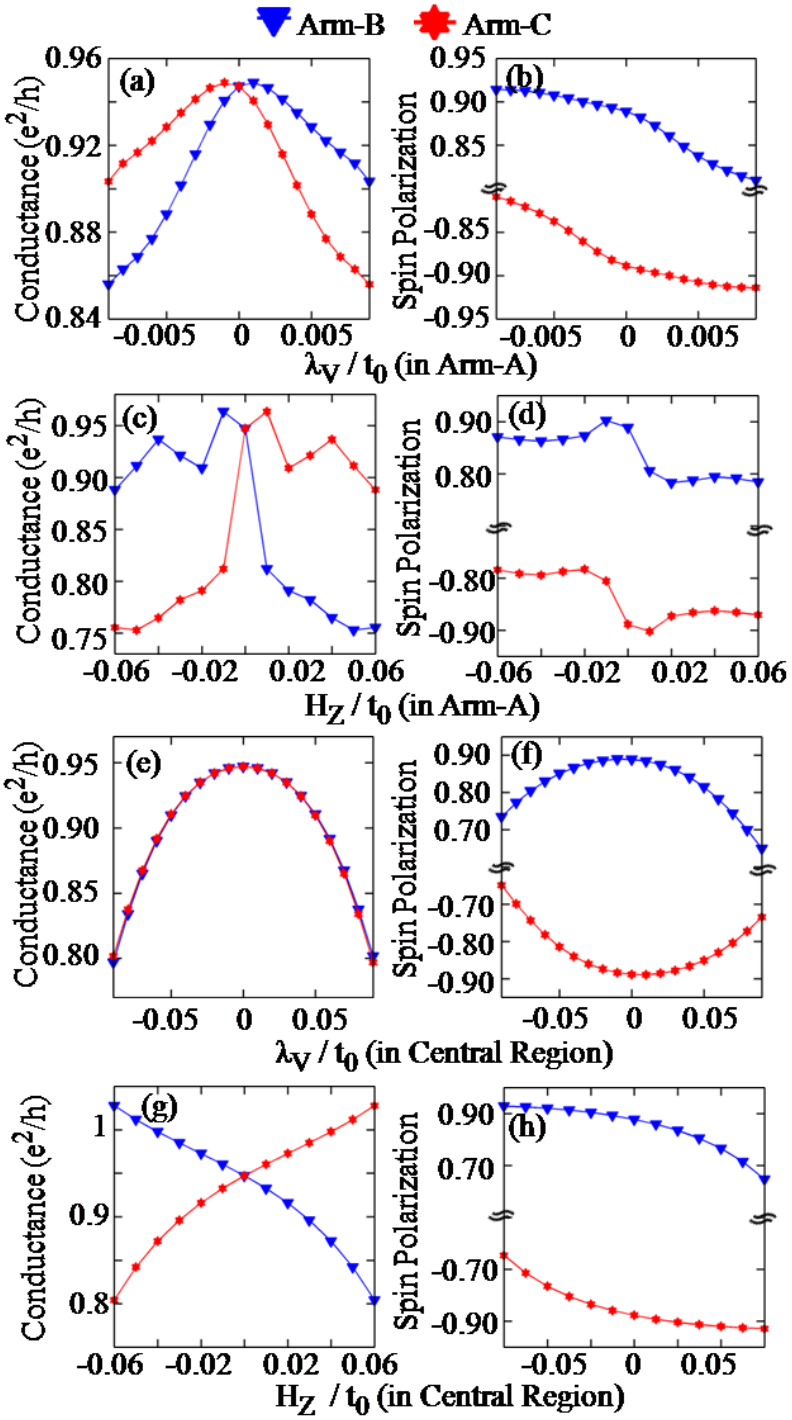

Figure 4.3 Effect of buckling field (λ_V) (a,b,e,f) and magnetic (H_Z) (c,d,g,h) field on Conductance (a, c, e, g) and Spin-Polarization (SP) (b, d, f, h) (broken y-axis) of current through Arm-B (blue triangle) and Arm-C (red star) of Germanene device. (a-d) fields are applied in Arm-A (see Fig 4.1(a)). (e-h) fields are applied in central region. E_f = 5 meV, V_{BA} (V_{CA}) = 4 mV. Refer to Fig. B.4 for LDOS distribution and Fig. B.6 and B.7 for spin distribution plots for exemplar cases.

In Fig. 4.3, we examine the effect of control parameters, i.e. buckling field and perpendicular magnetic field. For the subsequent discussion, the reader should also refer to Appendix-B.3 for better visual understanding through detailed spin distribution plots of Eq. (2.13). In Fig. 4.3(a), the Arm-A is in QSH phase, as expected from the energy-dispersion plot of a nanoribbon of same width under the buckling field of the same magnitude. From the dispersion (see Fig. 2.1) we observe that because of λ_V there is a relative shifting of quasi-Fermi level for type-A and type-B atoms. For type-A, $+\lambda_V$ ($-\lambda_V$) moves energies in higher (lower) transmission window (see Fig. B.5(c)), whereas for type-B, $+\lambda_V$ ($-\lambda_V$) moves electron energies in lower (higher) transmission regime. For instance, compare Arm-A edges for Fig. B.6(a), B.6(b) and B.6(c) to observe the relative decrease in charge on bottom (top) edge for $+\lambda_V$ ($-\lambda_V$) w.r.t. top (bottom) edge. Also note that because of this shift, the electron transport through both channels would see mode-mismatch on transit from Arm-A to Arm-B and Arm-C and hence the conductance decreases on both edges with increasing magnitude of λ_V.

However, on the bottom edge i.e. for the down-spin path the mode-mismatch is stronger (compare the shape of band-structure for up and down spin for Arm-A and Arm-B or Arm-C which have zero λ_V). Hence, there are stronger reflections at the interface between Arm-A and Arm-C than with Arm-B, which result in the faster roll-off for conductance in Arm-C for positive λ_V. Negative λ_V shows mirror effect because of the opposite shift in the band-structure for up and down spins on the top and bottom edge. For understanding Fig. 4.3(b), refer to the spin-polarization distribution in device in Fig. B.7(b) and B.7(c) and Fig. B.4(a). Observe that the DOS on the bottom edge spreads for positive λ_V and this region is strongly down polarized, whereas the region around the top-edge in Arm-A in Fig. B.7(b) diminishes. This

reduces the spin-polarization of charge on top-edge while it increases on the bottom edge. Exactly opposite happens for negative λ_V, as expected from Fig. B.7(c).

In Figs. 4.3(c, d), we consider the effects of an applied perpendicular magnetic field, which results in Zeeman splitting of the bands and different change in the phase of the electron wavefunction on top and bottom edges (also see section B.2). It is observed (not shown) from the equilibrium transmission distribution along the energy-grid, that in the constructive interference regime ($-\lambda_{SO}$ to $+\lambda_{SO}$) the positive (negative) H_Z decreases the transmission more (less) strongly on the top-edge, while on the bottom-edge it decreases less (more) strongly. However, beyond this, in the energy-range of the destructive interference, the transmission improves on both the edges but the increase is weaker (stronger) for the top-edge, and stronger (weaker) for the bottom-edge. The spin-polarization of the carriers flowing along the edges thus undergoes a concomitant change. As a result, for positive H_Z the current more strongly decreases on the top-edge (see Fig. 4.3(c)) and marginally on the bottom-edge. The oscillations occur because of the competing effects of shift in quasi Fermi-levels for spin-up (spin-down) into higher (lower) energy regime with respective changes in the transmission, which in our operating conditions goes unilaterally down (up) from low-to-high injection energies for small H_Z, but may not unilaterally go up for down-spins for higher H_Z fields because larger band-shift induces larger mode-mismatch in the transport path. The effect of H_Z is opposite when the direction of the field is reversed.

Consequently, the device behavior changes significantly when the fields are applied in the central region instead of Arm-A, as shown in Figs. 4.3(e-h). As discussed previously, the central region has an armchair interface with all three edges with only limited spatial interaction with the zigzag region, and therefore, it is

affected weakly by shifts of the quasi Fermi-level. Since energy bands for the triangular-box like central region are not well defined, we consider the fields acting qualitatively on all three types (3p, 3p+1 and 3p+2) of armchair nanoribbon (NR) energy bands by artificially modulating these bands in order to gain an understanding of their behavior. A crude justification for contemplating all three types of NRs is that along the y-axis there are a certain number of hexagonal rings, determined by the width of Arm-A. The number of these rings decreases by one successively in +x-direction in the Y-shaped device, and due to this variable width, the central region can accommodate all three types of super-cells.

Firstly, we examine effect of the buckling field (see Fig. 4.3(e, f)). Within the range of applied field strengths, for either polarity, the bandgap opens (closes) up for 3p+2 (3p and 3p+1) armchair NRs, where '3p+offset' is the number of hexagonal rings along the width. From the equilibrium transmission distribution along energy-grid, it is observed that buckling field of either polarity degrades transmission from source to either of the drains by equal magnitude across the entire energy-range, with a concomitant degradation of the spin-polarization (also see Fig. B.6(e) and B.7(e)). The effect becomes stronger for stronger fields, and a monotonic decrease is observed in both conductance (Fig. 4.3(e)) and spin-polarization (Fig. 4.3(f)). In non-equilibrium condition, although the unilateral degradation of transmission is still observed, the effect is marginally stronger for transport from Arm-A to Arm-C. This path however has slightly stronger spin-polarization as illustrated in Fig. B.7(e). Nevertheless, observe that by applying the field in central region, for a sizeable change in current (non-equilibrium) field is much larger compared to its application on Arm-A for similar degree of current-modulation. Next, the effect of applying magnetic field (H_Z) in the central region is illustrated in Figs. 4.3(g, h). In contrast to

the case for field over Arm-A, the field is now observed to slightly increase the transmission on the bottom-edge instead of just weakly impairing it. The transmission on the top-edge however weakens as for field over Arm-A. Spin-polarization of the carriers gets accordingly stronger or weaker. Therefore, the current (Fig. 4.3(g)) decreases (increases) for Arm-B (Arm-C) for $+H_Z$ field, deteriorating (improving) SP (Fig. 4.3(h)) with it. The weak shift in quasi Fermi-level at the bends is insufficient to induce a strong competing effect, like it does when field is applied in Arm-A. Without the competing effect, the SP exhibits a monotonous change in conductance without any oscillations. The opposite effect for $-H_Z$ can again be expected from the above discussion as seen in Figs. 4.3(g) and 4.3(h).

After examining different electronic and magnetic controls for the operation of our device, we now discuss their implications. Figs. 4.3(a-d) show that by applying fields in Arm-A more current can be steered into one of the drain-arms with SP modulation ranging up to 20%. The differential current signal between Arm-B and Arm-C is complemented with modulation of SP to give us two bits of information, which could be the basis of quaternary digital logic, and double (theoretical maximum) the information density. Next, Fig. 4.3(h) shows that one spin can be controlled while the other is held constant, if the central region is biased via $|H_Z|$ around $0.05 \bullet t_0$ (t_0 is transfer energy). The bias field, that fixes SP of one arm, may be superposed with a small alternating signal (ac) field that would induce a corresponding swing in the SP of the other arm. This oscillatory SP signal coupled with the oscillatory differential current signal may be utilized in devising circuits.

4.4. Conclusion

In conclusion, we discuss the design of an efficient spin separator based on Group-IV 2D materials (Si, Ge, Sn), operating in the quantum spin Hall phase within

$\pm\lambda_{SO}$ energy range. Effects of external controls such as the buckling field and perpendicular magnetic field, unique to this family of materials, are evaluated comprehensively along with those of more regular controls such as the bias and Fermi-level. It is shown that for sufficiently large widths of the device close to 100% polarized spins of opposite polarity can be spatially separated. It is also shown that effective manipulation of buckling field and perpendicular magnetic field can preferentially steer current between the two drains to create a differential charge current with a complementary effect on spin polarization. We also show that applying field in Arm-A (source arm) or the central region can enable exotic circuits that are analogous, but more content rich than the conventional digital and analog circuits. Our study advances the field of spintronics towards charge-spin hybrid circuits.

Chapter 5

Effect of Phase Transition on Quantum Transport in Group-IV Two-Dimensional U-shape Device

The effect of phase-transition from the quantum-spin-hall to the band-insulator phase on the transport through a three-terminal U-shape spin-separator has been computationally investigated via Non-Equilibrium Green Function formalism. Two-dimensional Group-IV elements have been comprehensively appraised as the device material. The device separates the unpolarized current injected at the source-terminal into nearly 100% spin-polarized current of the opposite polarity at the two drain terminals. The phase-transition activated by the electric-field orthogonal to the device is shown to extensively influence the current magnitude and its spin-polarization, and the effect is stronger for materials with smaller intrinsic spin-orbit coupling. Moreover, the device length and the area under field are shown to critically affect the device characteristics on phase change. It is shown that the same device can be operated as a spin-filter by inducing phase-transition selectively in the channel. The results are important for designing spin-devices from Group-IV monolayers.

5.1. Introduction

Since the successful isolation of graphene [38], there has been extensive research focused on the carbon monolayer devices for both pure electronics [142, 143] and spintronics [63, 144] applications. Graphene, however, has very small intrinsic spin-orbit coupling (SOC) (λ_{SO}) (~1 μeV [134]) and therefore despite of having spin-polarized metallic edge current in the zigzag nanoribbon form [145, 146] it does not seem to be the solution, because the operating conditions may drive the transport into unpolarized energy range, even for the near-equilibrium condition. The defects and

vacancies have been shown to increase λ_{SO} to 1 meV [139] in graphene but they may also make graphene structurally unstable [147]. Silicene (Si), Germanene (Ge), Stanene (Sn), and Plumbene (Pb), the other two-dimensional (2D) Group-IV materials, have honeycomb structure analogous to graphene, as predicted by theoretical studies [119, 120, 140] and already been experimentally validated for silicene [122, 148, 149] and germanene[123, 150]. These materials possess Dirac cones akin to graphene and are expected to have high electron mobilities [125, 151] which may make them amenable for high-speed electronics. Additionally, very large spin dephasing lengths have been projected for these materials, for instance 0.5 μm and 1.5 μm for the silicene and germanene sheets respectively [152], and 3 μm for the silicene armchair nanoribbon [153]. However, because of the infancy of the research in these materials, the experimental values have not yet been reported to the best of our knowledge.

Moreover, these Group-IV materials possess significant buckling due to sp^2-sp^3 bond hybridization [133] which results in large λ_{SO} [65]. Since, the energy range for an efficient spin operation extends from $-\lambda_{SO}$ to λ_{SO} eV ($2\times\lambda_{SO}$ energy window) for the zigzag nanoribbon device [48], these materials qualify for room-temperature non-equilibrium operation with a channel bias of at least 1 mV [154]. Furthermore, abundance of the topological phases[155, 156] in these materials, achievable by an external electric field [157], a magnetic field [158] and photo-irradiation [159], such as quantum-spin-Hall state (QSH), band-insulator state (BI), quantum-anomalous-Hall state, and valley-polarized-metal state [65] facilitates rich set of spin-devices like a spin-separator [127], a giant magnetoresistance device [132], and a spin-valley filter [160].

Realizing spintronic devices controlled solely by the electric field is a key goal of the spintronics [31, 161]. It has been recently shown that a three-terminal Y-shape

device [46] works (see **Chapter 4**) as an efficient spin-separator even without any magnetic field in the QSH phase, but the device operation has been investigated under both the exchange and the buckling field (λ_V), where buckling field refers to the field orthogonal to the device and produced by the difference between the top and bottom gate potentials, which tunes the buckling in the material and is distinct from the phenomenological potential applied to adjust the Fermi-level (E_F) in the device.

However, λ_V may drive the system from the QSH-phase to the BI-phase [157], and more easily for the materials with small λ_{SO} like silicene and germanene. Moreover, Y-shape device with edge-transport is afflicted with Fano interference [162], because of the physical bending in the channel, in the quantum transport which decimates the transmission on transition from the spin-polarized ($-\lambda_{SO}$ to λ_{SO} energy range) to the unpolarized energy levels. This deteriorates the conductance at both of the drain terminals. Therefore, there is a need to investigate the effect of the buckling-field driven phase-transition in the Group-IV monolayer spin-separators and to improve the conductance at drains to enhance the performance of the device.

Hence, via Non-Equilibrium Green Function (NEGF) formalism [81], we computationally investigate the effect of phase-transition from the QSH to the BI phase on the transport through a three-terminal U-shape (see Fig. 5.1) spin-separator made of Group-IV monolayers. The absence of the bend in the path of the transport, which is along the edges of the zigzag nanoribbon channel, is shown to maintain a large transmission from the polarized to the unpolarized energy range. The quantum transport calculations at low energy, furthermore, show that for all of the four materials (Si, Ge, Sn, and Pb) a highly efficient spin-separator is realized even without buckling and exchange field. The high-efficiency is appraised over a wide range of device dimensions within experimentally accessible regime [163]. This

enables a deeper appreciation of the effect of λ_V on the quantum transport in U-shape device, especially of the peak-current obtained from the device for different materials and dimensions. The phase-transition activated by λ_V is shown to extensively influence the current magnitude and its spin-polarization (SP), and indeed the effect is stronger for materials with smaller λ_{SO}. It is also shown that current-modulation in the device using λ_V can transform the U-shape spin-separator into a spin-filter, adding to its potential as a spintronic device using electric field as a sole control.

This chapter is organized as follows: Sec. 5.2 explains the device setup used in this study, Sec. 5.3 discusses the results of our simulation and how phase-transition affects the current and its spin-polarization for the spin-separator, which can further be extended to a spin-filter operation. This is followed in Sec. 5.4 with the summary and conclusions of our study. Appendix C serves as the supplement for the discussion on the spin-filter.

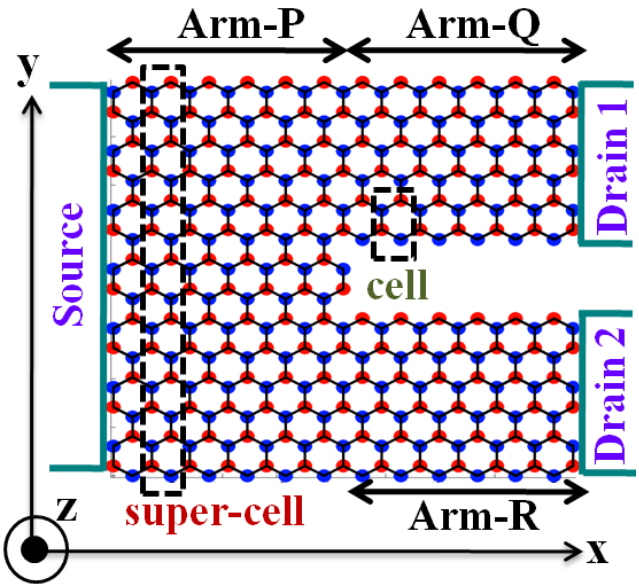

Figure 5.1 A three-terminal U-shape device. Arm-P is connected to a source, and Arm-Q and Arm-R are connected to the drain terminals. The device lies in the *x*-*y* plane. The red (type-A) atoms are out-of-plane from the blue atoms (type-B) by Δ_C along the *z*-axis because of the buckling in the material. Four-atom unit-cell is labeled as a cell and one chain of cells along the transverse axis is labeled as super-cell. These are used to earmark device dimensions along *y* and *x*-axis respectively.

5.2. Computational Setup

Figure 5.1 illustrates the three-terminal U-shape device used for investigating the effect of phase-transition from the QSH to the BI phase in patronage of the bucking field (λ_V). Arm-P is connected to the source-terminal, while Arm-Q and Arm-R are connected to the drain-terminals drain-1 and drain-2 respectively. The width of Arm-Q is kept equal to that of Arm-R. For '*nWp*' cells wide Arm-P, the width of each drain-arm is set to ⌈nWp/2⌉−1 cells. As a representative case, the length of each of the arms is set to 14 super-cells, the widths of arms P, Q, and R to 14-cells, 6-cells, and 6-cells, respectively, Fermi-level E_F to 1 meV, and the source-to-drain voltage V_{DS} or V_{PQ} (V_{PR}) to 1 mV, unless specified otherwise.

For more detailed analysis of the effect of λ_V on the device transport, Si or Ge is chosen as an exemplar material for some of the cases but the results are expected to be applicable for all of the four materials. The transport is simulated at zero Kelvin because of the small energy range, dictated by $\lambda_{SO,}$ of the spin-polarized bands in the 2D Group-IV materials that can be fabricated currently. The future technological advances in fabricating 2D-devices with the elements of large SOC like tin [140, 141] and lead may, however, allow room temperature operation of the U-shaped spin-separator at a small bias. Successful attempts at increasing the intrinsic λ_{SO}, for example by halogenations [128, 164], may also expedite the physical implementation of such a device.

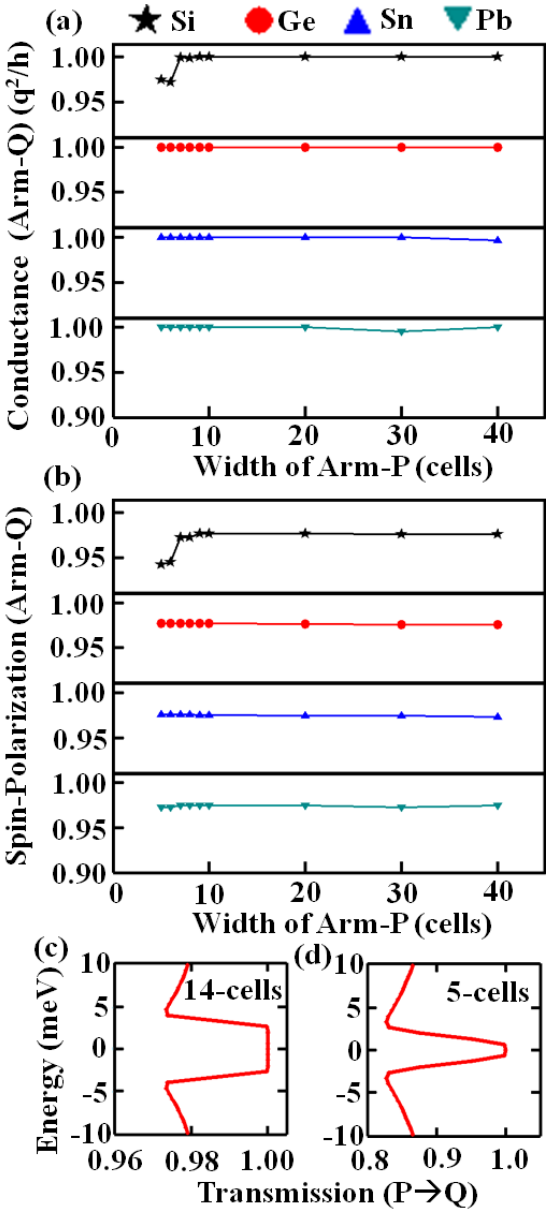

Figure 5.2 Effect of the channel width at zero λ_V on the conductance (a) and the spin-polarization (SP) of the current (b) at Arm-Q for Si (black rectangle), Ge (red circle), Sn (blue triangle), and Pb (cyan triangle). Transmission in the equilibrium condition for a Si-device with Arm-P width of 14-cells (c) and 5-cells (d).

5.3. Results and Discussion

When no buckling field is applied, the results illustrated in Fig. 5.2 reveal that the U-shape device acts as an efficient spin-separator for all of the four materials. The current flowing from the top (bottom) edge of Arm-P through the outer-edge of Arm-Q (Arm-R) along type-A (type-B) atoms have the same magnitude as the current flowing through the opposite arm but possess +z or ↑ (−z or ↓) SP. In Fig. 5.2(a, b),

the analysis of the width of Arm-P shows that the conductance at the drain-arms is nearly held constant at 0.995 q^2/h and SP at 97.5%, even down to 5-cell device-width for Ge, Sn, and Pb and 7-cells for Si. In this range, both conductance and SP are also found to be invariant with respect to the device length and the non-zero gap between the two drain-arms (not shown).

For $nWp \leq 6$ there is a drop observed both in conductance and SP for the Si-device. To understand this drop, the transmission in equilibrium condition is next illustrated in Fig. 5.2(c) and 5.2(d) for 14 and 5 cell device-widths respectively for a Si-device. It is observed that at a very small width the energy window for the unity transmission is reduced, whereas for the large arm widths, a full-mode transmission is available in the entire $2\times\lambda_{SO}$ energy range. This is because for the smaller width there is a larger overlap between the wavefunction of the two edges which supple opposite spins [46]. However, the larger SOC for other heavier materials exercises a stronger confinement on the wavefunction to the respective edges and hence abates the overlap. Therefore, the drop in conductance and SP for the Si-device stems from the shrunk energy window for transmission even at E_F = 1 meV and V_{DS} = 1 mV. This shows that for the extremely narrow Si-devices the operating temperature and the source-to-drain voltage range may be restricted and therefore the wider silicene spin-separators may be more appropriate for the applications.

Therefore, the conductance and SP is invariant to the device-width only above a certain dimension, which depends on the SOC of the material, and therefore the presented results are expected to be valid for even larger device-widths than examined in Fig. 5.2. Moreover, the presented characteristics are invariant to the length only in purview of the ballistic transport. At high temperatures, the phonon scattering may degrade the device characteristics. The edge transport is, however, robust to the edge

disorder (see supplementary of Ref. [65]), indicating that the edge disorder should not deter the device behaviour. Next, observe in Fig. 5.2(c, d) that beyond the spin-polarized energy-window (± 4.2 meV), the transmission for the U-shape device is substantially larger than for the Y-shape device (compare with Fig. B.2.1 or the Supplementary Fig. S2 of Ref. [46]). The absence of any geometrical bend in the channel, therefore, empowers this architecture with a higher conductance over a larger energy range and hence may enable the device operation for even larger voltages.

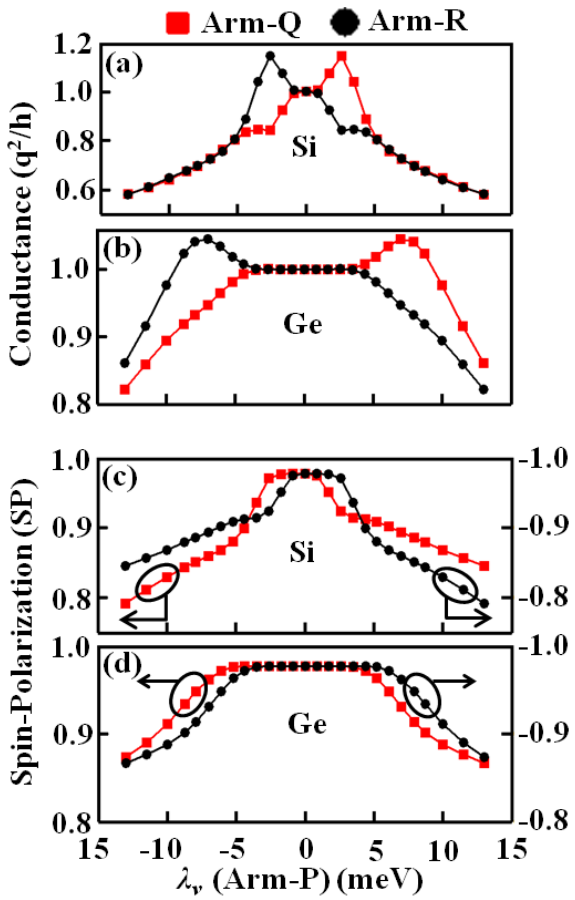

Figure 5.3 Effect of λ_V on Arm-P of the silicene ((a) and (c)) and germanene ((b) and (d)) device. Observe a local maximum in the conductance at Arm-Q (Arm-R) as the device transitions from the QSH to the BI phase for a positive (negative) λ_V. The peak-conductance (G_{max}) for the Si-device is observed to be larger than that of the Ge-device (see text for the details). For the Sn and Pb devices the local maximum is absent (not shown). (c, d) Spin-polarization for both the arms degrades for the increasing magnitude of λ_V, albeit at different rates that switch with the polarity of λ_V.

The effect of λ_V on the quantum transport in silicene and germanene device is thereafter illustrated in Fig. 5.3. Firstly, λ_V is applied only on Arm-P, and is swept from −13 to 13 meV. As λ_V is increased (decreased) from zero, initially a plateau at a

unit conductance is observed for both the arms. The plateau extends up to larger λ_V for the Ge-device as compared to the Si-device. A steady increase in the conductance for Arm-Q (Arm-R) is observed following the plateau, which reaches a peak before showing a continuous roll-off. The peak-conductance (G_{max}) is observed to be significantly higher for the Si-device (1.15 q^2/h) than for the Ge-device (1.04 q^2/h). It is to be noted that the λ_V at which the G_{max} occurs for Arm-Q (Arm-R) for the Si-device is 2.6 (−2.6) meV, considerably smaller in magnitude than for the Ge-device at 7 (−7) meV. The conductance through Arm-R (Arm-Q) degrades continuously following the plateau, however, the rate of decay changes ostensibly after Arm-Q (Arm-R) conductance goes past the peak which is more vivid for the Si-device (see Fig. 5.3(a)) than the Ge-device (see Fig. 5.3(b)). Therefore, because of the smaller λ_V at G_{max} for Si-device, the minimum conductance (G_{min}), in purview of λ_V used for this analysis, is 0.58 q^2/h, compared to 0.82 q^2/h for Ge-device.

The SP of Arm-Q (Arm-R) displays a similar plateau as the conductance for an increasingly positive (negative) λ_V, but unlike the conductance, the SP for both arms decay with the increasing magnitude of λ_V as illustrated for the Si and Ge device in Fig. 5.3(c) and 5.3(d) respectively. Initially, SP decay for Arm-Q (Arm-R) is greater than the other arm, but as seen in Fig. 5.3(c) and Fig. 5.3(d) the spin-decay rate for both the arms changes after Arm-Q (Arm-R) experiences the peak in the conductance, and the roll-off may become steeper for Arm-R (Arm-Q). Nevertheless, like the conductance trends, the SP degradation is triggered at larger λ_V for the Ge-device (Fig. 5.3(d)) than for the Si-device (Fig. 5.3(c)) which enables relatively high SP on both arms for former even at large field-strengths. For the Sn and Pb devices, no significant deviations of the arm-conductance and the SP are observed for the range of λ_V applied (not shown); hence a pattern of an increasing insensitiveness to λ_V emerges with the

increasing λ_{SO}. These results are next demystified with the assistance of detailed analysis of the quantum transport in the Ge-device in Fig. 5.4 and Fig. 5.5.

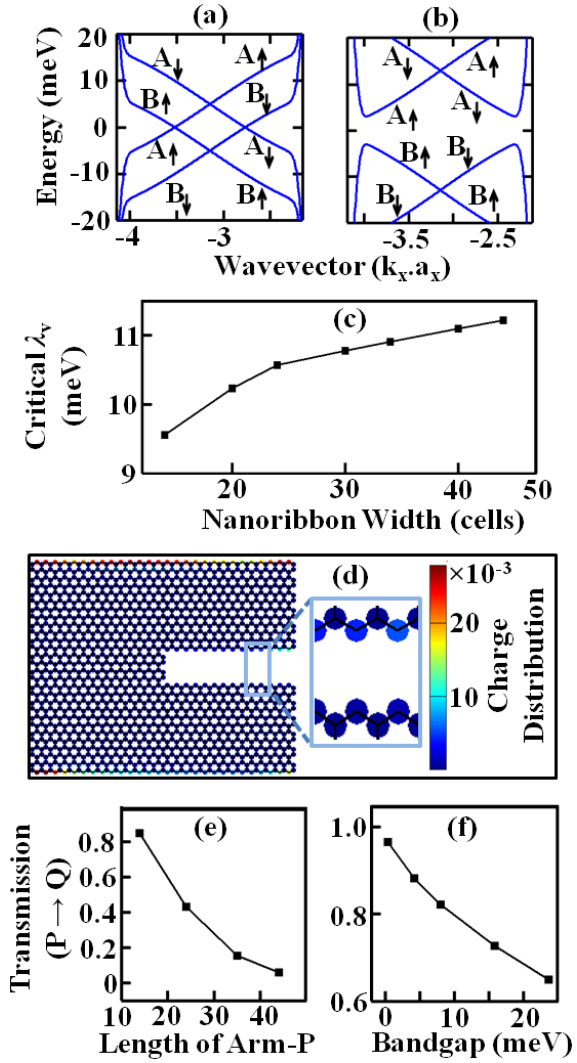

Figure 5.4 Energy-dispersion of 14-cell wide zigzag germanene nanoribbon in (a) QSH phase (λ_V = 5 meV) and (b) BI phase (λ_V = 13 eV). The forward moving channel in the conduction band changes from B↓ to A↓ after the phase-transition, along with the opening of the bandgap. (c) The critical λ_V (λ_C) at which phase-transition occurs is plotted against the width of the Ge nanoribbon. (d) Charge distribution on the bottom-edge of Arm-Q, for a Ge-device with λ_V = 7 meV applied on Arm-P, implying a current flow through the bottom-edge of Arm-Q. (e, f) The tunneling phenomenon in a 14-cell wide Ge U-shape device in the BI phase is illustrated by plotting the transmission from Arm-P to Arm-Q for (e) different lengths of Arm-P at λ_V = 13 meV and (f) different bandgaps (computed for nanoribbon) with λ_V applied only over Arm-P.

Figure 5.4(a, b) examines the effect of λ_V on the energy-dispersion of a 14-cell wide Ge zigzag nanoribbon. For Fig. 5.4(a) the nanoribbon is in the QSH-phase (λ_V = 5 meV), and it is observed that the forward moving states in the conduction-band are localized on type-A atom on the top-edge and on type-B atom on the bottom-edge of

the device with ↑ and ↓ SP, respectively. Nanoribbon has transitioned to the BI-phase for a large λ_V value of 13 meV in Fig. 5.4(b), which swaps the spin-polarized states, across the edges, between the conduction and valence bands to depolarize both the forward and backward moving edge-channels on the nanoribbon. We note that the λ_V at which the phase-transition is instigated is numerically defined in this work to be the value at which the system transforms from the QSH to the BI phase at a very small wavevector offset at the left-side of the left Dirac-point in the dispersion diagram, and is subsequently referred as the critical buckling field (λ_C).

There are three important characteristics of λ_C which would subsequently aid in understanding the transport results. Firstly, as shown in Fig. 5.4(c), λ_C scales with ribbon width and is expected to approach 11.8 meV or λ_{SO} at which the phase should transit in a Ge 2D-sheet [65]. On the same note, the λ_C for the nanoribbon of an identical width is larger for material with larger λ_{SO}. Thirdly, applying λ_V splits the bands along both the energy and momentum axis (see Hamiltonian in Ref. [65] or Eq. (2.1)). Since, the slope of the bands in the spin-polarized region depends on λ_{SO} and also since the critical field λ_C scales with λ_{SO} of the material, the phase transition from the QSH to the BI phase happens at larger λ_{SO}. This results in following two observations- firstly, there is a larger splitting of the bands along the energy-axis, and secondly, there is a larger separation between the band-edges along the momentum-axis when the material with larger λ_{SO} undergoes phase-transition. The choice of the material and the ribbon-width therefore regulates (i) the field required for the phase-transition and (ii) the momentum-mismatch which carriers confront on transition from the area under λ_V to the field-free region of the device. Specifically, we observe that the λ_C for a 14-cell wide Ge nanoribbon, corresponding to Arm-P width of the representative device, is found to be 9.56 meV (see Fig. 5.4(c)), at wavevector (scaled

by translation vector along *x*-axis) of −3.911, which would map close to the K-valley in the first Brillouin zone.

In the BI phase for the positive λ_V, because of the band-inversion from B↓ to A↓ eigen-state, the modes of the transmission for type-A (type-B) atoms on the top (bottom) edge of Arm-P increases (decreases). Charge distribution in the device plotted in Fig. 5.4(d) confirms this and furthermore suggests that a larger fraction of current is flowing through the top-edge (type-A atoms) than on the bottom-edge (type-B atoms). The unpolarized (A↓ and A↑) current injected along the top-edge of the Arm-P partially flows through the bottom-edge of Arm-Q, which supports ↓ current through type-B atoms because Arm-Q is still in the QSH-phase (λ_V = 0 meV over Arm-Q). The current redistribution results in larger (smaller) conductance for Arm-Q (Arm-R) following the plateau of the unit-conductance for the QSH-phase in Arm-P. The mode-mismatch at G_{max} is, however, stronger for the Ge-device than the Si-device because of larger λ_V, which counters the increase in modes for type-A atoms and results in a larger magnitude of G_{max} for the Si-device than the Ge-device.

Furthermore, note that because of the finite-length, an effect dealt more comprehensively later in Fig. 5.5, the Arm-P is in metaphase at G_{max} (λ_V = 7 meV) in Fig. 5.3(b), i.e. in an amalgam of the QSH and the BI phase. For the increasingly strong fields, the BI phase gradually sets in to induce the band-inversion and open the bandgap. The metaphase in Arm-P coupled with the QSH-phase in Arm-Q actuates the effects of the phase-transition to be spread over a range of λ_V rather than be localized at a particular λ_V, which may have been opined from energy-dispersion plots. Next, the roll-off of the conductance for Arm-Q beyond G_{max} arises from the bandgap, created concurrently with the phase-transition, which becomes increasingly more influential for larger λ_V. It can, however, be observed in Fig. 5.3 that even at relatively

large λ_V of 13 meV, at which the bandgap in a Si and Ge nanoribbon would be 18.9 meV and 6.1 meV, respectively, and therefore no channel for transport may exist from the source to drain-arms, both the SP and conductance for drain-arms is substantial.

Figure 5.4(e, f) illustrates further investigations into this observation. Illustrations advance that a large current at relatively large λ_V in Fig. 5.3 is incited by electron tunneling, where the tunneling barrier is characterized by the length of Arm-P (see Fig. 5.4(e)) which regulates the barrier length and the magnitude of the bandgap which regulates the barrier height (see Fig. 5.4(f)). The decay in the transmission observed for both the increasing bandgap and the length of Arm-P, on which λ_V is applied, for the Ge-device in equilibrium at 0.5 meV electron-injection energy substantiates the tunneling phenomenon. The different rates of the SP decay for the drain-arms in Fig. 5.3(c, d), is also attributed to the phase-transition and concomitant bandgap formation. For Arm-Q (Arm-R) under increasing λ_V, firstly the depolarization (loss) of the channel by the onset of the BI-phase causes the SP to degrade, and subsequently, the degradation rate is determined by the bandgap widening after the phase-transition, which causes the rate of degradation for each arm to change (see Fig. 5.3(c)).

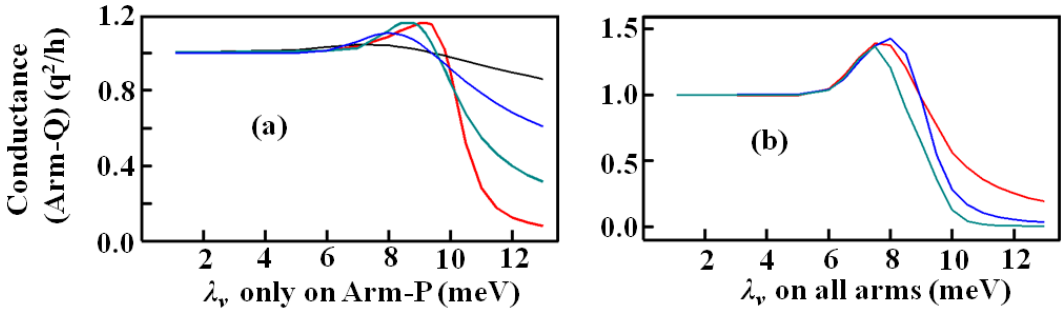

Figure 5.5 Effect of λ_V on the conductance at Arm-Q for a Ge device. (a) λ_V applied on Arm-P of lengths 14 (black line), 20 (blue line), 28 (Cyan line) and 42 (red line) super-cells shows that the G_{max} for Arm-Q increases in magnitude and shifts to larger λ_V for longer Arm-P. (b) Effect of λ_V applied throughout the device with each of the arm lengths set to 14 super-cells (red line), 20 super-cells (blue line), and 28 super-cells (cyan line). The trend lines saturate when the entire energy window for the transport lies in the bandgap.

Next, for the deeper understanding of the mechanics and the effect of the phase-transition on the transport through the device, we investigate the Ge-device by considering two different schemes of applying the buckling field. Firstly, the field is applied only over Arm-P in Fig. 5.5(a). As the length of Arm-P is increased, G_{max} increases because the arm properties increasingly feature the nanoribbon case which should have more (less) type-A (type-B) channel in the BI-phase (see Fig. 5.4(b)). The G_{max} for the Ge-device significantly changes from 1.044 q^2/h for device with 14 super-cell long Arm-P (black squares) to 1.155 q^2/h for 42 super-cell long Arm-P (red triangles). The λ_V for attaining G_{max} also increases with an increasing length, approaching λ_C of 9.56 meV for a nanoribbon of the same width as Arm-P (see Fig. 5.4(c)). Concurrently, G_{max} also tends to saturate with the increasing length as evident from the plots for devices with 28 (green line) and 42 super-cell long Arm-P (red line). Therefore, the effect of phase-transition is stronger for the longer arm, which may be useful for designing devices with a different built-in G_{max} and correspondingly different buckling-field.

Furthermore observe in Fig. 5.5(a), the current for λ_V = 10 meV is larger for 42 super-cell than 28 super-cell long Arm-P, contrary to the expectation that when the bandgap is present the longer the Arm-P the lower should be the current (see Fig. 5.4(f)). The expectation is, howbeit, not justified for λ_V very close to λ_C, because the increase in λ_V for attaining G_{max} for increasing length implies that the conductance roll-off due to the bandgap dawns at larger λ_V. Therefore, despite of the steeper roll-off in the conductance for longer Arm-P, the larger λ_V at G_{max} for 42 super-cell case does not permit enough deterioration of the conductance. However, the steeper roll-off does result in the lowest conductance for 42 super-cell long Arm-P device for λ_V = 13 meV.

Next, the uniform field is applied over all three arms in Fig. 5.5(b), which yields an interesting appraisal of the metaphase. For this case, the G_{max} may be higher than obtained in Fig. 5.5(a) because the dual type-A channel exist in both the source and drain arms which also alleviates the mode-mismatch. For instance, when λ_V is applied only over Arm-P, even by increasing the length, the largest G_{max} obtained is 1.155 q^2/h (red triangles in Fig. 5.5(a)), but when the field is applied over the entire channel the G_{max} even with only 14 super-cell long arms is 1.376 q^2/h (red line in Fig. 5.5(b)). However, it transpires that the G_{max} is not necessarily larger for the device with a longer channel length, when the field is applied over the entire channel, as illustrated in Fig. 5.5(b) by blue and cyan trend-lines for 20 and 28 super-cell long arms respectively. Since the width of the drain-arms is smaller than the source-arm, the drain-arms undergo phase-transition for smaller λ_V than the source-arm. This can lower the G_{max} because larger bandgap may exist, whose effect will scale with the arm-length, on arm Q and R when Arm-P undergoes phase-transition.

Therefore, the value of G_{max} and corresponding λ_V is arbitrated by induction of dual-channel and the bandgap in the channel region under field. Nevertheless, as expected for large field value of λ_V = 13 meV, the existence of bandgaps in both the source and drain arms (see red line in Fig. 5.5(b)) results in smaller conductance compared to the case (black line in Fig. 5.5(a)) where bandgap exists only in Arm-P.

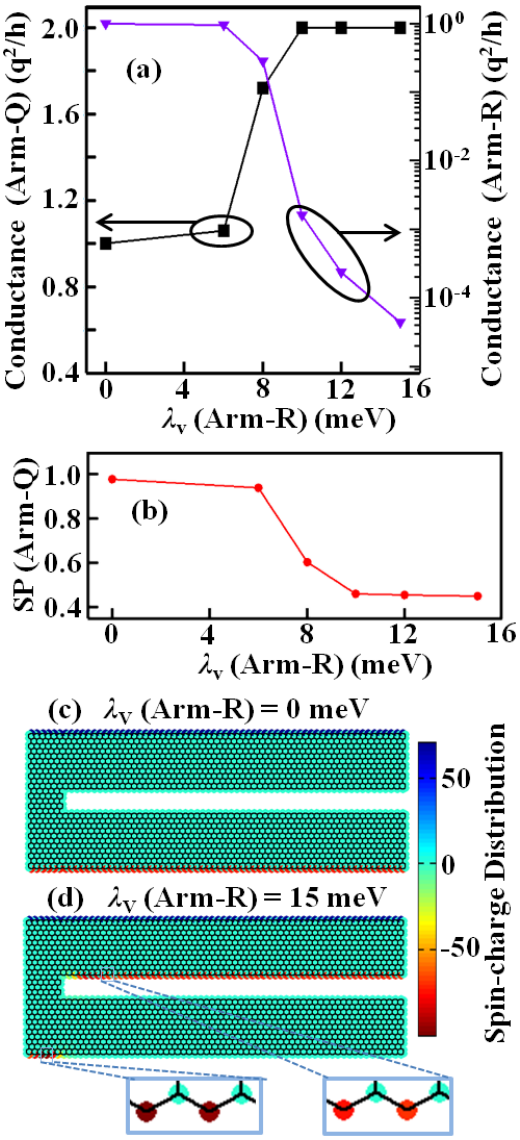

Figure 5.6 Spin-filter realized by applying λ_V on one of the drain-arms (Arm-R) of a Ge-device with P, Q, and R arm-lengths of 6, 60, and 60 super-cells respectively at E_F = 1 meV and V_{DS} = 1 mV. (a) Arm-R conductance is effectively blocked at high λ_V whereas Arm-Q transporting ↑ spin has a saturating conductance of nearly 2 q^2/h. (b) Spin-polarization for the Arm-Q decays from unity to yet an acceptable value of 0.45 at λ_V = 15 meV. The spin-filter filters out of the oppositely-polarized current through the other drain-arm. (c, d) Spin-charge distribution, computed via Trace(σ_z.G^n) and integrated over entire energy range, for λ_V = 0 meV (c) and λ_V = 15 meV (d) insinuates that for λ_V = 15 meV B↓ current from the bottom-edge of the source-arm is partly re-routed along the inner-edge of Arm-Q which counters the A↑ on the outer-edge, in contrast to the zero-field case in which ↑ and ↓ current completely flow along the outer-edges of the two drain-arms. The zoomed insets suggest the SP decay of B↓ current on migrating from Arm-P to Arm-Q.

Finally, Fig. 5.6 shows that the spin-separator can be functionally extended to a spin-filter by applying the buckling field on a drain-arm in lieu of the source-arm. As gleaned from Fig. 5.4(e), in the BI-phase, the bandgap induces potential-barrier in the channel which attenuates the transmission and the effect gets stronger as the

length of the tunneling-barrier is increased. Therefore, for the spin-filter operation, long drain-arms of 60 super-cell length are examined, over which λ_V is selectively applied to turn-off the conduction through the corresponding drain-arm.

In Fig. 5.6(a), λ_V is applied over Arm-R and swept from zero to a large value of 15 meV. For such a large field, the bandgap induced barrier results in the current roll-off of four orders, while the entire current is routed through Arm-Q, as apparent from its nearly two-unit conductance for λ_V = 15 meV. Figure 5.6(b), furthermore, shows that the SP for the Arm-Q degrades with the increasing λ_V (see Appendix-C for comments on the SP of Arm-R) to yet an acceptable value of 0.45 for λ_V = 15 meV. To achieve higher SP, the device can be operated at a smaller λ_V, although there would be a trade-off against current annulment at Arm-R and hence with the efficiency of the spin-filter.

Alternatively, to reduce the λ_V for the spin-filter, the width of the drain-arms can be reduced to achieve BI-phase at lower λ_V (see Fig. 5.4(c)). To apprehend the additional current in Arm-Q and the degradation of its SP, the spin-charge distribution, which is computed from integration over the energy-grid for Trace(σ_z.G^n), in the device is appraised for the two extreme cases of λ_V = 0 eV and λ_V = 15 meV in Fig. 5.6(c) and 5.6(d), respectively. On comparison, it is observed that the charge does disappear from Arm-R for λ_V = 15 meV but it is sustained on the bottom-edge of Arm-Q, in contrast to the distribution for λ_V = 0 eV only on the two outer-edges of Arm-Q and Arm-R. This implies that at λ_V = 15 meV the current is forced from the bottom-edge of Arm-P to the bottom-edge of Arm-Q through type-B atoms, while there is almost no current through Arm-R. Despite of almost an equal current of the opposite polarity flowing through the two edges of Arm-Q, the SP of 0.45 is relatively high and unexpected. This large value is observed because the migration of the

current from the bottom-edge of Arm-P to that of Arm-Q through the bulk of the channel depolarizes it, resulting in the loss of its SP which is validated by comparing the intensity of red-color in two insets of Fig 5.6(d). Therefore, the unequal magnitude of SP of the current flowing on the two edges of the Arm-Q makes the realization of the spin-filter possible. The polarity of the output current can, additionally, be switched by applying the buckling field on the alternate drain-arm.

5.4. Conclusion

The Group-IV monolayer zigzag edges based U-shape device behaves as an efficient spin-separator in QSH-phase and can beget nearly 100% spin-polarized current of the opposite polarity at the two drain terminals. It is shown that the phase-transition from the QSH to the BI phase induces an additional current along one of the arms while destroying on the other, depending on the polarity of the buckling field.

Phase-transition, furthermore, opens up a bandgap which may result in a current-peak at one of the drain terminals while the SP degrades at both of the drain terminals. The peak-current is larger for the material with a smaller λ_{SO}. If buckling field is only applied on the source-arm, increasing the length of source-arm engenders larger peak-current but at larger buckling field. Application of the buckling field on the entire device may result in an even larger peak-current. The peak-current and the λ_V at which it occurs are determined by the contention between the effect of the width of the drain-arm and the device-length. The bandgap induced after the phase-transition can extend the functionality of the spin-separator to the spin-filter by applying the buckling field selectively on one of the drain-arms. Therefore, this work computationally shows that by judiciously exploiting the electric-field orthogonal to the device, arising from difference in the top and bottom gate potentials, an efficient spin-separator and spin-filter can be realized from the Group-IV monolayers.

Chapter 6

Carrier Transport in Bi_2Se_3 Topological Insulator Slab

This chapter presents a model for quantum transport in the thermal activation regime (> 50 K) in a Bi_2Se_3 slab, which is based on using a non-equilibrium Green's function approach in which bulk and surface states are modeled realistically, and the effects of phonon scatterings are included. Resistivity is computed for different temperatures, slab thickness, bias and strengths of the electron-phonon coupling at various doping levels in order to gain a handle on how various factors interact and compete to determine the overall resistance of the slab. Depending on values of the operating parameters, the temperature dependence of the slab is found to exhibit a remarkably complex behavior. Temperature dependence of resistivity is found to display an insulating trend when the slab is biased at the Dirac point even in the presence of strong electron-phonon coupling. In sharp contrast, for carrier doping, the material displays a metallic behavior induced by acoustic scattering effects, even though purely ballistic transport yields an insulating trend, explaining contradictory trends reported in transport experiments on Bi_2Se_3. Our analysis, furthermore, suggests an experimental strategy for obtaining a handle on the strength of electron-phonon coupling in topological insulators via temperature-dependent transport measurements.

6.1. Introduction

Strong spin-orbit coupling underlies the unique properties of the recently discovered class of novel materials, the three-dimensional (3D) topological insulators (TIs) [49, 51, 165-168], which support the existence of gapless surface states

protected by time-reversal-symmetry lying in the insulating band gap of the bulk material. Surface states of a TI can exhibit a single Dirac band with helical-electronic states, i.e. states in which directions of spin and momentum are locked with respect to each other. Such theoretically predicted spin-momentum locking [169, 170] and the robustness of these surface states to non-magnetic impurities [59, 60] has been verified by various experiments, and provides a new basis for potential applications in spin based electronics [63] and optics [171].

Practical device applications of the TIs require that transport be dominated by the topological surface states at room temperature. Although topological surface states are not allowed to backscatter due to symmetry constraints, the key to developing applications of TIs is to understand how the current is carried in the material at finite temperatures in the presence of electron-phonon couplings, and how carriers in topological surface states compete with bulk carriers. In this connection, Bi_2Se_3 with a bulk band gap of ~ 0.3 eV [52, 71] is an attractive candidate, although the pristine Bi_2Se_3 is electron-doped due to the presence of Se vacancies [172], which push the Fermi level into the bulk conduction bands. A variety of methods such as p-type doping [173, 174] and electrical gating [175] have been attempted for the purpose of lowering the Fermi-level so that it lies closer to the Dirac-point.

Theoretical analysis suggests that the temperature dependence of resistance in a TI, if transport is dominated by the surface states, would display an insulating trend (resistance decreasing with increasing temperature) [176]. Experimental results on Bi_2Se_3, on the other hand, show contradictory results in that some experiments observe metallic behavior [55, 175, 177-179], while others find insulating trends [54, 173]. A local maximum in resistance between 100 and 225 K, whose origin remains unclear, has also been reported in some experiments [54, 173-175, 180, 181]. In fact,

even the strength of electron-phonon coupling (λ) for Bi_2Se_3 surface states, whether it is strong [53, 56, 182] or weak [60, 183-185], is still a point of contention with estimated values of λ varying by as much as five orders of magnitude based on various theoretical arguments [53, 56, 184] and results adduced from angle-resolved photoemission spectroscopy (ARPES) [60, 183, 185, 186] and helium scattering [182] experiments.

The need for developing a viable temperature-dependent model of transport in the thermal activation regime in TIs is thus clear. Accordingly, in this study, using a realistic model of topological surface as well as bulk electronic states, we present a systematic investigation of how the factors of slab thickness, channel length, Fermi-level (carrier doping), voltage bias, temperature and the strength of electron-phonon coupling [186] compete in a TI in the presence of surface and bulk carriers. Effects of the strength of electron-phonon coupling and how resistivity evolves as the doping of the surface state is changed are delineated.

Our calculations show that inclusion of acoustic phonon scattering in Bi_2Se_3 reproduces the characteristic experimentally observed insulating and metallic trends depending on the position of E_f relative to the Dirac point. This investigation helps in proper understanding of experimental results and a possibility of a new method of detecting surface states via purely electrical transport experiments. Non-equilibrium Green Function (NEGF) approach is used for investigating transport through a slab of Bi_2Se_3 using a realistic model of surface and bulk states. Ballistic transport is considered first, followed by the inclusion of effects of acoustic phonons in the modeling. Our analysis shows that the interplay between various aforementioned factors leads to considerable complexity in the nature of transport in TIs; for example, experimental observation of an insulating trend in a TI need not simply imply

operation in surface bands. To the best of our knowledge, our study is the first to realistically model transport through individual layers of a TI slab in the thermal activation regime.

This chapter is organized as follows. In Section 6.2, the simulation approach used for simulating ballistic and acoustic carrier transport through a Bi_2Se_3 slab within the NEGF framework is presented. This is followed by the derivation of deformation potential and the self-energy for modeling acoustic phonons in Section 6.3. Section 6.4 discusses results for ballistic transport, and it is broken up into several subsections. Subsection 6.4.1 establishes an operating bias for low field-transport, followed by an evaluation of the temperature dependence of resistance in the thermal activation regime in Subsection 6.4.2, and a discussion of effects of slab thickness and Fermi-level (E_f) in Subsection 6.4.3.

In Section 6.5, we bring together various results to provide a more comprehensive understanding of transport in TIs in different regimes of carrier concentration, and discuss how our modeling gives insight into the contradictory experimental observations noted above, by focusing on the effect of channel length and temperature in subsection 6.5.1 and 6.5.2 respectively. Section 6.6 validates the model against the experimental data and presents microscopic explanation of few important points from the data. Subsequently, Section 6.7 suggests an experimental strategy for obtaining a handle on the strength of electron-phonon coupling in topological insulators via temperature-dependent transport measurements. Finally, Section 6.8 provides a summary of our results and makes a few concluding remarks.

6.2. Simulation Approach

Quantum transport was modeled via the Keldysh NEGF approach [81] using self-consistent Born approximation. Details of the Hamiltonian are summarized in

Chapter 2. Perfect contacts have been considered in this study. Modeling metallic contacts with hard wall boundary condition [83] for side contacts or even top contacts just modifies the results quantitatively because the current redistributes across the quintuple layers (QL; 1QL ~ 0.943 nm [71]) to flow on both the top and bottom surface layers. Comprehensive analysis of the contact effects for 3D-TI is presented in the **Chapter 7** [187].

As a representative case, a slab of 30 nm in length and 13 QLs in thickness [73] was chosen unless specified otherwise. The resistivity of the slab was computed over the temperature range of 50 to 250 K [188] at different doping levels under low field condition, i.e. the difference between source (μ_S) and drain (μ_D) electrochemical potential is only 40 meV unless specified otherwise. Due to the low-field condition [82], the charge correction arising from Poisson equation was neglected. This temperature range is appropriate for capturing thermally activated transport because the crossover to the variable-range-hopping regime is estimated to occur at around 40 K [176, 189].

Acoustic phonon scattering was modeled under the condition of momentum relaxation [81, 190]. The Fermi velocity (v_f), extracted from the slope of the surface bands in Fig. 2.2(a), is taken to be 4.1×10^7 cm/s, which is at the higher end of the experimental range of $2.8–5 \times 10^7$ cm/s as adduced from ARPES measurements [53-56]. In order to relate our E_f values to the experimental doping densities, obtained from the current contribution through the surface layer calculated via NEGF, we have extracted the surface free carrier density from the Drude model (see Table 6.1).

Table 6.1 Estimated surface carrier density at 100K for v_f = 4.1 × 10^7 cm/s and λ = 0.25 for different values of the Fermi energy (E_f).

E_f (eV)	Surface free-carrier density (/cm^2)
0	5.62×10^9
0.05	2.16×10^{10}
0.1	4.77×10^{10}
0.2	7.21×10^{10}

6.3. Deformation Potential for Acoustic Phonon Scattering

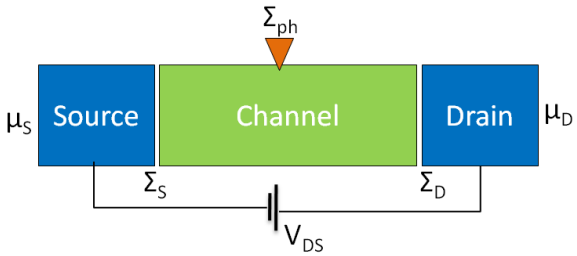

Figure 6.1 Schematic for modeling acoustic phonon scattering in quantum transport [82].

The impulse response of a quantum transport system (Fig. 6.1) comprising source, channel, and a drain in nonequilibrium condition is given by

$$[G] = \left[EI - H_0 - U_0 - \Sigma_S - \Sigma_D - \Sigma_{ph} \right]^{-1} \tag{6.1}$$

where, G is the Green's function, E is the energy at which response is evaluated, U_0 is potential distribution in the system, H_0 is the Hamiltonian that models the entire system, Σ_S and Σ_D are self-energies of source and drain contacts, respectively, and Σ_{ph} is the self-energy of acoustic phonons [175]. Specifically,

$$\left[\Sigma_{ph} \right] = D_{ac} \left[G \right] \tag{6.2}$$

where D_{ac} is the deformation potential for modeling acoustic phonons via momentum relaxation. However, for momentum relaxation [82, 191], only submatrices with the dimension of *basis*, where *basis* is the size of the square matrix used to describe each sampling point on the main-diagonal of [G], are required, and other elements of Σ_{ph} are taken to be zero.

As discussed in **Sec. 2.1.2**, size of the *basis* used to describe each sampling point in our case is four. The level broadening for source, drain, and phonon is, respectively, calculated as

$$\Gamma_S = i\left[\Sigma_S - \Sigma_S^\dagger\right];\ \Gamma_D = i\left[\Sigma_D - \Sigma_D^\dagger\right];\ \Gamma_{ph} = i\left[\Sigma_{ph} - \Sigma_{ph}^\dagger\right] \tag{6.3}$$

Furthermore,

$$A = i\left[G - G^\dagger\right]$$
$$imag(G) = -\frac{A}{2} = -\frac{2\,\pi\,a_x\,a_y\,DOS}{2} = -\frac{2\,\pi\,a_x\,a_y}{2}\,\frac{1}{2\,\pi}\,\frac{E_f}{\hbar^2\,v_f^2} \tag{6.4}$$

where A is the spectral function (per electron volt), DOS is the density of states (per electron volts per square meter (considering one unit-cell), a_x and a_y are the sampling distances in the direction of transport (x-axis) and the transverse direction (y-axis), respectively, v_f is the Fermi velocity, and E_f is the Fermi level.

Then, from Eq. (27) of Ref. [56],

$$imag(\Sigma_{ph}) = -\pi\,\lambda\,K_B\,T \tag{6.5}$$

where, λ is the strength of electron-phonon coupling, K_B is Boltzmann constant, and T is the temperature in Kelvin. The preceding equations yield,

$$D_{ac} = \frac{2\,\pi\,\lambda\,K_B\,T\,\hbar^2\,v_f^2}{E_f\,a_x\,a_y} \tag{6.6}$$

By substituting $\hbar$ = 6.582 × 10^{-16} eV-s, E_f = 0.28 eV [56], v_f = 5 × 10^5 m/s, K_B = 8.617 × 10^{-5} eV/K, T = 300 K, λ = 0.25 (0.08), a_x = a_y = 1 nm, and we obtain $D_{ac_300\,K}$ = 0.0157 eV^2 (0.005026 eV^2), and:

$$D_{ac} = D_{ac_300K}\left(\frac{T}{300}\right)\left(\frac{v_f}{5\times10^5}\right)^2\ eV^2 \tag{6.7}$$

Note, however, that instead of the exact value of D_{ac} [192], the empirical strength of D_{ac} is more important for this study because the exact strength of the electron-phonon coupling for electron transport is difficult to estimate.

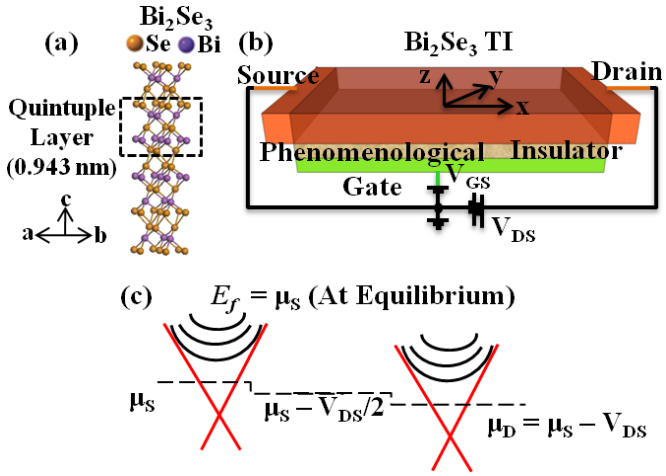

Figure 6.2 (a) Atomic structure of Bi_2Se_3. (b) Semi-infinite slab of Bi_2Se_3 with finite thickness along the z-axis and an infinite width along the y-axis. Electron transport is along the x-axis. Gate voltage shifts the Fermi-level (E_f) uniformly in the entire slab. E_f is defined to be zero at the Dirac point. (c) Illustration of potential distribution through the energy bands along the transport direction.

6.4. Ballistic Transport

This section examines ballistic transport through a Bi_2Se_3 slab. The purpose is to delineate appropriate physical conditions for the study of quantum transport, and to also build a systematic basis for an intuitive understanding of transport as we go from the simpler case of ballistic transport to the more complex behavior when acoustic phonons are included in Section 6.5 below.

6.4.1. Source to Drain Bias (V_{DS})

A large voltage might allow electrons to traverse through the bulk bands even if the Fermi-level is tuned to the Dirac-point because the current is primarily carried by electrons with energies lying between the source and drain electrochemical potentials, i.e. between μ_S and μ_D (see Fig. 6.2). In contrast, at very low voltages, the magnitude of current will be very small and the signal may be masked by the noise floor in a real setup. With this in mind, we simulated low-field transport with bias

voltage (V_{DS}) varying from –0.16 V to 0.16 V in a 13 QL thick Bi_2Se_3 slab at 100 K for Fermi-level at the Dirac-point (E_f = 0 eV) as a representative case in Fig. 6.3.

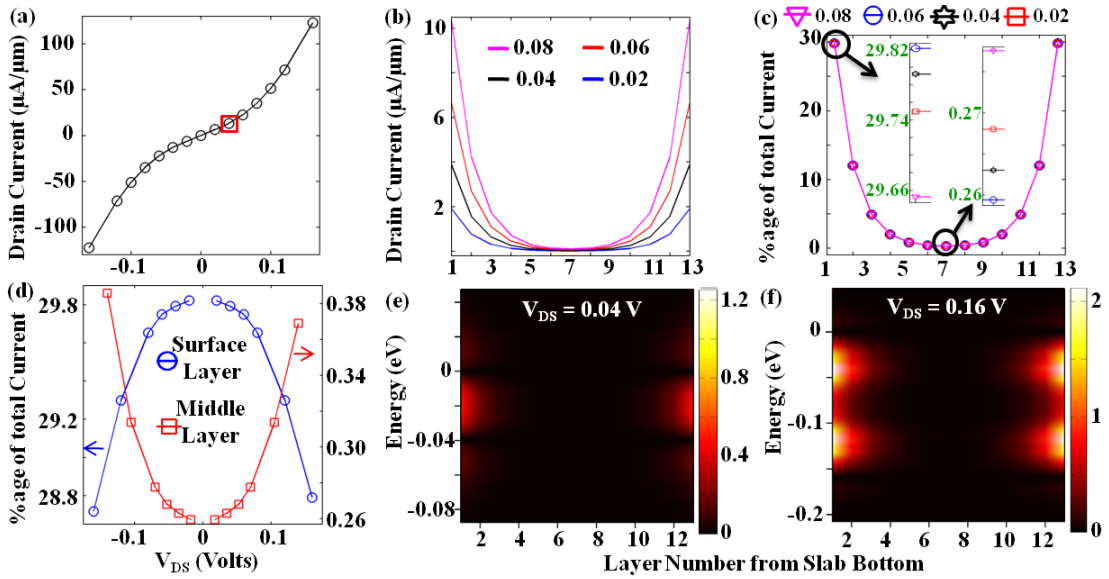

Figure 6.3 (a) Ballistic I-V characteristics of 13 QL thick Bi_2Se_3 slab at 100 K for Fermi-level (E_f) at Dirac point. Red square is at V_{DS} = 40 meV, where the simulations in panels (b)-(f) in this figure have been carried out. (b) Drain current through various layers for four different values (see legend) of V_{DS}. (c) Percentage contribution of various layers to the total drain current for four different values of V_{DS}. Small differences as a function of V_{DS} are not visible in the main plot, and are blown up for layers 1 and 7 in the insets. (d) Surface (bottom layer) and middle (7^{th} layer) layer contribution to the total drain current as a function of for V_{DS}. (e, f) Contribution to the total current from electrons of various energies in different layers (in μA/μm) for V_{DS} = 0.04 V (e) and 0.16 V (f).

The results for the total current through the slab are shown in Fig. 6.3(a), while Figs. 6.3(b) and 6.3(c) show how this total current is distributed among the various layers. In general, the absolute current through each layer in Fig. 6.3(b) is seen to increase with increasing bias voltage, reflecting an increasing number of electrons contributing to transport. Figure 6.3(d) shows that the role of bulk bands now starts to increase, which indicates that for high bias, subsurface transport will begin to dominate over surface contribution even when we operate at the Dirac point. This effect will be stronger for thicker slabs as we will see in Section 6.4.3 below. Figure 6.3(d) also illustrates that for the positive bias, the bulk contribution scales faster with the increase in the magnitude of V_{DS} compared to a negative bias. This is because most of the electron energies lie in the valence band, where mode density is

higher around the Dirac point (see band structure in Fig. 2.2(a)), compared to the mode density in the conduction band, where most of the Fermi-distribution lie for a negative bias.

Furthermore, to justify the choice of 40 mV as an appropriate bias for this study, the energy-resolved current from different layers is presented in Fig. 6.3(e) and contrasted with the corresponding results at a higher bias of 160 mV in Fig. 6.3(f). The two color bars are on different scales for better readability. The white (black) regions correspond to the maximum (minimum) current density. The current distribution in Fig. 6.3(e) illustrates that most electrons flow through the surface layers (1^{st} layer is the bottom surface, 13^{th} layer is the top surface) for energies approaching the average of the contact electro-chemical potentials, corresponding to the maximum in the difference of Fermi-distributions between the source and the drain ($f_{Source} - f_{Drain} = \Delta f_{SD}$).

In Fig. 6.3(e), the black streaks at 0 and –0.04 eV (–0.16 eV in Fig. 6.3(f)) reflect the zero density of states (DOS) due to Dirac point at the source and drain ends, respectively. Similarly, dark-red region in the center of the yellowish-white region for surface layers in Fig. 6.3(f) corresponds to low DOS in the channel (see the potential profile in Fig. 6.2(c)), resulting in two peaks in energy between μ_S and μ_D. This slight drop in transmission at energy exactly between μ_S and μ_D corresponds to the Dirac-point in the channel and is evident only at high bias or for a long channel device, because the smeared energies in the channel, due to energy level broadening, complemented by non-zero DOS for the contacts at the stated energy level together mask the effect. This point is discussed further in Section 6.5 below. Note that spread of the dark-red region (also compare the two color scales) on increasing bias in going from Fig. 6.3(e) to 6.3(f) shows that the drain current is infiltrated by electrons

flowing through bulk states. These considerations justify our choice of 0.04 V as a reasonable bias voltage, which generally limits quantum transport to the surface layers with only minor contribution through the bulk material.

6.4.2. Temperature

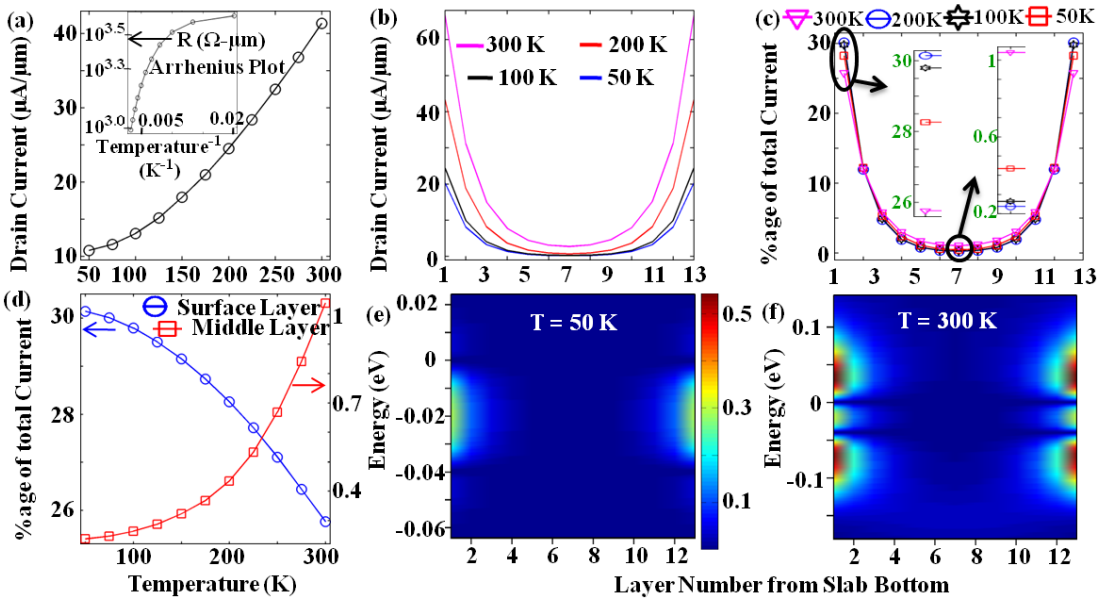

Figure 6.4 (a) Ballistic current as a function of temperature for the 13 QL thick Bi_2Se_3 slab for Fermi-level (E_f) at the Dirac point (V_{DS} = 0.04 V). The inset gives an Arrhenius plot of resistance. (b) Drain current through various layers at four different temperatures. (c) Percentage contribution to the total current from various layers at four different temperatures. Differences as a function of temperature are fairly small in the main plot, and are blown up for layers 1 and 7 in the insets. (d) Surface (Bottom layer) and middle (7th layer) layer contribution to the total drain current. (e, f) Contribution to the total current from electrons of various energies in different layers (in μA/μm) at T = 50K (e) and 300K (f).

For understanding transport in the thermal activation regime [176], it is important to delineate variations in resistance with temperature, E_f and slab thickness under ballistic conditions. Accordingly, we consider a 13 QL thick Bi_2Se_3 slab over the temperature range of 50 K to 300 K at a bias of 40 mV with E_f = 0 (Dirac-point). Figure 6.4(a) shows that the enhanced thermal activation of the carriers at higher temperatures results in a higher current through the slab. This trend is further seen in the Arrhenius plot in the inset to Fig. 6.4(a). Even though thermal activation increases the current through each layer in Fig. 6.4(b), the percentage contribution to the net current in Fig. 6.4(c) reveals a gradually increasing dominance of subsurface transport

(see Fig. 6.4(d)), which is not obvious from the absolute current calculations of Fig. 6.4(b).

The current distributions in Figs. 6.4(e) and 6.4(f) at 50 K and 300 K give insight into the mechanism of increase in subsurface transport at higher temperatures. The yellowish-green region, corresponding to the average of contact electro-chemical potentials, shows that most electrons flow through the surface layers. The red-region in Fig. 6.4(f) corresponds to the higher energy states, with larger DOS, where the Fermi-distribution is still substantial, yielding a larger effective current density. Spread of the light blue region along the energy axis for the top and bottom surface layers further exhibits the effect of thermal activation, which corresponds to a spread in the Fermi-distribution for the source and drain contacts. This spread, however, also allows electrons to flow through the bulk bands contributed by the subsurface layers. At 300 K (see Fig. 6.4(f)), even the bulk valence band of the middle layer contributes to conduction (light blue region in middle-bottom) due to increased hole carrier concentration. By contrast, at the lower temperature of 50 K, much of the conduction remains confined close to the surface.

6.4.3. Effects of Slab Thickness and Fermi-Level

Bi_2Se_3 slabs, 13 QL to 43 QL thick, were studied at 100 K at a 40 meV voltage bias (V_{DS}) with E_f varying from 0 eV to 0.2 eV, corresponding to the bottom surface carrier density of ~ 5.62×10^9 cm^{-2} to 7.21×10^{10} cm^{-2}. This density lies within the experimental range for low carrier doping measurements [55, 173, 177]. In Fig. 6.5, the experimentally observed thickness-dependent [178] as well as thickness-independent [179] behavior is reproduced by using different values of the Fermi-level. When the Fermi-level lies in the conduction band (black stars and magenta triangles in Fig. 6.5), i.e. at high carrier doping, spread of the Fermi-distribution, Δf_{SD}, occurs

mainly through the bulk bands, and therefore, conduction increases with increasing thickness of the slab. This is reflected in the steeper slopes in Fig. 6.5 for higher E_f values, which correspond to higher mode density. However, for the red-squares in Fig. 6.5, E_f is at the Dirac point, and therefore, for low bias (40 mV) and low temperature (100 K), the spread of Fermi-distribution is mainly concentrated in the surface bands. As a result, despite the increase in the thickness of the slab, conduction remains nearly constant.

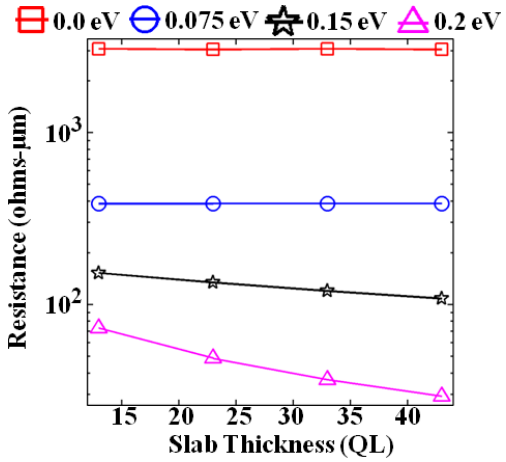

Figure 6.5 Variation in ballistic resistance as a function of slab thickness at 100K (V_{DS} = 0.04 V) for four different values of the Fermi-level (E_f), see legend.

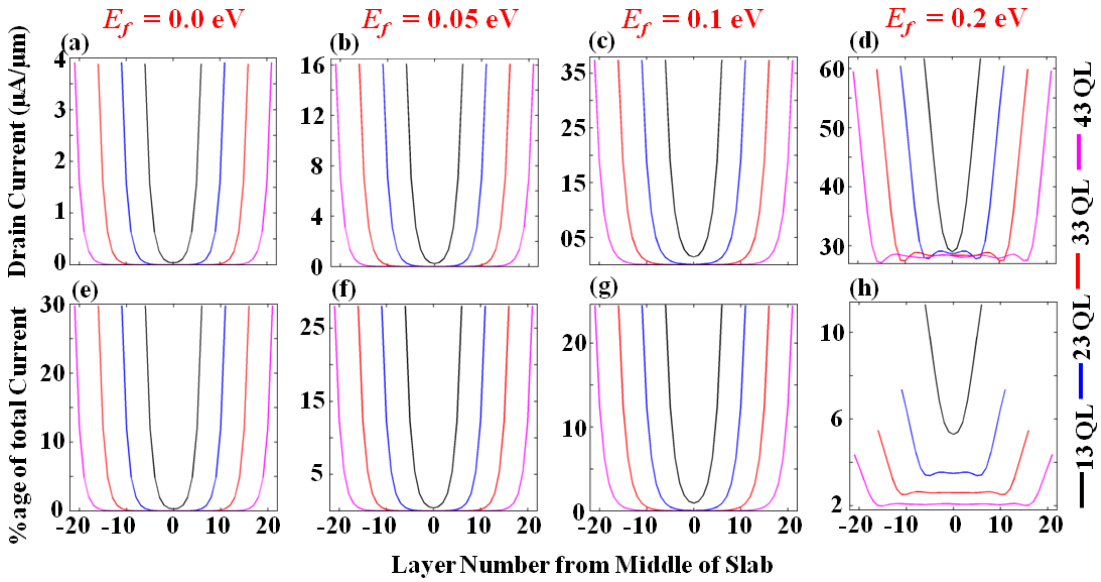

Figure 6.6 (a-d) Ballistic current through various layers for slabs of four different thicknesses, see legend on right hand side of the figure, at 100K (V_{DS} = 0.04 V) for different values of the Fermi-levels (E_f) shown on the top of the figure. (e-h) Corresponding percentage contribution to the total drain current.

Further insight is provided by Fig. 6.6, which shows how the total current is distributed among the various layers as a function of slab thickness for different values of the Fermi level. When the Fermi-level is set at the Dirac-point in Fig. 6.6(a), transport is suppressed to virtually zero after a few layers, being confined mainly to the four subsurface layers adjacent to the top and bottom surfaces. This shows that, for $E_f \sim 0$ eV, the surface states dominate transport, and that increasing the thickness of the slab now has little effect on the contribution of the surface layers (see Fig. 6.6(e)).

Comparing the magnitude of current in going from Fig. 6.6(a) to 6.6(d), however, we see that the current through various layer approximately scales with E_f or the carrier density (note changes in vertical scale in Fig. 6.6). When the bulk current is sizeable, increasing the slab thickness reduces the effective contribution of the surface (compare Figs. 6.6(f)-(h)). Moreover, for higher values of the E_f, even though surface layers have a large contribution, they do not dominate the total current. These results indicate that dominance of the surface layers in conduction can be achieved by fine-tuning the Fermi level to lie close to the Dirac point, or by taking a sample, which is thin enough to reduce the bulk contribution. Figure 6.6 should serve as a rough guide for estimating the relative contribution of the surface layer in transport measurements for various carrier densities at the Fermi-level.

6.5. Acoustic Phonon Scattering

A few experiments have observed an insulating trend in temperature dependent resistance measurements from Bi_2Se_3 samples, similar to the ballistic behavior discussed in the preceding section. However, since the sample length is usually longer than the electronic mean free path (~20 nm [193, 194]), the aforementioned trend cannot be associated with ballistic transport. The metallic trend

and crossover [54, 173-175] from metallic to insulating behavior has also been observed in the thermal activation regime, which we now turn to discuss.

Acoustic phonons interact with electrons to exchange momentum resulting in the relaxation of electrons, with the resulting scattering strength scaling directly with temperature. However, at higher temperatures more carriers are excited into the conduction bands leading to an increase in current. Effects of thermal activation and scattering thus compete to determine the overall temperature dependence of resistance. Scattering of electrons, in effect, broadens the density of states, and may equivalently be viewed as a smearing of the energy levels [195, 196]. If the Fermi-level is at the band-edge, an increase in temperature spreads out the Fermi-distribution, leading to a decrease in the carrier density and the magnitude of maxima in Δf_{SD}. However, if the Fermi-level is offset from the band-edge, the spread in Δf_{SD} increases the carrier density (thermal-activation), and the effect of thermal activation gets enhanced. Note that the strength of this effect depends on the relative energy values of the band edge and the Fermi-level, the temperature-dependent spread in the Fermi-distribution, and the strength of acoustic scattering, effects which we now turn to discuss.

6.5.1. Effect of Channel Length

Figures 6.7(a)-(d) illustrate the effect of channel length on resistance under low-field conditions for different Fermi-levels at a constant temperature. When the Fermi-level (E_f = 0.2 eV; Fig. 6.7(a)) lies in the conduction band, the dominance of in-plane acoustic phonon scattering is demonstrated via constant resistance for ballistic transport and the increase in resistance with channel length seen in the presence of phonons. Impact of the strength of electron-phonon coupling can be seen from the larger slope for λ = 0.25 (strong coupling) compared to the weak coupling

case of λ = 0.08. However, when the Fermi-level lies in the surface bands close to the bulk band edge (E_f = 0.1 eV; Fig. 6.7(b)), the phonon assisted spread of bulk states enhances the effect of thermal activation, which counters the effect of in-plane phonon scattering. This is evident from the relatively smaller variation in the slopes of resistance versus channel length plots for λ=0.08 and 0.25. Next, we consider the case when the Fermi-level lies even closer to the Dirac point (E_f = 0.05 eV; Fig. 6.7(c)). Here, the in-plane acoustic scattering is further weakened, and therefore, slopes of resistance vs. channel length plots are almost the same for two significantly different strengths of electron-phonon coupling. On further reducing doping, to tune the Fermi-level to the Dirac-point, little difference is seen in resistance for different values of λ, but interestingly, resistance increases with channel length for ballistic transport.

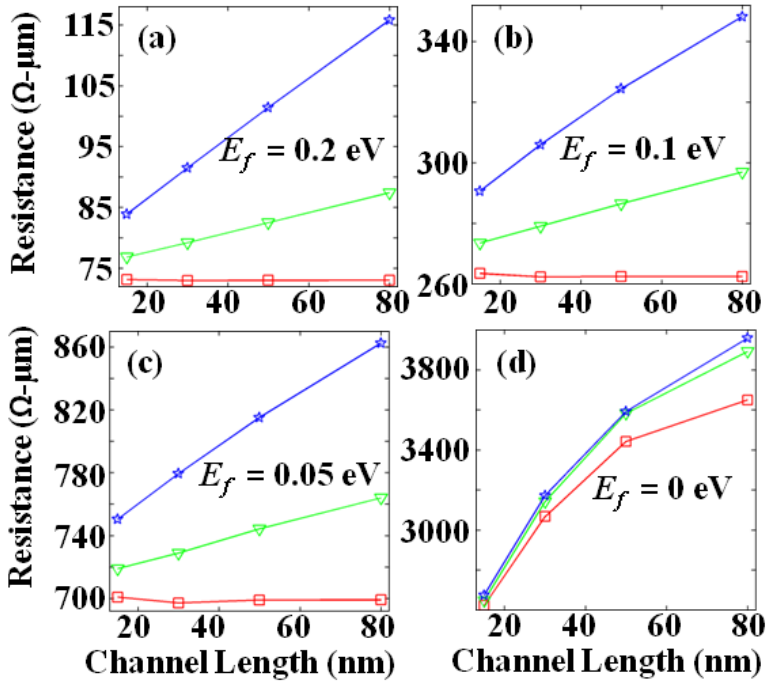

Figure 6.7 (a-d) Resistance vs. Channel Length (L_x) for ballistic (red squares) and acoustic transport for weak (λ=0.08; green triangles) and strong (λ=0.25; blue star) electron-phonon coupling, for different Fermi-levels at 100 K for 13 QL thick Bi_2Se_3 slab biased at 40mV.

Figures 6.8(a) and 6.8(b) further examine these results by comparing the details of transmission (dashed color lines, top horizontal scale) and bottom-surface DOS (solid color lines, bottom horizontal scale) in the middle of the channel for two

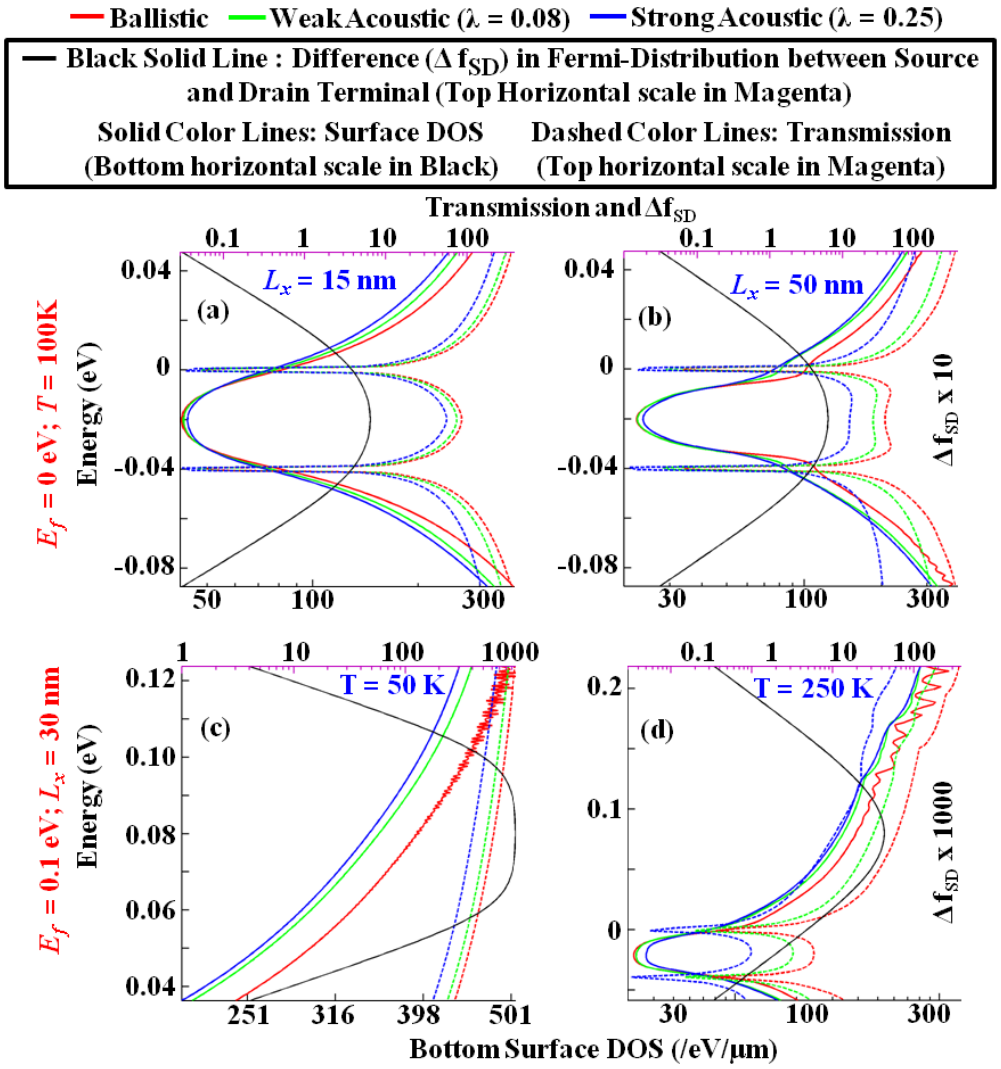

Figure 6.8 Competition between the effects of phonon induced level broadening, thermal activation and in-plane scattering is shown through plots of energy (y-axis) vs transmission, *T(E),* through the slab, density of states, *DOS(E,)* of the bottom surface in the middle of the channel, and the difference in Fermi-distribution, $\Delta f_{SD}(E)$, between the source and drain for various values of the parameters. Values of *T(E)* and $\Delta f_{SD}(E)$ are shown on the top horizontal scale (logarithmic) in magenta, while those of the DOS are given on the bottom horizontal scale (logarithmic). *Top Row*: E_f = 0 at 100 K for channel lengths (L_x) of 15 nm (a), and 50 nm (b). *Bottom Row*: E_f = 0.1 eV, L_x = 30 nm at temperatures of 50 K (c) and 250K (d). For better illustration, the values of $\Delta f_{SD}(E)$ are scaled in different panels by the factors given on the right hand side of each row. *T(E)* and *DOS(E)* are scaled up by 2π in all panels. Note that a finer transverse mode grid in the computations will smooth the high energy serrations seen in some of the curves. Red, green and blue colors represent ballistic, weak-acoustic scattering and strong-acoustic scattering cases respectively.

different channel lengths (15nm and 50nm) for E_f = 0 at 100 K to ensure same Fermi-distribution for both cases. The sharp dips in dashed lines show nearly zero transmission at 0 and –0.04eV energies, indicating the Dirac-points at the source and drain ends. The DOS at energies further from the Dirac-point (closer to bulk states) is larger for the ballistic case (red solid lines), and decreases with increasing scattering

strength. On the other hand, the spread of DOS results in larger values of DOS for stronger scattering (compare green and blue solid lines) in the energy region where Δf_{SD} maximizes (see DOS in energy range between 0 and –0.04 eV), and hence results in high transmission, while phonons reduce transmission at all energies.

Next, for the ballistic transport for the longer channel length in Fig. 6.8(b), a local minimum at –0.02 eV for the transmission (dashed red line) is observed, while there is no such inflection in Fig. 6.8(a). The reason can be attributed to the Dirac-bands in the source (drain) terminal that have Dirac point at 0 eV (–0.04 eV), and the half V_{DS} drop is assumed in the channel (see Fig. 6.2(c)) which results in a Dirac point pinned at –0.02 eV in the channel and contributes to minimum surface DOS. For small channel lengths, the DOS from contacts dominate in the transmission, but the weight age of contribution from the channel increases with its length. Therefore, it can be observed that in addition to two dips at the Dirac points of the contacts, transmission at E = –0.02 tends to form a local minimum which gets stronger as the channel length increases[a]. It explains the increasing trend in ballistic resistance seen in Fig. 6.7(d)., Nevertheless, the phonon induced level broadening further smears the

[a] The coupling of the channel with the contacts and hence smearing of the energy levels, due to finite wavefunction penetration into the channel from the contacts, result in the continuous shift of this minimum from the source to the drain terminal from 0 to –0.04 eV. The transmission is computed as Trace(Γ_{Source} G Γ_{Drain} $G^{\surd}$), where Γ is contact level broadening and G is Green's functions, and DOS as $(i/2\pi)$ $(G–G^{\surd})$. The transmission therefore illustrates a cumulative effect of contact level broadening and DOS at terminals and the channel. At 0 eV (–0.04 eV), since there are no states for injecting (receiving) the electron into (from) the channel, the transmission goes to zero. The DOS corresponding to source (drain) end Dirac-bands increases below (above) 0 eV (–0.04 eV) and hence the effect of DOS because of the contacts is maximum in the middle. The wavefunction from the contacts decays after certain penetration depth into the channel. Therefore, for the long enough channel length, beyond the penetration depth, the minimum for the DOS is held at –0.02 eV level. Transmission which integrates, via Trace operation, over each point in the contacts and channel, therefore sees increasing weight of DOS in the channel for longer channel lengths. This effectuates a local minimum in transmission plot whose impact scales directly with the channel length.

energy level (compare red, green and blue dashed lines in Fig. 6.8(b)) and overrides the effect of minimum in the channel.

These results give insight into how the Dirac cone states in a TI could be probed via low temperature transport experiments. For this purpose, one would need to measure the resistance of a high quality sample for a range of channel lengths (say from 10-100 nm), in which the Fermi-level is tuned to shift the (expected) Dirac cone to lie between the electro-chemical potentials of the contacts. If one finds an increasing trend with channel length, similar to the case of the red curve in Fig. 6.7(d), that would then suggest the presence of a Dirac cone.

6.5.2. Effect of Temperature

Figure 6.9 illustrates that when effects of acoustic phonon scattering are included, the temperature dependence of resistivity exhibits a variety of behaviors depending on the specifics of the parameters used. The resistivity is seen to be insulating in some cases, metallic in others, displays a local maximum around 125 K in Fig. 6.9(c), and a saturation effect in Fig. 6.9(b), much like the behaviors reported experimentally in various transport measurements on Bi_2Se_3 slabs [54, 173-175]. In Fig. 6.9(a), ballistic transport results (red squares) are mainly due to thermal activation of electrons regulated by the spread in the Fermi-Dirac distribution, whereas acoustic transport for weak electron-phonon coupling (green triangles) reflects the dominance of phonon scattering, which becomes stronger for larger values of λ (blue stars).

Figure 6.9(c, d) and Fig. 6.10 consider interplay of various factors in the overall resistance of the slab by considering the transmission, DOS and Δf_{SD} for various values of the parameters in the simulations. Figure 6.8(c, d) show that as phonon scattering scales up with temperature, it results in a larger spread of DOS

(solid color lines, bottom horizontal scale), and a stronger reduction of transmission (top horizontal scale, note differences in scale in panels Fig. 6.8(c) and 6.8(d)), which generally increases the resistance in Figs. 6.9(a-c).

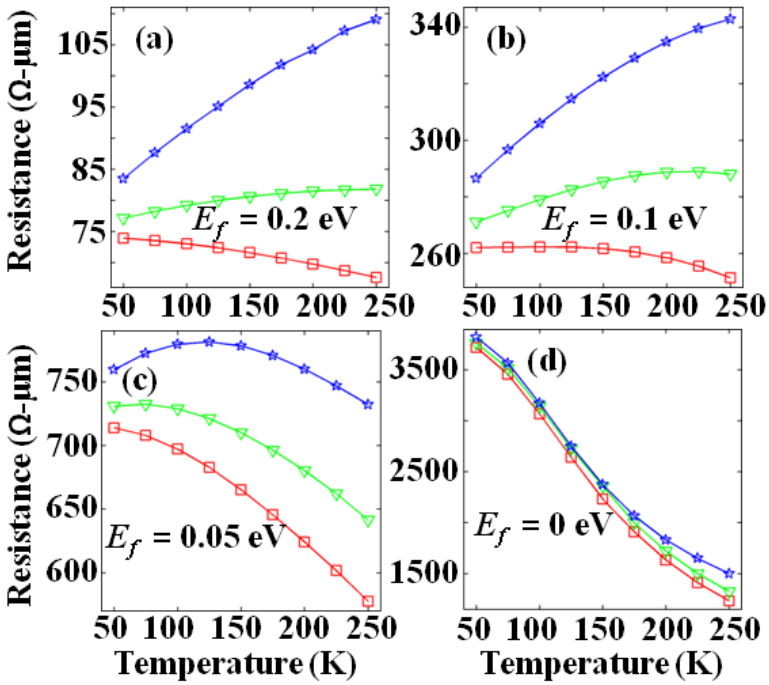

Figure 6.9 Resistance vs. temperature for ballistic (red squares) and acoustic transport for weak (λ=0.08; green triangles) and strong (λ=0.25; blue star) electron-phonon coupling for four different values of the Fermi-level at 30nm channel length for 13 QL thick Bi_2Se_3 slab biased at 40 mV.

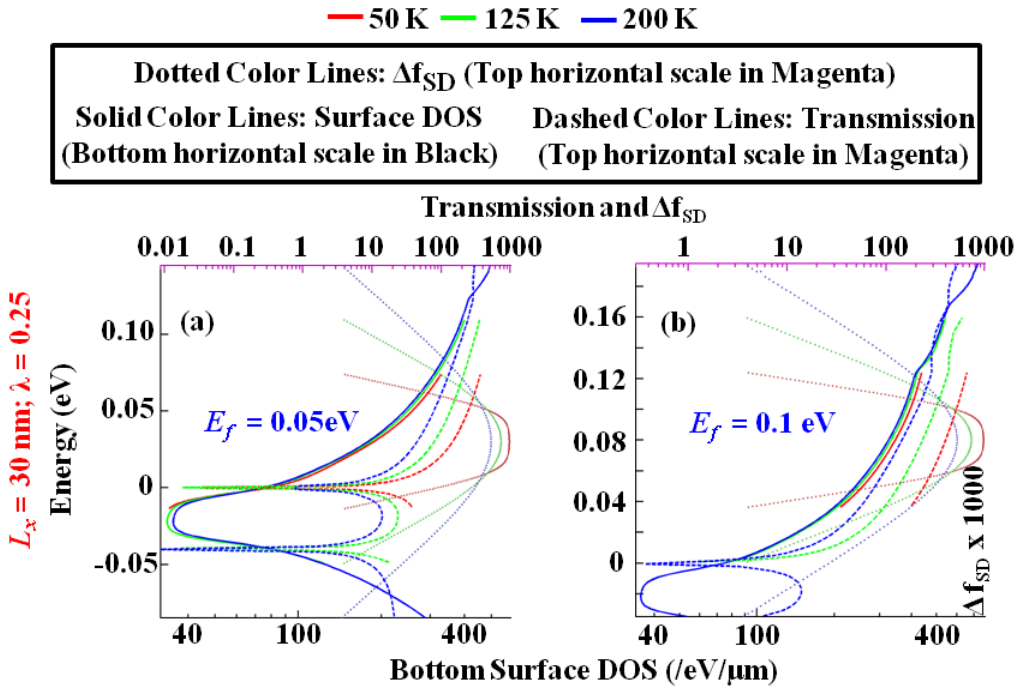

Figure 6.10 Same as Fig. 6.8 but for L_x = 30 nm, λ = 0.25 for E_f values of 0.05 eV (a) and 0.1 eV (b). Red, green and blue colors represent temperature of 50 K, 125 K and 200 K respectively.

Nevertheless, as also shown in Fig. 6.9, for the strong electron-phonon coupling (blue stars), there is a transition from absolutely metallic trend for E_f = 0.1 eV (see Fig. 6.9(b)) to one with a local maxima for lower E_f at 0.05 eV (see Fig. 6.9(c)), and merits even closer examination of all three effects. Results in Fig. 6.10 show that in the presence of strong acoustic phonons (λ = 0.25), as phonon scattering increases with temperature, it induces a decrease in transmission (dashed lines of various colors), and spreads the DOS (solid lines of various colors) and Fermi-distribution over a wider energy range (dotted lines of various colors).

The difference in trends between Fig. 6.10(a) and 6.10(b) originates from the contention among the three effects at low energies where difference in Fermi-distribution (Δf_{SD}) is low. In Fig. 6.8(d), a lower transmission throughout the energy grid for higher temperature results in the metallic trend while the spread of Fermi-distribution with increase in temperature in Fig. 6.10(a), eventually leads to the inclusion of significantly more states for the carriers to traverse the channel and outweighs the effect of transmission. We would also like to note that even though the same Fermi-distribution spread occurs in Fig. 6.10(b), the contact electrochemical potentials are not at appropriate values (close enough to Dirac-point) to induce the local maxima in resistance trend line. This evinces the importance of relative positioning of the Fermi-level on the energy grid to observe the effect of phonon induced level broadening.

6.6. Validation of Model against Experimental Data

Figure 6.11(a) illustrates the experimentally measured resistance of a Bi_2Se_3 slab as a function of temperature for different levels of Sb doping [173], which allows one to balance the Se vacancy induced *n*-type carriers [175] in Bi_2Se_3 and thus tune E_f around the Dirac point. For our device (see Fig. 6.11(b)), we simulate quantum

transport for two illustrative cases: (i) E_f at 0.05 eV from the Dirac point as shown schematically in Fig. 6.11(c); and (ii) E_f is moved into the conduction band at 0.2 eV as shown in Fig. 6.11(d). Our transport calculations capture salient trends in the experimental data as can be seen by comparing Figs. 6.11(a) and 6.11(e). The experimental observation of an insulating trend in the resistance can thus be understood as follows: When E_f is close to the Dirac point, for instance at 0.05 eV (red curve in Fig. 6.11(e)), corresponding to a surface carrier density of ~2.16 × 10^{10}cm^{-2}, thermal activation into higher energy levels overrides the effect of phonon-induced scattering.

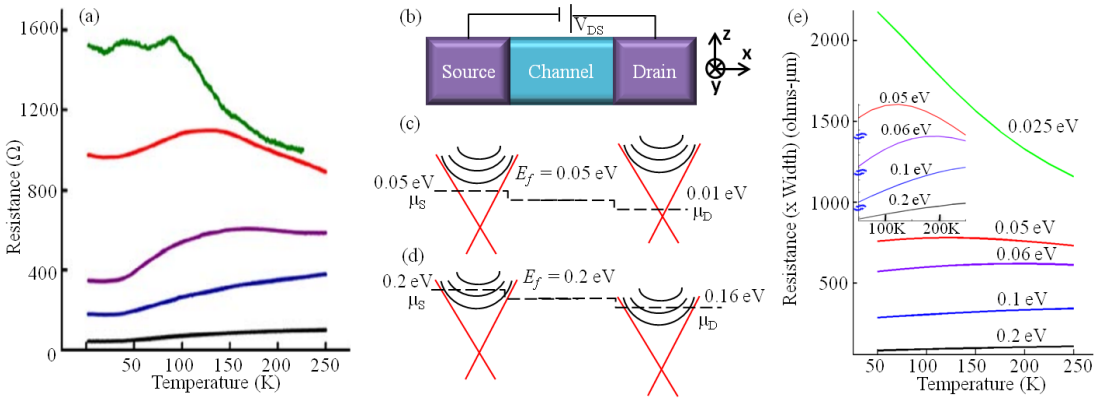

Figure 6.11 (a) Experimentally observed resistance of a Bi_2Se_3 nanoribbon taken from Fig. 2(a) of Ref. [173] (Readapted with permission). (b) Schematic of the simulated semi-infinite slab of Bi_2Se_3. (c) Schematic of the potential profile (dashed line) through the energy bands for E_f = 0.05 eV. (d) Potential profile for E_f = 0.2 eV (positioned within bulk conduction bands). (e) Computed (resistance×width) vs temperature for different positions of E_f (shown over various curves) for acoustic transport (λ = 0.25). The inset shows an enlargement of the bottom four curves from the main figure with same color scheme but broken (by blue hyphens) with a shifted *y* axis (unchanged scale) to emphasize the features (*x* axis gives temperature from 50 to 250 K) of trend lines. Note the local maximum in the red and purple curves at around 125 and 200 K, respectively.

Further insight is obtained by decomposing the total current into contributions from various sets of QLs and noting how the current is distributed into different electronic energy channels. Such spectral level information at 50 and 250 K is given in Fig. 6.12 (Fig. 6.13) for the case where E_f lies 0.05 eV (0.2 eV) above the Dirac point. In all cases considered, maximum current density is carried by the surface layers (1st and 13th layers), see Fig. 6.14 for comparing energy-integrated results.

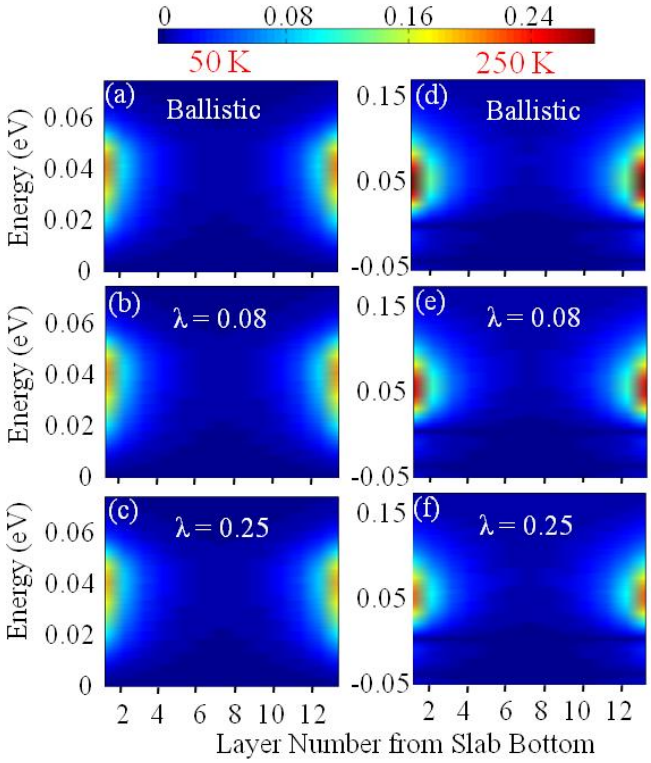

Figure 6.12 Contributions from different energy channels and different sets of QLs to the total current for the 13-QL-thick slab for E_f = 0.05 eV. (a)–(c) refer to results at 50 K, while (d)-(f) refer to those at 250 K. Ballistic transport is considered in (a) and (d), weak electron-phonon coupling with λ = 0.08 in (b) and (e), and strong coupling case with λ = 0.25 in (c) and (f).

Furthermore, the energies of electrons that carry much of the current lie near the midpoint (μ_{mid}) between μ_S and μ_D as seen, for example, from Figs. 6.12(a)-(c), which corresponds to the maximum difference between the Fermi distribution function at drain and source terminals ($f_{Source} - f_{Drain} = \Delta f_{SD}$). At low temperature (50 K), under ballistic conditions (Fig. 6.12(a)) and weak electron-phonon coupling (λ = 0.08; Fig. 6.12(b)), there is a negligible contribution from the middle layers of the slab and from electrons with energies away from contact electrochemical potentials.

However, for strong electron-phonon coupling (λ = 0.25), there is increased scattering of carriers to the middle layers for energies corresponding to the peak of Δf_{SD}, depicted by the light blue region in the center of Fig. 6.12(c) (also see Fig. 6.14). At 250 K, for ballistic transport (Fig. 6.12(d)), the effect of higher temperature is primarily reflected through the spread of the Fermi function. Now acoustic phonons induce significant scattering in surface layers even in the presence of weak phonon

coupling (Fig. 6.12(e)). Strong phonon coupling naturally enhances the effect, which can be observed from the larger spread of the orange-yellow region over a broader range of electron energies (Fig. 6.12(f)). Although acoustic scattering decreases the net current flowing through the surface layers, this effect is overridden by thermal activation to higher energy states. Therefore, the sample manifests an overall insulating trend, i.e., decreasing resistance with increasing temperature, even in the presence of strong electron-phonon coupling.

We next consider the E_f = 0.2 eV case with the corresponding surface carrier density of ~7.21 × 10^{10} cm^{-2}. As shown in Fig. 6.13(a), even under ballistic condition, the middle layers contribute significantly to the total current, resulting in reduction of the net resistance of the slab by an order of magnitude compared to the E_f = 0.05 eV case. Furthermore, at 250 K (see Fig. 6.13(d)), thermal activation increases the current through all layers, a trend that is especially visible for the middle layers at electron energies close to the peak of Δf_{SD}, as shown by the change in color from light blue to yellowish-green as T increases from 50 to 250 K. Thus, for ballistic transport, we find an insulating trend of resistance.

In sharp contrast, the reverse occurs in the presence of phonon scattering. As shown in Fig. 6.13 (also see Fig. 6.14), although the absolute current is reduced in all layers due to phonon scattering, the reduction is proportionately greater for the surface layers, and thus the relative contribution from the bulk current increases. This trend is further enhanced as the strength of phonon coupling increases. However, when the temperature increases to 250 K, even weak electron-phonon coupling can strongly counter the effects of thermal activation resulting in increased resistance (see Fig. 6.13(e)), a trend that has been observed in most experiments. In Fig. 6.13(f), the energy spectrum reveals that the current flowing through middle layers is comparable

to subsurface layers (yellowish-green region). Therefore, stronger phonon scattering results in a net reduction of current and increase in resistance. This also results in a steeper increase in resistance with temperature for stronger phonon coupling.

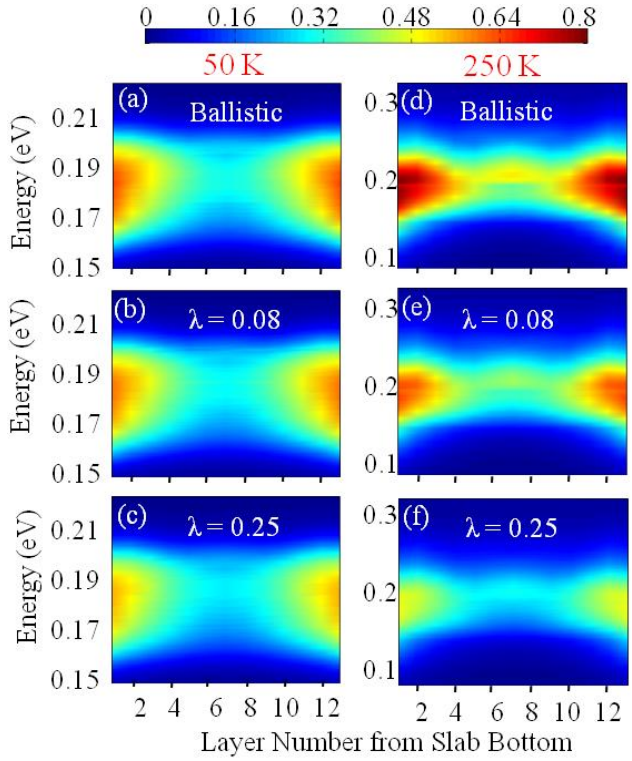

Figure 6.13 Contributions from different energy channels and different sets of QLs to the total current for the 13-QL-thick slab for E_f = 0.2 eV. (a)–(c) refer to results at 50 K, while (d)-(f) refer to those at 250 K. Ballistic transport is considered in (a) and (d), weak electron-phonon coupling with λ = 0.08 in (b) and (e), and strong coupling case with λ = 0.25 in (c) and (f).

Notably, electronic energy levels are broadened due to scattering effects, and the concomitant reduction in the density of states (DOS) peaks at the bulk band edges (spread of DOS) [81] play an important role in transport [197]. This effect, coupled with the thermal activation of carriers, underlies the local maxima observed in resistance vs temperature plots when the Fermi level lies in between cases exhibiting purely insulating and metallic trends. In principle, increasing temperature results in a larger spread of the Fermi distribution and a reduction in the magnitude of the peak in Δf_{SD}. Therefore, when μ_{mid} lies at the bulk band edge, there will be a decrease in the carrier density, which is mainly contributed by electrons close to the peak of Δf_{SD}.

On the other hand, when it lies at the energy offset from the bulk band edge, the carrier concentration is dominated by electrons in the tail of Δf_{SD}, and increases via thermal activation. As a result, the spread of the Fermi distribution enhances the effect of thermal activation, and at around 125 K (200 K) thermal activation and broadening begin to override the effect of in-plane phonon scattering and resistance starts to decrease with temperature, as shown by the red (purple) line in the inset to Fig. 6.11(e).

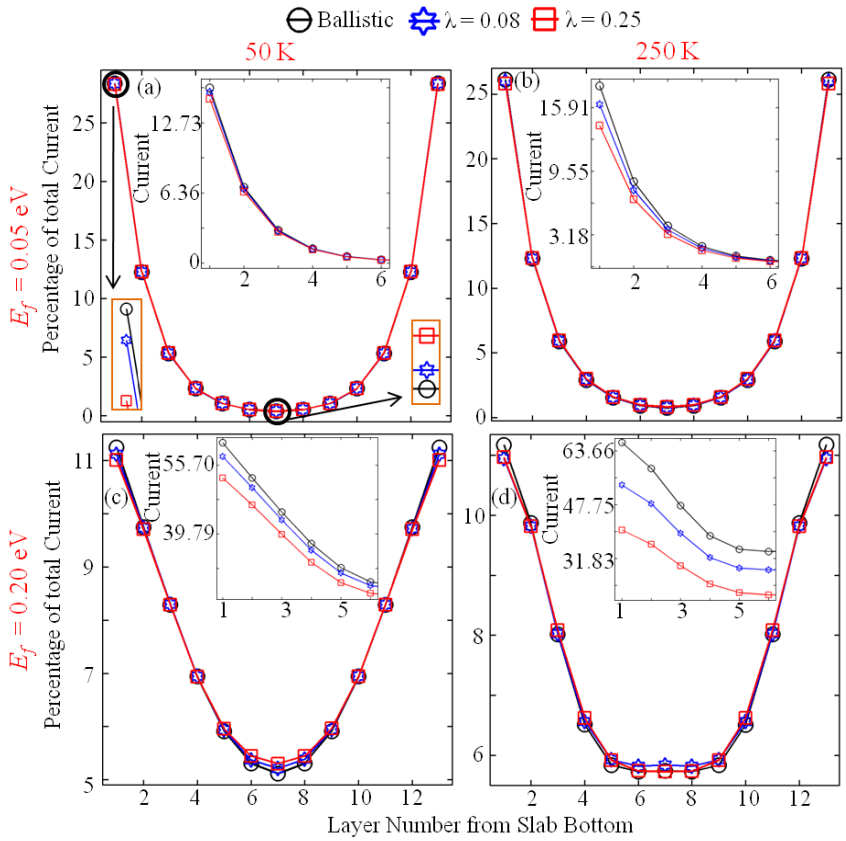

Figure 6.14 Energy integrated partial contribution (given as a percentage of the total current) of various layers to the total drain current for ballistic transport (blue circles), weak acoustic scattering (red squares), and strong acoustic scattering (black stars). Insets give absolute drain current (in μA/μm) flowing through various layers for the bottom half of the slab. Cases (a) and (b) refer to energy integrated result of Fig. 6.12, and (c) and (d) of Fig. 6.13. The energy-integrated results reemphasize that the maximum current is carried by the surface layers (1st and 13th layers). The percentage contribution illustrates a large decrease in surface current for strong acoustic scattering. Comparison of the insets in (a) and (c) or (b) and (d), shows that for E_f = 0.2 eV, even under ballistic conditions, the middle layers contribute significantly to the total current, resulting in reduction of the net resistance of the slab compared to the E_f = 0.05 eV case. By comparing the corresponding curves from the insets of (c) and (d), we can also observe a reduction in the surface current due to increased scattering at 250 K.

This trend in resistivity as a function of temperature reflects competing effects of thermal activation, phonon scattering from the surface to middle layers, strong in-plane scattering in bulk bands, and the strength of electron-phonon coupling. Referring to Fig. 6.11(e), as the Fermi level moves from the Dirac point (red line at ~0.05 eV) into the conduction band (black line at ~0.2 eV), various competing factors play out as follows: (i) Resistance decreases due to thermal excitation into the bulk bands; (ii) resistance increases due to acoustic scattering, which is stronger in bulk bands, and starts to dominate over thermal activation at higher temperatures, resulting in the change from an insulating to a metallic trend; and (iii) energy level broadening due to acoustic scattering, which may accentuate the effect of thermal activation for certain temperatures and E_f.

6.7. Electronically Detecting Topological Surface

In Fig. 6.15, we characterize the temperature dependency of a relative decrease in the surface current on transitioning from the ballistic to the acoustic regime, considering cases of both weak and strong electron-phonon coupling. We see that when T increases from 50 to 250 K with E_f at the Dirac point, the percentage decrease for weak coupling is from 1 to 7%, whereas for strong coupling, the decrease is from 3 to 18.5%. However, for E_f = 0.2 eV, the percentage decrease is from 5 to 19% for weak, and 13 to 39% for the strong coupling case.

Therefore, with reference to Fig. 6.15 [198], the relative decrease in surface current at 50 K and the slope of the trend line suggest a new strategy for obtaining an experimental handle on the strength of electron-phonon coupling in Bi_2Se_3. More specifically, one would measure electron transport in two different samples, where channel length of one sample is much shorter than the mean-free path and therefore lies in the ballistic regime, while the other sample is longer than the mean-free path

and thus lies in the acoustic regime. By keeping the Fermi level close to the Dirac point (surface carrier density of ~10^{10}cm^{-2}), and comparing the percentage decrease in the surface current across two samples as a function of temperature, the strength (weak versus strong) of electron-phonon coupling can be roughly assessed. Even though this will reveal only a rough estimate of λ, it will still be of practical significance as currently the disputed values of λ vary by as much as five orders of magnitude.

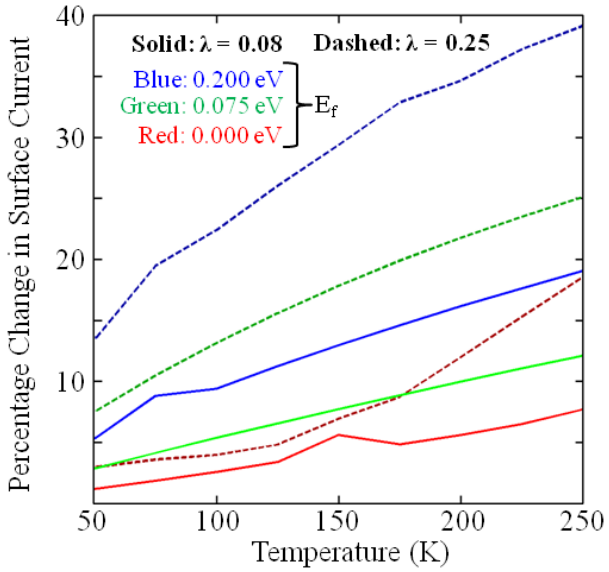

Figure 6.15 Percentage decrease in the current in the surface layer as a function of temperature. Acoustic regime (long sample length) for weak (λ = 0.08, solid lines) and strong (λ = 0.25, dashed lines) electron-phonon coupling are compared to the ballistic regime (sample length smaller than mean-free path ~20nm).

6.8. Conclusion

Our analysis indicates that an insulating trend of TI resistance measurement vs. temperature is not a sufficient condition for adducing that the Fermi-level in a TI is at or close to the Dirac-point, or that the surface transport is dominant [199, 200]. Such an insulating trend only indicates that the overall effect of electron-phonon coupling is weaker than that of thermal activation under the operating conditions. A more detailed understanding of the material specific electron-phonon coupling strength and other factors discussed above is needed for a reliable interpretation of the

experimentally observed temperature dependence of the resistivity in the TIs. Another caveat that is material specific is inclusion of optical phonon scattering. In Bi_2Se_3 3D-TI, the optical phonons had been shown to be significant only above 250 K [55, 201]. Our objectives however were (a) explain the contrasting resistance vs temperature trends in thermal activation regime (> 50 K) especially local maxima observed between 100-150 K (b) examine the contested strength, from 0.08 to 0.43, of acoustic phonon-electron coupling parameter. Hence, this work did not included optical phonons, and limited the phonon based study to 250 K only. This 50 K – 250 K temperature regime was sufficient to answer the questions raised in this work. However, this could be specific to Bi_2Se_3 material and may not be true for all 3D-TIs in general.

Finally, since most experiments have seen metallic behaviour, for understanding purpose and gaining top level insight into peculiar resistance behaviour, it may be useful to compare 3D-TI with normal metals which universally show increase in resistance with temperature. In TI literature, 'insulator-like' trend is referred to increasing resistance with decreasing temperature, whereas decreasing resistance trendline is termed metallic trend. This is because in metals, due to phonon scattering, the resistance increases with temperature. In normal metals, Fermi-level (E_f) is already well above the conduction band edge and therefore the effect of small increase in carrier density due to thermal activation is easily masked by phonon scattering whose strength scales directly with temperature. However, for insulators, provided E_f, although below conduction band edge, if it is still in purview of thermal activation energy, more electrons can populate conduction band as the temperature is increased which results in decreased resistance.

To put it simply, the Dirac-bands and phonon scattering in 3D-TI provide an interesting competition between these effects. For Dirac-bands, Density of states increases linearly with energy (referenced w.r.t Dirac point), and therefore as electrons populate higher energies current should increase, however weighted by the Fermi-Distribution function. Therefore, in absence of phonon scattering (ballistic transport) resistance always decreases with increasing temperature. In fact when operating close to the Dirac point for 3D-TI, we show that still phonon scattering cannot override the thermal activation into higher energies and hence insulating trend is observed. However, as E_f gets closer to the bulk bands, resulting in electronic condition similar to metals, the phonon scattering transcends the overall characteristics. Moreover, this transition should result in local maxima in resistance vs temperature trendline as observed in some of the experiments.

In summary, we have developed a NEGF-based approach that incorporates a realistic treatment of both ballistic and acoustic transport through a slab of a TI. We discuss electronic transport in a Bi_2Se_3 slab as an exemplar TI system in the thermal activation regime (> 50 K). Simulations are carried out for a range of values of electron-phonon coupling strength, slab thickness, channel length, Fermi-level (carrier doping), voltage bias across the slab and temperature. In this way, we show how the interplay between the competing effects of thermal activation, phonon induced level broadenings and in-plane scatterings can yield quite complex temperature dependencies of the overall resistivity of the slab. When the Bi_2Se_3 slab is biased at the Dirac point, the temperature dependence of the resistance is found to display an insulating behavior even in the case of strong electron-phonon coupling strength.

However, when the Fermi-level lies within or close to the bulk conduction band (heavy electron doping), phonon scattering dominates and results in a metallic

behavior, although the insulating trend is retained in the limit of ballistic transport. Depending on operating conditions, resistance of the slab can thus exhibit a metallic or an insulating character or a local maximum in resistance as a function of temperature, much like the types of contradictory trends seen in various experimental measurements. An analysis of our results allows us to adduce an experimental strategy for determining the approximate size of the electron-phonon coupling λ through temperature-dependent transport measurements on appropriate samples in which transport is dominated by ballistic or acoustic scattering regimes. Our quantum transport model provides a viable basis for optimizing conduction from surface layers. Our study provides a systematic basis for understanding aspects of the complex transport properties of TIs and their dependencies on various operating parameters needed for practical exploitation of the topological surface states in potential applications of the TIs.

Chapter 7

Contact Effects in thin 3D-Topological Insulators: How does the current flow?

The effect of different contact configurations (semi-infinite extended-channel, normal metal and ferromagnetic metal) on quantum transport through thin Bi_2Se_3 three-dimensional (3D) topological insulator (TI) slab (channel) has been investigated through Non-Equilibrium Green Function. The issue of contact dependent current flow and distribution across quintuple layers of 3D-TI has been addressed in this chapter and applied to expound the explanation for a recent experiment on electrical detection of spin-momentum locking on topological surface for long channel device.

A theoretical model is propounded to develop a microscopic understanding of transport in 3D-TI in which contact type and magnetization concur with helical surface states of the TI channel to manifest seemingly counter-intuitive current distribution across layers. The quantum transport calculations for short channel devices with magnetic source and drain contacts postulate negative surface current for anti-phase magnetization whose axis is transverse to both current and quintuple layers. For in-phase magnetization at the two terminals, it is shown that observations can change fundamentally to result in anomalous current distribution. Such results are explained to stem from the confinement of 3D-TI between ferromagnetic contacts along the transport direction. A simple mechanism to validate topological insulators via quantum transport experiments has also been suggested.

7.1. Introduction

The peculiar suppression of backscattering [202] of helical fermions in odd-number [166] of gapless Dirac [167] surface bands of three-dimensional (3D)

topological insulators (TI) [51, 166], accompanied with an insulating bulk, has recently drawn tremendous interest for Very-Large Scale Integration (VLSI) interconnect [62], spintronic [63, 168] and quantum computing [203] applications.

Time-reversal symmetry (TRS) renders this protection to surface states against scattering from non-magnetic impurities and vacancies because in these states the spin of an electron is locked to its momentum vector, which results in a distinct momentum-space spin-texture, and therefore without spin-flip mechanism (e.g. doping with magnetic impurities) or breaking of TRS (e.g. application of a perpendicular magnetic field) an electron cannot be backscattered. The spin-texture which is left (right) handed for top-surface (bottom-surface) conduction band (see Fig. 7.1(a)) and vice-versa for valence bands has recently been shown to engender spin-polarized surface current [204, 205] with an average polarization transverse [206] to non-equilibrium transport direction. Kramer's degeneracy theorem [207, 208] posits that these surface bands with antagonistic spin-texture on opposite surfaces are degenerate.

If 3D-TI is thin enough, but thicker than 5 quintuple layers [204] (QL) (1 QL ~ 0.943 nm) to eschew crossover to two-dimensional limit [78], the wavefunction overlap between opposite surfaces then enables an electron to be backscattered from forward moving state of one surface to backward moving state of opposite one. However, for very large thickness a sizeable fraction of current flows through the bulk layers which weakens the signature of topological surface in electrical transport [204]. Thin 3D-TI (thickness ~ 10 nm [209]) with weak inter-surface coupling but surface dominant transport is therefore especially interesting and important [210]. We show in this chapter that this thickness regime may also provide a simple way to validate spin-momentum locking on topological surfaces through quantum transport experiments,

in comparison to more complicated Berry-phase matching [170] and optical (Spin-ARPES [211] and Circular Dichroism [169]) experiments.

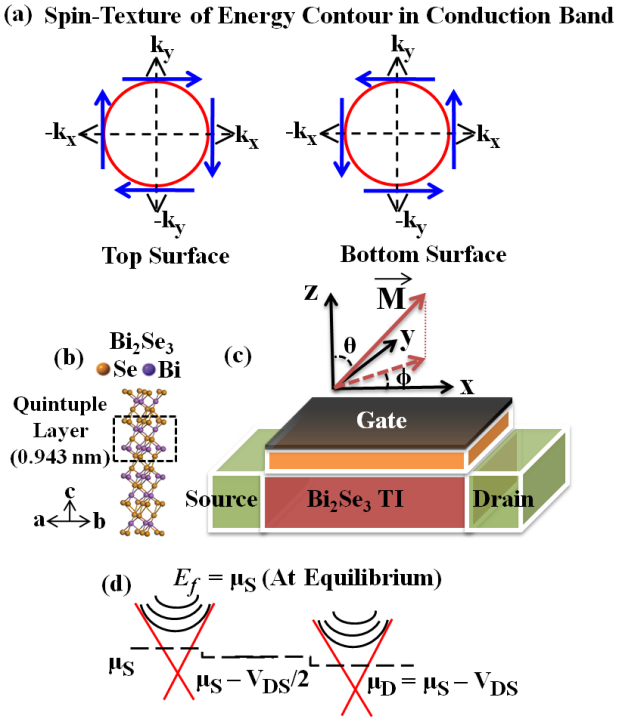

Figure 7.1 (a) Spin-texture in momentum space for conduction bands for top and bottom surface. Blue arrows are spin vectors, red circle is energy contour and black arrows denote momentum vectors. (b) Atomic structure of Bi_2Se_3 (3D-TI). 5 atomic layers constitute one quintuple layer (QL ~ 0.943 nm). (c) Device Structure for quantum transport modeling through Bi_2Se_3 slab. The axis is given over the device along with convention for polar representation of Magnetization vector (M). θ is polar angle and $\emptyset$ is azimuthal angle. Slab dimensions of 10 QL thickness – periodic width (uncoupled mode space) – 65 nm channel length – 10 nm contact on both side of channel, , temperature of 0 K, a potential drop of 35 mV across channel (V_{DS}) and Fermi-level (E_f) = 0.075 eV has been considered as a representative case throughout this chapter unless specified otherwise. (d) Illustration of the potential distribution through the energy bands along the transport direction. μ_S (μ_D) is electrochemical potential at source (drain) end.

Furthermore, for the observation of the topological properties the device should be electronically operated (i) at small channel bias with Fermi-level (E_F) close to the Dirac-point, to avoid the dominance of trivial bulk bands in observed results; and (ii) at low temperature to circumvent phonon scattering [200]. Physically, defect-free or compensated [173] 3D-TI of short channel must be used because strong spin-charge coupling [212, 213] in 3D-TI would limit the spin-relaxation length [214] to the mean-free path. Small channel length becomes especially important for the study of novel magneto-electric effects that may arise in 3D-TI due to ferromagnetic contacts

[213, 215]. Most experiments have, howbeit, been performed on very long channel devices [204, 216] because placing multiple probes for measurements that can accurately characterize the carrier transport become very challenging for small channel lengths.

Therefore, despite of recent emphasis on the importance of short channel for investigating topological insulators, study of quantum transport and current distribution through such a device is completely lacking. For short-channel device the issue is further exacerbated by the confinement along transport direction. We show in this chapter that confinement especially due to ferromagnetic contacts can radically influence the experimental investigation of transport in 3D-TI.

In this chapter, therefore, we carry out a systematic and comprehensive study of quantum transport and current distribution in thin 3D-TI based on Bi_2Se_3 for different contact configurations, which not only enables us to explain a recent experiment on electrical detection of spin-momentum locking on topological surface for long channel device, but also allows us to make new predictions for short-channel TI device like negative surface current and an exotic current distribution which may not be expected from conventional understanding of spin-texture for surface states of 3D-TI.

Therefore, in this work, first a simple system with 'Ferromagnetic Metal source-TI Channel-Extended TI Drain' (FM-TI-exTI) is comprehensively examined to understand the recently published experimental data [204] (long channel device). We then present a more microscopic analysis for different combinations of three different contact-types i.e. ferromagnetic metal (FM), normal metal (NM) and extended-TI (exTI), which finally evolves into more complicated results predicted in this chapter for short-channel devices with both metallic source and drain contacts where quantum

effects may manifest exotic results and provide entirely new ways of identifying a topological insulator via electrical transport experiments.

This chapter is organized as follows. Subsequent to this introduction, computational setup describes the modeling of various types of contacts to appraise their effect on transport. Results and Discussion section then presents our results on the effect of contacts on transport and more specifically on current distribution in 3D-TI. Finally, we conclude our findings with suggestions for experiments. Appendix D serves as supplementary to the discussion in this chapter.

7.2. Simulation Setup

The parameters for device Hamiltonian and methodology for simulating Bi_2Se_3 3D-TI slab are explained in **Chapter 2**. Defect-free slab has been considered in this study. Effect of various defects has been investigated in **Chapter 8**. To model the effect of infinitely or semi-infinitely long channel, computationally one or both of the terminal contacts are treated as if made of the same material as the channel [81, 83] This is done by applying open boundary condition at the contact for reflection less propagation of the plane wave and the contact self-energy is computed from the self-consistent solution of the surface green function [84]. This type of contact is referred as exTI (extended TI or extended channel) to distinguish it from other contact configurations. From the experiment's point of view, this refers to the scenario where terminals are far away from the surface probes to affect the measurements i.e. when voltage probes (VPs) (measurement probes) are sufficiently far from the current-injection probes (CPs) for very long channel device (typically in μm range). The measurement characterizes only the region between VPs, and captures the transport only in the TI material.

Semi-infinite 3D-TI contacts are more appropriate to model such a system. On the other hand, modeling metallic contacts induces the effect of confinement and a hard wall boundary condition. When metallic (normal or ferromagnetic) contacts are applied at both ends, the system is referred to be a short-channel device. For such systems, the confinement and the type of contact is expected to influence the readings. For accurate modeling of the contacts, an ab-initio computation is required to determine the hopping energy between Bi2Se3 and specific contact material. Nonetheless, as we show in the discussion section, the conclusions are not sensitive to the exact value. Furthermore, acoustic phonons scattering [200] is modeled as self-energy in the channel and converged self-consistently.

For ferromagnetic metal contact, Δ (see Eq. (2.7)) was magnetized by modifying the coupling for spin-up (down) by a factor of $1+(-)C_M/100$, where C_M is contact magnetization (in percent). Then depending on the magnetization vector, the unitary transformation [217] was applied on Δ. Here, we would emphasize that coupling parameters for metallic contacts describe the transport only phenomenologically [85] to help us to understand the underlying physics and neglects more complex effects like exchange interaction at the interface. The charge correction from Poisson equation has also been neglected because of the low-field condition [200] (near-equilibrium transport).

7.3. Results and Discussion

Firstly, we investigate a FM-TI-exTI system. Figure 7.2(a) shows the effect of quality of FM source contact-coupling (α) with the channel on the drain current and its spin-polarization (SP). 'α' is a material dependent parameter as each material (even NM) will have different coupling strength with the TI. With the improvement in the quality of the contact-coupling, the metallic reservoirs more easily inject electrons

into the channel. This enhances the current through all the layers. On the basis of Fig. 7.2(a), it is stressed that absolute value of α does not affect the conclusions qualitatively because the results only get scaled with the actual value of current. Therefore, for the subsequent discussion, we select the value of 0.6 for α i.e. a moderate quality contact. It is also observed that despite of electron injection from 100% ($-y$) magnetized source (M_S), drain current is only ~ 34.7% spin-polarized because of non-zero current through sub-surface layers.

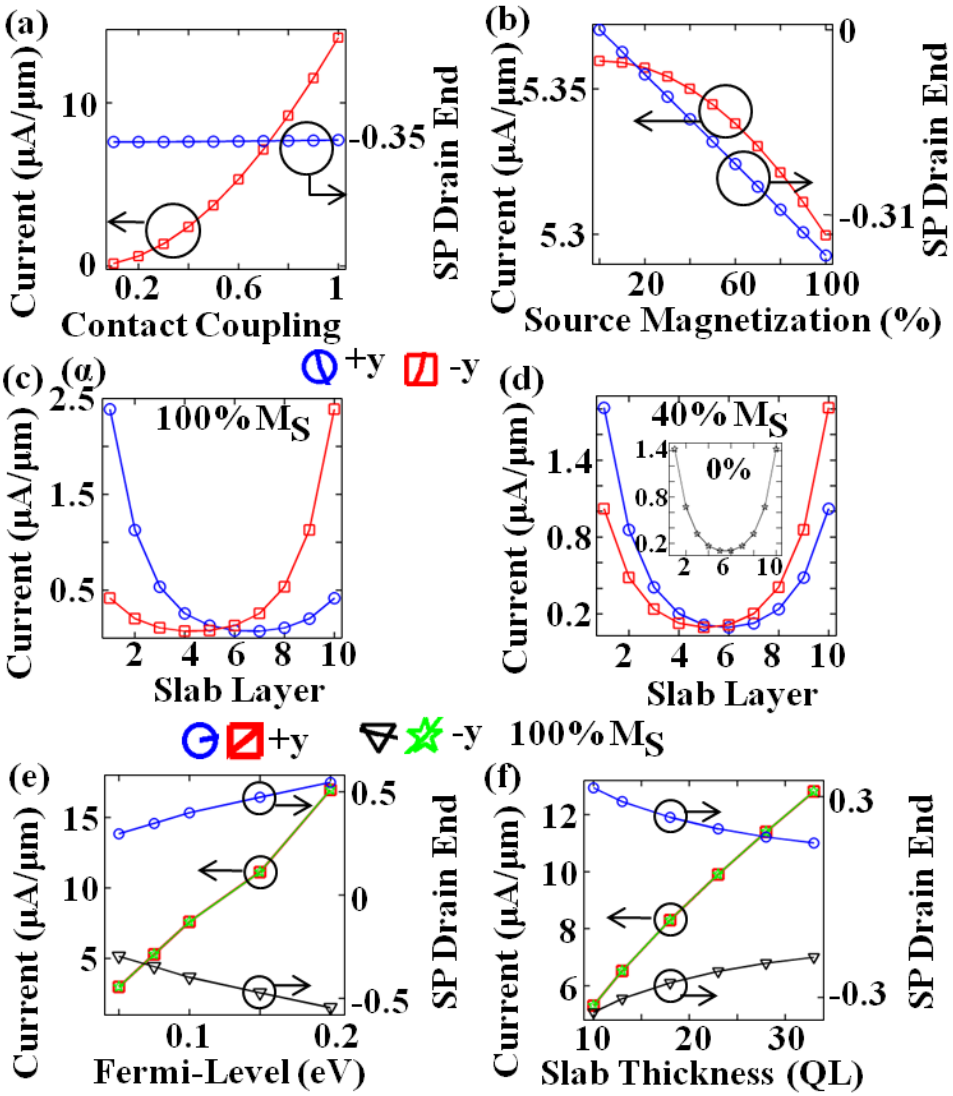

Figure 7.2 FM-TI-exTI system. Spin-Polarization (SP) at Drain end and current through slab over a range of (a) contact-coupling strength (α) for 100 % '$-y$' source magnetization (M_S); (b) '$-y$' M_S for α = 0.6. From here on only α = 0.6 is considered for moderate quality of contact. Current distribution across slab layers for (c) 100 % and (d) 40 % M_S along $\pm y$ axis. Note that current chiefly flows through layer with conducive spin-texture (see Fig. 7.1(a)). Inset shows the symmetric current distribution for 0 % M_S. SP at drain end and current for 100 % M_S along $\pm y$ axis over a range of (e) Fermi-level (E_f) (f) slab thickness.

We would also like to note that this phenomenon cannot be captured in the usual 2×2 Dirac-model used for modeling topological surface which normally overestimates this effect [218]. Since, only the normal mode (k_y = 0) for electron energy very close to Dirac-point has complete $-y$ spin orientation (see Fig. 7.1(a)), for higher energies the spin-vector starts to go out-of-plane [219] and for larger transverse modes ($k_y \neq 0$) spin-vector has $\pm x$-spin component, together they result in low SP. Furthermore, SP is independent of actual magnitude of current injection in this system because contact is uniformly coupled to all layers of the slab and hence, scales the current through each layer proportionally. A real contact, which probably can be simulated via ab-initio models, may slightly differ in this aspect because the contact coupling is material dependent and spin-injection efficiency into the channel depends on the contact-channel interface.

Next, Fig. 7.2(b) illustrates that SP scales directly with degree of source magnetization (M_S), where 0% M_S corresponds to Normal Metal. Therefore, a contact material with larger magnetization at source end should result in higher SP at the drain end. A small decrease in current is observed with increasing M_S. It is due to mismatch between magnetized contact and TI channel, which increases with increasing M_S because of different coupling with $\pm y$ spins for asymmetric injection. It is captured in the contact self-energy. Since, M_S and α are material dependent parameter, although the qualitative effect is same, the observed magnitudes of drain current and SP will depend on the choice of FM (e.g. Fe or Co [204]).

Figure 7.2(c, d) next present a clear evidence of spin-momentum locking on the topological surface. For $-y$ spin injection, current flows chiefly on the top-surface and on bottom-surface for $+y$ electron spin in conformance with spin-texture (see Fig. 7.1(a)). In Fig. 7.2(c) (100 % M_S), note that there is a finite current through other

layers, even on opposite surface. This can chiefly be attributed to two reasons. Firstly, the current in the channel is not 100 % spin-polarized and transport has modes other than $k_y = 0$. Secondly, topological behavior of the system forces the current to flow on the surfaces. Only very near to the source contact current is verified to be least on the opposite surface. Therefore, there is a small transition region after source-contact where current redistributes across layers, as elaborated later in the discussion, with conservation in *y*-*z* plane. Accordingly, going from full (100%) magnetization to weaker source magnetization of 40% in Fig. 7.2(d) the current becomes less anti-symmetric about middle layers. Subsequently, the effect of Fermi-level is shown in Fig. 7.2(e).

For ballistic operation at 0 K in surface metallic bands of TI, the current through the device increases with increase in channel-bias (V_{DS}) (see Fig. 6.3) and Fermi-level (E_f) (see Fig. 6.6). For the operation in surface bands the increase in surface current is much more compared to sub-surface layers for both E_f and V_{DS}, unlike the effect of scaling contact-coupling α. Higher current through surface results in higher SP at the drain end (see Fig. 5(a) of Ref. [204]) but of opposite polarity for $\pm y$ spin injection. Note that if the E_f is eventually moved close to or in the bulk bands, then inspite of higher current (see Fig. 6.5 and 6.6), SP may reduce because of unpolarized bulk bands. Next, as illustrated in Fig. 7.2(f), the increase in slab thickness nevertheless reduces the fraction of current flowing through surface layer inspite of increase in total current due to current flow through more layers. This results in decreasing spin-polarization at the drain end with increasing slab thickness (see Fig. 5(b) of Ref. [204]).

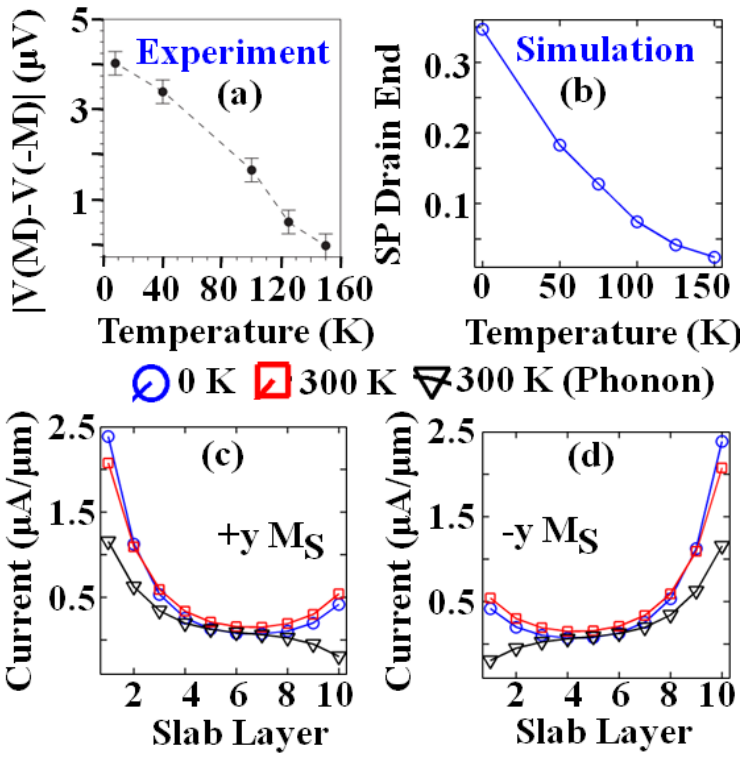

Figure 7.3 FM-TI-exTI system. (a) Experimentally observed trend for signature of spin-momentum locking on Bi_2Se_3, taken from Fig. 5(c) of Ref. [204] (Adapted by permission from Macmillan Publishers Ltd: [Nature Nanotechnology] [204], copyright (2014)). (b) Computed spin-polarization at drain end across temperature (without phonons) for $+y$ (100%) M_S contact. $-y$ Magnetization produces same values but with opposite polarity. (c, d) Current distribution across slab layers for ballistic transport at 0 K ($|SP_{Drain}| \sim 34.7\%$) and 300 K ($|SP_{Drain}| \sim 0.43\%$) and with acoustic scattering at 300 K ($|SP_{Drain}| \sim 0.32\%$) for 100 % source magnetization (M_S) along (a) '$+y$' and (b) '$-y$' axis.

The analysis of the effect of temperature reproduces the experimental data in Fig. 7.3(a, b) which showed that the signature of spin-momentum locking rapidly erodes with increasing temperature. Evaluation at room-temperature is thereafter illustrated in Fig. 7-3(c, d) for both $\pm y$ spin injection. Although the ballistic current through surface layer increases from 0 K to 300 K (see Fig. 6.4(b)), the spread in Fermi-distribution drives the electron energies into higher energy states which are unpolarized [200]. This causes the degradation of the SP at drain end from 34.7% to mere 0.43%. Both current and SP further degrade when electron-phonon interactions are further taken into account. Besides phonon scattering, note that at higher temperatures the thermal effect on the magnetization of the ferromagnetic leads in an experiment may also result in the suppression of the spin polarization. However, since

the ferromagnetic leads are typically quite large (60-80 μm) there will be minimal superparamagnetic effect. Hence, significant thermal effect on its magnetization would occur only close to its Curie temperature, which is above 1000 K for iron or cobalt, much higher than the temperature considered in our simulation. It would thus not be critical to the main conclusions drawn in this chapter, which focuses more on near zero Kelvin operation. Consequently, it is important to execute such experiments at low temperature (see Fig. 5(c, d) of Ref. [204] where measurement signal was lost by 125 K) in order to suppress the phonon scattering and get reasonably spin-polarized current.

We have construed the recent experimental results for the electrical transport that observed spin-polarization resulting from spin-momentum locking on the surfaces of 3D-TI. This, however, pertains to a long-channel device and as stated earlier there could be more exciting phenomena at smaller channel lengths where physics at or due to contacts becomes more significant. Before discussing our observations for such devices, we briefly digress to investigate the effect of contacts more closely to develop a better understanding of underlying mechanism. In the subsequent discussion, f_S (f_D) is Fermi-distribution at source (drain), E is the energy grid for electron injection for energies from μ_D to μ_S for positive channel bias V_{DS}. At 0 K, $f_S(E = \mu_S) = 0.5$ otherwise it is 1 whereas $f_D(E = \mu_D) = 0.5$ otherwise it is 0 on the energy grid. Therefore, drain contact injects charge (in-scattering) into the channel (see Eq. (2.10)) only for $E = \mu_D$.

Consider the simplest case of only one energy point (see Fig. 7.4) for normal mode ($k_y = 0$) electron transport for ($-y$) 100% M_D FM drain contact, because for normal mode spin-vector exactly aligns with in-plane contact magnetization, and three configurations of source contact i.e. exTI (extended-TI) and ($\pm y$) 100% M_S.

Firstly, to focus on the drain we set $E = \mu_S$, $f_S(E) = 0$ (note that it is normally 1 for transport at 0 K), $f_D(E) = 1$ in Fig. 7.4(a-c). It is observed that for exTI source, there is roughly no top layer current, whereas for $\pm y$ M_S there is significant positive current through the top layer.

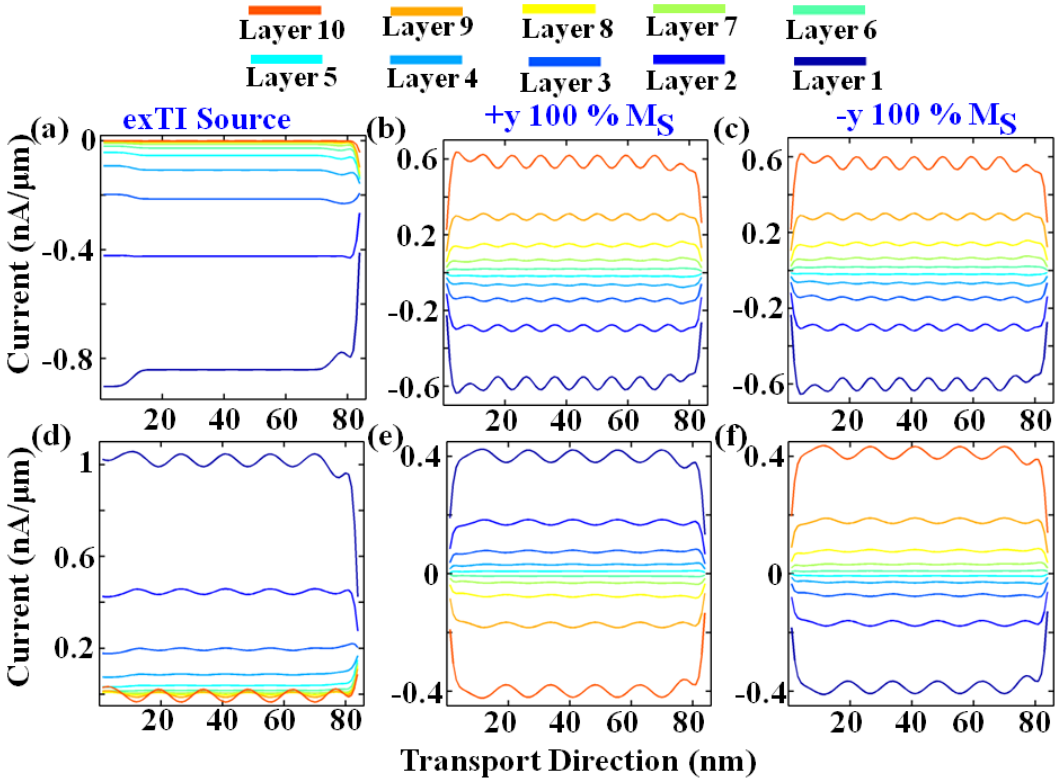

Figure 7.4 Current distribution along transport direction for ($-y$) 100 % M_D FM Drain for normal mode ($k_y = 0$). Source contact-type is stated over each column. Operating condition is as follows: (a-c) $E = \mu_S$, $f_S = 0$, $f_D = 1$; (d-f) $E = \mu_D$, $f_S = 1$, $f_D = 0$. Refer text for symbols.

For exTI configuration, there is a negative current (current direction opposite to voltage bias) in bottom layer in Fig. 7.4(a) because for injection from drain i.e. in $-k_x$ direction the bottom surface has the appropriate spin-momentum state (see Fig. 7.1(a)). A similar isolated injection from source ($-y$ M_S) results in entire current on top surface (not shown). For $+y$ FM source, magnitude of top and bottom layer current is same but it shows the opposite polarity. For $-y$ FM source, although magnitude of current simultaneously increases through both layers, there is more current through bottom layer. This indicates that magnetic contacts are causing some

reflection in the current. For $-y$ source, since source-contact has same phase as drain, the transmission through contact is higher and hence, there is weaker reflection compared to $+y$ FM source configuration. Close examination reveals that even at the exTI source-contact there is a very small reflection current. Note that in Fig. 7.4(a-c) the injected spin from the drain is constant and only the reflection gets modified with source-contact type.

Next, to focus on the source, we set $E = \mu_D$, $f_S(E) = 1$, $f_D(\mathrm{E}) = 0$ (note that it is normally 0.5 for transport at 0 K) in Fig. 7.4(d-f) for injection from the source contact. Before examining the current distribution, we comment on two subtle observations that are evident from the plots: (a) the cyclic trend (oscillations) for surface layer current along transport direction due to the reflection from the drain contact; (b) the wavelength of oscillation is a function of electron energy (compare the two rows of sub-plots in Fig. 7.4) but nearly independent of channel length (verified by simulating from devices of various lengths from 30 nm to 120 nm), with lower energy electrons having longer wavelength as expected from De Broglie's relation. The amplitude of the oscillation is a function of degree of in-plane magnetization along y-axis and the percentage of magnetization (strength) (verified by simulating for entire range of polar and azimuthal angles).

Now by appraising current distribution in Fig. 7.4(d-f), it is observed that for $+y$ FM source positive current flows through the bottom layer (see from spin-texture in Fig. 7.1(a) that forward mode of bottom layer supports $+y$ spin) and negative reflection current through the top layer. The magnitude of current is same although of opposite polarity. Here, we would note that this is equal only for $k_y = 0$ mode (the simplest case under consideration). For $-y$ FM source, positive current flows through the top layer and negative reflection current through the bottom layer. The magnitude

of top current is greater than that of bottom (*measured via cursor in matlab, this may not be clearly visible from the figure*) again because of better phase matching at drain end which gives relatively weaker reflection current and higher transmission.

Nevertheless, for exTI source, it is observed that there is positive current through bottom layer and close to zero current on top layer. Spin polarization shows that this current has $+y$ spin. This is counter-intuitive because it would be expected from spin-texture in Fig. 7.1(a) that $-y$ drain spin-polarization matches with the forward moving state of top surface, therefore suggesting that current should flow through the top layer. Even a single energy level model with spin (2×2 matrix) [217] with 'β up' and 'β down' coupling for up and down spin respectively would imply that we have source coupling to both $+y$ and $-y$ spins (exTI source) whereas for the drain the coupling should only be finite for $-y$ spin, and therefore $-y$ spin should flow through top layer.

Conversely, our calculation results indicate otherwise. This can be explained on the basis of transmission and reflection concept as follows. Consider that source injects 'I_1' μA/μm of $-y$ current on the top layer and 'I_0' μA/μm of $+y$ current on the bottom layer (in forward) direction. Because drain is $-y$ magnetized, entire current on bottom layer is reflected through the top layer i.e. top layer has a reflection current of '$-I_0$' μA/μm. The current injected in the top layer, sees same phase (magnetization direction) in drain and has non-zero transmission (lower reflection). Therefore, '$-(I_1-I_2)$' μA/μm current is reflected through the bottom layer. As a result, net current on the top layer is 'I_1-I_0' and on bottom it is '$I_0-I_1+I_2$'. Since, TI contact injects roughly equal 'I_0' and 'I_1', we have nearly zero current on the top layer and '$+I_2$' μA/μm on the bottom layer.

In general:

$$\text{Top Layer Current:} \quad \mathrm{T}(-\mathrm{y})\mathrm{I}_{\mathrm{Top_Surf}} - R(+y)\left(T(+y)I_{Bottom_Surf}\right) \tag{7.1}$$

$$\text{Bottom Layer Current:} \quad \mathrm{T}(+\mathrm{y})\mathrm{I}_{\mathrm{Bottom_Surf}} - R(-y)\left(T(-y)I_{Top_Surf}\right) \tag{7.2}$$

where, T (R) is transmission (reflection), in range of 0 to 1, of a particular spin from source to channel and $I_{Top(Bottom)_Surf}$ is surface current for TI system with exTI contacts (approximately without any reflection because some reflection will still be there caused by mode mismatch in non-equilibrium condition).

Here, T and R are function of (i) strength of contact magnetization (for instance 40% or 100%), (ii) azimuthal angle, (iii) polar angles of each contact (i.e. type of magnetization), (iv) electron injection energy E_i, and (v) k_y mode. For (iv) and (v) the TI spin-texture and thus $I_{Top(Bottom)_Surf}$ depend on them. Also note that although Eq. (7.1) and (7.2) only consider the top and bottom layer, the surface current can be affected by transmission and reflection for all sub-surface layers and therefore the expression is just for an empirical understanding of the underlying physics and lays the foundation for subsequent discussion. The exact modeling of Eq. (7.1) and (7.2) is beyond the scope of current work.

We now transition to short channel devices for which neither of the contacts can be modeled as exTI. Figure 7.5(a) illustrates transmission spectrum over finely discretized grid for energy and transverse modes (k_y) for device in equilibrium condition (for more clear figure see zoom-in in Appendix D.3). Unlike infinite channel length (contacts modeled as semi-infinite extended channel), the confinement along the transport direction (x-axis) quantizes the bands, and is therefore highly subjective to channel length, which cannot be captured in energy-dispersion along transport direction because energy-dispersion calculation presumes plane wave propagation along the corresponding wave-vector axis.

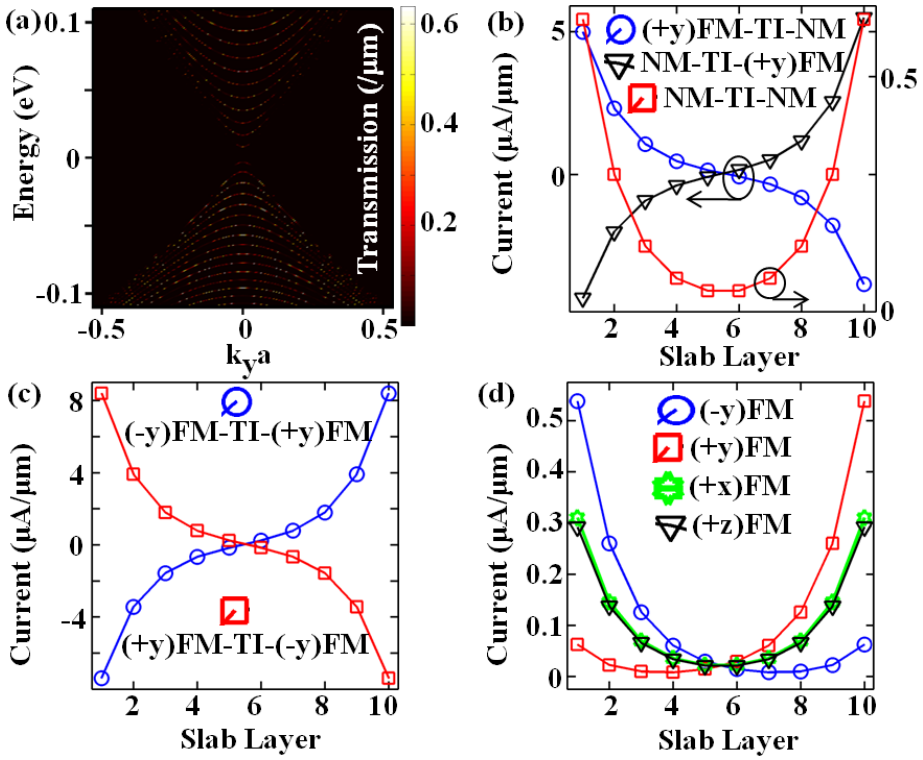

Figure 7.5 (a) Transmission distribution at equilibrium (V_{DS} = 0 V) for normal metal contacts at both ends of the TI channel (see enlarged version of (a) in Appendix D.3 for better visibility) Note that the confinement along the transport direction quantizes the bands which cannot be captured in energy-dispersion along transport direction (*x*-axis). Current distribution across slab layers for (b) three different combinations with normal metal contact, (c) with anti-phase ferromagnetic contacts, and (d) in-phase ferromagnetic contacts.

This is, however, revealed clearly in transmission spectrum simulated over all relevant transverse momentum and energy modes. The current depends on all five criterions discussed above for Eq. (7.1) and (7.2) for both contacts. The transverse mode (k_y) which contributes most for a given energy point on grid will depend on the choice of that E point. For high energies it will in principle be further from k_y = 0 centre-point on k_y grid, unless it is through sub-band edge at k_y = 0, as illustrated from distribution of red-yellow spots in transmission spectrum. Furthermore, this can also be understood in terms of various cross-sectional energy contours from the conical frustum of energy-dispersion curve of surface conduction band and analyzing the permissible k_x and k_y modes in non-equilibrium. Note that at equilibrium it should be exactly at the intersection of chosen k_y mode and energy-point on the sub-band as illustrated in Fig. 7.5(a). Furthermore, as advanced later in discussion for Fig. 7.5(d),

the distribution of dominant k_y modes leads to some non-trivial counter-intuitive results because the overall result is governed by spin-momentum locking at these dominant modes instead of the normal mode (k_y = 0) which was discussed above. Figure 7.5(b) illustrates the effect of normal-metal contacts on both sides (see Appendix-D.1 for top contacts).

If both contacts are normal-metal (red squares) indicating that we have symmetrical distribution of current about the middle layer, the most of which flows on surface layers as expected from topological properties of the 3D-TI. This distribution is same as that obtained by modeling both contacts as exTI, only the magnitude is different because of the difference in magnitude of contact coupling. For (+y) 100% FM source contact (blue circles) positive current flows through the bottom surface, in accordance with spin-texture, however, there is strong reflection current in top layer because backward moving state of top layer has +y spin-vector locked to $-k_x$ momentum on an average. Here we stress that net current along y-z plane is conserved throughout transport direction and total current is indeed positive. For NM source with (+y) 100% FM drain contacts (black triangles), the positive current flows through top layer and negative reflection through the bottom. This case is exactly opposite of the one discussed for Fig. 7.4(d) and so is the current distribution across layers.

Figure 7.5(c) then considers both contacts to be ferromagnetic but anti-phase with each other. Similarly, the current distribution is as expected from the spin-texture for each surface but with larger magnitudes because the forward moving state of one surface exactly matches with the backward moving state of opposite surface. The same phase of ferromagnetic contacts is considered in Fig. 7.5(d) (see Appendix-D.2 for the effect of slab thickness on current distribution for anti-phase and in-phase

contact configuration). $\pm x$ or $\pm z$ spin-injection can be equally resolved along $\pm y$-axis and hence, we get the same current distribution as for NM or exTI source and drain contacts. Therefore, magnetization orientations along $\pm x$ or $\pm z$ for both or either contact is not expected to show any spin-momentum locking signature in transport experiments (see Fig. 3(e, f) of Ref. [204]).

For $\pm y$ in-phase magnetization, which should see small (high) reflection (transmission) at drain, we have the counter-intuitive results as pointed out earlier. If normal mode had dominated the transport, then as evident from Fig. 7.4(c, f), the largest fraction of positive current would have flown through the top layer and a negative current through the bottom surface. However, the spin-dependent transmission and reflection at k_y modes away from $k_y = 0$ point dominates the transport resulting in more current through top (bottom) surface for $+y$ $(-y)$ magnetization and a sizeable positive current through respective opposite surfaces.

To get deeper physical insight into this phenomenon by developing step-by-step understanding, Fig. 7.6 illustrates the energy resolved information for important quantum transport parameters for three sample contact configuration (NM contacts, FM contacts in in-phase and anti-phase 100% magnetization along y-axis) as follows: current (I) (Fig. 7.6(a)) as a function of slab layers (spatial distribution along z-axis), Transmission (TE) (Fig. 7.6(b, c)), and spin-polarization of the current (SP) for top (Fig. 7.6(d) and bottom surface (Fig. 7.6(e)) as a function of k_y modes. Firstly, current distribution in Fig. 7.6(a) affirms the topological behaviour of the system by illustrating that the current is mainly flowing through top and bottom surface layers but through certain energy-eigenmodes. As illustrated by the red-yellow color in Fig. 7.6(a1), for NM contacts, the current flows equally through both surface layers, and sub-surface layers (light-blue color) have lower current contributions.

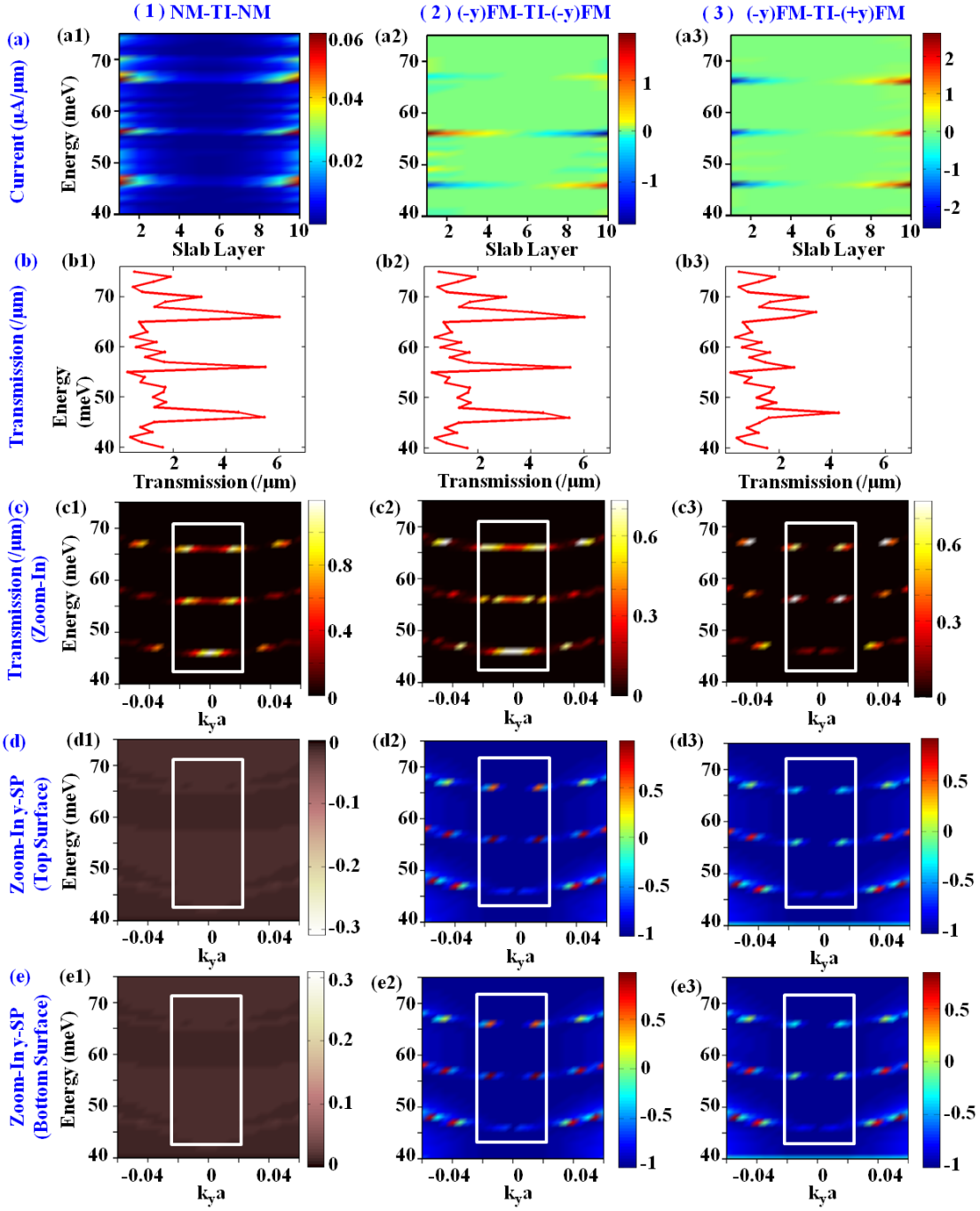

Figure 7.6 Energy resolved microscopic examination of current (a), Transmission (b), k_y-resolved Transmission spectrum (c), spin-polarization of current through top (d) and bottom surface (e) layers for three sample cases (as stated over each column (1)-(3)) taken from Fig. 7.5. Zoom-in plots are illustrated instead of showing full-information to emphasize on the key features. Square box are drawn to draw attention to dominant modes (see text). Specifically, observe the confinement induced band quantization which limits the current through certain dominant energy and k_y modes in (c). Also note that the current through surface layers is symmetrical about middle of the slab for NM contacts, but is spin-dependent for FM contacts. The net current integrated over all layers is always positive in above cases. Spin-polarization of certain dominant energy and k_y modes in (d) and (e) decide the selection of topological surface for transport illustrated in (a). Note that NM contacts strictly comply with spin-texture diagram in Fig. 7.1. In contrast, for FM contacts the net solution atleast depends on magnetization axis of source and drain, sub-band quantization, transverse mode and injection energy.

Subsequently, Fig. 7.6(a2) and 7.6(a3) illustrate energy resolved current flow for FM contacts, where red and blue color, respectively, show strong positive and negative values. The respective energy integrated values result in trends observed in Fig. 7.5. Specifically, notice the energy dependent selection of layers in Fig. 7.6(a2) which corresponds to the exotic behavior observed in Fig. 7.5(d) for in-phase ($-y$) FM contacts. To demystify this observation, we now break down the transport parameters of Eq. (2.5 to 2.14).

Next, the transmission in Fig. 7.6(b) shows that the metallic source and drain contacts confine the channel to induce the discretization of bands and certain energy modes have higher contribution (see peaks) to the transport. We note that this band-quantization is not caused by the confinement along z-axis. Only z-axis termination (periodic width with semi-infinite contacts) results in Dirac-surface bands whose transmission and DOS are linear function of energy as shown in Ref. [200, 220]. Figure 7.6(b) is further decomposed with respect to k_y modes in Fig. 7.6(c).

By comparing Fig. 7.6(c) with peaks of 7.6(b) we can determine the dominant k_y modes (within square box) at dominant energy-modes. Fig. 7.6(c) also shows that the transmission is a function of contacts' (source and drain together) magnetization (compare color-bars and golden spots among three systems within the square box). This analysis which explains current distribution along energy-axis in Fig. 7.6(a) is insufficient to explain surface layer selection for different contact configuration.

Therefore, Fig. 7.6(d, e) next examine the spin-polarization of current at each energy and k_y-mode through top and bottom surface layer, with dominant modes enclosed in square box. For NM contacts in Fig. 7.6(d1) and 7.6(e1) observe that $-y$ ($+y$) spins are flowing through top (bottom) surface as expected from spin-texture, but the values integrated over entire y-z plane would result in zero polarization for the

net current. For $-y$ FM source in Fig. 7.6(d2, d3, e2, e3), the spin-polarization of current flowing through each surface is strongly influenced by drain's magnetization and can in fact be of opposite polarity for certain ky modes (positive (red) in Fig. 7.6(d2, e2) while nearly zeros but negative (light bluish-green) for Fig. 7.6(d3, e3)). In addition to FM contacts, this is probably due to combined effect of confinement induced band-quantization and the non-equilibrium condition which breaks the symmetry along x-direction. The *y*-spin component is opposite in adjacent quadrants in *k*-space for a given ky and therefore, spins for projections of Dirac bands on k_y-axis in non-equilibrium, which may be larger for certain modes than others, may result in either of the polarities.

Although a further study, for instance ab-initio modeling with FM contacts, might be needed to give the detailed understanding of this kind of phenomenon, our investigation in this chapter consequently reveals that the net solution for spin-polarization at least depends on magnetization axis of source and drain, sub-band quantization, ky and Ei, and hence strongly influences the Transmission (*T*) and Reflection (*R*) coefficients in Eq. (7.1) and (7.2). Therefore, from microscopic dissemination of quantum information, we note that for ferromagnetic contacts the current distribution is highly subjective to the choice of Fermi-level, bias (determines electron injection-energy) and contact magnetization, which may result in exotic observations for current distribution across layers of 3D-TI. Next, we observe that negative top surface current can be driven for certain configurations of metallic contacts (see Fig. 7.5(b, c)) for short channel devices. Therefore, the experimental observation of negative resistance for surface transport on thin slabs of potential candidates for 3D-TI can serve as a simple way to verify spin-momentum locking and hence validate the existence of topological insulator.

Finally, we would like to note that presence of helical surface state is necessary but not the sufficient condition for detecting a TI because the count of Dirac cones must also be unraveled. More specifically, Z2 class [166] of TI has odd number of Dirac cones whereas another class called topological crystalline insulator (TCI) [221] has even number [222, 223] of Dirac cones with same helicity for a given surface. Since only Bi_2Se_3 has been studied in this work, which belongs to Z2 class, we could be right in suggesting our method for the electrical detection of the topological insulators for this system only. Hence, as part of future work we would suggest to further mature this methodology for conclusively predicting topological insulators via electrical detection.

7.4. Conclusion

In summary, we address the issue of influence of different contact types and configurations on current flow through thin Bi_2Se_3 3D-TI. Specifically, we examined the current distribution across layers as it flows through the device for the extended-channel, normal metal and ferromagnetic metal contacts. Our model is shown to explain the recent experimental work [204] on electrical detection of spin-momentum locking on topological surface.

For experimental observations, it is suggested to perform the experiment on thin samples at low temperatures with magnetic contacts of high-polarization. We also show that for short channel devices the spin-dependent transmission and reflection at the contacts can result in observations seemingly counter-intuitive from simple spin-texture understanding of the topological surfaces.

For the anti-phase magnetization between terminal contacts, along the y-axis, negative surface current can be generated which may provide a simple mechanism to validate topological insulators via quantum transport experiments by observing

negative surface resistance. Recently various optical [224, 225] and magnetic [226] techniques have been established for selectively probing edge and surface transport of materials and may help in validating the predictions made in this chapter.

Furthermore, for the in-phase configuration, it is shown that confinement and hence induced quantization of energy and momentum modes may result in current distribution antagonistic to trend expected from general understanding of spin-texture. The comprehensive understanding of transport in 3D-TI with ferromagnetic contacts should expedite the development of novel spintronic devices based on topological insulators.

Chapter 8

Evaluation of mobility in thin Bi_2Se_3 Topological Insulator for prospects of Local Electrical Interconnects

Three-dimensional (3D) topological insulator (TI) has been conjectured as an emerging material to replace copper (Cu) as an interconnect material because of the suppression of elastic scattering from doping and charge impurities for carrier transport on TI surface. In this chapter, therefore via full real-space simulation, we examine the feasibility of using thin 3D-TI (Bi_2Se_3) wire for the local electrical interconnects in the presence of edge roughness, vacancies, acoustic phonons and charge impurities across temperature and Fermi-level by simulating quantum transport through Non-Equilibrium Green Function algorithm. We found that because of the scattering induced by the acoustic phonons, the mobility[b] reduces considerably at the room temperature which complemented with the low density of states near Dirac-point does not position Bi_2Se_3 3D-TI as a promising material to replace Cu for local interconnects. Properties required in suitable TI material for this application have also been discussed.

8.1. Introduction

Three-dimensional (3D) topological insulator (TI) is a recently [51] discovered material which exhibits gapless topological insulating electronic phase [166] on its surface and an insulating phase in its bulk. The spin-orbit interaction in 3D-TI results in the band inversion [166] for the surface bands and serves as

[b] This work is on effective mobility, not Hall mobility, because former defines the interconnect behaviour. In 3D-TI literature, it is more common to report hall mobility which may even be 2-3 orders higher than effective mobility (e.g. see S. Cho et al., Nano Lett., 2011, 11 (5), pp 1925–1927).

important criteria for the search of new 3D-TIs. Among these, Bi_2Se_3 [52] (see Fig. 8.1(a)) has been the most extensively examined for experimental and theoretical studies owing to its relatively larger bulk bandgap (~ 0.3 eV) that provides greater isolation of surface states from trivial bulk states compared to other TI materials. The fermions on the surface states of 3D-TI have their spins locked to their momentum ensuing chiral spin-texture which protects electrons from backscattering [202]. This atypical material, therefore, warrants investigation of new quantum phenomenon for applications in spintronics [63, 168, 227]. Furthermore, in a Very-Large-Scale Integration (VLSI) circuit, functional blocks communicate data and share clock, ground and power signals among them through a network of wiring system called interconnects, whose bandwidth, dimensions and current carrying capability depends on the signal to be propagated. Due to the suppression of backscattering, TI has been proposed to be a future interconnect material [62], as a replacement for copper (Cu) [228] for thickness greater than 5 nm because a five quintuple layer [52] (QL) thick sample (~ 4.7 nm) and thinner are 2D-TI [48, 78, 229, 230] in which the edge-transport severely limits the current carrying capability of the wire.

A 6-layer thick Bi_2Se_3 sample (~ 5.658 nm) marks the transition to the 3D limit [78]. Furthermore, beyond 10 QL the coupling between the surface-state wavefunction of the top and bottom surfaces becomes sufficiently weak [209] and the sample is, therefore, expected to evince the above-stated topological properties. These propositions are, however, based purely on the electrical and spin properties (spin-momentum locking) of the surface states and neglect the interactions and the role of intermediate bulk layers. As a result, there is a clear need to scrutinize the feasibility and limits of the proposals by modeling real-space quantum transport through 3D-TI

wire (see Fig. 8.1(b)), accounting for all layers and the realistic effects including acoustic phonons and defects.

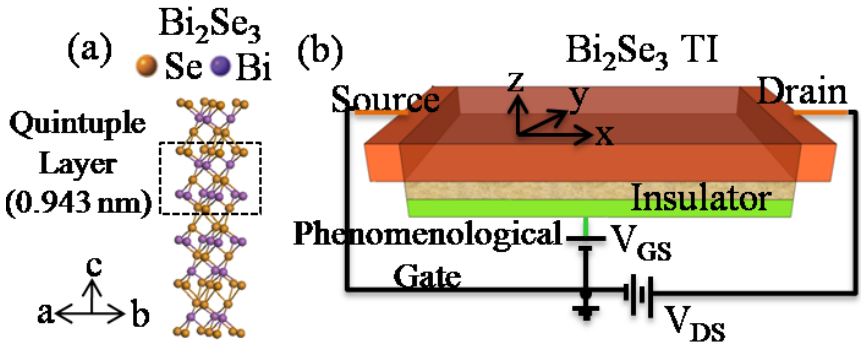

Figure 8.1 (a) Atomic structure of Bi_2Se_3 (3D-TI). (b) Device Structure for quantum transport modeling through Bi_2Se_3 nanowire.

In this chapter, the electron mobility in 10 QL to 13 QL thick Bi_2Se_3 3D-TI wire has been comprehensively examined to evaluate its prospects for the electrical interconnect application. Quantum transport through Bi_2Se_3 TI-wire of dimensions suggested for local interconnects was modeled across a range of temperature, and Fermi-level in the presence of edge roughness, vacancies, acoustic phonons and charge impurities within the scope of experimental concentrations.

The results show that for the electrical interconnects there is a considerable degradation of mobility at the room temperature due to phonons, even though mobility is relatively robust to other defects. Therefore, the trade-off to gain mobility by operating in topologically protected surface states which inherently have low density of states (DOS) is not very promising for interconnect application, at least at the room temperature.

The rest of this chapter is organized as follows: in computation setup section, the simulation approach has been elaborated. Next, in the results section, the important scattering mechanisms, which affect the electron transport through the interconnect wire, are discussed. The evaluation of Bi_2Se_3 TI for interconnect application have been subsequently analyzed in discussion section. Finally, our key

findings have been summarized in conclusion section. Appendix E has illustrations to help the reader develop more intuitive understanding of results discussed in this chapter. Appendix-E.1 illustrates non-equilibrium and near-equilibrium transport through defect-free Bi_2Se_3 TI-nanowire which especially aids in understanding the methodology. Appendix-E.2 illustrates the effect of different defects on transport and helps in appreciating the conclusions drawn for interconnects. Appendix-E.3 shows the effect of acoustic phonons on non-equilibrium transport through Bi_2Se_3 3D-TI slab.

8.2. Computational Setup

The details of the Hamiltonian, energy-dispersion and NEGF are described in **Chapter 2**. Perfect contacts were considered in this study. For simulating the effect of acoustic phonons in Bi_2Se_3, the transverse direction (y-axis) was considered in k-space rather than real space, in order to converge, the correlation function (G^n in NEGF) in reasonable computational time. However, all other defects in the Bi_2Se_3 wire (vacancies, edge roughness and charge impurities) of 10 QL thickness - 60 nm width and 80 nm length were modeled in full real-space.

The transport and mobility was calculated via Eq. (2.5) to (2.17). The evaluation of mobility for interconnects was, however, carried out for near-equilibrium transport to get results across entire temperature range within reasonable computational time. The effective mobility from both (phonon and rest of the defects) was then added according to Matthiessen's rule (Eq. (8.1)) to compute the net effect of all contributory factors. The charge correction from Poisson equation had been neglected because of the low-field condition [82].

$$\frac{1}{\mu_{eff}} = \sum_j \frac{1}{\mu_j} \tag{8.1}$$

where j includes all effects including ballistic, defect, phonons and so on. In additions, charge (ionic) impurities were modeled as delta-onsite potentials whose position and strength were set via constrained random number generator for a given impurity concentration. We note that a corresponding change in Fermi-level due to the impurities was not accounted because in our model we only consider a phenomenological gate via which we shift the Fermi-level to the same energy value as for the defect-free wire.

To model the vacancies, selected lattice points were removed from the Hamiltonian matrix along with all the corresponding interactions in three dimensions. The positions of the vacancies were also regulated by a constrained random number generator. Furthermore, we need to include edge roughness, which originates, e.g., when a sample is cleaved to form a channel, an operation that introduces dangling bonds and vacancies at random lattice sites depending on bond strength at the cleaved interface. The edge roughness was modeled [65, 138, 231-234] by creating vacancies on the side surfaces i.e. on x-z plane in the channel. The ‘m%’ roughness in simulation results implies that independently for each sampling point on the wire, for a random number less than ‘m’ a vacancy was created on the outermost side surface and the one adjacent (inner) to it. For a random number between ‘m’ and ‘100-m’ a vacancy was created only on the outermost side-surface. Therefore, random number of less than ‘m’ creates a vacancy defect on the side surface while one greater than ‘100-m’ emulates a dangling bond. In this work, edge-roughness of 2% and 10% is appraised. Here, we note that this way of defining edge-roughness is different from experimental literature, for which 2% and 10 % edge-roughness translate to 0.20 nm and 0.45 nm rms-height on side-surfaces. And since all the lattice-points are treated

independently, the correlation length for both cases along y-axis is 0.5 nm and along z-axis is 0.47 nm.

To further validate the model and appropriateness of operation conditions (physical and electronic), non-equilibrium transport current was computed as per Eq. (2.12), and near-equilibrium transport was simulated for a defect-free Bi_2Se_3 wire of 10 QL thickness - 60 nm width and 80 nm length as illustrated in Appendix-8A. The results for random defects were averaged over 25 simulations (refer Fig. E.3 for standard deviation for each defect). The effect of these defects on non-equilibrium transport is illustrated in Fig. E.4.

8.3. Results

8.3.1 Defect Scattering

The helical Dirac surface states which arise due to strong spin-orbit coupling (SOC) and subsequent band inversion in Bi_2Se_3 topological insulator (a strong-TI) are protected by the time-reversal symmetry (TRS), i.e. $\hat{H}(-\boldsymbol{k}) = -\hat{H}(\boldsymbol{k})$. The existence of a single-Dirac cone on the surface prohibits backscattering for perturbations, like non-magnetic charge impurities and vacancies, which cannot break TRS. The odd number of spin-half electrons for surface bands should, however, obey Kramer's degeneracy [208]. In concurrence to this theorem, it is construed that the bands from top and bottom surface are degenerate but with opposite helicity i.e. they have counter-clockwise and clockwise spin-texture [235] on top and bottom surface, respectively. If the thickness of TI is very small, the wavefunction of the two surfaces can overlap (inter-surface coupling or crosstalk) and therefore the electron in the forward moving state of one surface can backscatter into the backward moving state

of the other surface. For a sufficiently thick TI with negligible crosstalk, the surface transport in principle should be immune to the charge impurities and vacancies.

This theoretical assertion is, however, based on a semi-classical scattering picture for momentum conserved interaction (elastic process) of electrons with defects and overlooks other aspects of electronic interaction with defects in a device [236]. Vacancies, for example, can induce trap states in the bulk bandgap of TI [237] and charge impurities may affect the carrier transport by scattering the electrons to bulk layers [238] or by creating a localized resonant state [239, 240] that even though does not destroy the Dirac-point (locally), can significantly modify the local density of states (LDOS) [241]. The effect of defects is, however, felt only in the vicinity of the defect [239]. Therefore, even though the theoretical [240] and experimental [202, 239, 241, 242] examination of the TRS protected surface state for 3D-TI in presence of non-magnetic defects has found it to be robust around the Dirac-point [80], there is a limit to the robustness depending on the magnitude, density and spatial distribution of the defects. Even if the individual impurity potential is weak but occur in sufficiently high spatial density, then the defects can scatter the electrons and reduce the mobility [243]. Large impurity concentration can also modulate the energy band to drive the topological insulator into a trivial insulating state [244], which becomes especially important because of the large de facto concentration of vacancies and impurities in freshly prepared samples.

Therefore, due to the qualified invulnerability of quantum transport to the elastic scattering mechanisms, the effect of charge impurities and vacancies on carrier mobility deserves scrutiny and has been comprehensively examined over a broad range of concentration in discussion section.

8.3.2 Phonon Scattering

The uniformly packed atoms in a lattice at 0 K start to vibrate like coupled springs as the temperature is increased. The coherent collective motion of these atoms i.e. the acoustic phonons exchange momentum with the electrons to relax the latter's momentum. Since, negligible energy is exchanged in this phenomenon the electrons continue to propagate at the same energy but are forced to change the direction (momentum vector). At non-equilibrium, this may gradually lead to the scattering of the electrons despite their initial forward moving state. For low non-magnetic defect density, the topologically protected surface states are therefore most vulnerable to acoustic phonon scattering processes [200].

The impact of acoustic phonons scales with the temperature and length of the channel which makes this phenomenon even more important for interconnect wires operating at room temperature or even at elevated temperature in packaged integrated circuits. In the most comprehensively studied material Bi_2Se_3, the strength of electron-phonon coupling (λ) although contended over a large range (from 0.08 to 0.43) is still relatively strong [56].

At a subtler level, temperature induces two opposing trends –it not only scales the strength of acoustic phonons that make the transport more resistive, but also thermally activates the carriers into higher energy states in accordance to Fermi-Dirac statistics, which usually enhances the conductivity of the Dirac-band material. The energy level broadening induced by the phonon scattering furthermore may aid in the thermal activation depending on the Fermi-level of the system. Since, the Fermi-level of pristine Bi_2Se_3 lies in the bulk conduction bands due to the selenide vacancies, for systems operating without gate control, the most common scheme is to dope with p-type impurities [173, 245] to bring down the Fermi-level closer to the Dirac-point.

Therefore, due to the multitude of factors competing or complementing with one another, the prospects of Bi_2Se_3 3D-TI interconnect has been investigated in presence of all defects across temperature and Fermi-level in discussion section for different wire widths and thicknesses.

8.4. Discussion

Some of the key properties being sought in a material to replace Cu as the electrical interconnect at the room temperature are high mobility, passivity to edge roughness and defects. Therefore, each of these have been individually examined in Fig. 8.2, and finally the collective effects of all the defects and phonons have been put together in Fig. 8.3 and Fig. 8.4 to appraise the prospects of 3D-TI for interconnects.

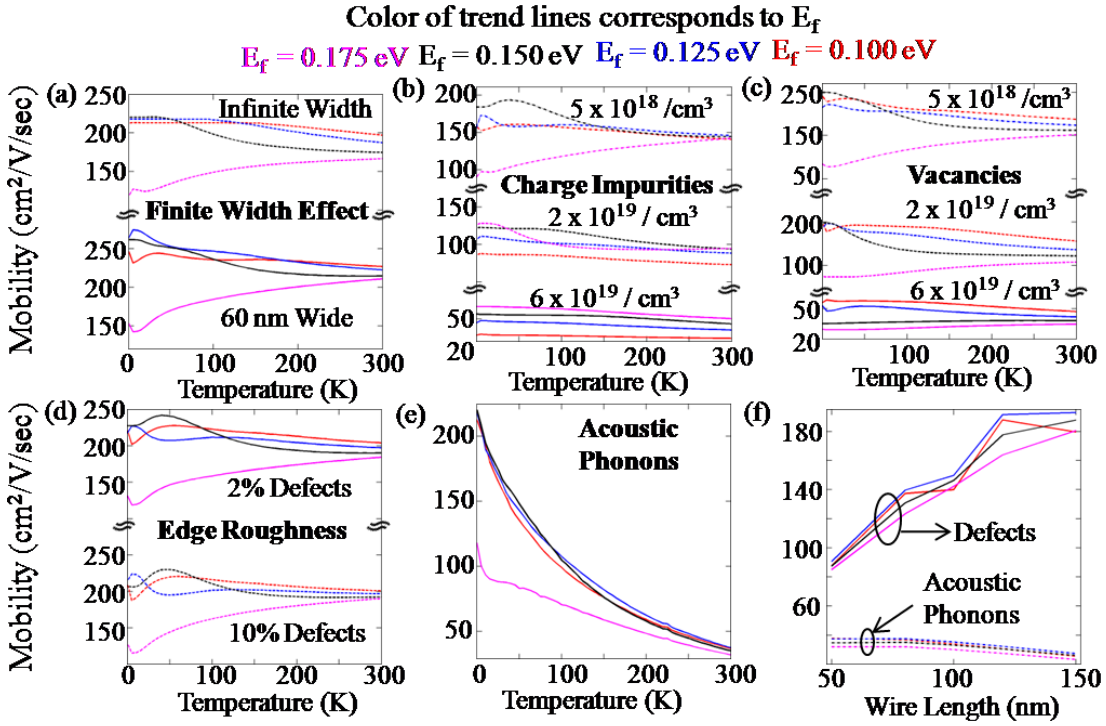

Figure 8.2 Mobility characterization across temperature at different Fermi-Levels (E_f). (a) Ballistic Mobility for a finite width and an infinitely wide wire. Effect of charge impurities (b), vacancies (c), edge roughness (d) and acoustic phonon (e) on mobility. (f) Effect of defects (10% Edge Roughness + 5 x 10^{18} /cm^3 Charge Impurities + 5 x 10^{18} /cm^3 vacancies) and phonons on mobility at 300 K with the scaling of the wire length. Note that for low defect concentration mobility trends follow approximately ballistic results.

As shown in Fig. 8.2(a), the confinement due to finite width (see also Fig. E.2) of wire limits the propagation modes, quantizes the surface band and induces a mini-bandgap. The scaling of both DOS and transmission (see Eq. (2.15)-(2.17)), however, results in approximately the same ballistic mobility values. This shows the robustness of TI to finite width effects which is an important requirement for interconnects. The mobility is also significantly good for interconnects (Cu ~ 30 $cm^2/V/s$ [246]). In Fig. 8.2(b) and Fig. 8.2(c) charge impurities and vacancies are then considered in a 60 nm-wide wire at experimentally observed concentrations in Bi_2Se_3 [210, 247, 248].

For premium quality (Se vacancy compensated) Bi_2Se_3 [209] samples with low defect concentration (good quality samples [209]) and operating close to the Dirac-point, the mobility is practically immune to charge impurities. It is because non-magnetic impurities do not break time-reversal symmetry on TI surface, and therefore cannot result in backscattering. Moreover, for low defect concentration, as explained in the results section for defect scattering, electron cannot be scattered from defect to defect because of localized influence of defect-site due to non-overlapping wavefunction of the defects.

De-facto fabrication of Bi_2Se_3 TI, however, has very high impurity and vacancy concentration [247]. At large concentrations, the mobility degrades and makes the wire more resistive and less useful as an interconnect-wire. (see Fig. E.3 for plots of DOS, transmission and charge distribution and Fig. E.4 for current distribution across layers for each type of defect to develop an intuitive understanding of the transport and mobility behaviour in a TI-wire). Similarly, the insensitivity of mobility to edge roughness (see Fig. 8.2(d)) that results from transport being chiefly through the lateral centre of the wire (along the y-axis) (see Fig. E.3) and high thermal

conductivity [249] which is required to circumvent electromigration problems, seemingly qualifies 3D-TI as a good candidate for interconnects.

However, as shown in Fig. 8.2(e), the acoustic phonons substantially reduce the mobility at higher temperatures because of strong electron-phonon coupling. Furthermore, the effect of low defect concentration and phonons on mobility at 300 K has been separately examined in Fig. 8.2(f) over a wide range of length of local interconnect-wires. As expected, the trend line for the effect of defects is reminiscent of approximately ballistic behaviour (see Eq. (2.17)), whereas phonons can scatter electrons more strongly for longer wire lengths. For pure ballistic behaviour (absence of any scattering mechanism) the density of states per unit length and transmission are both independent of the channel length, and hence mobility scales-up linearly with wire length. For ohmic conductors [82], in presence of scattering mechanisms, the conductance scales with the length as being inversely proportional to the sum of mean-free path and the channel length, while density of states per unit length is still held nearly constant as the length scales. Hence, for ohmic conductors initially the mobility increases with the channel-length and when length becomes much larger than mean-free path the mobility saturates (channel-length + mean-free path ~ channel-length) because numerically the channel-length in numerator cancels out with the channel-length in the denominator (see Eq. (2.17)). The transport characteristics of Bi_2Se_3 3D-TI are however much more complex than ohmic conductors (see section 6.5.1 for effect of channel length on transport characteristics in presence of acoustic phonons). In Fig. 8.2(f) for acoustic phonon scattering, the transmission in the operational energy-regime scales-down faster than inverse of channel-length, especially for longer channels. Therefore, as the channel-length increases, the transmission and hence conductance rolls-off faster than it can be compensated by the

channel-length term in the numerator for mobility calculation, which results in slight decrease in mobility as channel-length increases. For a simple ohmic conductor this would have been the diffusive regime of transport and mobility would have saturated.

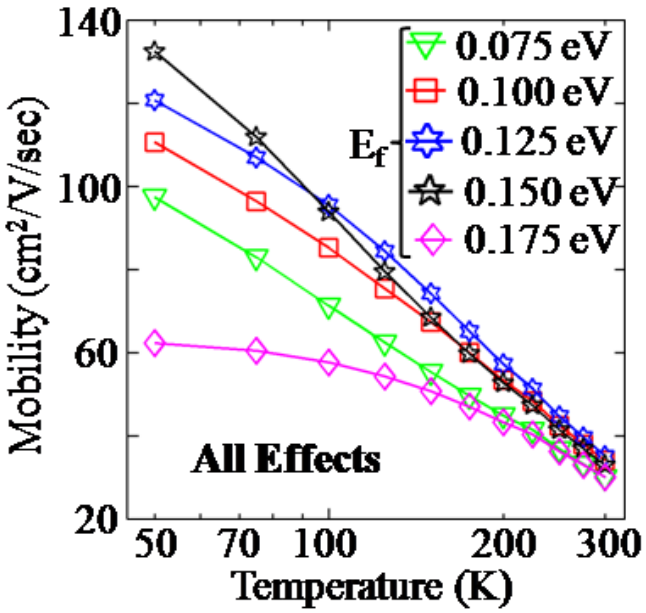

Figure 8.3 Effective mobility in presence of all the defects (Phonons + 10% Edge Roughness + 5 x 10^{18} /cm^3 Charge Impurities + 5 x 10^{18} /cm^3 vacancies) as described by Matthiessen's rule (see Eq. (8.1)) for different Fermi-Levels.

Furthermore as shown in Fig. 8.3, the collective effect of all the defects (in real-space) in low-concentration along with phonons (uncoupled transverse modes in k-space) computed via Matthiessen's rule (see Eq. (8.1)) (also see Ref. [250] for detailed technique of adding partial mobilities) successfully emulates the experimentally [251] observed trends, and matches closely with experimentally observed value of field effect mobility in Bi_2Se_3 3D-TI (Ref. [177] observed 10 $cm^2V^{-1}sec^{-1}$ at 245 K for 3.5 nm thick sample in which inter-surface scattering would be much stronger than 10-13 QL samples, while Ref. [252] observed 23 $cm^2V^{-1}sec^{-1}$ at room temperature for 30 nm thick sample). Specifically, note that phonons dominate the high temperature characteristics of mobility, because the mobility values for wire with phonons are much lower than cases with defects (see Eq. (8.1)).

Thereafter, the effect of interconnect wire width and thickness has been examined at room temperature in presence of phonons and other defects as illustrated in Fig. 8.4. In Fig. 8.4(a), for a given thickness, although total DOS increases with width, inter-surface coupling is constant. Therefore, for the wire width in topological regime the mobility is approximately constant. We, however, note that in our simulation, this could also be because phonons which have dominant effect on mobility have been evaluated for same (periodic) width and may therefore mask the effect of defects and increased DOS for larger widths. To validate this hypothesis, the phonons should be simulated in the same nanowire in real-space which is computationally prohibitive presently and may be addressed in future. Hence, based on the current observations, Bi_2Se_3 TI wire exhibits good robustness to finite width effects.

For increased wire thickness the inter-surface coupling should reduce and defect-scattering should become weaker as explained in results section, but DOS increases due to increased number of layers with only a small change in transmission, due to operation in surface bands, resulting in a small decrease in mobility as illustrated in Fig. 8.4(b).

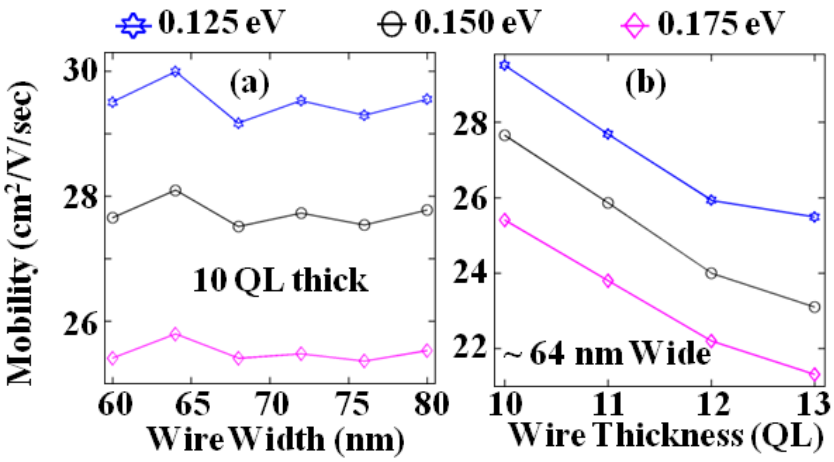

Figure 8.4 80 nm long – 64 nm wide TI-wire at 300 K. (a) Effect of wire width and (b) thickness on the mobility in presence of all the defects (Phonons + 10% Edge Roughness + 5 x 10^{18} /cm^3 Charge Impurities + 5 x 10^{18} /cm^3 vacancies) for different Fermi-Levels at 300 K.

As a possible future interconnects material, 3D-TI has to compete with other materials among which the major contenders for replacement are single-walled carbon-nanotubes (SW-CNT) and graphene-nano ribbons (GNR). Between these two variants of carbon, recently the later has been more strongly pursued because of relatively simpler fabrication process [253]. Therefore, we now briefly discuss their properties in order to understand the relative prospects of topological insulators vis-à-vis the above carbon-based competitors.

At room-temperature bulk Cu [246] has mobility of ~ 30 $cm^2/V/sec$ and conductivity of ~ 2.5-3.3 x 10^7 $(\Omega\text{-m})^{-1}$ (2005 ITRS for 52 nm – 90 nm wide Cu wire) (free electron density of ~ 10^{29} $/m^3$). Copper interconnects for such small wire widths suffer from electromigration effects and grain-boundary scattering (edge effects). The large current densities (> 10^9 A/cm^2 [253]) without material breakdown can be sustained in GNR by its in-plane strong sp^2 hybridized sigma bonds. Additionally, electromigration is suppressed in GNRs due to their large thermal conductivity [254], and high momentum relaxation time arising from long mean-free path (~ 1 μm) indeed positions GNR as a good interconnect material. However, the low mode density and low DOS of monolayer GNR interconnect [255] makes it highly resistive, whereas the electron mobility is degraded because of the inter-layer coupling in multi-layer GNR (MLGNR). Therefore, a prospective solution [256] is to consider an intercalated zigzag edged MLGNR (side-contacts) of high specularity (p ~ 1) and of sufficient inter-layer separation. On the other hand, even though single SWCNT also suffer from low DOS problem, they can be bundled [257] together to enhance their performance. For more detailed discussion on prospects of these two materials as a replacement of Cu, the reader is referred to a recent review article [258].

To induce topological protection from elastic scattering in 3D-TI, Fermi-level should be close to the Dirac-point. The DOS is considerably low around Dirac-point compared to large mode density in Cu at Fermi-level, and in fact tends to zero at the Dirac-point. The low DOS corresponds to bulk carrier density of ~ 10^{23} /m^3 [248] and conductivity even at low-temperature (~ 2K) lies in the range of only 8.9-34.5 x 10^3 $(\Omega\text{-m})^{-1}$ [173].

However, to the best of our knowledge, no multi-layer stacks or bundles, or any such technique to exploit multiple 3D-TI channels exists to substantially increase the conductivity while operating close to the Dirac-point. Therefore, even though at low-temperatures 3D-TI has experimentally shown high mobility [245], at the room temperature the topologically protected surface states exhibit low mobility due to acoustic phonons, coupled with their low DOS.

8.5. Conclusion

Although the topological surface states of 3D-TIs have high mobility at low temperature (~ 2 K) and are immune to edge roughness, charge impurities and vacancies in reasonable concentrations, the mobility is significantly lower at room temperature due to acoustic phonon scattering. Therefore, the trade-off to gain mobility by operating in topologically protected surface states, with inherently low Density of States (DOS) near the Dirac-point, is not encouraging enough to suggest thin Bi_2Se_3 3D-TI as a good candidate for the replacement of Cu as the local interconnects material especially at the room temperature.

However, we note that some other 3D-TI material with large bandgap, for greater isolation between high-mobility topologically protected surface with bulk layers [259], and weak acoustic phonon scattering may still be a good contender for interconnect wires. It is also noted that very thick Bi_2Se_3 3D-TI may exhibit large

mobility as shown in a recent experimental work [260], which implies that for applications where thick interconnects are permissible 3D-TI may be a viable option, and an interesting possibility for future investigation. Other possible alternative is to experimentally devise innovative schemes like to bundle or have stacks of 3D-TI which may improve their electrical properties for interconnects. If the viability of transport is established, one of the subsequent steps would be to appraise electromigration in the chosen material for interconnects [261-265] as has been done previously for Cu [266-270], Al [271-273], Cu-Al alloys [274-277], and some preliminary studies have been published for Bi_2Te_3 [278] and Cu-doped Bi_2Se_3 [279].

Chapter 9

Effect of Band-Alignment Operation on Carrier Transport in Bi_2Se_3 Topological Insulator

Band-alignment induced current modulation in Bi_2Se_3 three-dimensional topological insulator slab has been investigated by quantum transport simulations for three different device designs, one for purely lateral transport and other two with vertical transport. Non-Equilibrium Green Function formalism has been deployed to understand the transport mechanism in band-alignment devices to appraise the possibility of a 3D-TI based resonant device. A resonance condition is observed when the Dirac-points (bands) are aligned. This results in the maximum current at resonance for the design with only lateral transport. However, current ratio between resonant and non-resonant condition is found to be relatively small and strong temperature dependence is also noticed. The other two designs with vertical transport have degraded transfer characteristics, although from state-of-art literature they are expected to manifest nearly an ideal resonance peak. The physical insights for these observations have been posited along with the suggestions for attaining close to an ideal operation for the first design, which we also suggest for the pursuit in the future for spintronic oscillators and analog multipliers based on band-alignment induced resonance.

9.1. Introduction

Graphene-like gapless linear Dirac-bands, but in odd numbers, on the surface of three-dimensional (3D) [51] topological insulators (TI), with bulk insulating phase, have excellent transport properties. Time-reversal symmetry protects these surface states against any non-magnetic perturbation [241] to ensure high conductivity by

suppressing backscattering, which makes 3D-TI suitable for applications like interconnects [62] and quantum computing [203]. Furthermore, spin-momentum locking[211] for carrier transport in these helical surface states projects TI also as a promising candidate for spintronic applications [63, 280], which gives it an advantage over spin-degenerate dual-valley graphene Dirac-bands. Among the extant 3D-TI, Bi_2Se_3 [71] has the largest bulk bandgap of 0.3 eV [52] which provides large energy window for exploiting these exotic surface states in TI, and hence has been chosen as representative material in this work.

Recently, there has been a surge in device proposals [281-283] to regulate electron flow in Dirac-band materials via band-modulation by filtering out unwanted momentum states. Furthermore, by leveraging on the Dirac-bands of graphene, recently there has been a proposal of the symmetric Field Effect Transistor (SymFET) [284], a novel device with a resonant current peak for an appropriate balance of channel bias (V_{DS}) with Fermi-level (E_f). This device based on vertical tunneling from n-doped layer to p-doped layer, separated by an insulator, is expected to exhibit a large current switching ratio which is symmetrical about resonance peak, at which the Dirac-points (bands) exactly align between two layers (see Fig. 4(b) of Ref. [284]). The device operation has also been shown analytically [284] to be robust against temperature variation. Consequently, this device has been considered as a good candidate for designing high-speed analog multipliers and oscillators [284]. Such high-speed multipliers and oscillators in spintronic circuits would serve an important role in hybrid logic based systems [285] with 3D-TI serving a common platform for components.

In this chapter, therefore, we comprehensively investigate the transport mechanism in band-alignment devices to appraise the possibility of a similar

resonance state in 3D-TI which may serve as an analogue of multipliers and oscillators in the spintronic circuits. For this purpose three different device designs are evaluated, one purely for lateral transport (Design-A) and two for vertical transport (Design-B and Design-C), to operate in the helical surface bands.

Design-A presents a simple understanding of band-alignment concept and explains the effect of mode-matching (electron momentum modes), gate-tunable density of states (DOS) and temperature on transfer characteristics of the device. Design-B emulates the symFET concept in 3D-TI to peruse its assumptions via quantum transport investigation. Although a similar resonant state is observed, its effectiveness is much weaker than originally expected for which reasons have been discussed. Design-C takes the ideal symFET operation to a more practical case on 3D-TI. However, there is a complete loss of resonance in Design-C. Therefore, best results are obtained for Design-A although the current ratio, between resonance state (I_R) and non-resonance state at zero gate voltage (I_0), is still relatively small and the device transfer characteristic is sensitive to temperature. Accordingly, suggestions to further improve the ratio for Design-A are provided.

This chapter is organized as follows. Results and Discussion section discusses the results of our simulations and unravels the effect of band-alignment operation on the carrier transport in 3D-TI devices. This is followed with the summary and conclusions of our study. The Appendix F provides the mathematical proofs of some important concepts discussed in this chapter. Appendix-F.1 gives a brief on the effect of mode mismatch at the contact-channel interface. Appendix-F.2 provides the mathematical insight into band-alignment operation by analyzing the effect of gate potential on the transport through the Dirac-Band. Appendix-F.3 complements the results and discussion of the chapter by expounding on the effect of channel bias on

the transport through all three device designs for the sake of completeness of this chapter.

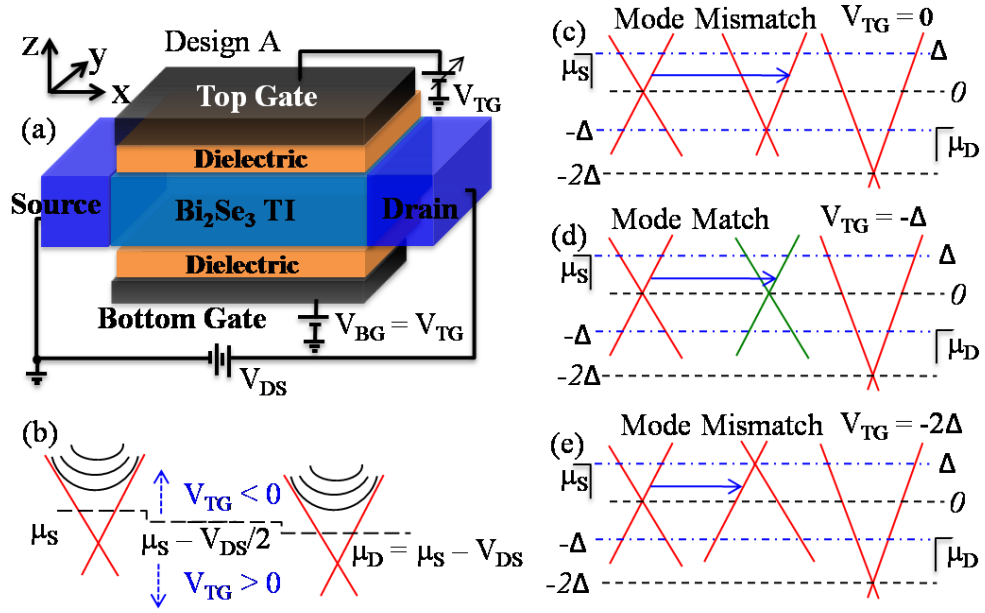

Figure 9.1 (a) Device Structure (Design-A) for quantum transport modeling through Bi_2Se_3 slab with shorted top and bottom gates. (b) Potential distribution along the transport direction. μ_S and μ_D are electrochemical potential at the source and drain end respectively. Gate voltage V_{TG} shifts the potential energy in the channel. Δ represents the energy difference between μ_S and the Dirac-point in the source contact and is used as a reference energy scale throughout this chapter. (c, d, e) Schematic of the band profile along the transport direction (source, channel and drain from left to right) for three different gate voltages, illustrating the mechanism of mode matching. At 0 K transport is within the energy window delineated with blues dot-dashed line. Blue arrows depict ballistic transport along the transport direction with conserved transverse (along y-axis) momentum. Green bands in (d) emphasize the band-aligned condition between source and channel region.

9.2. Results and Discussion

Transport behaviour in three different band-alignment device designs is expounded in this section. For Design-A, the transport is only in lateral direction which makes it easy to understand the band-alignment concept. It is furthermore supported with derivations in Appendix-F.1 and Appendix-F.2 to provide clear insights into the mechanism. Next, we delve into more complex S-shape devices for vertical transport to be in-line with a similar symFET [284, 286] proposal on graphene. The transport mechanism and limitations have also been discussed for each design.

The detailed potential distribution for Design-A and Design-B-C has been elaborated in section for lateral and vertical transport, respectively. The gates are

phenomenologically modeled with a translation factor of one to regulate the potential in the channel. We note that self-consistent solution of channel potential with a Poisson solver would disturb the perfect band-aligned resonant condition. Since, this would both degrade the results and eclipse the transport concepts which we in particular want to stress upon, the Poisson equation has not been exercised in this work. However, if the device performance is to be examined for practical implementation, the NEGF transport must be solved self-consistently with Poisson to correct the charge induced potential variation in the system.

9.2.1 Band-Alignment for Lateral Transport

Figure 9.1(a) illustrates the device structure for Design-A with 13 QL thickness (z-axis) and 30 nm channel length (x-axis) along with semi-infinite contact on either sides of the channel. The sample thickness has been chosen to be sufficiently large so that inter-surface coupling effects are negligible [209] because the surface wavefunction decays to nearly zero beyond 10 QL [200]. Top and bottom gates are shorted to have uniform influence on all layers of 3D-TI slab.

The potential profile along the transport direction is shown in Fig. 9.1(b) to illustrate the equal drop of bias voltage (V_{DS}) at the source and drain terminals and a flat potential in the channel, which shifts the energy-bands in the channel and drain region by $-V_{DS}/2$ and $-V_{DS}$ respectively. An important conceptual point to note here is that the energy bands are strictly defined only in the equilibrium condition i.e. in the absence of channel bias. However, in non-equilbrium, understanding in terms of the shift of energy-bands along the transport direction to follow quasi Fermi-level distribution ia a good approximation and provides simple insights into transport behaviour (see M. Lundstrom, Fundamentals of Carrier Transport: Cambridge University Press, 2009).

Next, also note that because of selenide vacancies [175] a typical sample of Bi_2Se_3 TI is n-doped and a small bias applied to electrically characterize the material for ballistic transport should approximately follow potential distribution of Fig. 9.1(b). Application of gate voltage over such a system would result in a commonly observed ambipolar V-shaped transfer characteristics [172] which are just a signature of Dirac-bands. However, despite of similar device geometry the band-alignment device operates differently as shown in this chapter.

To assay the transfer characteristics of band-alignment device, a channel bias of $V_{DS} = 2\Delta$ (see Fig. 9.1) has been applied across the device, where Δ represents the energy difference between μ_S and the Dirac-point in source contact and is used as a reference energy scale throughout this chapter. Therefore, in equilibrium condition Δ equals Fermi-level (E_f), with zero-energy level calibrated at the Dirac-point. Energy-bands in the channel are shifted by applying the gate voltage (V_{TG}), which configures it from a purely n-doped ($V_{TG} = 0$ volts) to purely p-doped ($V_{TG} = -2\Delta$ volts) state (see Fig. 9.1(c-e)). The resonant condition in this device architecture is achieved at $V_{TG} = -\Delta$, when the bands in the source region are exactly aligned with the bands in the channel so that wavevector modes along both x-axis (k_x) and y-axis (k_y) are conserved resulting in perfect transmission across the source-channel interface. Also, observe that there is a mode-mismatch across the channel-drain interface, and degrades as the V_{TG} is swept from zero to -2Δ. This effect manifests clearly in the transport results which we discuss next.

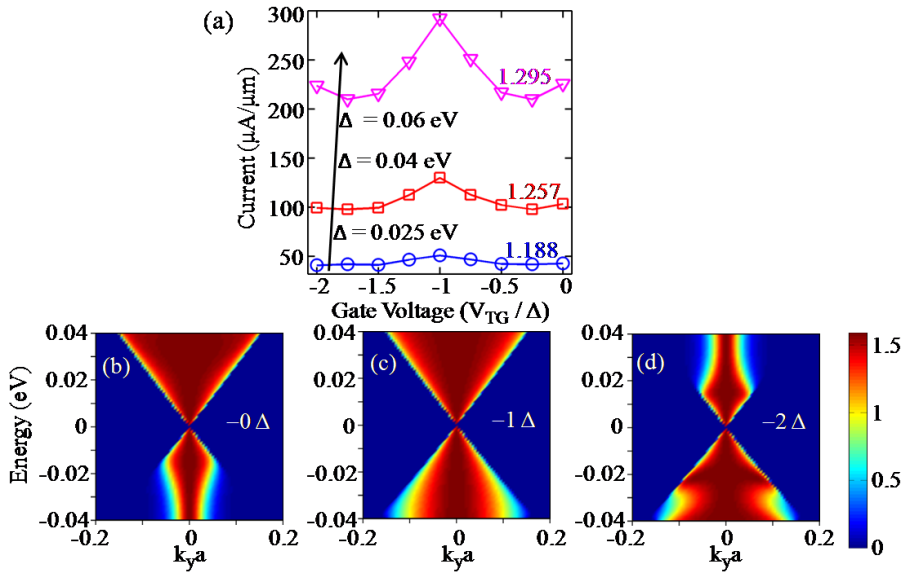

Figure 9.2 Design-A. (a) Operation for 13 QL thick 3D-TI for three different Fermi-Levels in the surface bands (V_{DS} = 2 Δ) at 0 K. Observe the resonant peak at −Δ. I_R/I_0 ratio is defined between V_{TG} = 0 (I_0) and V_{TG} = −Δ (I_R) and stated over each trendline with respective color. (b-d) Transmission spectrum (in per μm) for V_{TG} equal to 0 (b), −Δ (c) and −2Δ (d) at 0 K for Δ = 0.04 eV as a representative case from (a).

Figure 9.2(a) illustrates the transfer characteristics of Design-A. It shows a clear evidence of resonant current peaks at V_{TG} = −Δ (see Fig. 9.1(d)), for different Fermi-levels (E_f). For operation in the linear Dirac-bands, the current increases with the increasing magnitude of E_f because the density of states (DOS) scales linearly with E_f [93] for Dirac bands, which subsequently increases the current (see Eq. (F.1)). Furthermore, I_R/I_0 ratio which is defined between V_{TG} = 0 and V_{TG} = −Δ also increases with the current and becomes more clear at higher E_f.

However, note that since resonance condition requires V_{TG} = −Δ and V_{DS} = 2Δ, further increase in E_f will drive transport energy range into the bulk bands, while for spintronic applications we need to operate in the surface-bands to leverage the spin-momentum locking for electrons. This also shows that a new 3D-TI material in future with a larger bulk bandgap may improve the ratio.

The transport characteristics are further illustrated via transmission spectrums in Fig. 9.2(b-d). Specifically notice the band-alignment with nearly symmetric operation

about the Dirac-point for $V_{TG} = -\Delta$ in Fig. 9.2(c). Next, since the transverse modes (k_y modes) for carrier propagation in the device, which is uniform along the y-axis, should always be conserved [100], the transit from the larger to smaller modes is prohibited and they are filtered out (see Fig. 2 of Ref. [96]). Therefore, light bluish-yellow region in Fig. 9.2(b) and 9.2(d) show significant mode filtering in valence and conduction band region respectively for V_{TG} equal to 0 and -2Δ. Mode-filtering also clearly manifests for valence band region in Fig. 9.2(c) and 9.2(d) because of the mode-mismatch between channel and drain (see Fig. 9.1(c-e)). Although, the mode-filtering may seem unlikely for resonance condition in Fig. 9.2(c), note that unlike graphene, the conduction and valence bands of Bi_2Se_3 3D-TI are not symmetric [52, 200]. Valence band has smaller Fermi-velocity than conduction band. Therefore, there is mode-filtering in low-energy range even at resonance because electrons attempt to transit from large k_y modes of valence band in the channel to conduction band in the drain (see Fig. 9.1(d)) which does not support those modes.

There are two additional observations from the transfer characteristics in Fig. 9.2(a). Firstly, the current at two extremes of V_{TG} (0 and -2Δ) is not equal (higher at $V_{TG} = 0$). Secondly, there is a local minimum on either sides of resonance. The first happens because of mode-mismatch (see Appendix-F.1) between bands in the channel and drain and therefore is strongest for $V_{TG} = -2\Delta$. The effective DOS in the transport energy window between μ_S and μ_D (see Fig. 9.1) is responsible for the second observation, which is mathematically proven in Appendix-F.2. As the V_{TG} is swept from $-\Delta$ to 0 (or -2Δ), the potential in the channel starts to move the higher DOS out of energy window on one end of the energy-grid and replaces it with lower DOS at another end of the grid, which should have resulted in continuous decrease in current. However, the effect of DOS competes with the mode matching between the source

and channel and results in actually higher current at $V_{TG} = -\Delta$. The inflection points mark the transition of dominance of one effect over another.

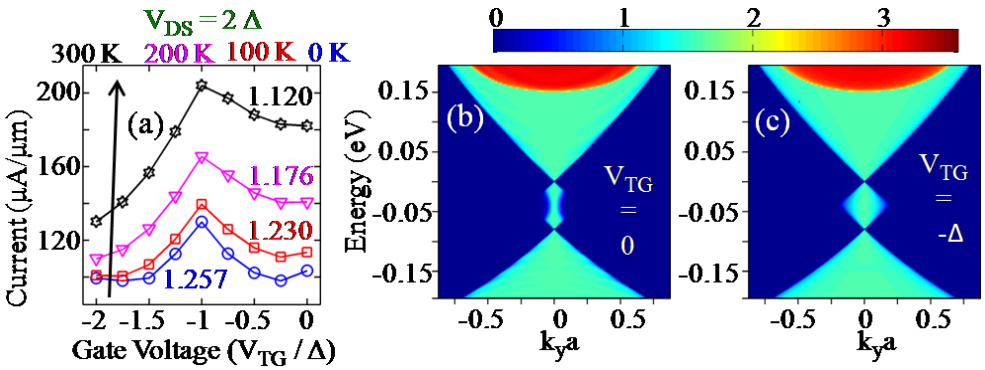

Figure 9.3 Design-A. (a) Current vs gate voltage at 0 K (blue circles), 100 K (red square), 200 K (magenta triangle) and 300 K (black stars) for Δ = 0.04 eV. I_R/I_0 ratio and temperature are stated with respective colors for each trendline. Observe that signature of mode matching is severely weakened due to spread in Fermi-distribution. (b, c) Transmission spectrum (in per μm) for two gate voltages at 300 K. Compare it with Fig. 9.2 to observe the extinction of signature of mode match/mismatch in quantum transport. Dark red region is bulk conduction band.

The effect of temperature on operation of Design-A is next appraised in Fig. 9.3. The temperature results in the spread of Fermi-distribution and therefore results in the inclusion of wider energy range and k_y modes for the transport. This results in more number of energy and transverse modes which suffer mode-mismatch either at the source-channel or at the channel-drain interface, mainly the later one, which results in near complete loss of resonance at 300 K as illustrated in Fig. 9.3(a) by plotting the transfer characteristics and further confirmed via transmission spectrum in Fig. 9.3(b) and 9.3(c) respectively for V_{TG} equal to zero and $-\Delta$.

In the spectrums, observe that the two zero transmission points (blue dots) at zero $k_y a$ correspond to the Dirac-points for bands in the source and drain terminal. The resonance condition for $V_{TG} = -\Delta$ can also be observed by comparing the width of bluish-green region between the two Dirac-points. Furthermore, the bulk conduction band (in red) is more clearly visible than the valence bulk bands (light green-yellow lines) because the Fermi-level is in the conduction band and since the contribution of energy points is weighted by the Fermi-distribution, the transmission

is stronger in the bulk conduction band which are nearer to source electro-chemical potential than in the valence bands. Therefore, precisely the averaging of results over more mode-filtered wavevectors wanes the resonance at higher temperatures. Since the I_R/I_0 ratio falls short of values that can be comfortably measured in experiments, for instance around ten [287], it is important to enhance the ratio.

To improve the I_R/I_0 ratio a mode selective switch should be implemented in the channel or at the source-channel interface to completely filter out the non-normal modes ($k_y \neq 0$). This would in general force the device to operate at only one energy point between μ_S and μ_D at which k_y would be conserved, but at resonance condition electrons would be able to conduct at all the energy points because the band-alignment would enable the k_y conservation at all of the electron energies. This would result in large I_R/I_0 ratio as expected for Graphene symFET in Ref. [284]. To achieve the suppression of non-normal modes, tilted gates or an insulating physical barrier like a lens can be implemented in the channel [142]. Heterostructures [288] is another possibility which can be investigated in the future work.

9.2.2 Band-Alignment for Vertical Transport

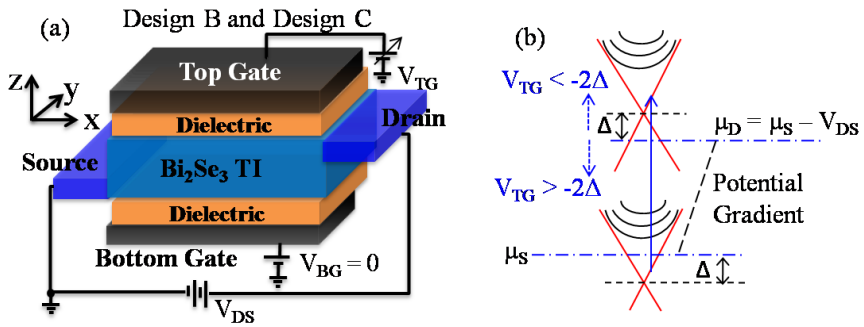

Figure 9.4 (a) Device Structure for vertical transport in 3D-TI. Source is coupled to bottom few layers (bottom slab) and drain to top few layers (top slab). As a representative case, bottom and top slabs are 13 QL each, whereas middle region is 4 QL. Electrons injected from the source have to tunnel through the middle slab for operation in the bulk band gap. For Design-B, the top and bottom gate voltages uniformly modulate the doping electronically in the respective slabs. For Design-C, a more practical scenario for 3D-TI is presented with uniformly n-doped sample. (b) Potential distribution in x-z plane for band-aligned condition. Blue arrow depicts vertical transport from Dirac-bands of bottom slab to that of top slab, tunneling through the middle region. For channel bias, all layers of bottom (top) slab are hold at μ_S (μ_D) electro-chemical potential of source (drain), while a linear gradient is considered in the middle. Gradient for gate potential in Design-B is assumed to be only in the middle region, whereas for Design-C it is from bottom to top layer of the device (across all three regions).

This section investigates two S-shape devices whose architecture is illustrated in Fig. 9.4(a). The semi-infinite source contact is coupled to 13 bottom QLs (bottom slab), while semi-infinite drain to top 13 QLs (top slab) with 4 QLs in the middle (middle slab). Large thickness of bottom and top slab ensure zero value of surface wavefunction in the middle region. Therefore, for operation solely in the surface bands, electrons must tunnel through the bulk bandgap to transit from source to drain.

Next, for Design-B, the top and bottom gate voltages uniformly modulate the doping electronically in respective slabs. For the channel bias V_{DS}, all layers of bottom (top) slab are hold at μ_S (μ_D) electro-chemical potential of the source (drain), while a linear gradient (vertically) is considered in the middle. Note that the physical isolation of layers with contacts on either ends should hold the potential closer to respective contact electrochemical potentials [289, 290], in contrast to Design-A in which both sides of the channel were equally coupled to contacts across all layers and hence had equal drop at both ends (see Fig. 9.1(b)). Nonetheless, the precise drop at contacts should be computed by solving poisson equation self-consistently which has been explicitly not done as explained above.

Gradient for gate potential in Design-B is assumed to be only in the middle region which ensures degeneracy for both the Dirac-bands in source and drain region each. The potential-profile for Design-B warrants that there is absolutely no mode mismatch between bottom (top) layer surface band of source (drain) and bottom (top) slab of the channel. The bottom gate is grounded and top gate voltage is applied to achieve band-alignment condition of resonance which is now expected at $V_{DS} = 2\Delta$ and $V_{TG} = -2\Delta$ because potential in top and bottom slab is assumed to be on par with electrochemical potential of the respective contacts, instead of fifty-percent drop as considered for Design-A. Therefore, for operation of Design-B, doping in the top slab,

including drain contact to eliminate mode-mismatch at the top slab-drain interface, is regulated by an electronic equivalent of V_{TG} value (see Fig. 9.4(b)). This profile is necessary to emulate the scenario similar to graphene symFET [286] for perfect resonant transmission from the bottom Dirac-band to the top Dirac-band.

For Design-C, a more practical scenario for 3D-TI is presented with a uniformly n-doped (de-facto sample) material because experimentally, at least at present to the best of our knowledge, it should be difficult to precisely control the doping to specific layers in 3D-TI. The gate potential gradient is taken from bottom to top layer of device (across all three regions) (see Fig. 9.4(b)) to follow an expected setup. Such a profile, however introduces mode-mismatch at the top slab-drain interface, as well as, at the top layer of the source contact and the bottom slab.

The purpose of having two device designs is to first via Design-B examine the symFET operation comprehensively through quantum transport, to go beyond the analytical evaluation in Refs. [284, 286], and then via Design-C assess its feasibility in 3D-TI because the relaxed and more realistic gate potential gradient in an n-doped sample may deteriorate band-alignment operation.

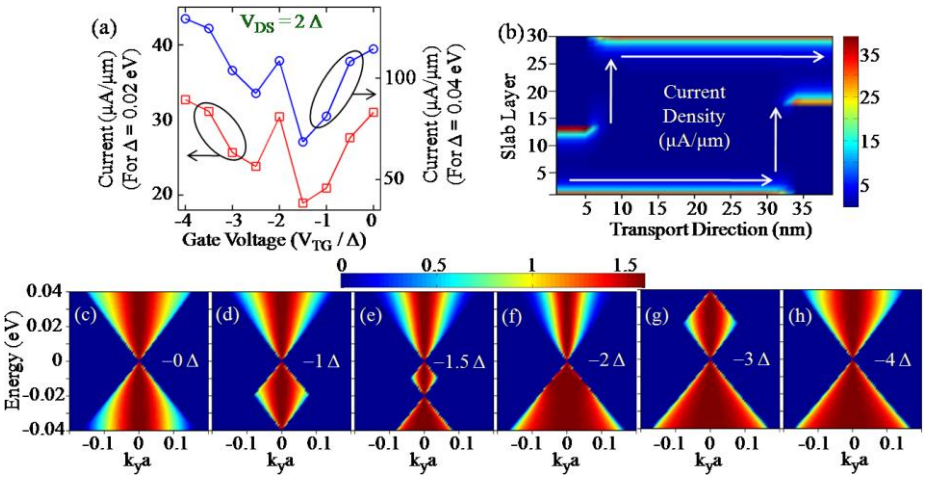

Figure 9.5 Design-B. (a) Current vs top gate voltage at 0 K for Δ = 0.02 eV (red squares) and Δ = 0.04 eV (blue circles). Observe the resonant condition at $V_{TG} = -2\Delta$. (b) Illustration of current flow in the device. Observe that the current mainly flows laterally (along x-axis) on top and bottom surface but is forced to transit vertically (z-axis) at the device boundary. (c-h) Transmission spectrum (in per μm) for V_{TG} equal to 0 (a), −Δ (b), −1.5Δ, (c) −2Δ (d), −3Δ (e) and −4Δ (f) at 0 K for Δ = 0.04 eV as a representative case from (a).

Figure 9.5(a) illustrates the transfer characteristics of Design-B. It shows a clear evidence of resonant current peaks at $V_{TG} = -2\Delta$, for two different Δ values. Since, larger Δ also enforces higher Fermi-level for the band-alignment devices discussed in this chapter, a larger current is observed for $\Delta = 0.04$ eV (red-squares) than for $\Delta = 0.02$ eV (blue circles) because higher E_f also results in transport through energy range with larger DOS (see Eq. (15) of Ref. [93] or Eq. (F.2)). However, interestingly Fig. 9.5(a) also illustrates very strong asymmetry about resonant condition, with larger current for more electronegative gate potentials in strong contrast to Design-A which shows lower current for similar condition.

To analyze this anomaly, Fig. 9.5(b) illustrates the current spectrum in the device. Its ordinate axis represents the QLs of the device (z-axis) while abscissa denotes lateral direction (x-axis). The reddish-yellow color shows the region where current is mainly concentrated in the device while arrows mark the region where most current transits vertically from bottom to top slab. Observe that current flows vertically mainly at the device boundary, otherwise it flows laterally (in-plane) along x-axis. This is in sharp contrast to graphene symFET in which the transport is assumed to be only along the z-axis [284]. In symFET, if the current flow is only along the z-axis, then both k_x and k_y wavevectors together constitute the transverse modes (net magnitude equals root of sum of square of both wavevectors), and their conservations acquiesce just one energy point between μ_S and μ_D for conduction in the non-resonant state and through the entire energy grid for resonant condition resulting in a sharp resonance peak.

Since, NEGF quantum transport simulation in Fig. 9.5(b) shows current flow along x-axis as well, the result implies that only k_y wavevector must be conserved, analogous to Design-A. A strong resonance peak therefore may not be expected for

such a system. Other implications from current distribution in Fig. 9.5(b) are that firstly the transfer characteristics should strongly be regulated by lateral transport and secondly the vertical tunneling based band-alignment effect may be weaker than initially anticipated. Nevertheless, note that the perfect mode-matching atleast at the contact-channel interface for both the top and bottom slabs simplifies the transport mechanism with respect to Design-A.

Furthermore, to advance the understanding of the asymmetry in transfer characteristics, Transmission spectrums for a few V_{TG} values are illustrated from Fig. 9.5(c-h) for increasingly negative values. The dark blue spot at 0 eV energy in all spectrums corresponds to the Dirac band for the source contact and the bottom slab, whereas the other dark blue dot for $k_y = 0$ in Fig. 9.5(d-h) is consistent with movement of the Dirac-band in the drain contact and the top slab (see Fig. 9.4(b)). For analyzing these spectrums, recall that valence bands in 3D-TI have lower Fermi-velocity than in conduction bands. Therefore, DOS is higher in valence band region (see Eq. (F.2)), which results in wider energy-dispersion.

For Fig. 9.5(c), the transport in low energy range is from wider valence band region to more steep conduction band region, which results in mode-filtering (see clipped light blue region in low energy range). All transverse modes are perfectly filtered out at the energy value corresponding to Dirac-point in the top-slab. Red region in spectrum for $V_{TG} = -2\Delta$ in Fig. 9.5(f) shows the band-alignment condition which clearly evinces the largest transmission in comparison to Fig. 9.5(d), 9.5(e) and 9.5(g).

However, also recall from the discussion for Design-A and the proof in Appendix-F.1 that a band-aligned condition results in the lowest DOS configuration in transport energy window. The lateral transport in top layer in high DOS region of

conduction band for V_{TG} = 0 and even higher DOS of valence band for V_{TG} = −4Δ, results in even higher transmission (see Fig. 9.5(c) and 9.5(h)) and current than the resonant condition. Larger DOS in valence bands is also a precursor for the asymmetry observed in Fig. 9.5(a) (see Eq. (F.1)). Therefore, although we observe resonant condition in Design-B, the multi-mode conduction and dominance of DOS effect due to lateral transport does not position Design-B as a switch.

Figure 9.6(a) illustrates the transfer characteristics of Design-C for two different Δ values and does not show any resonance behavior. The current is higher for larger Δ for the same reason as Design-B above. However, the lowest current point is not at V_{TG} = −2Δ as would have been expected for operation in low DOS configuration for the band-aligned condition. The current distribution in Design-C is qualitatively same as illustrated for Design-B in Fig. 9.5(b); vertical transport is chiefly at the device boundary.

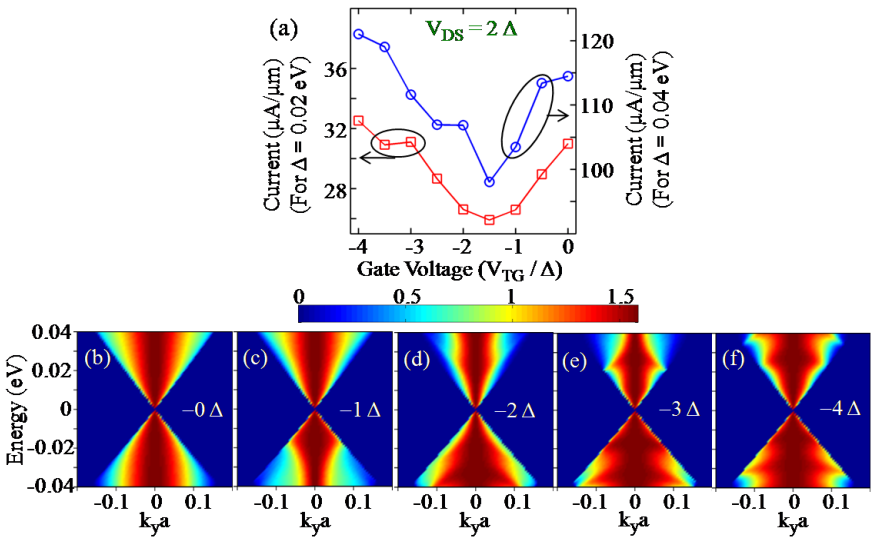

Figure 9.6 Design-C. (a) Current vs top gate voltage at 0 K for Δ = 0.02 eV (red squares) and Δ = 0.04 eV (blue circles). Observe the absence of resonance condition at V_{TG} = −2Δ. (b-f) Transmission spectrum (in per μm) for V_{TG} equal to 0 (b), −Δ (c), −2Δ (d), −3Δ (e) and −4Δ (f) at 0 K for Δ = 0.04 eV as a representative case from (a).

Therefore, we follow a similar approach to understand these observations, by investigating DOS and mode-matching via Transmission spectrum in Fig. 9.6(b-f) for

increasingly electronegative V_{TG}. For Fig. 9.6(b) at $V_{TG} = 0$, there is absolutely no difference between Design-B and Design-C, however subsequent application of V_{TG} in Design-C does not affect the doping in drain contact and it retains same doping as the source terminal. Therefore, V_{TG} now introduces strong mode-mismatch at the drain-channel interface which degrades further for the larger magnitudes of V_{TG}, a problem similar to Design-A. Besides, the DOS in the transport energy window and band-alignment for Dirac-bands of the top and bottom slab vie for the effective results.

For $V_{TG} = -\Delta$, bands in the bottom slab, top slab and drain are positioned similar to Fig. 9.1(c) for Design-A and therefore Fig. 9.6(c) shows mode-filtering through yellowish arc in the valence band similar to Fig. 9.2(b). The surrounding light blue region results from near-perfect lateral transport from the source contact to the bottom slab because there is no mode-mismatch at bottom most layer of the device, although there is a minor mismatch at top of the bottom slab due to the gate-potential gradient.

Next, Fig. 9.6(d) illustrates the band-alignment condition in Design-C (see Fig. 9.1(d)). It is this band-alignment operation between the bottom and top slab which results in slightly higher current than $V_{TG} = -1.5\Delta$ in Fig. 9.6(a), for an otherwise operation in the lowest DOS configuration (see note for Design-C in Appendix-F.2). Figure 9.6(e) illustrates mode-filtering scenario in Design-C, a case similar to Fig. 9.1(e) and its corresponding spectrum in Fig. 9.2(d) of Design-A (compare yellow arc in the conduction band). The light blue region is again due to near-perfect lateral transport in the bottom slab. As V_{TG} is further increased, the red-region in Fig. 9.6(f) reveals the high DOS states of valence band and predicts an increase in the current through the device which is observed in Fig. 9.6(a). Therefore, from transmission spectrum we understand that Design-C inherits few characteristics of both Design-A

and Design-B, in which vertical and lateral transport, band-alignment between the top and bottom slab and mode-mismatch at contact-channel interface have to be analyzed simultaneously to understand its transfer characteristics.

Finally, we would like to note that our model indeed shows side surfaces as illustrated in Fig. 1 of our previous work [200] (see section 2.1.2). However, since the thickness of each slab, we consider, is only 13 QL (and additional intermediate slab of only 4 QL for Design-B and C), the strong confinement effect along the z-axis destroys topological side surface states. The previous studies on side-surface for energy-dispersion [77] and transport [291] had considered this axis to be infinite or semi-infinite. Similarly, experimental works to claim evidence of quantum transport through side-surfaces were performed on extremely thick Bi_2Se_3 nanowire (140 nm in Ref. [260] and 200 nm in Ref. [292]). In fact, if a similar strong confinement were applied along the y-axis, the topological states on the top and bottom surfaces should also be destroyed.

9.3. Conclusion

In summary, this chapter expatiates on the concept of band-alignment or mode-matching induced resonance to examine the feasibility of a resonant device for Bi_2Se_3 3D-TI, a spintronic material. The three different device-designs are evaluated for this purpose. Design-A, which is based only on lateral transport, shows that operation in low DOS energy-range at resonance competes with mode-matching and mode-filtering to manifest the observed transfer characteristics. It is found that despite of a resonance peak, the I_R/I_0 ratio is not very exciting. The degradation of the ratio is chiefly because the transport in non-resonant condition is not exactly limited to one energy point between contact electro-chemical potentials (μ_S and μ_D) as may be expected for Graphene symFET. Therefore, the solutions to limit the transverse

modes for improving the device performance have been suggested for future improvements.

It is also observed that the rise in temperature degrades the resonance behaviour because of averaging over wider energy and k_y modes with mode-mismatch. In Design-B and Design-C the vertical and lateral transport, band-alignment between the top and bottom slab and mode-mismatch at contact-channel interface have to be analyzed simultaneously to understand its transfer characteristics. Design-B although exhibits a resonance peak, is found to be less effective than Design-A. Design-C which could be a more realistic implementation on 3D-TI; there is a complete loss of resonance peak. Therefore, as a future direction we suggest to further improve the Design-A design to enhance the ratio for implementing spintronic circuits using 3D-TI.

Chapter 10

Conclusion and Future Works

This chapter summates the notable contributions of the thesis and their implications. Subsequently, the extant problems in the carrier transport in the Dirac-band materials that can be approached based on the understanding and results of thesis are explained.

10.1. Conclusions

In this thesis, firstly the motivation for investigating carrier transport in Dirac-band materials and their devices is promulgated. The electronic model is subsequently provided for exemplar materials investigated in this work and the NEGF algorithm used for developing quantum simulator is then summarized.

A computational comparison of device performance for two proposed Graphene electro-optic transistors was then evaluated to examine a non-conventional approach of achieving high current-switching ratio in gapless Dirac-bands without actual bandgap opening that degrades the material properties. The calculated results show that the two designs are functionally similar and are able to provide sub-threshold slope smaller than 60 mV/decade at the room-temperature, which is extremely important for low power devices. Both designs showed similar device performance but marginally top one another under different operating constraints. These results serve as a guide to circuit designers in selecting the appropriate design as per their system specifications and requirements.

Then charge and spin transport in 2D Group-IV monolayer materials, with spin-orbit coupling (SOC), in quantum spin hall (QSH) phase (which renders them as

2D-TI) for an extremely efficient three-terminal Y-shaped spin-separator was investigated. It demonstrated the separation of unpolarized current at the source terminal into spin-polarized current of opposite polarity at the two drain terminals. It was shown that by applying magnetic or differential electric field (λ_V) orthogonal to the channel plane it is possible to preferentially steer current between the two drains to create a differential charge current with complementary spin polarization, thus enabling a convenient regulation of the output signal for spintronic applications. However, λ_V may drive the system from the QSH-phase to the band-insulator (BI) phase, and more easily for the materials with small SOC like silicene and germanene.

Nonetheless, Y-shape induced Fano interference, because of the physical bending in the path of the electron flow (edge-transport), in the quantum transport which decimated the transmission, and conductance, on transition from the spin-polarized to the unpolarized energy levels. Therefore, the effect of phase-transition from the QSH to BI-phase was next investigated in U-shape device which does not have geometrical bends in the operational region. This helped in understanding the effect of phase-transition on the current magnitude and its spin-polarization, and the effect was found to be stronger for materials with smaller intrinsic SOC. Moreover, the device length and the area under field were shown to critically affect the device characteristics on phase change. These results are important for designing spin-devices from Group-IV monolayers.

The quantum transport was then comprehensively investigated in Bi_2Se_3 3D-TI slab, with the inclusion of acoustic phonon scattering, in which bulk and surface states were modeled realistically. Resistivity computed across different temperatures, slab thickness, bias and strengths of the electron-phonon coupling at various doping levels provided a handle on how various factors interact and compete to determine the

overall resistance of the slab, a remarkably complex behavior. This investigation explained the contradictory trends reported in transport experiments on Bi_2Se_3. Furthermore, an experimental strategy was suggested for obtaining a handle on the strength of electron-phonon coupling, which is disputed over five orders of magnitude, in topological insulators via temperature-dependent transport measurements.

The effect of different contact configurations on quantum transport through Bi_2Se_3 3D-TI slab was then investigated for deeper understanding of carrier transport in 3D-TI. The results were applied to explain another experiment on electrical detection of spin-momentum locking on topological surface, and another simple mechanism to validate topological insulators via quantum transport experiments was proposed.

The carrier transport investigation was then furthered by examining the feasibility of using thin 3D-TI (Bi_2Se_3) wire for the local electrical interconnects, as a replacement of Cu for future chips, in the presence of edge roughness, vacancies, acoustic phonons and charge impurities across temperature and Fermi-level, via full real-space simulation on GPGPUs. It was found that because of the scattering induced by the acoustic phonons, the mobility reduces considerably at the room temperature which complemented with the low density of states near Dirac-point does not position Bi_2Se_3 3D-TI as a promising material to replace Cu for local interconnects. The properties required in suitable TI material for this application were also discussed.

Finally, an investigation of band-alignment induced current modulation in Bi_2Se_3 3D-TI slab for three different device designs, one for purely lateral transport and other two with vertical transport, was appraised for the possibility of a 3D-TI based resonant device. A resonance condition was indeed observed when the Dirac-points (bands) were aligned. This resulted in the maximum current at the resonance

for the design with only lateral transport. However, current ratio between resonant and non-resonant condition was found to be relatively small and strong temperature dependence was also noticed. The other two designs with vertical transport had degraded transfer characteristics, although from state-of-art literature they are expected to manifest nearly an ideal resonance peak. The physical insights for these observations had been posited along with the suggestions for attaining close to an ideal operation for the first design. These results are important for understanding the electronic behaviour of 3D-TI for designing topological insulator devices.

Therefore, this thesis helped in understanding the carrier transport in Dirac-band materials and some of their prospective devices that should assist in developing next generation of low-power computing systems.

10.2. Future Works

Based on this work following research directions are suggested.

10.2.1. Valley-Valve effect in 2D Group-IV monolayers

The Y-shape and U-shape spin-separators, discussed in **Chapter 4 and 5** respectively, based on 2D group-IV monolayers exhibit sharp decline in both conductance and spin-polarization for large channel bias ($>\lambda_{SO}$) when their Fermi-level is at the Dirac-point. There is a maximum operation window of $2.\lambda_{SO}$ for spin-polarized transport but the deleterious conductance roll-off beyond it limits the device applicability. The initial investigation reveals that beyond $\pm\ \lambda_{SO}$, the transport of electron from the first conduction band (CB) to the valence band (VB) or vice versa is prohibited. This band selective transport called Valley-Valve Effect [293, 294] is peculiar to the zigzag nanoribbons of atleast Group-IV monolayer elements.

To enable transport across pair of prohibited bands, the symmetry along the width must be broken, which is done by spin-orbit coupling in $\pm\ \lambda_{SO}$ energy-range

about the Dirac-point. To break this symmetry over the entire energy range anti-zigzag nanoribbon should be considered. This would provide larger conductance and hence larger spin-polarized current for the spin-separator device. Therefore, for future work it is suggested to comprehensively examine the Valley-Valve effect in presence of spin-orbit coupling in Group-IV monolayers and subsequently examine the performance of spin-separator device.

10.2.2. Threshold of Scattering Angle on the Topological Surface

The thesis shows the conspicuous role of sub-surface layers in the carrier transport, a point which is missed in simple 2x2 Dirac equation based transport studies. In **Chapter 8** the investigation of the defects like impurities and vacancies in 3D-TI furthermore show that in sizable concentrations they can impede the carrier transport at low temperatures. Fundamentally, time-reversal symmetry (TRS) for surface states prohibits only backscattering. Similarly, scanning tunneling microscopy (STM) investigation [295] show that despite of operation in bulk band gap the surface states may interfere with bulk continuum states to effectuate very strong scattering. However, another recent study of STM on $Bi_{1.5}Sb_{0.5}Te_{1.7}Se_{1.3}$ 3D-TI [59] claims that electrons cannot be scattered over 100^{o} for transport in 3D-TI, and hence there is a robust protection from backscattering for operation in surface bands. Therefore, as a natural extension of the thesis it is imperative to investigate the strength of the scattering and the threshold of scattering angle for operation in the surface bands. There is a need to theoretically demystify the experimental observations for understanding the precise scattering mechanism on topological surfaces.

To investigate the stated problem, evolution of decoherence [296] should be studied by computationally injecting the wave-packet and tracking its trajectory and

dephasing after the scattering event for statistically reasonable samples. Wigner-Boltzmann transport (WBT) [83] equation should be solved ideally in three-dimensional space but this is computationally prohibitive. However, solving WBT for 2D surface [297] using simple Dirac equation may give a good first order understanding of the scattering physics in this system.

10.2.3. Obtain Real-Space spin-texture on Topological Surface

The helical surface states of the 3D-TI have spin-momentum locking which results in a spin-texture in the momentum space. The spintronic devices, based on the electric and magnetic field control, however manipulate spins in the real-space. To map spins from the momentum to the real-space, we speculate Corbino geometry with radial transport to be a good system for investigation [298, 299]. This would be an extension of real-space modeling of 3D-TI computed on GPGPUs in **Chapter 8** because of the contacts in the centre and periphery [300]. The transport should result in spin-vortex whose chirality depends on the polarity of the drain terminal for a grounded source terminal. The chirality may further be used for manipulating information, for instance in optospintronic applications, or to represent a digital bit in a spintronic system.

10.2.4. Effect of Strain

Strain in a material can be induced due to various factors like lattice constant mismatch with substrate (or adjacent layers) and thermal effects or it can be artificially engineered to modify device properties. It becomes especially important for TI because after certain strain (4-6% for Bi_2Se_3 [301, 302]), TI loses topological behavior. Therefore, careful selection of adjacent materials has to be done to ensure that strain more than a critical value is not induced. However, strain can be used to

increase bulk bandgap [301, 303] and enhance the effective contribution of topological states. Moreover, strain has been shown to modify spin and charge properties of Topological Insulator [304, 305]. To study the effect of strain, TBM parameters, akin to section 2.1.2, for the Hamiltonian have to be extracted from ab-initio simulations for each given strain value and plugged into the quantum transport simulator developed in this work for 3D-TI.

Appendix A

Derivation of Gate-Voltage for I_{OFF} in Chapter 3

Source is externally connected to anode of battery and therefore injects electrons into graphene channel, whereas drain is connected to cathode and collects the electrons. Therefore, current flows from drain to source via graphene channel, which is electrostatically segmented into two parts, each of which is controlled by different gate voltage over it i.e. V_{G1} and V_{G2}.

In unbiased state, electrochemical potential of entire graphene channel (μ_1 and μ_2), source (μ_S) and drain (μ_D) is in equilibrium ($V_{eq}=0$ *V*) i.e. at same level. When we apply a small positive drain to source voltage V_{DS}, μ_S remains at V_{eq} but μ_D moves down to $V_{eq}-V_{DS}$. μ_S and μ_D move down to $V_{eq}-V_{DS}/2$. Now, if capacitive gate transfer factor is 'α' for both gates (taken to be one in this simulation), then application of gate voltage changes electro chemical potentials to $V_{eq}-\alpha V_{G1}-V_{DS}/2$ and $V_{eq}-\alpha V_{G2}-V_{DS}/2$ for segment 1 and 2 respectively. In our simulations, we have considered V_{eq} to be zero because all the voltages used in equations are relative to $V_{eq.}$ Note that all energies are in eV. The set of equations we have used is described as follows.

Relative refractive index,

$$\eta_{21} = \frac{E-(V_{eq}-\alpha V_{G2}-V_{DS}/2)}{E-(V_{eq}-\alpha V_{G1}-V_{DS}/2)} \qquad (A.1)$$

where, E is injected electron energy in eV.

Transmission probability [96] across electrostatically separated graphene segments,

$$T(E) = A_1 \frac{\cos\theta_i \,.\cos\theta_r}{\cos^2\left(\frac{\theta_i+\theta_r}{2}\right)} \qquad (A.2a)$$

for design-A: $A_1 = \Theta(\theta_C - |\theta_i|).\Theta(|\theta_i| - |\theta_B|)$ $\qquad (A.2b)$

for design-B: $A_1 = \Theta(\theta_C - |\theta_i|) = \Theta(|\theta_C| - |\delta|)$ $(A.2c)$

where, Θ is unit Heaviside step function.

Drain current for ballistic transport is given as follows,

$$I_D = \frac{2q}{h}\int dE\,\frac{h\,D(E)\,v_F}{2\,L}\,T(E)\,(f_S(E) - f_D(E))$$

$$\Rightarrow \frac{I_D}{W} = \frac{2q}{h}\int dE\,\frac{\pi\,\hbar\,D(E)\,v_F}{W\,L}\,T(E)\,(f_S(E) - f_D(E))$$

where, density of states/area,

$$\frac{D(E_{DOS})}{W\,L} = \frac{1}{2\,\pi\,\hbar^2\,v_F^2}\,|E_{DOS}|$$

$$\Rightarrow \frac{I}{W} = \frac{2q}{h}\,\frac{1}{4\,\pi}\,\frac{1}{\hbar\,v_F}\int dE\,|E_{DOS}|\,T(E)\,(f_S(E) - f_D(E)) \qquad (A.3)$$

where, $E_{DOS} = \min(E - (V_{eq} - \alpha V_{G2} - V_{DS}/2), E - (V_{eq} - \alpha V_{G1} - V_{DS}/2))$.

Note that, in general, above E_{DOS} approximation is valid only if difference in two compared values is large. Nevertheless, it gives a qualitative picture and in fact holds good for ballistic model even quantitatively in purview of our simulation constraints.

For symmetrically placed barrier ($\phi = \theta_B$ in design-A) and gate inclination ($\phi = \delta$ in design-B), range of energies E_1 to E_2 blocked are given by [96],

$$+\sin\phi = \frac{E_1 - (V_{eq} - \alpha\,V_{G2} - V_{DS}/2)}{E_1 - (V_{eq} - \alpha\,V_{G1} - V_{DS}/2)}; \qquad -\sin\phi = \frac{E_2 - (V_{eq} - \alpha\,V_{G2} - V_{DS}/2)}{E_2 - (V_{eq} - \alpha\,V_{G1} - V_{DS}/2)}$$

$$E_1 = V_{eq} - \frac{\alpha(V_{G2} - V_{G1}\sin\phi)}{1 - \sin\phi} - \frac{V_{DS}}{2}; \qquad E_2 = V_{eq} - \frac{\alpha(V_{G2} + V_{G1}\sin\phi)}{1 + \sin\phi} - \frac{V_{DS}}{2}$$

$$\Rightarrow \Delta E = E_1 - E_2 = BandGap = \frac{2\alpha(V_{G1} - V_{G2})\sin\phi}{\cos^2\phi} \qquad (A.4)$$

Moreover, analytically I_{OFF} will correspond to V_{G2} at which barrier angle blocks maximum of Fermi distribution i.e. when E_1 and E_2 are symmetrical about the

peak for '$f_S(E)$-$f_D(E)$' which lies at $(-V_{DS}/2)$. Therefore, E_1-$(-V_{DS}/2)$=$(-V_{DS}/2)$-E_2. Therefore, corresponding V_{G2} is given as,

$$V_{G2} = V_{G1}\sin^2\phi + \frac{(V_{eq})}{\alpha}\cos^2\phi \qquad (A.5)$$

Since, V_{eq} is taken to be zero, Eq. (A.5) implies non-zero V_{G2} for I_{OFF}, which is a drawback given the voltage levels of contemporary switching logic.

However, if we physically eliminate V_{G1} and chemically dope the graphene channel [98] to V_{dope} in equilibrium unbiased state, than

$$V_{G2} = -V_{dope}\cos^2\phi + \frac{(V_{eq})}{\alpha}\cos^2\phi \qquad (A.6)$$

This still leads to non-zero V_{G2} corresponding to I_{OFF}.

On the other hand, if we retain V_{G1} along with doping V_{dope}, then Eq. (A.5) becomes,

$$V_{G2} = V_{G1}\sin^2\phi - V_{dope}\cos^2\phi + \frac{(V_{eq})}{\alpha}\cos^2\phi \qquad (A.7)$$

Now, it is possible to attain zero V_{G2} for I_{OFF} by tuning V_{dope} for given specification of V_{G1} and ϕ. Moreover, we can have top gate, with transfer factor 'β', as compensation pin to tune the operating logic voltages such that,

$$V_{dope} = \frac{(V_{G1} - V_{G2})}{\beta}\tan^2\phi - \frac{V_{G2}}{\beta} + \frac{(V_{eq})}{\alpha\beta}\cos^2\phi \qquad (A.8)$$

Note that for chemical doping we have taken β to be one.

Appendix B

Supplementary for Chapter 4

Appendix-B.1 on Local Density of States (LDOS) shows DOS distribution (color scale is per eV) in the Y-device as a visual aid for developing an intuitive understanding of the device operation. Appendix-B.2 on transmission helps in comprehending results presented in this chapter. Appendix-B.3 serves as a supplementary for visualizing the concepts pertaining to the effects of the buckling field and magnetic field on the device operation by illustrating spin distribution in the device.

B.1. Local Density of States Distribution for 14 cell wide Y-shaped Device

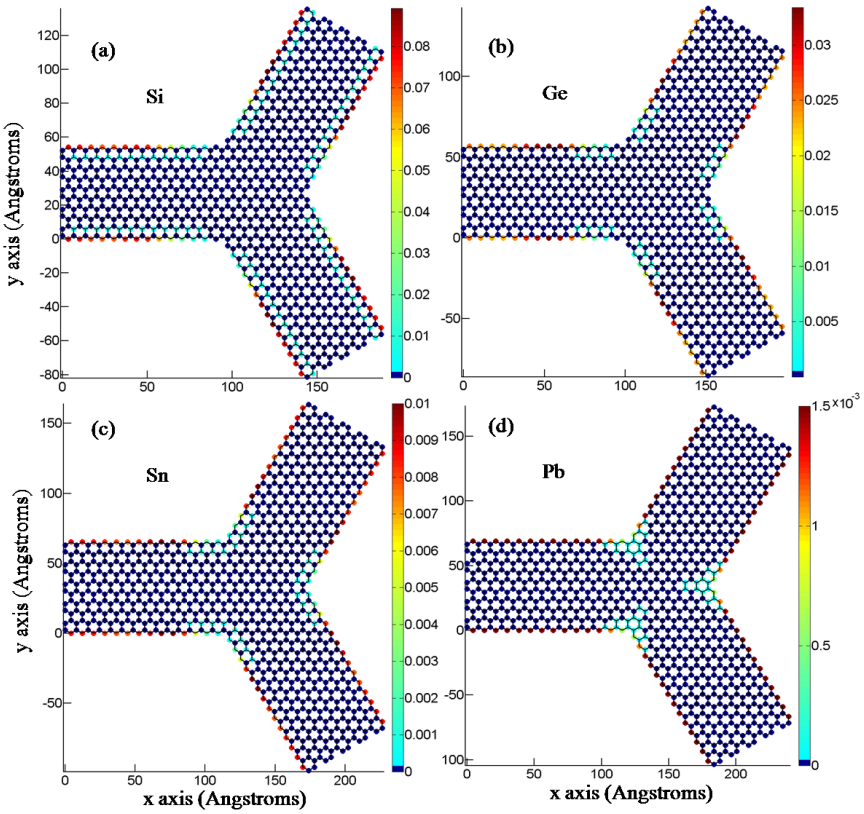

Figure B.1 5-cell wide device for the configuration of Figs. 4.2 (a, d), i.e. E_f = 1 meV and V_{BA} (V_{CA}) = 1 mV. Note stronger confinement towards the edges on all three arms, observed from relative distribution of red region in individual plots, as the intrinsic spin orbit coupling (λ_{SO}) strength becomes progressively stronger from (a) to (d).

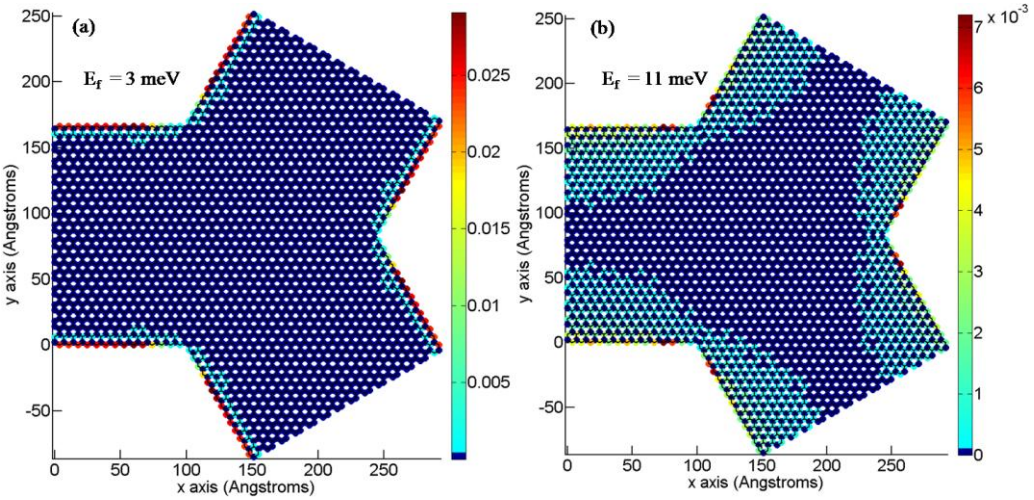

Figure B.2 Ge device corresponding to Fig. 4.2(c, d), i.e. 1 mV bias for two Fermi-levels (E_f).

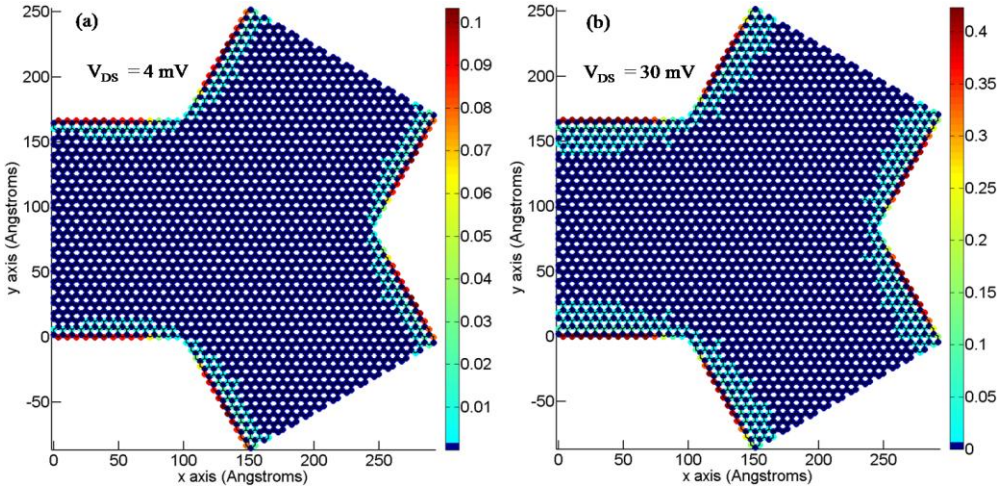

Figure B.3 Ge device corresponding to Fig. 4.2(e, f) i.e. E_f = 5 meV for two bias (V_{DS}).

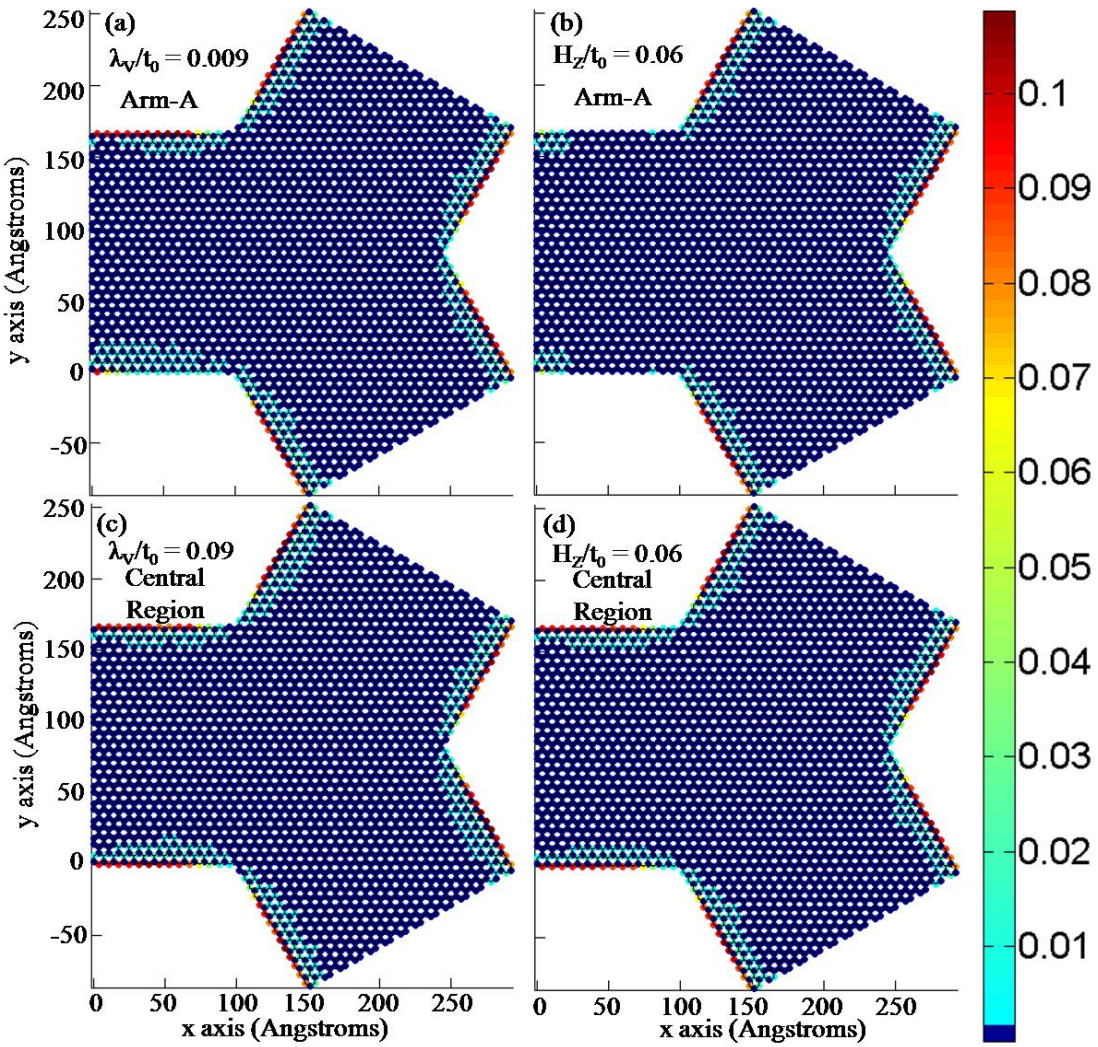

Figure B.4 Ge device corresponding to Fig. 4.3, i.e. E_f = 5 meV and bias = 4 mV.

B.2. Transmission in Equilibrium Condition

Figure B.5(a) shows T(E) for a two-terminal Ge-NR strip. The points of inflection and the magnitude can be easily matched against the band edge and mode density, respectively. Figs. B.5(b-f), however, illustrate T(E) from Arm-A to Arm-B for a Y-shaped device where SOC is switched off in Fig. B.5(b). The explanation for this is as follows.

Bending of the channel results in interference in the propagating modes at all energies due to the wave nature of the electrons. A similar study has been performed on a tapered nanographite channel previously [306] to discuss these interference effects. Ref. [307] shows that even a small bend in the strip geometry (broken strip

geometry) induces quantum interference. Quantum interference results in the bound states below the eigenvalues for a curved strip [308, 309]. These bound states interfere with the continuum states of propagating modes, i.e. the Fano resonance [162] to yield dips observed in T(E).

For Y-shape device, without SOC, there is destructive interference (Fig. B.5(b)). The presence of SOC in 2 λ_{SO} energy range, however, provides an additional phase-shift resulting in constructive interference which results in near unity transmission from $-\lambda_{SO}$ to $+\lambda_{SO}$, with gradual degradation towards the edges of the energy-grid. Beyond, this energy-range, destructive interference is again evident in Fig. B.5 for Group-IV materials with SOC, and T(E) joins as a continuous curve along the energy-axis for unpolarized states with low transmission. The application of buckling-field (λ_V) and/or Zeeman-field (H_Z) not only shifts the spin-polarized bands, it also induces additional phase-shift for electrons propagating at different energies and corresponding wavelengths. Therefore, the application of these fields improves the transmission in regions of destructive interference and degrades it in energy-regime of constructive interference. The effect of these fields is symmetrical (asymmetrical) on the edges in the absence (presence) of SOC. The U-Shape device in Chapter 5 also evidences this effect but it is much weaker and less noticeable because of less acute bends in the channel, and becomes even less noticeable for two-terminal strip, with complete absence if SOC is artificially switched-off in two-terminal geometry. This last case is a more common scenario in many materials of interest and hence integer transmission at equilibrium is reported in them. Hence, unlike simple systems of non-SOC materials without any bends or curvature in the channel, the devices of Chapter 4 and 5 belong to category of Quantum-Interference Devices (QIDs) [310]. Therefore, in devices of Chapter 4 and 5, the equilibrium transmission strongly depends on the

device geometry and hence induced interference patterns, SOC, electron injection-energy, channel-width (affects coupling between wavefunctions apparently localized on the opposite edges), mode-mismatch induced due to band-shifts and phase-transition in Group-IV materials due to buckling and Zeeman fields. The spin-polarization of the carriers is affected accordingly and may seem counter-intuitive if predicted just based on shifts in the energy-bands. Next, on application of channel bias, the non-equilibrium condition additionally shifts the quasi Fermi-level across the channel and further modifies the results. These devices thus need pure quantum mechanical treatment as did in this work via NEGF to explain and predict transport results. In the chapters, however, we have either just reported the observations or limited the discussion to the shift in the bands under influence of fields and the phase-transition to help reader develop more intuitive but less precise understanding of the transport. Furthermore, note that in this work the contacts were modeled as extended-channel (semi-infinite) i.e. of same material as the channel but without effect of buckling and/or Zeeman fields, if however metallic contacts are used, the finite channel length or more precisely the hard-wall boundary conditions along the transport direction may induce strong confinement and subsequent quantization effects akin to Chapter 7 on TI.

From the above discussion we observe that if λ_{SO} is sufficiently strong then spin-polarized high-transmission can be obtained for a large energy range to implement a spin-separator device. Here we would like to draw attention to the fact that as width of the nanoribbon increases, the first bulk band edge would move closer to $\lambda_{SO,}$ and therefore, for sufficiently wide ribbon the T(E) would not decrease as we transition out of the spin-polarized edge states at higher magnitudes of energy. This is the reason for roughly flat T(E) for Pb in Fig. B.5(f).

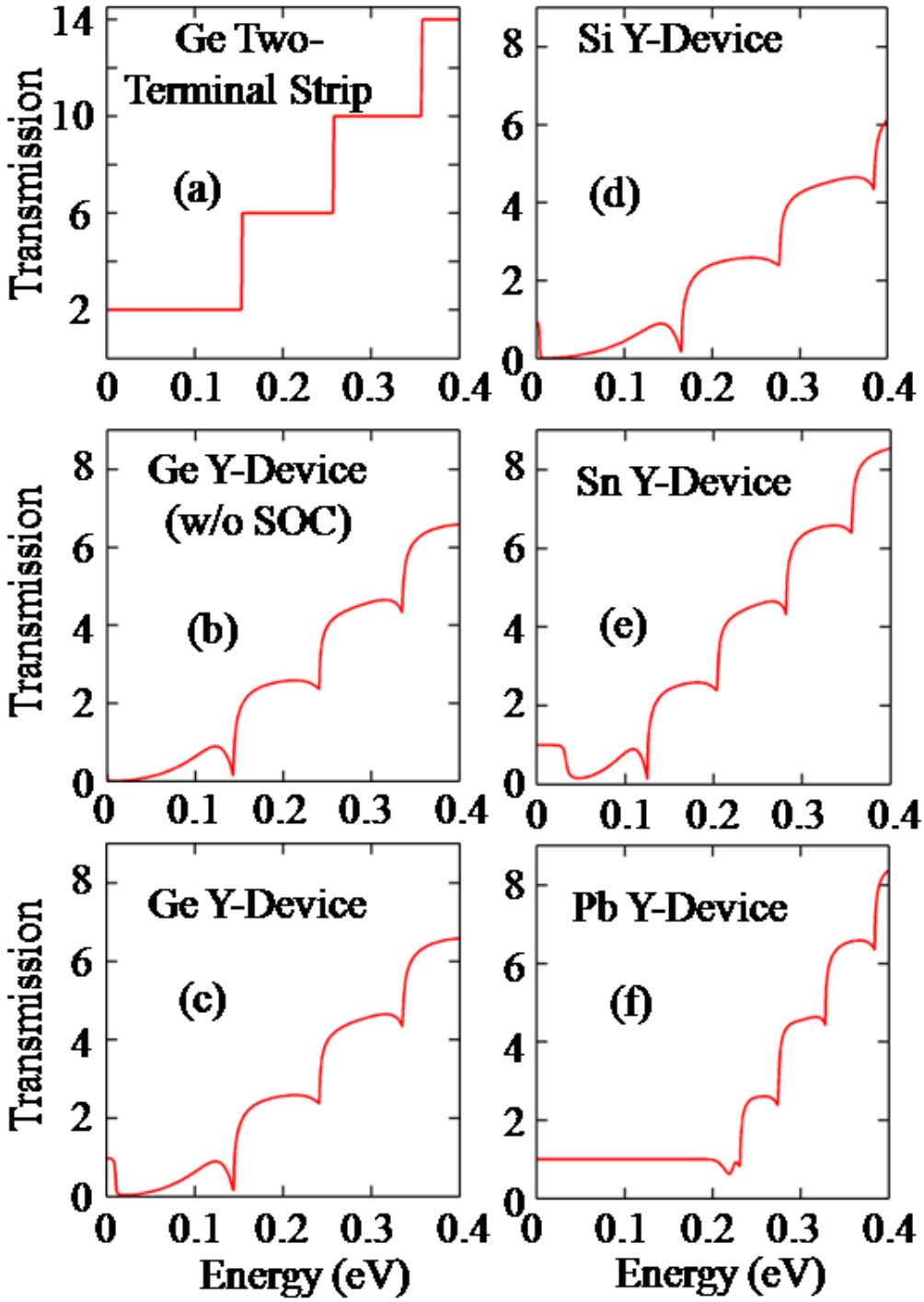

Figure B.5 Transmission (T) vs Energy (E) for different devices for transport at equilibrium. (a) Two-terminal Ge device (with SOC). Here, T(E) corresponds to the band structure. Absence of SOC just changes the energy value for inflections in T(E) plot (driven by the change in band-structure). (b) Three-terminal Y-shaped Ge device without SOC. (c) Y-shaped Ge device with SOC. (d) Y-shaped Si device with SOC. (e) Y-shaped Sn device with SOC. (f) Y-shaped Pb device with SOC. (a-f) For various systems T(-E) = T(E). Note that SOC creates spin-polarized edge states that drive the T(E) to one in $\pm \lambda_{SO}$ energy range, around which T(E) declines similar to the case without SOC (b). If device is sufficiently wide to have first bulk band edge at ~ λ_{SO} eV, then T(E) will be roughly flat throughout $\pm \lambda_{SO}$ energy range. The local minima of Fig. 4.2(b) and local maxima of Fig. 4.2(c) should be absent for such widths.

B.3. Spin Distribution for 14 cell wide Y-shaped Device

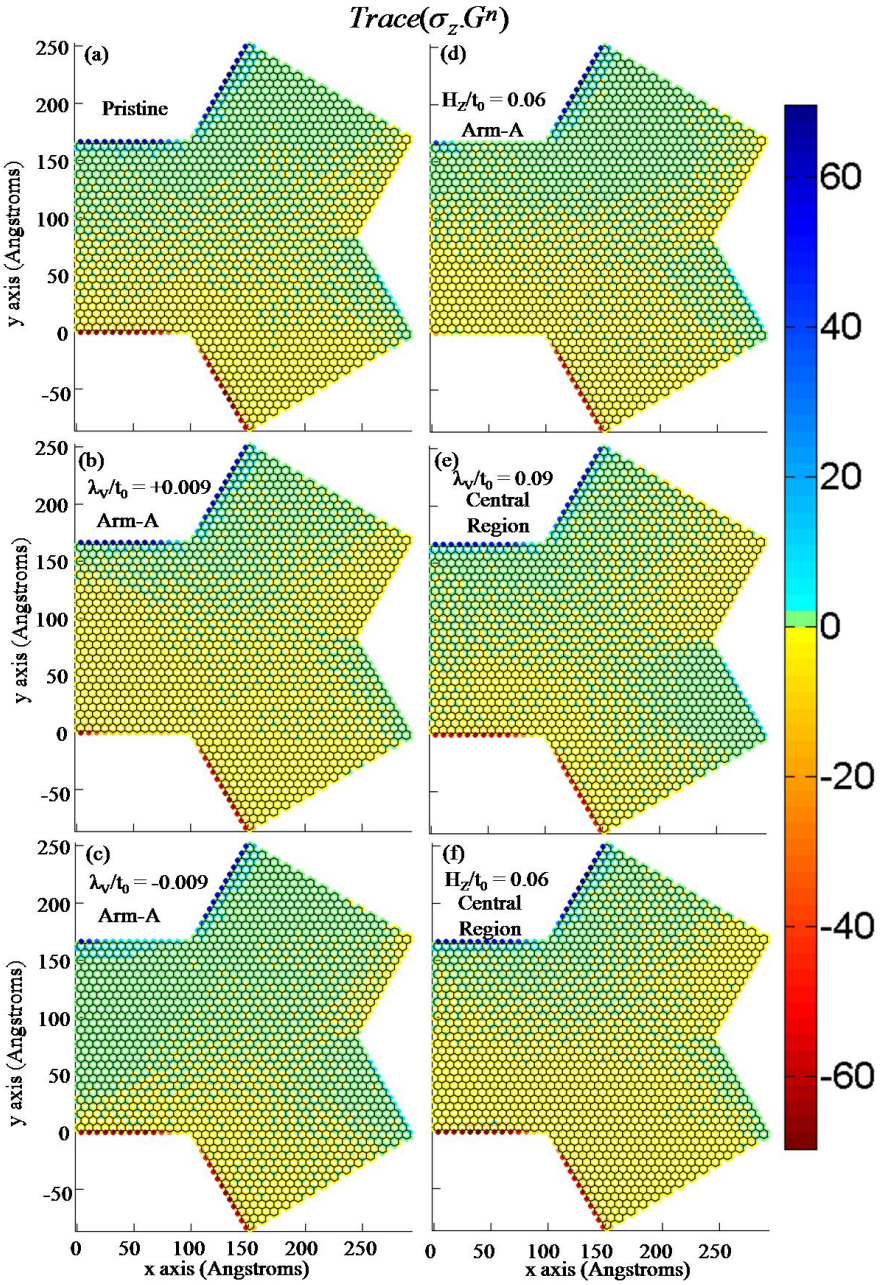

Figure B.6 Spin and charge distribution for the Germanene Device of Fig. 4.3, i.e. E_f = 5 meV and bias = 4 mV, where color scale gives the magnitude of Trace(σ_Z.G^n). Observe that Fig. 4.3(e) shows that SP should increase for Arm-C and decrease for Arm-B on applying λ_V on Arm-A. However, (b) shows a reduced magnitude of color intensity. This is due to reduced current as shown in Fig. 4.3(a). Increase in spin polarization is verified by plotting the normalized spin distribution as shown in Fig. B.7(b). Color scale has units of per eV.

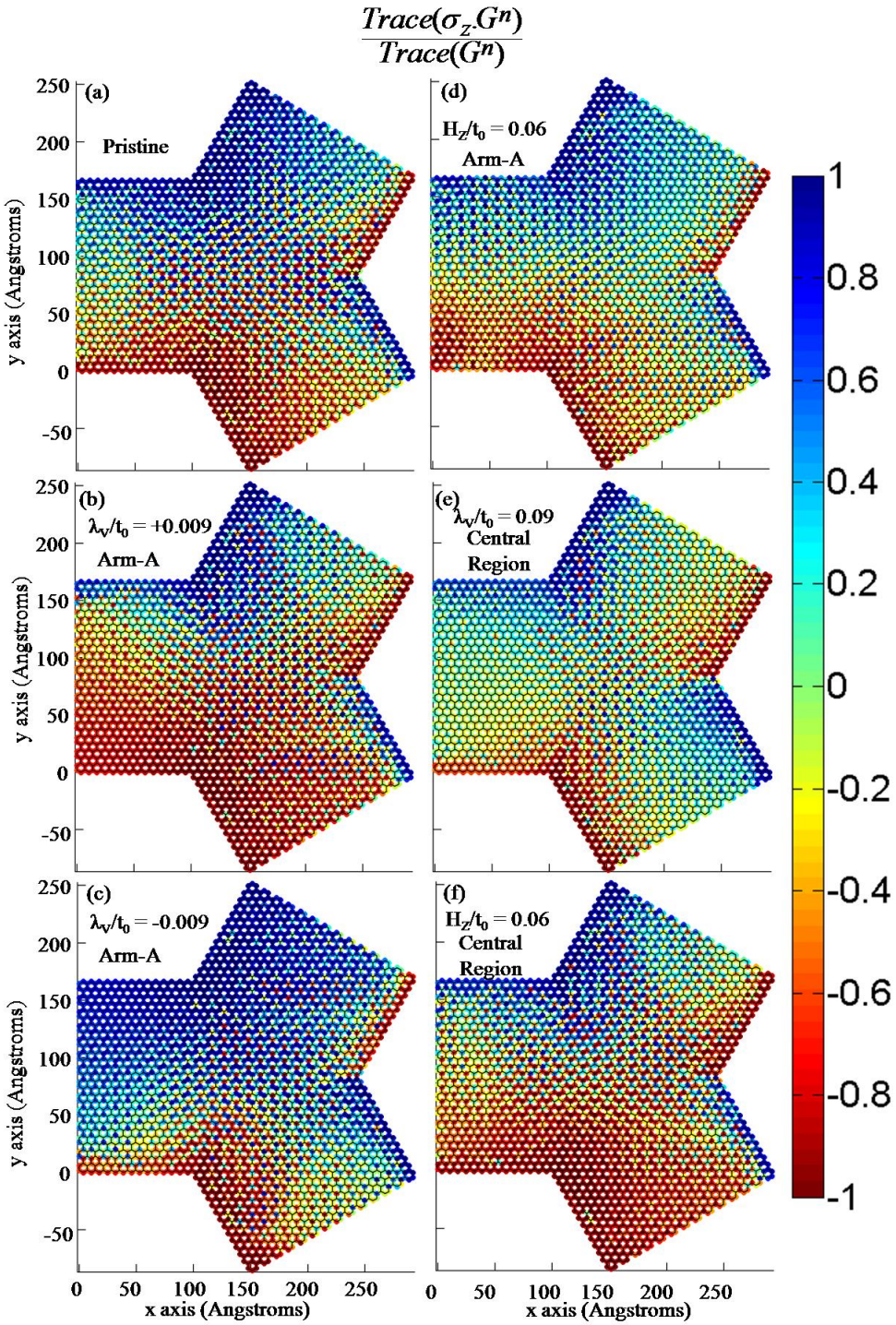

Figure B.7 Normalized Spin-Polarization (SP) distribution (color scale) in Germanene Device for Fig. 4.3, i.e. E_f = 5 meV and bias = 4 meV. Note that color information does not convey full information on spin flux through the device because charge may not be flowing through a certain region. Therefore, the results should be studied together with LDOS (Section B.1) and un-normalized spin-polarization (Fig. B.6) for understanding the concepts presented in chapter 4.

Appendix C

Spin-Polarization of Current for Arm-R for the Spin-Filter Operation in Chapter 5

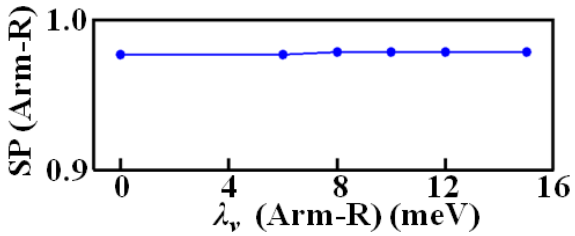

Figure C.1 The spin-polarization of Arm-R of a Ge-device with P, Q, and R arm-lengths of 6, 60, and 60 super-cells respectively at E_F = 1 meV and V_{PQ} (V_{PR}) = 1 mV when λ_V is applied only on Arm-R for the spin-filter operation.

The spin-polarization of the current through Arm-R (see Fig. C.1) remains nearly constant during the spin-filter operation, when λ_V is applied only over Arm-R. The current that manages to tunnel through the bandgap induced in Arm-R in the BI-phase is strongly polarized because of the ↓-polarized electrons injected via Arm-P which is in the QSH-phase. Electrons traverse through the same chain of type-B atoms as it is incident from Arm-P. However, the current itself is strongly repressed (see Fig. 5.6(a)) when Arm-R is driven into the BI-phase because of the potential-barrier induced by the bandgap in the energy-window of the quantum transport at the examined electronic conditions. Therefore, along with the current, the barrier filters out the down-spins from the device.

Appendix D

Supplementary for Chapter 7

This appendix provides discussion and plots for effect of top conrtacts on transport behaviour in 3D-TI in section D.1, which is followed by appraisal of effect of layer thickness in short-channel device with FM conatcts in section D.2.

D.1. Effect of Top-Contacts on on Short-Channel Device

Figure D.1 illustrates the carrier transport through a short channel device with normal-metal contacts at both source and drain terminal. It demonstrates that although current is initially only at the top surface (red region) at the source terminal, it redistributes after entering TI across layers as per topological properties to flow on both top and bottom surface (green color), and again gets to the top layer at the drain end (red region). Therefore, in general the examination of transport characteristics in TI channel at sufficient distance from the contacts is expected to be independent of the configuration i.e. side vs top contacts.

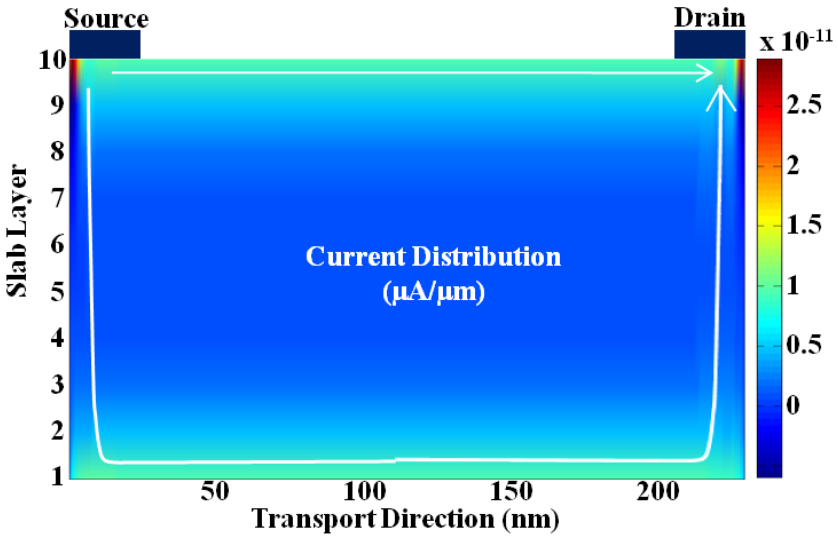

Figure D.1 Transport at 0 K for k_y = 0 (normal mode) for V_{DS} = 30 mV through 230 nm long and 10 QL thick TI channel with normal-metal contacts on the top.

D.2. Layer-Dependence for Short-Channel Device with FM Contacts

This section provides a supporting plot for layer dependence of short-channel device with anti-phase and in-phase ferromagnetic contacts to emphasize the effect of contact magnetization and confinement along the transport direction. The microscopic dissemination of quantum information resolved in energy (E) and transverse-mode (k_y) space reiterates that the current distribution for short-channel device with FM contacts is highly subject to the electronic and physical operating condition which may result in exotic observations for current distribution across layers of 3D-TI.

Figure D.2(a) shows that for thickness ranging from 10QL-28QL, the current distribution across quintuple layers of the Bi_2Se_3 topological insulator with anti-phase ferromagnetic contacts show the same qualitative trend as Fig. 7.5(c). The positive current is flowing on the bottom layer while the negative current is through top surface layer, which is in accordance with spin-texture for top and bottom surface shown in Fig. 7.1(a).

The transmission distribution resolved in E and k_y-space in Fig. D.2(b-f) for different slab thickness illustrates increase in the transmission modes in the operating energy window for the transport. These plots furthermore illustrate the quantization of momentum-modes due to longitudinal confinement and clearly show that normal mode ($k_y = 0$) may or may not be the dominating one (also see discussion for Fig. 7.6). The absolute quantity of current flowing through each layer therefore depends on these quantized energy levels, the k_y mode and its distribution across layers.

However, for Fig. D.2(g) for in-phase ferromagnetic contacts it is observed that it is possible to have an exotic current distribution, akin to Fig. 7.5(d), for certain thickness. This again depends on the dominating k_y modes as illustrated via Fig. D.2(h-l), which may be different from the set obtained for anti-phase contact configuration (compare

transmission plots in two columns), and their spin-polarization (see Fig. 7.6 and corresponding discussion).

We however acknowledge that due to extremely sensitive operating conditions like Fermi-level, bias, channel length, slab thickness and temperature, which governs the quantization of both energy and momentum modes and their spin-polarization, it may be a challenging experiment.

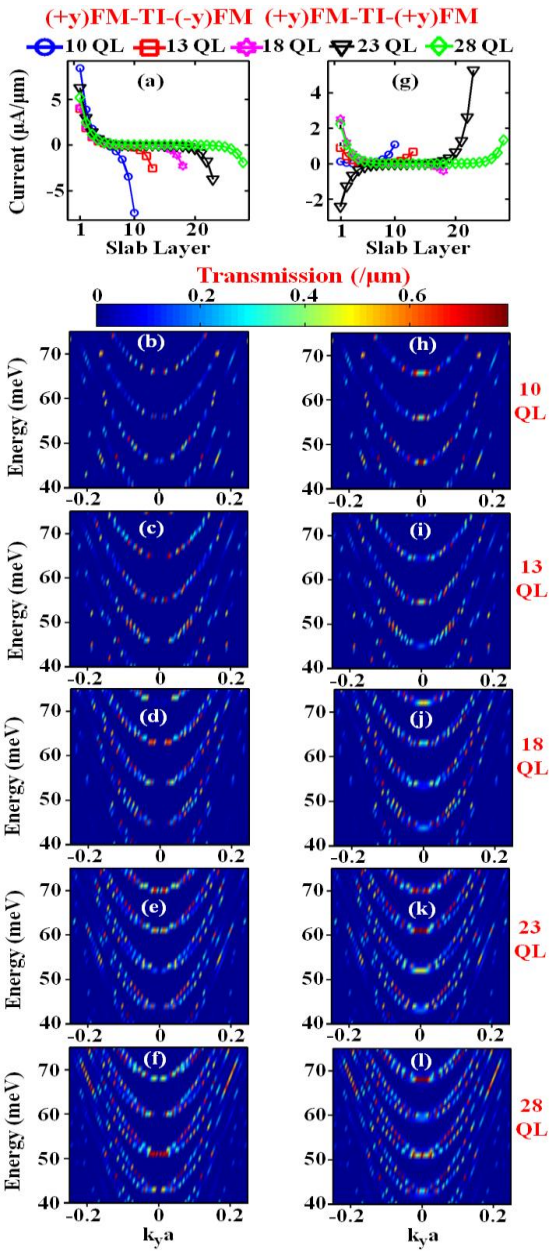

Figure D.2 Transport at 0 K for V_{DS} = 35 mV through 65 nm long TI channel with 100 % polarized ferromagnetic contacts at both ends. Source terminal is magnetized along '+*y*' whereas drain terminal is magnetized along '–*y*' (a-f) and '+*y*' (b-l). (a, g) Current distribution across slab layers of different thicknesses. (b-f, h-l) Energy and transverse mode $k_y a$ resolved Transmission corresponding to current distribution in respective columns for thickness stated on right side in each row.

D.3. Enlarged Figure 7.5(a)

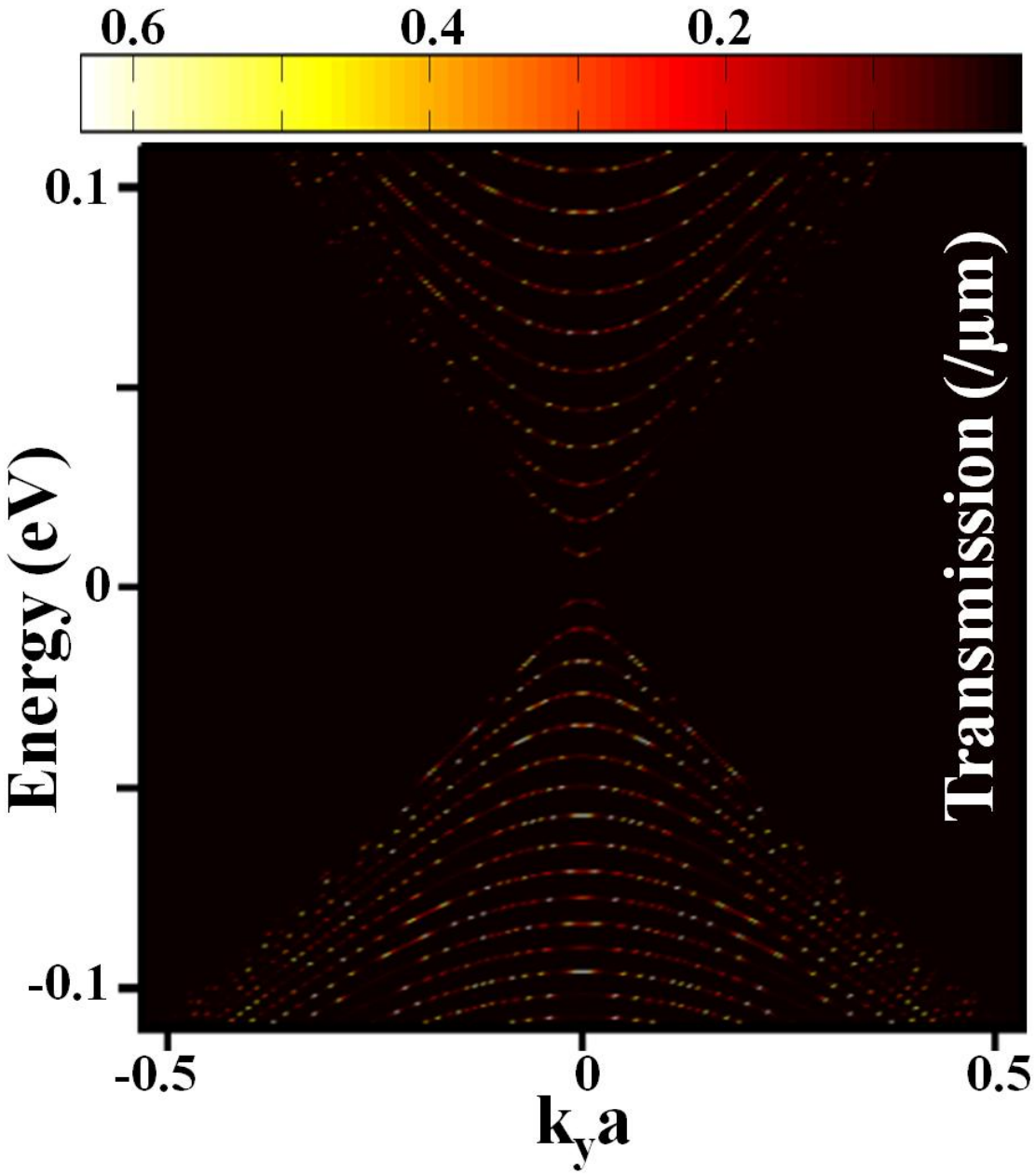

Appendix E

Supplementary for Chapter 8

This appendix provides supporting plots that should help in developing an intuitive understanding of the results presented in the chapter 8. Section E.1 illustrates non-equilibrium and near-equilibrium transport through defect-free Bi_2Se_3 TI-nanowire which especially aids in understanding the methodology given in the main text. Section E.2 illustrates the effect of different defects on transport and helps in appreciating the conclusions drawn for interconnects. Section E.3 shows the effect of acoustic phonons on non-equilibrium transport through Bi_2Se_3 3D-TI slab. For comprehensively understanding of role of phonons readers are referred to our previous work[200]. Section S4 presents corrections to our previous work[311] on evaluating mobility in sub-10 nm thick 3D-TI for electrical interconnects.

E.1. Transport through defect-free Bi_2Se_3 TI-Nanowire

Figure E.1 presents the electron transport characteristics of a 10 QL – 60 nm wide – 80 nm long defect free Bi_2Se_3 TI-wire at 0 K for the different aspects, such as the current distribution in the real space and energy domain to understand its ballistic behaviors under a small bias (V_{DS} = 40 mV) at E_f = 0.1 eV. Contact region (beyond 80 nm channel) in transport direction has been removed from the plots. As shown in (a), the currents constantly flow by energy from 0.06 to 0.1 eV through the nanowire, and it can be found that current is lower at Energy = 0.1 eV and 0.06 eV because Fermi-distribution is 0.5 at source and drain end respectively. Similarly, (b) shows the current (in μA) distribution across layers along the channel. It confirms that current is conserved in each layer along the transport direction and demonstrate the ballistic transport behaviors in our simulations. Next, to understand the current distribution in

the layers, we plot current distribution per energy in (c) and total current in (d). Both plots show the larger current occupying at the first or the last few layers, indicating current flowing through the surface states.

However, it is also very obvious that current is not only at the first or the last layer because the inter-surface coupling fractionally increases the current through the sub-surface layers as it propagates across the channel. However, the net current in each y-z plane is conserved along transport direction for each energy point as can be attested from (a). Eq. (2.12) is used in Fig. 8.2(d) to attest that the current chiefly flows through the topological surfaces.

Observe that for thin nanowire (10 QL) the surface state (wavefunction) essentially penetrates through entire material and therefore middle layers also have non-negligible contribution in the net transport. In (e), bottom layer charge distribution (arbitrary units) i.e. $|\psi^*\psi|$ is presented. It is observed that the highest concentration happens at the center of the bottom surface corresponds to lowest eigen-value for confinement in y-direction. The wavefunction shifts towards source end and peaks at some distance from it.

Compare this with $|\psi^*\psi|$ for near-equilibrium case which can be easily identified with first eigenvector solution for confined system in Fig. E.2 and cases for various defects in Fig. E.3. Figure E.1(f) and E.1(g) show density of states across energy and transmission across electron-energies. Both cases present the standard 1D quantization characteristics, a peak of DOS in the band-edge and flat transmission as energy across the bands.

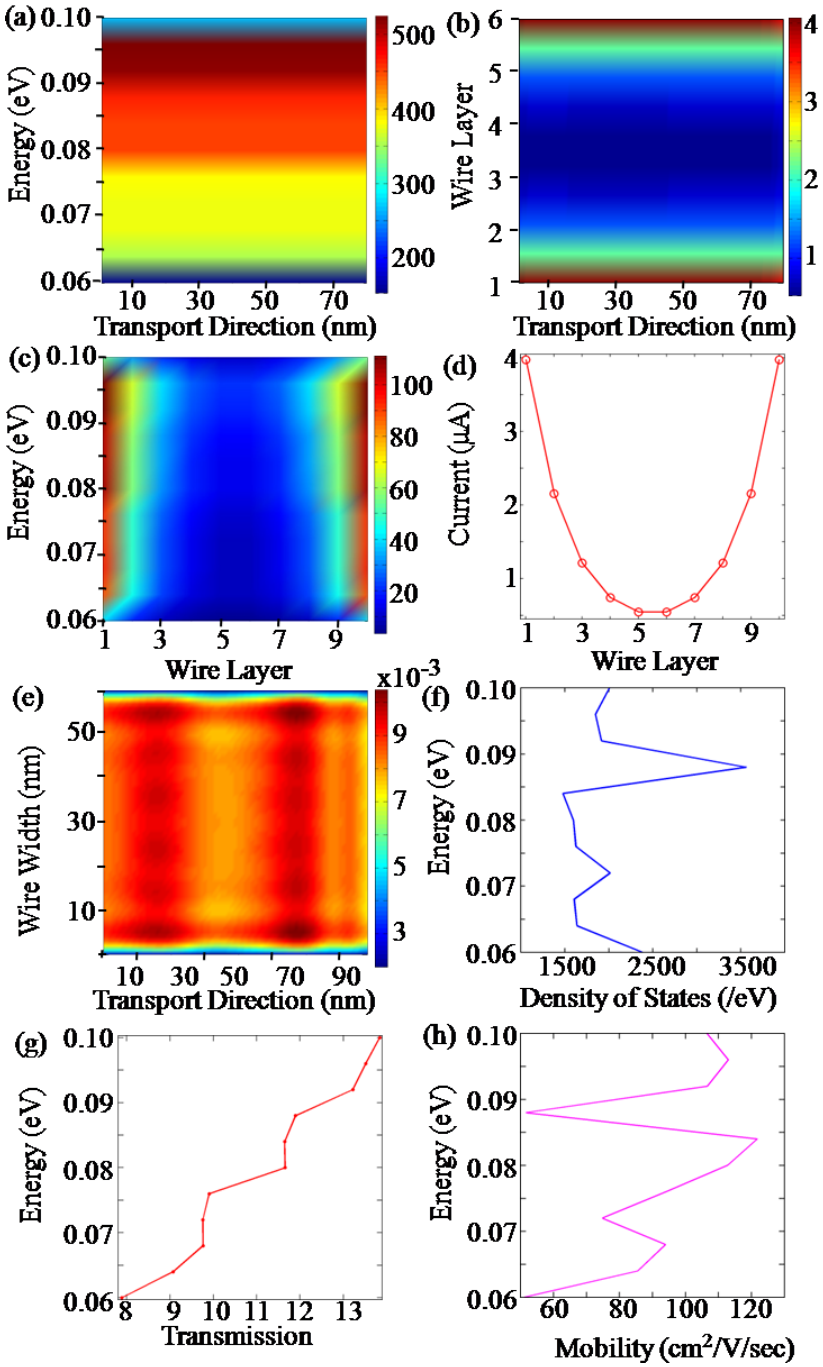

Figure E.1 Non-equilibrium current distribution at 0 K across layers for 10 QL – 60 nm wide – 80 nm long defect free Bi_2Se_3. The ballistic transport properties is presented in (a) current distribution (in uA/eV) along the transport direction, (b) energy integrated current (in μA) distribution across layers and along the channel, (c) current distribution (in uA/eV) across layers of the nanowire, (d) current distribution at source and drain end, (e) bottom layer charge distribution (arbitrary units) i.e. $|\psi^*\psi|$ for the given non-equilibrium condition. (f) Density of states across energy, (g) Transmission across electron-energies, and (h) Mobility distribution across energy.

Figure E.2(a) and E.2(b) show density of states (DOS) and transmission as a function of energy, respectively for a defect-free Bi_2Se_3 TI-wire (10 QL thick – 60 nm wide – 80 nm long) under equilibrium condition. Here, we would like to note the

absence of states in confinement-induced mini-gap, resulting in zero transmission. Otherwise, transmission is the perfect staircase structure (small step-like) corresponding to the number of bands for electron transport. (c) presents the bottom layer charge distribution (arbitrary units) i.e. $|\psi^*\psi|$.

In (d), we calculate mobility in the channel under a bias of 12 mV with the considerations of near-equilibrium transport. As width increases the jagged peaks resulting from 1-D nanowire quantized sub-bands translate into a smooth continuous trend. Note that at higher Fermi-levels, conduction is mainly through bulk bands which do not have topological protection.

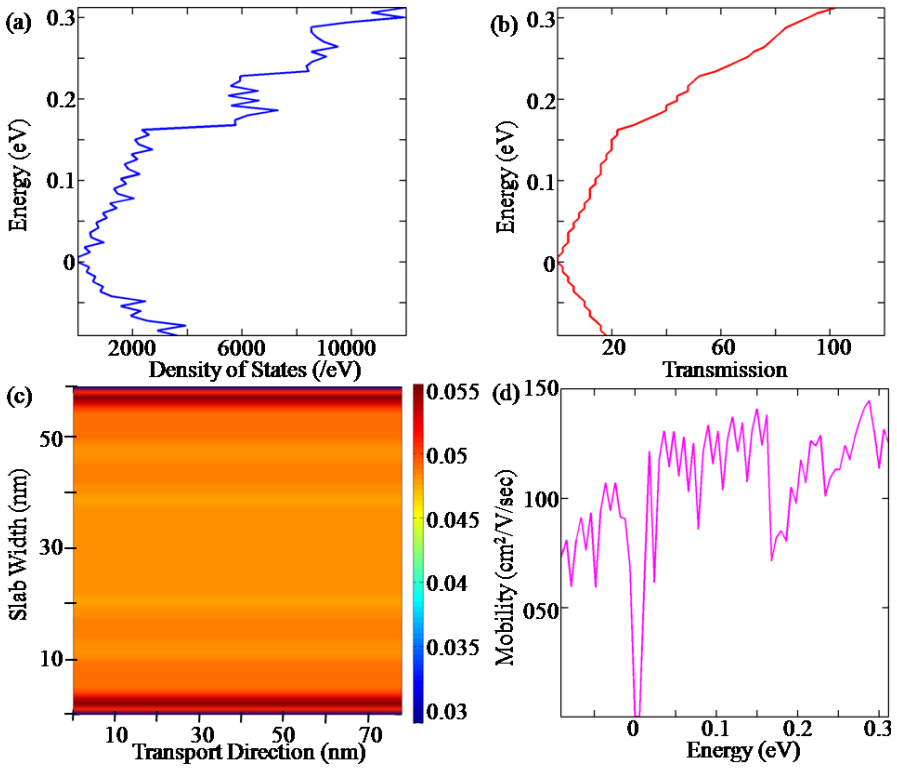

Figure E.2 (a) Density of states (DOS) vs. Energy and (b) Transmission vs Energy of a defect-free Bi_2Se_3 TI-wire (10 QL thick – 60 nm wide – 80 nm long). (c) Bottom layer charge distribution (arbitrary units) i.e. $|\psi^*\psi|$ of the same system. (d) Mobility vs Energy.

E.2. Transport through Bi_2Se_3 TI-Nanowire with defects

In this section, we will introduce the transport properties with different defect conditions, such as charge impurities (I), vacancies (II), and edge roughness (III) in Fig E.3 and Fig. E.4 for near and non-equilibrium transport respectively. In order to

compare to the perfect case, we use the same size of Bi_2Se_3 TI-wire as section E.1. We simulate 25 random samples for each condition, i.e. different type and concentration of the defects. Similar to Fig. E.2, the subplots order as follows: (a) Density of States (DOS) vs. Energy, (b) Transmission vs Energy, (c) Bottom Layer Charge Distribution (arbitrary units) i.e. G^n (n.b. charge density is given by $G^n/2/\pi$ where G^n is correlation function) corresponding to lowest eigen-value for confinement in y-direction for equilibrium-condition, and (d) Standard-deviation (σ) for Mobility vs Energy for four Different Fermi-Levels (E_f).

It can be found that in Fig. E.2, the clear DOS peaks and the prefect staircase in transmission of the perfect TI NW confirm the unique 1D characteristics of the wire. However, due to the defects, DOS and T(E) vary. Especially, as the defect concentration increases, their behaviors will be far away from the perfect case. Therefore, it leads the variation in mobility (calculated under a bias of 12 mV) around the mean-value across 25 random cases for respective defects. Low value of σ compared to its mean value demonstrates relative robustness of transport to corresponding defect.

The reported mobility values have been averaged over 25 simulation runs. Especially note (i) the vacancies captured in bottom layer in LCDP plots and (ii) the relative immunity of transport to edge roughness because transport is mainly through the centre (along y-axis) of wire. Next, Fig. E.4 illustrates that defects can force the current path to change. It can be routed through sub-surface layers if not backscattered.

This is especially important because previous models predict transport results only on the basis of surface layers and hence overestimate the robustness of current. More specifically, observe that negative ionic impurities deflect the current through sub-surface layer whereas positive ionic impurities can electrostatically pull the sub-

surface current into surface layer (note the peaks in Fig. E.4(g) and compare with the position of impurities in E.4(h)). Since, Bi_2Se_3 has Fermi-level in the conduction band due to selenide vacancies; we have considered only negative impurities as a much simplified approximation in this work.

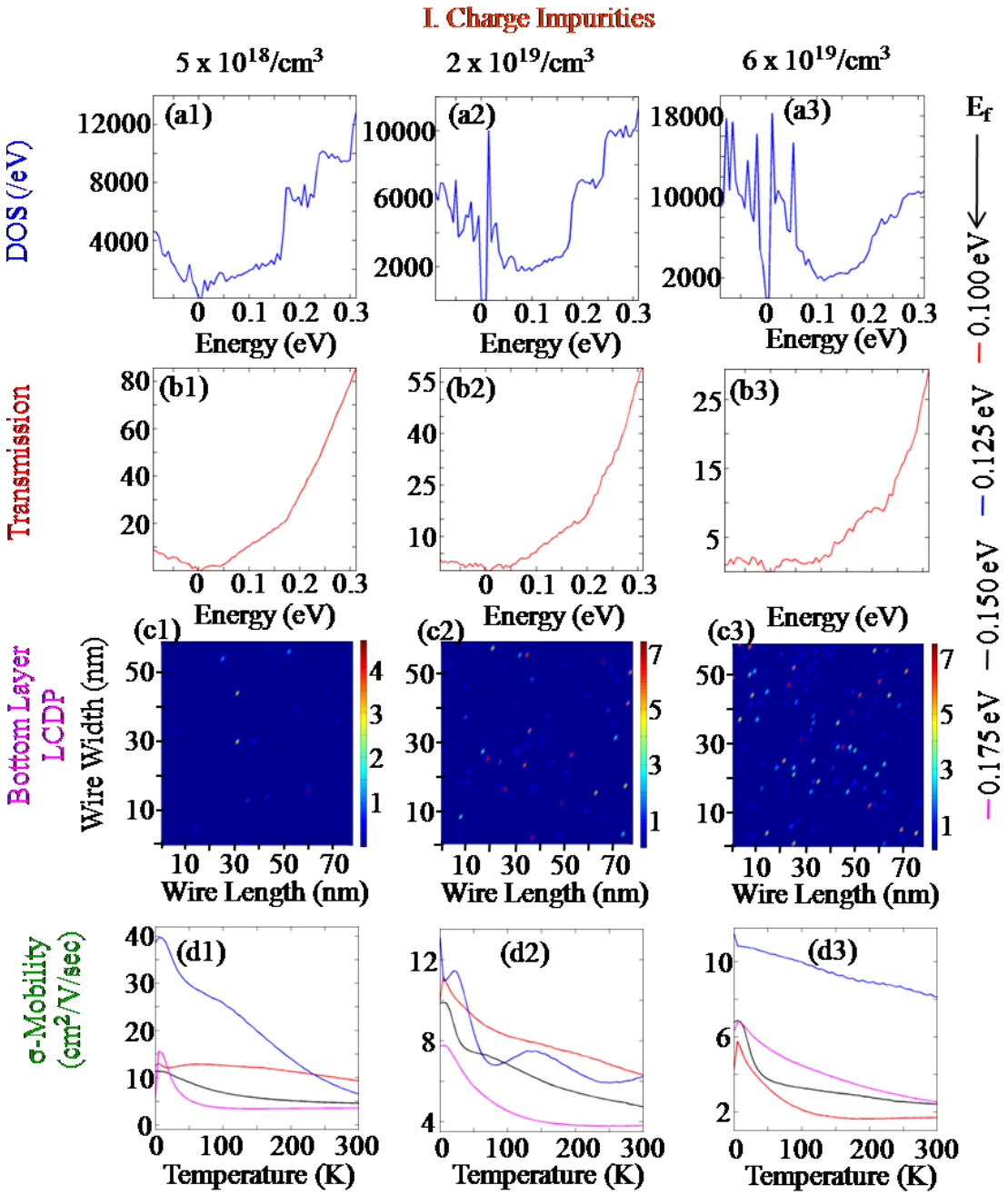

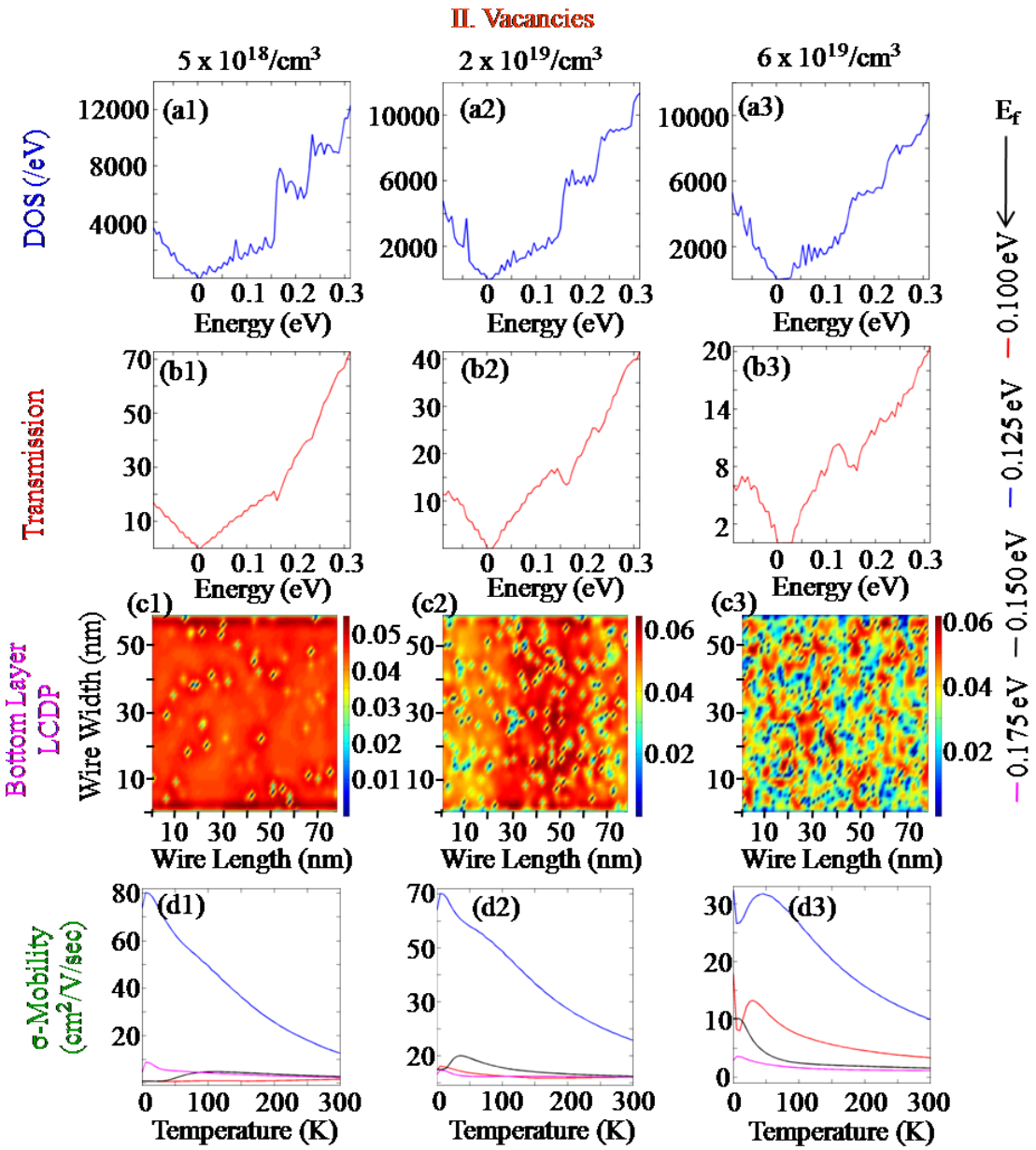
II. Vacancies
5 x 10^18/cm^3
2 x 10^19/cm^3
6 x 10^19/cm^3
DOS (/eV)
(a1)
(a2)
(a3)
Energy (eV)
Transmission
(b1)
(b2)
(b3)
Bottom Layer LCDP
(c1)
(c2)
(c3)
Wire Width (nm)
Wire Length (nm)
σ-Mobility (cm²/V/sec)
(d1)
(d2)
(d3)
Temperature (K)
E_f
0.100 eV
0.125 eV
0.150 eV
0.175 eV

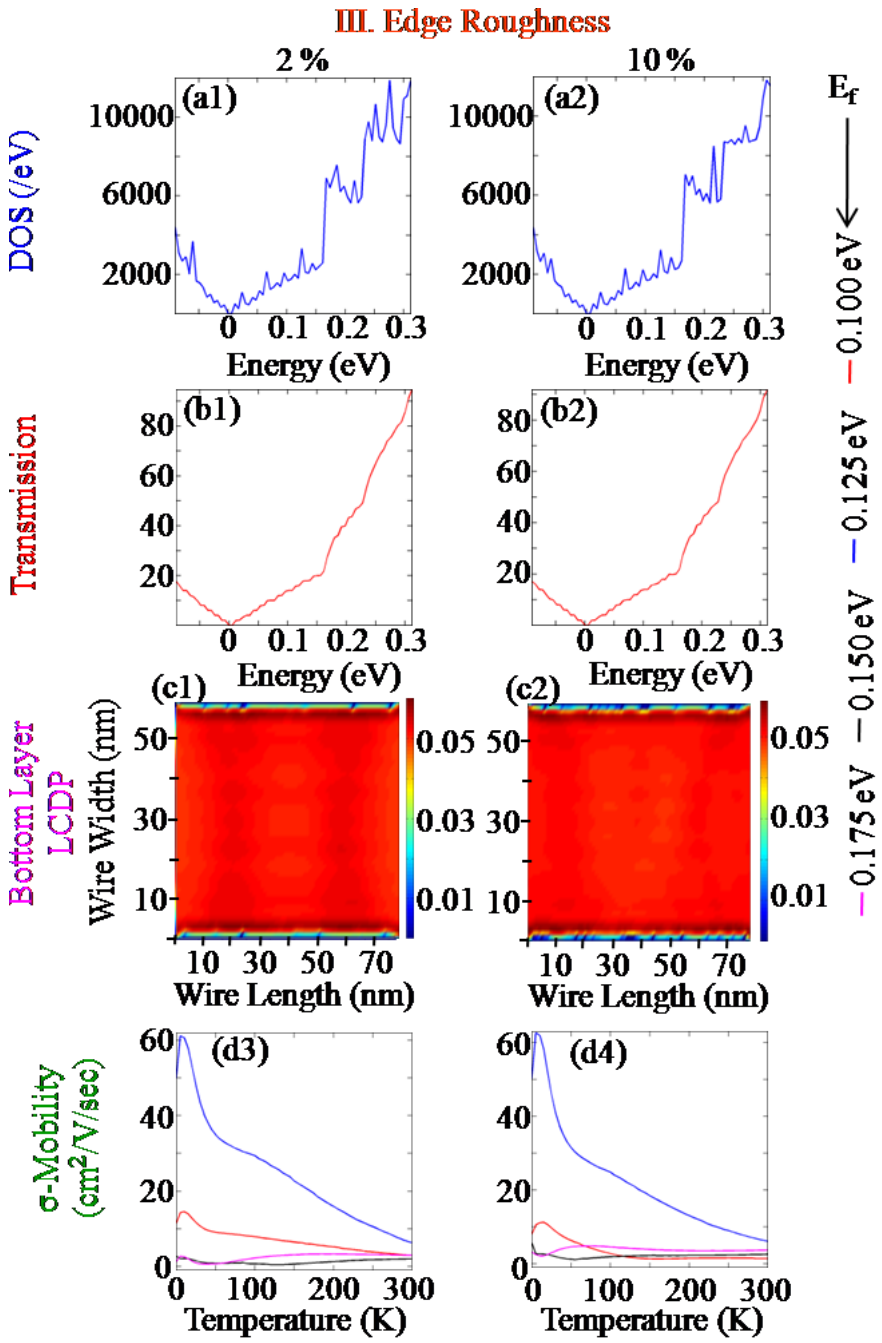

Figure E.3 Near-Equilibrium transport through Bi_2Se_3 TI-wire (10 QL thick – 60 nm Wide – 80 nm Long) with defects (I. Charge Impurities; II. Vacancies; III. Edge Roughness) as stated in the heading for each sets of plots (a-c). (a) Density of States (DOS) vs. Energy. (b) Transmission vs Energy. (c) Bottom Layer Charge Distribution. (d) Standard-deviation (σ) for Mobility vs Energy for four Different Fermi-Levels (E_f).

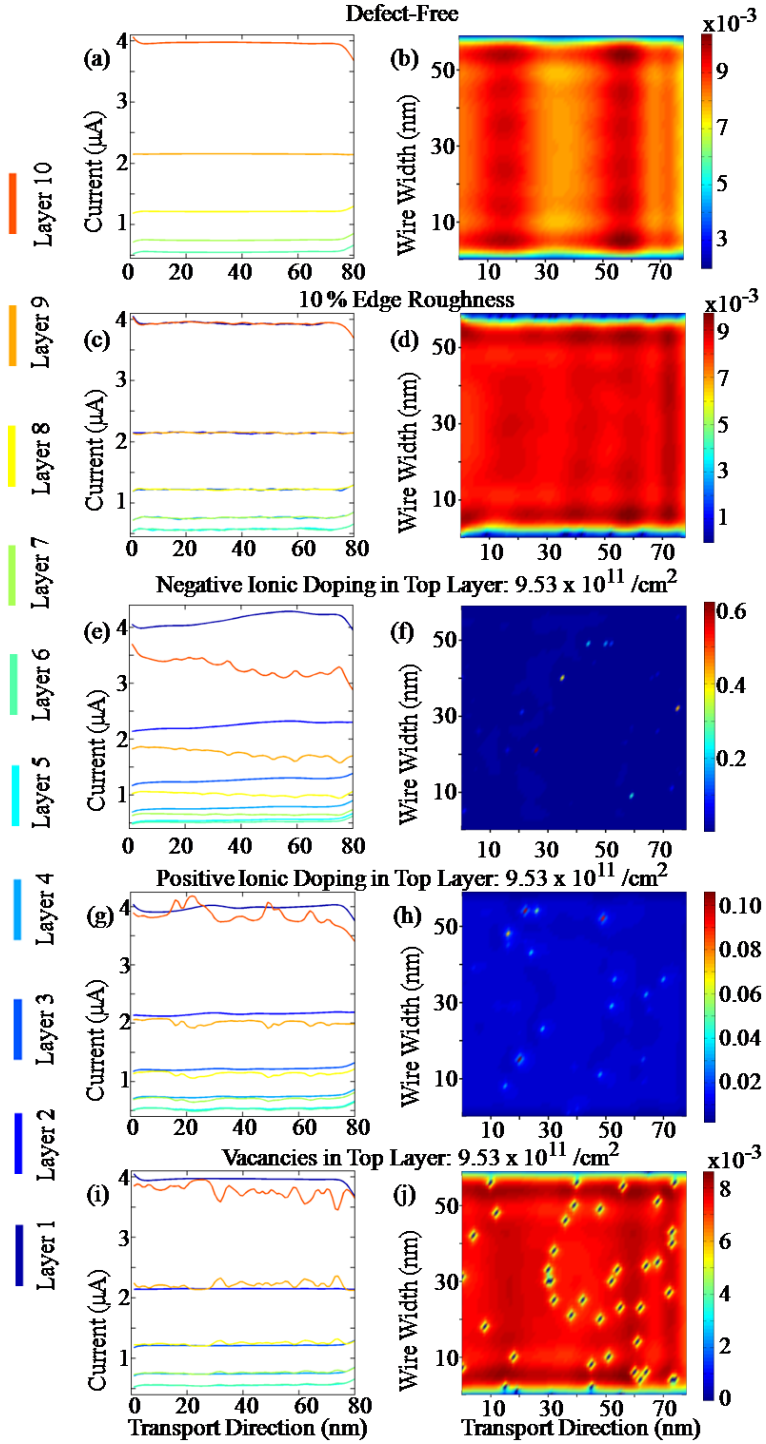

Figure E.4 Non-Equilibrium transport through Bi_2Se_3 TI-wire (10 QL thick – 60 nm Wide – 80 nm Long) with defects stated over each row. (a,c,e,g,i) Current distribution across layers along the direction of transport. Note that in defect-free case current is perfectly symmetric across middle layer and hence the trend lines overlap. (b,d,f,h,j) Bottom Layer Charge Distribution for respective case.

E.3. Non-Equilibrium Transport through Bi_2Se_3 TI-Slab with Acoustic Phonons

In this section, we will introduce the phonon effects on carrier mobility of Bi_2Se_3 TI-Slab with infinitely wide (periodic condition along y-axis) and 80 nm long at 150 K as E_f = 0.1 eV under V_{DS} = 40 mV. Firstly, the subplots present the density of states (DOS) vs. energy, transmission vs. energy, current density distribution across quintuple layers of the slab, and current density distribution along the transport direction for ballistic transport condition (Fig. E.5(a, b, c, and d)) and acoustic phonon scattering (Fig. E.5(e, f, g, and h)) respectively. Due to the infinite width along y-axis resulting in the absence of confinement induced quantization, DOS and transmission increase continuously. Furthermore, it can be found that acoustic phonon scattering has significant impacts on transmission and hence transport properties in TI NW as well. It is obvious that transmission (compare Fig. E.5(b) with E.5(f)) reduces dramatically in the scattering cases. Therefore, current density is significantly reduced for each energy point. All of these effects result in decreased mobility in TI-slab.

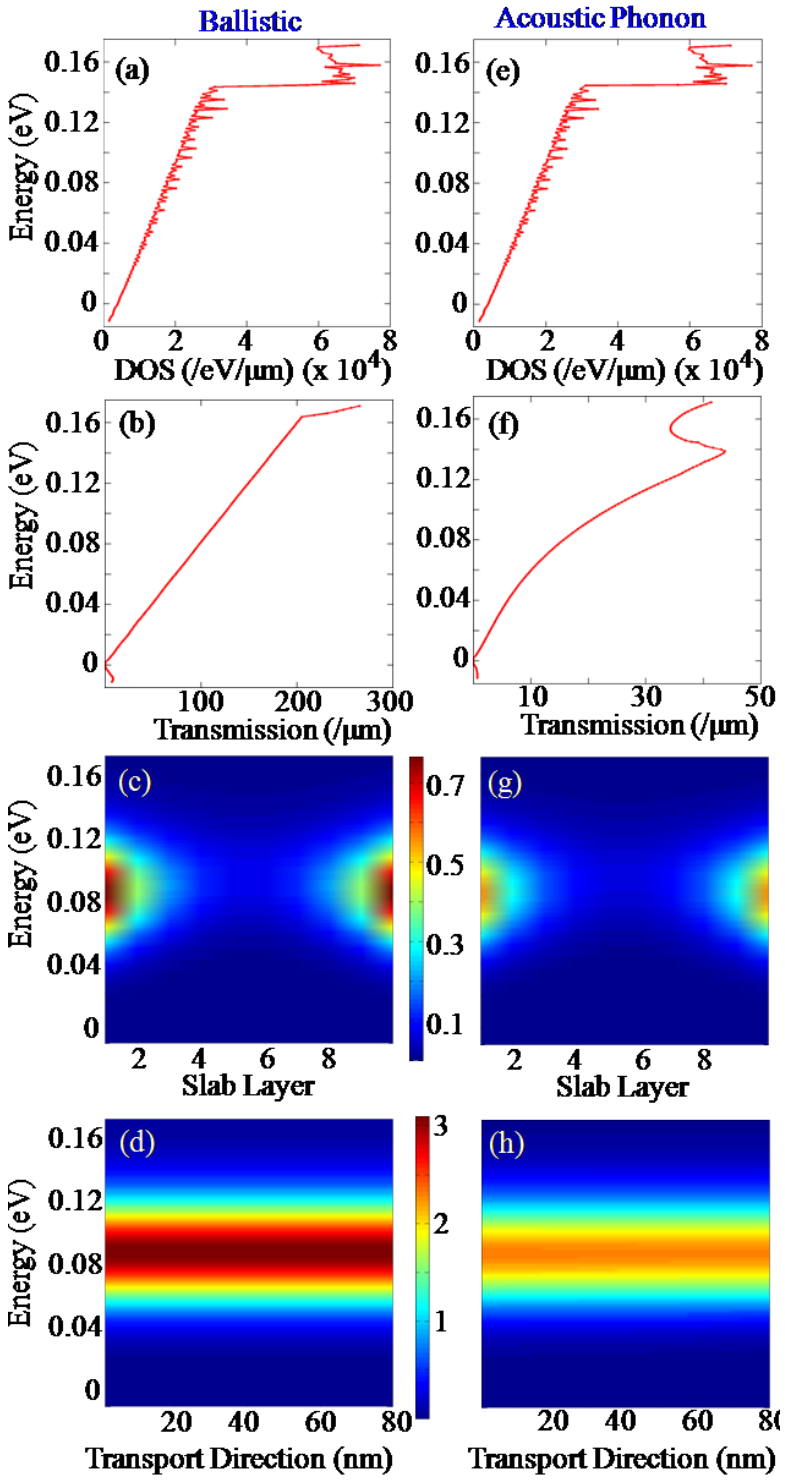

Figure E.5 Non-Equilibrium transport through Bi_2Se_3 Slab. (a ,e) Density of States (DOS) vs. Energy. (b, f) Transmission vs Energy. (c, g) Current Density distribution across quintuple layers of the slab. (d, h) Current Density distribution along the transport direction.

Appendix F

Supplementary for Chapter 9

In this appendix, section F.1 gives a brief on the effect of mode mismatch at the contact-channel interface. Section F.2 provides the mathematical insight into band-alignment operation by analyzing the effect of gate potential on the transport through the Dirac-Band. Finally, section F.3 complements the results and discussion of main text by expounding on the effect of channel bias on the transport through all three device designs for the sake of completeness of this work.

F.1. Effect of Mode Mismatch at Contact

Consider the transport equation for current [81] as follows,

$$I = \frac{q}{\hbar}\int_{-\infty}^{\infty} dE\; D(E-U)\,\frac{1}{1/\gamma_S + 1/\gamma_D}\;(f_S(E) - f_D(E)) \qquad (F.1)$$

where I is the total current integrated over energy grid, D is Density of states, f_S and f_D are Fermi-Dirac distribution at source and drain end respectively, U is the change in potential energy in the channel, γ_S and γ_D are in-scattering rate at source and drain end. Physically, in-scattering rate represents the ease with which electron can move across the channel into the contact. As the mode-mismatch between channel and drain (source) terminal increases, γ_D (γ_S) reduces which subsequently reduces the current.

F.2. Effect of Gate Potential on Transport through Dirac-Band

For a single linear Dirac-band, the Density of states per unit cell as a function of energy [93] is given by,

$$DOS(E) = \frac{D}{a_x a_y} = \frac{1}{2\pi}\,\frac{|E|}{\hbar^2\, v_f^2} \qquad (F.2)$$

where a_x and a_y are unit-cell's dimension along x and y-axis, v_f is the Fermi-velocity. Substituting, Eq. (F.2) into Eq. (F.1) and we next consolidate all constants and terms

unaffected by the gate potential into a positive constant value β. Note that strictly β is a constant only if in-scattering rates are independent of energy E, which is a common assumption [81] for such analytical treatment of transport problems, at 0 K for E ϵ (μ_D, μ_S). This condition enables us to mask all other terms and completely focus on the effect of gate potential on DOS in subsequent derivation. Now, from Eq. (F.2) the expression for current becomes,

$$I = \int_{-\infty}^{\infty} dE \,|\, E - U \,|\, \beta \qquad (F.3)$$

At 0 K, for operation condition in Fig. 9.1(c-e),

$$I = \int_{-\Delta}^{\Delta} dE \,|\, E - U \,|\, \beta = \int_{-\Delta}^{U} dE\, (U - E)\, \beta + \int_{U}^{\Delta} dE\, (E - U)\, \beta, \; where \; U \in [-\Delta, \Delta] \qquad (F.4)$$

$$I = \beta\, (U^2 + \Delta^2) \qquad (F.5)$$

Now, for Design-A, U (in electron volts) = $-V_G - \Delta$ (in volts) for an equal drop of Δ volts at source and drain contacts for ballistic transport.

$$I = \beta\, ((V_G + \Delta)^2 + \Delta^2) \qquad (F.6)$$

$$\frac{\partial I}{\partial V_G} = 2\beta\, (V_G + \Delta) \quad and \quad \frac{\partial^2 I}{\partial^2 V_G} = 2\beta \qquad (F.7)$$

Therefore, from Eq. (F.7) we note that the current is minimum for $V_G = -\Delta$. Here, we note that a similar derivation for Design-B and Design-C would require substituting $U = -V_G - 2\Delta$ in Eq. (F.5), whose solution would show current minima at $V_G = -2\Delta$.

Another way to conceptually look at the same problem for Design-A (Design-B and Design-C) is to observe that as V_G is swept away from $-\Delta$ (-2Δ) value, we move-out the low DOS region of bands, out of transport energy window at one end of energy grid and move-in the high DOS region of bands, into the energy window at another end of the grid. Therefore, if the transport is solely through Dirac-band

positioned symmetrically in energy window (see green band in Fig. 9.1(d)), the current should be minimum. However, in non-equilibrium the complete system characterizes the quantum transport. Besides affecting the channel potential profile, gate potential also affects the in-scattering rate substantially in a band-alignment device (Design-A and Design-C).

For Design-A, at the resonant condition ($V_{TG} = -\Delta$), both k_x and k_y wavevectors are unchanged for electrons transiting from source to channel. The conservation of both momentum and energy results in high γ_S which tends to increase the current (see Eq. (F.1)) by competing against the effect of low DOS in transport energy window. On the other hand, mode-mismatch is highest between channel and drain for $V_{TG} = -2\Delta$ which lowers the γ_D and hence reduces the current (see Eq. (F.1)). Note that for Design-B and Design-C the vertical transport further complicates the transport behaviour as explained in results and discussion section 9.3.2 on vertical transport.

F.3. Effect of Channel-Bias V_{DS}

Figure F.1 illustrates the effect of channel bias on the output characteristics of all three devices presented in chapter 9. In contrast to graphene symFET, which is the first proposal of a band-alignment device and predicts resonance peak in output characteristics [286], the 3D-TI based band-alignment devices studied in this chapter universally show an increase in the current. Generally, a linear increase is expected [312] for Dirac-bands because of increase in DOS and charge in the transport energy window with an increase in bias voltage. Simple device architecture for Design-A in Fig. F.1(a) represents this case. However, a small decrease in current around $V_{DS} = \Delta$ is observed in Fig. F.1(b) for Design-B. This is because in this range of bias the DOS in top slab is reduced (refer results and discussion section on vertical transport for

potential distribution) and since the transport is primarily in-plane along x-axis (see Fig. 9.5(b)), the current marginally reduces. However, after band-alignment condition at $V_{DS} = 2\Delta$, characteristics are dominated by DOS. The main reason for absence of resonance peak is that only k_y mode is conserved because transport is in x-z plane, whereas for symFET both k_x and k_y are assumed to be conserved as transport is supposed to be only along z-axis (see results and discussion section on vertical transport for details). Finally, Design-C, as again explained in results and discussion section on vertical transport, inherits few characteristics of both Design-A and Design-B which also reflects in its output characteristics illustrated in Fig. F.1(c).

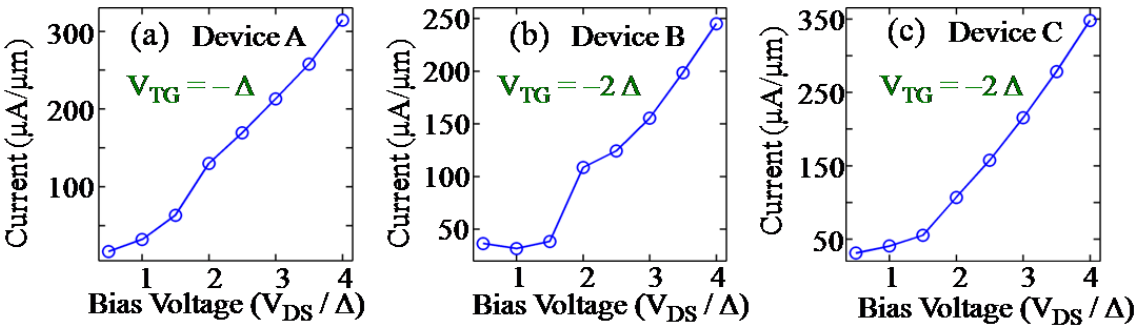

Figure F.1 Current vs channel bias for $\Delta = 0.04$ eV at 0 K for a fixed V_{TG} of $-\Delta$ for Design-A (a) and -2Δ for Design-B (b) and Design-C (c). The resonant condition is expected at $V_{DS} = 2\Delta$ in each, but instead observe the increase in current with bias voltage.

Appendix G

List of Publications and Awards

Journals

[J1] **Gaurav Gupta**, Mansoor Bin Abdul Jalil, Bin Yu and Gengchiau Liang, "Performance evaluation of electro-optic effect based graphene transistors", Nanoscale 4, 6365-6373 (2012).

[J2] **Gaurav Gupta**, Hsin Lin, Arun Bansil, Mansoor Bin Abdul Jalil, Cheng-Yi Huang, Wei-Feng Tsai and Gengchiau Liang, "Y-Shape Spin-Separator for two-dimensional Group-IV Nanoribbons". Applied Physics Letters 104 (3), 032410 (2014).

[J3] **Gaurav Gupta**, Hsin Lin, Arun Bansil, Mansoor Bin Abdul Jalil and Gengchiau Liang, "Role of Acoustic Phonons in Bi_2Se_3 Topological Insulator Slabs: A Quantum Transport Investigation". Physical Review B 89, 245419 (2014).

[J4] **Gaurav Gupta**, Mansoor Bin Abdul Jalil, and Gengchiau Liang, "Effect of Band-Alignment Operation on Carrier Transport in Bi_2Se_3 Topological Insulator", Scientific Report 4, 6220 (2014).

[J5] **Gaurav Gupta**, Mansoor Bin Abdul Jalil and Gengchiau Liang, "Evaluation of mobility in thin Bi_2Se_3 Topological Insulator for prospects of Local Electrical Interconnects". Scientific Reports 4, 6838 (2014).

[J6] Mohammad Abdullah Sadi*, **Gaurav Gupta*** and Gengchiau Liang, "Effect of phase transition on quantum transport in group-IV two-dimensional U-shape device", Journal of Applied Physics 116 (15), 153708. (*Authors contribute equally)

[J7] **Gaurav Gupta**, Mansoor Bin Abdul Jalil and Gengchiau Liang, "Contact Effects in thin 3D-Topological Insulators: How does the current flow?", Scientific Reports 5, 9479 (2015).

[J8] **Gaurav Gupta**, Hsin Lin, Arun Bansil, Mansoor Bin Abdul Jalil and Gengchiau Liang, "Carrier Transport in Bi_2Se_3 Topological Insulator Slab", Physica E: Low-dimensional Systems and Nanostructures 74, 10-19 (2015).

Conferences

[C1] **Gaurav Gupta**, Mansoor Bin Abdul Jalil and Gengchiau Liang, "Comparison of Electro-Optic Effect based Graphene Transistors," 2012 International Conference on Solid State Devices and Materials (SSDM 2012) September 25-27, 2012, Kyoto International Conference Center, Kyoto, Japan.

[C2] **Gaurav Gupta**, Argo Nurbawono, Minggang Zeng, Mansoor Bin Abdul Jalil and Gengchiau Liang, "Theoretical study on Topological Insulator based Spintronic Tristable Multivibrator," 2013 International Conference on Solid State Devices and Materials (SSDM 2013) September 24-27, 2013, Hilton Fukuoka Sea Hawk, Fukuoka, Japan.

[C3] **Gaurav Gupta**, Mansoor Bin Abdul Jalil and Gengchiau Liang, "Is Sub-10nm Thick 3D-Topological Insulator Good for the Local Electrical Interconnects?", IEEE International Electron Devices Meeting (IEDM 2013), December 9-11, 2013, Washington DC, USA.

[C4] **Gaurav Gupta**, Mansoor Bin Abdul Jalil and Gengchiau Liang, "Band-Alignment Induced Current Modulation in Bi_2Se_3 Topological Insulator," 2014 International Conference on Solid State Devices and Materials (SSDM 2014) September 8-11, 2014, Tsukuba International Congress Center, Tsukuba, Ibaraki, Japan.

[C5] Mohammad Abdullah Sadi*, **Gaurav Gupta***, and Gengchiau Liang, "Effect of Phase Inversion on Quantum Transport in Group IV Two-Dimensional U-shape Device," 2014 International Conference on Solid State Devices and Materials (SSDM 2014) September 8-11, 2014, Tsukuba International Congress Center, Tsukuba, Ibaraki, Japan. (*Authors contribute equally)

[C6] **Gaurav Gupta** and Gengchiau Liang, "Quantum Transport in Two-Dimensional Group-IV monolayers and Topological Insulators", World Congress of Smart Materials (WCSM 2015), March 23-25, 2015, Busan, Republic of Korea.

Book-Chapters

[B1] **Gaurav Gupta,** Minggang Zeng, Argo Nurbawono, Wen Huang, and Gengchiau Liang, "Applications of Graphene Based Materials in Electronic Devices", Graphene Science Handbook, **CRC Press**, Chapter 19, Volume 6, 2016 (in press).

[B2] Wen Huang, Argo Nurbawono, Minggang Zeng, **Gaurav Gupta**, and Gengchiau Liang, "Electronic structure of graphene based materials and their carrier transport properties", Graphene Science Handbook, **CRC Press**, Chapter 26, Volume 2, 2016 (in press).

Patents

[P1] Hsin Lin, Wei-Feng Tsai, Chen-Yi Huang, Horng-Tay Jeng, Tay-Rong Chang, **Gaurav Gupta**, Gengchiau Liang and Arun Bansil, "Transition Metal Dichalcogenides-Based Spintronic Devices", US Provisional Application No.: 62/058,437, Priority Date: 1st October 2014.

Awards

[A1] IEDM 2013 Travel Grant Award of US $ 860.

[A2] President's Graduate Fellowship (PGF) for outstanding research and studies at NUS, January 2014 – July 2015.

[A3] SSDM 2014 Travel Grant Award of 70,000 Japanese Yen.

[A4] Innovation/Entrepreneurship Practicum Award of S$ 10,000 for Quantum-Technology Computer Aided Design (Q-TCAD) in November 2014.

Bibliography

[1] Zh I A 2013 The semiconductor revolution in the 20th century *Russian Chemical Reviews* **82** 587

[2] Yang J K W, Chen Y J, Huang T L, Duan H G, Thiyagarajah N, Hui H K, Leong S H and Ng V 2011 Fabrication and characterization of bit-patterned media beyond 1.5 Tbit/in(2) *Nanotechnology* **22** 385301

[3] Fuechsle M, Miwa J A, Mahapatra S, Ryu H, Lee S, Warschkow O, Hollenberg L C L, Klimeck G and Simmons M Y 2012 A single-atom transistor *Nat Nanotechnol* **7** 242-6

[4] Masuhara T 2013 Quest for Low-Voltage and Low-Power Integrated Circuits: Towards a Sustainable Future *Solid-State Circuits Magazine, IEEE* **5** 8-26

[5] 2013 *International Technology Roadmap for Semiconductors* **Emerging Research Devices**

[6] Rusu S, Muljono H, Ayers D, Tam S, Wei C, Martin A, Shenggao L, Vora S, Varada R and Wang E 2014 5.4 Ivytown: A 22nm 15-core enterprise Xeon® processor family. In: *IEEE International Solid-State Circuits Conference Digest of Technical Papers (ISSCC), 2014*, (San Francisco, CA: IEEE) pp 102-3

[7] Qadri M Y, Gujarathi H S and McDonald-Maier K D 2009 *Low Power Processor Architectures and Contemporary Techniques for Power Optimization – A Review* vol 4: Academy Publisher)

[8] Geng H 2014 *Data Center Handbook*: Wiley)

[9] 2014 Scaling Up Energy Efficiency Across the Data Center Industry: Evaluating Key Drivers and Barriers *Natural Resources Defense Council* **Data Center Efficiency Assessment**

[10] Cisco Visual Networking Index: Forecast and Methodology, 2013–2018 *Cisco*

[11] Zutic I, Fabian J and Das Sarma S 2004 Spintronics: Fundamentals and applications *Rev Mod Phys* **76** 323-410

[12] Pulizzi F 2012 Spintronics *Nat Mater* **11** 367-

[13] Wang K L and Amiri P K 2012 Nonvolatile Spintronics: Perspectives on Instant-On Nonvolatile Nanoelectronic Systems *SPIN* **02** 1250009

[14] Demidov V E, Urazhdin S, Ulrichs H, Tiberkevich V, Slavin A, Baither D, Schmitz G and Demokritov S O 2012 Magnetic nano-oscillator driven by pure spin current *Nat Mater* **11** 1028-31

[15] Wunderlich J, Irvine A C, Sinova J, Park B G, Zarbo L P, Xu X L, Kaestner B, Novak V and Jungwirth T 2009 Spin-injection Hall effect in a planar photovoltaic cell *Nat Phys* **5** 675-81

[16] Jozwiak C, Park C-H, Gotlieb K, Hwang C, Lee D-H, Louie S G, Denlinger J D, Rotundu C R, Birgeneau R J, Hussain Z and Lanzara A 2013 Photoelectron spin-flipping and texture manipulation in a topological insulator *Nat Phys* **advance online publication** 293–8

[17] Elezzabi A Y 2007 The dawn of spinplasmonics *Nano Today* **2** 48-

[18] Karenowska A D, Gregg J F, Chumak A V, Serga A A and Hillebrands B 2011 Spin information transfer and transport in hybrid spinmechatronic structures *J Phys Conf Ser* **303** 012018

[19] Goennenwein S T B and Bauer G E W 2012 SPIN CALORITRONICS Electron spins blow hot and cold *Nat Nanotechnol* **7** 145–7

[20] Bauer G E W, Saitoh E and van Wees B J 2012 Spin caloritronics *Nat Mater* **11** 391-9

[21] Baibich M N, Broto J M, Fert A, Vandau F N, Petroff F, Eitenne P, Creuzet G, Friederich A and Chazelas J 1988 Giant Magnetoresistance of (001)Fe/(001) Cr Magnetic Superlattices *Phys Rev Lett* **61** 2472-5

[22] Binasch G, Grunberg P, Saurenbach F and Zinn W 1989 Enhanced Magnetoresistance in Layered Magnetic-Structures with Antiferromagnetic Interlayer Exchange *Physical Review B* **39** 4828-30
[23] Julliere M 1975 Tunneling between ferromagnetic films *Phys Lett A* **54** 225-6
[24] Moodera J S, Kinder L R, Wong T M and Meservey R 1995 Large Magnetoresistance at Room Temperature in Ferromagnetic Thin Film Tunnel Junctions *Phys Rev Lett* **74** 3273-6
[25] Miyazaki T and Tezuka N 1995 Giant magnetic tunneling effect in Fe/Al2O3/Fe junction *J Magn Magn Mater* **139** L231-L4
[26] Khvalkovskiy A V, Apalkov D, Watts S, Chepulskii R, Beach R S, Ong A, Tang X, Driskill-Smith A, Butler W H, Visscher P B, Lottis D, Chen E, Nikitin V and Krounbi M 2013 Basic principles of STT-MRAM cell operation in memory arrays *Journal of Physics D: Applied Physics* **46** 074001
[27] Fukami S, Yamanouchi M, Koyama T, Ueda K, Yoshimura Y, Kim K J, Chiba D, Honjo H, Sakimura N, Nebashi R, Kato Y, Tsuji Y, Morioka A, Kinoshita K, Miura S, Suzuki T, Tanigawa H, Ikeda S, Sugibayashi T, Kasai N, Ono T and Ohno H 2012 High-speed and reliable domain wall motion device: Material design for embedded memory and logic application. In: *Symposium on VLSI Technology (VLSIT), 2012*, (Honolulu, HI: IEEE) pp 61-2
[28] Sugahara S and Nitta J 2010 Spin-Transistor Electronics: An Overview and Outlook *P Ieee* **98** 2124-54
[29] Behin-Aein B, Datta D, Salahuddin S and Datta S 2010 Proposal for an all-spin logic device with built-in memory *Nat Nanotechnol* **5** 266-70
[30] Shibata J, Tatara G and Kohno H 2005 Effect of spin current on uniform ferromagnetism: Domain nucleation *Phys Rev Lett* **94** 076601
[31] Awschalom D D and Flatte M E 2007 Challenges for semiconductor spintronics *Nat Phys* **3** 153-9
[32] Jungwirth T, Sinova J, Masek J, Kucera J and MacDonald A H 2006 Theory of ferromagnetic (III,Mn)V semiconductors *Rev Mod Phys* **78** 809-64
[33] Sato K, Bergqvist L, Kudrnovsky J, Dederichs P H, Eriksson O, Turek I, Sanyal B, Bouzerar G, Katayama-Yoshida H, Dinh V A, Fukushima T, Kizaki H and Zeller R 2010 First-principles theory of dilute magnetic semiconductors *Rev Mod Phys* **82** 1633-90
[34] Schmidt G, Ferrand D, Molenkamp L W, Filip A T and van Wees B J 2000 Fundamental obstacle for electrical spin injection from a ferromagnetic metal into a diffusive semiconductor *Physical Review B* **62** R4790-R3
[35] Liang D and Gao X P A 2012 Strong Tuning of Rashba Spin-Orbit Interaction in Single InAs Nanowires *Nano Letters* **12** 3263-7
[36] Valenzuela S O and Tinkham M 2006 Direct electronic measurement of the spin Hall effect *Nature* **442** 176-9
[37] Schliemann J, Egues J C and Loss D 2003 Nonballistic spin-field-effect transistor *Phys Rev Lett* **90** 146801
[38] Novoselov K S, Geim A K, Morozov S V, Jiang D, Zhang Y, Dubonos S V, Grigorieva I V and Firsov A A 2004 Electric field effect in atomically thin carbon films *Science* **306** 666-9
[39] Huang X, Yin Z, Wu S, Qi X, He Q, Zhang Q, Yan Q, Boey F and Zhang H 2011 Graphene-Based Materials: Synthesis, Characterization, Properties, and Applications *Small* **7** 1876-902
[40] Hwang C, Siegel D A, Mo S-K, Regan W, Ismach A, Zhang Y, Zettl A and Lanzara A 2012 Fermi velocity engineering in graphene by substrate modification *Sci. Rep.* **2**
[41] Mayorov A S, Gorbachev R V, Morozov S V, Britnell L, Jalil R, Ponomarenko L A, Blake P, Novoselov K S, Watanabe K, Taniguchi T and Geim A K 2011 Micrometer-Scale Ballistic Transport in Encapsulated Graphene at Room Temperature *Nano Letters* **11** 2396-9

[42] Zheng J X, Wang L, Quhe R G, Liu Q H, Li H, Yu D P, Mei W N, Shi J J, Gao Z X and Lu J 2013 Sub-10 nm Gate Length Graphene Transistors: Operating at Terahertz Frequencies with Current Saturation *Sci Rep-Uk* **3** 1314
[43] Petrone N, Meric I, Hone J and Shepard K L 2012 Graphene Field-Effect Transistors with Gigahertz-Frequency Power Gain on Flexible Substrates *Nano Letters* **13** 121-5
[44] Heo J, Byun K-E, Lee J, Chung H-J, Jeon S, Park S and Hwang S 2013 Graphene and Thin-Film Semiconductor Heterojunction Transistors Integrated on Wafer Scale for Low-Power Electronics *Nano Letters* **13** 5967-71
[45] Crosse J A, Xu X, Sherwin M S and Liu R B 2014 Low power ultra-broadband terahertz sideband generation in bilayer graphene *arXiv:1401.1055 [cond-mat.mes-hall]*
[46] Gupta G, Lin H, Bansil A, Abdul Jalil M B, Huang C-Y, Tsai W-F and Liang G 2014 Y-shape spin-separator for two-dimensional group-IV nanoribbons based on quantum spin hall effect *Appl Phys Lett* **104** 032410
[47] Natsui M, Suzuki D, Sakimura N, Nebashi R, Tsuji Y, Morioka A, Sugibayashi T, Miura S, Honjo H, Kinoshita K, Ikeda S, Endoh T, Ohno H and Hanyu T 2013 Nonvolatile logic-in-memory array processor in 90nm MTJ/MOS achieving 75% leakage reduction using cycle-based power gating. In: *Solid-State Circuits Conference Digest of Technical Papers (ISSCC), 2013 IEEE International*, pp 194-5
[48] Kane C L and Mele E J 2005 Quantum spin Hall effect in graphene *Phys Rev Lett* **95** 226801
[49] Kane C L and Mele E J 2005 Z(2) topological order and the quantum spin Hall effect *Phys Rev Lett* **95** 146802
[50] Bernevig B A, Hughes T L and Zhang S C 2006 Quantum spin Hall effect and topological phase transition in HgTe quantum wells *Science* **314** 1757-61
[51] Fu L, Kane C L and Mele E J 2007 Topological insulators in three dimensions *Phys Rev Lett* **98** 106803
[52] Xia Y, Qian D, Hsieh D, Wray L, Pal A, Lin H, Bansil A, Grauer D, Hor Y S, Cava R J and Hasan M Z 2009 Observation of a large-gap topological-insulator class with a single Dirac cone on the surface *Nat Phys* **5** 398-402
[53] Giraud S and Egger R 2011 Electron-phonon scattering in topological insulators *Physical Review B* **83** 245322
[54] Analytis J G, McDonald R D, Riggs S C, Chu J-H, Boebinger G S and Fisher I R 2010 Two-dimensional surface state in the quantum limit of a topological insulator *Nature Physics* **6** 960-4
[55] Kim D, Li Q Z, Syers P, Butch N P, Paglione J, Das Sarma S and Fuhrer M S 2012 Intrinsic Electron-Phonon Resistivity of Bi2Se3 in the Topological Regime *Phys Rev Lett* **109** 166801
[56] Giraud S, Kundu A and Egger R 2012 Electron-phonon scattering in topological insulator thin films *Physical Review B* **85** 035441
[57] Wray L A, Xu S Y, Xia Y Q, Hsieh D, Fedorov A V, Hor Y S, Cava R J, Bansil A, Lin H and Hasan M Z 2011 A topological insulator surface under strong Coulomb, magnetic and disorder perturbations *Nat Phys* **7** 32-7
[58] Roth A, Brune C, Buhmann H, Molenkamp L W, Maciejko J, Qi X L and Zhang S C 2009 Nonlocal Transport in the Quantum Spin Hall State *Science* **325** 294-7
[59] Kim S, Yoshizawa S, Ishida Y, Eto K, Segawa K, Ando Y, Shin S and Komori F 2014 Robust Protection from Backscattering in the Topological Insulator Bi1.5Sb0.5Te1.7Se1.3 *Phys Rev Lett* **112** 136802
[60] Pan Z H, Fedorov A V, Gardner D, Lee Y S, Chu S and Valla T 2012 Measurement of an Exceptionally Weak Electron-Phonon Coupling on the Surface of the Topological Insulator Bi2Se3 Using Angle-Resolved Photoemission Spectroscopy *Phys Rev Lett* **108** 187001
[61] Wang M-X, Liu C, Xu J-P, Yang F, Miao L, Yao M-Y, Gao C L, Shen C, Ma X, Chen X, Xu Z-A, Liu Y, Zhang S-C, Qian D, Jia J-F and Xue Q-K 2012 The

Coexistence of Superconductivity and Topological Order in the Bi2Se3 Thin Films *Science* **336** 52-5
[62] Zhang X and Zhang S C 2012 Chiral interconnects based on topological insulators *Micro- and Nanotechnology Sensors, Systems, and Applications IV* **8373** 837309
[63] Pesin D and MacDonald A H 2012 Spintronics and pseudospintronics in graphene and topological insulators *Nat Mater* **11** 409-16
[64] Williams J R, Bestwick A J, Gallagher P, Hong S S, Cui Y, Bleich A S, Analytis J G, Fisher I R and Goldhaber-Gordon D 2012 Unconventional Josephson Effect in Hybrid Superconductor-Topological Insulator Devices *Phys Rev Lett* **109** 056803
[65] Tsai W F, Huang C Y, Chang T R, Lin H, Jeng H T and Bansil A 2013 Gated silicene as a tunable source of nearly 100% spin-polarized electrons *Nat Commun* **4** 1500
[66] Liu C-C, Jiang H and Yao Y 2011 Low-energy effective Hamiltonian involving spin-orbit coupling in silicene and two-dimensional germanium and tin *Physical Review B* **84** 195430
[67] Liu C-X, Qi X-L, Zhang H, Dai X, Fang Z and Zhang S-C 2010 Model Hamiltonian for topological insulators *Physical Review B* **82** 045122
[68] Zhao Y H, Hu Y B, Liu L, Zhu Y and Guo H 2011 Helical States of Topological Insulator Bi2Se3 *Nano Letters* **11** 2088-91
[69] Fu L and Berg E 2010 Odd-Parity Topological Superconductors: Theory and Application to CuxBi2Se3 *Phys Rev Lett* **105** 097001
[70] Fu L 2009 Hexagonal Warping Effects in the Surface States of the Topological Insulator Bi2Te3 *Phys Rev Lett* **103** 266801
[71] Zhang H J, Liu C X, Qi X L, Dai X, Fang Z and Zhang S C 2009 Topological insulators in Bi2Se3, Bi2Te3 and Sb2Te3 with a single Dirac cone on the surface *Nat Phys* **5** 438-42
[72] Kuroda K, Arita M, Miyamoto K, Ye M, Jiang J, Kimura A, Krasovskii E E, Chulkov E V, Iwasawa H, Okuda T, Shimada K, Ueda Y, Namatame H and Taniguchi M 2010 Hexagonally Deformed Fermi Surface of the 3D Topological Insulator Bi2Se3 *Phys Rev Lett* **105** 076802
[73] *For operation in the surface bands, transport is independent of slab thickess (Phys Rev Lett 109, 116804 (2012)), although percentage contribution through individual layers will change accordingly. However, computational time scales exponentially with slab thickness and becomes especially demanding for acoustic phonons, with an insignifcant affect on data and discussion presented in this work.*
[74] Kim D, Cho S, Butch N P, Syers P, Kirshenbaum K, Adam S, Paglione J and Fuhrer M S 2012 Surface conduction of topological Dirac electrons in bulk insulating Bi2Se3 *Nature Physics* **8** 460-4
[75] Zhou B, Lu H-Z, Chu R-L, Shen S-Q and Niu Q 2008 Finite Size Effects on Helical Edge States in a Quantum Spin-Hall System *Phys Rev Lett* **101** 246807
[76] Zhang W, Yu R, Zhang H-J, Dai X and Fang Z 2010 First-principles studies of the three-dimensional strong topological insulators Bi2Te3, Bi2Se3and Sb2Te3 *New Journal of Physics* **12** 065013
[77] Moon C-Y, Han J, Lee H and Choi H J 2011 Low-velocity anisotropic Dirac fermions on the side surface of topological insulators *Physical Review B* **84** 195425
[78] Zhang Y, He K, Chang C Z, Song C L, Wang L L, Chen X, Jia J F, Fang Z, Dai X, Shan W Y, Shen S Q, Niu Q, Qi X L, Zhang S C, Ma X C and Xue Q K 2010 Crossover of the three-dimensional topological insulator Bi2Se3 to the two-dimensional limit *Nat Phys* **6** 584-8
[79] Chen Y L, Analytis J G, Chu J-H, Liu Z K, Mo S-K, Qi X L, Zhang H J, Lu D H, Dai X, Fang Z, Zhang S C, Fisher I R, Hussain Z and Shen Z-X 2009 Experimental Realization of a Three-Dimensional Topological Insulator, Bi2Te3 *Science* **325** 178-81
[80] Alpichshev Z, Analytis J G, Chu J H, Fisher I R, Chen Y L, Shen Z X, Fang A and Kapitulnik A 2010 STM Imaging of Electronic Waves on the Surface of Bi2Te3:

Topologically Protected Surface States and Hexagonal Warping Effects *Phys Rev Lett* **104** 016401
[81] Datta S 2005 *Quantum Transport: Atom to Transistor*: Cambridge University Press)
[82] Datta S 2012 *Lessons from Nanoelectronics: A New Perspective on Transport* vol 1 (Singapore: World Scientific Publishing Company Incorporated)
[83] Querlioz D and Dollfus P 2013 *The Wigner Monte-Carlo Method for Nanoelectronic Devices: A Particle Description of Quantum Transport and Decoherence*: Wiley)
[84] Sancho M P L, Sancho J M L and Rubio J 1984 Quick Iterative Scheme for the Calculation of Transfer-Matrices - Application to Mo(100) *J Phys F Met Phys* **14** 1205-15
[85] Liang G C, Neophytou N, Lundstrom M S and Nikonov D E 2008 Contact effects in graphene nanoribbon transistors *Nano Letters* **8** 1819-24
[86] Chauhan J and Guo J 2011 Assessment of high-frequency performance limits of graphene field-effect transistors *Nano Res* **4** 571-9
[87] Sanders J and Kandrot E 2011 *CUDA by Example: An Introduction to General-Purpose GPU Programming*: Prentice Hall)
[88] 2007 NVIDIA's Next Generation CUDA Compute Architecture: Fermi *Nvidia Whitepaper*
[89] Ihnatsenka S 2012 Computation of electron quantum transport in graphene nanoribbons using GPU *Comput Phys Commun* **183** 543-6
[90] 2011 System Drivers *International Technology Roadmap for Semiconductors*
[91] Colinge J P, Flandre D and Vandewiele F 1994 Subthreshold Slope of Long-Channel, Accumulation-Mode P-Channel Soi Mosfets *Solid State Electron* **37** 289-94
[92] Tura A and Woo J C S 2010 Performance Comparison of Silicon Steep Subthreshold FETs *Ieee T Electron Dev* **57** 1362-8
[93] Castro Neto A H, Guinea F, Peres N M R, Novoselov K S and Geim A K 2009 The electronic properties of graphene *Rev Mod Phys* **81** 109-62
[94] Schwierz F 2011 Graphene transistors 2011. In: *VLSI Technology, Systems and Applications (VLSI-TSA), 2011 International Symposium on*, pp 1-2
[95] Schwierz F 2010 Graphene transistors *Nat Nanotechnol* **5** 487-96
[96] Sajjad R N and Ghosh A W 2011 High efficiency switching using graphene based electron "optics" *Appl Phys Lett* **99** 123101
[97] Banerjee S K, Register L F, Tutuc E, Reddy D and MacDonald A H 2009 Bilayer PseudoSpin Field-Effect Transistor (BiSFET): A Proposed New Logic Device *Ieee Electr Device L* **30** 158-60
[98] Sohier T and Yu B 2011 Ultralow-voltage design of graphene PN junction quantum reflective switch transistor *Appl Phys Lett* **98** 213104
[99] Low T and Appenzeller J 2009 Electronic transport properties of a tilted graphene p-n junction *Physical Review B* **80** 155406
[100] Cheianov V V, Fal'ko V and Altshuler B L 2007 The focusing of electron flow and a Veselago lens in graphene p-n junctions *Science* **315** 1252-5
[101] Sung C-Y 2011 Post Si CMOS graphene nanoelectronics *International Symposium on VLSI Technology, Systems and Applications (VLSI-TSA)* 1 - 2
[102] Williams J R, Low T, Lundstrom M S and Marcus C M 2011 Gate-controlled guiding of electrons in graphene *Nat Nanotechnol* **6** 222-5
[103] Katsnelson M I, Novoselov K S and Geim A K 2006 Chiral tunnelling and the Klein paradox in graphene *Nat Phys* **2** 620-5
[104] Young A F and Kim P 2009 Quantum interference and Klein tunnelling in graphene heterojunctions *Nat Phys* **5** 222-6
[105] Bahat-Treidel O, Peleg O, Grobman M, Shapira N, Segev M and Pereg-Barnea T 2010 Klein Tunneling in Deformed Honeycomb Lattices *Phys Rev Lett* **104**
[106] Klein V O 1929 Die Reflexion yon Elektronen an einem Potentialsprung nach der relativistischen Dynamik yon Dirac **53** 157-65
[107] Stander N, Huard B and Goldhaber-Gordon D 2009 Evidence for Klein Tunneling in Graphene p-n Junctions *Phys Rev Lett* **102**

[108] Shytov A, Rudner M, Gu N, Katsnelson M and Levitov L 2009 Atomic collapse, Lorentz boosts, Klein scattering, and other quantum-relativistic phenomena in graphene *Solid State Commun* **149** 1087-93
[109] Cheianov V V and Fal'ko V I 2006 Selective transmission of Dirac electrons and ballistic magnetoresistance of n-p junctions in graphene *Physical Review B* **74** 041403(R)
[110] Hund F 1940 Materieerzeugung im anschaulichen und im gequantelten Wellenbild der Materie *Zeitschrift für Physik A Hadrons and Nuclei* **117** 1-17
[111] Dragoman D 2009 Evidence against Klein paradox in graphene *Phys Scripta* **79** 015003
[112] Hansen A and Ravndal F 1981 Klein's Paradox and Its Resolution *Phys Scripta* **23** 1036-42
[113] Sauter F 1931 Über das Verhalten eines Elektrons im homogenen elektrischen Feld nach der relativistischen Theorie Diracs *Z Phys* **69** 742-64
[114] Setare M R and Jahani D 2010 Electronic transmission through p–n and n–p–n junctions of graphene *Journal of Physics: Condensed Matter* **22** 245503
[115] Wiener A D and Kindermann M 2011 Signatures of evanescent mode transport in graphene *Physical Review B* **84**
[116] Low T, Hong S, Appenzeller J, Datta S and Lundstrom M S 2009 Conductance Asymmetry of Graphene p-n Junction *Ieee T Electron Dev* **56** 1292-9
[117] Zhao P and Guo J 2009 Modeling edge effects in graphene nanoribbon field-effect transistors with real and mode space methods *J Appl Phys* **105**
[118] Takeda K and Shiraishi K 1994 Theoretical Possibility of Stage Corrugation in Si and Ge Analogs of Graphite *Physical Review B* **50** 14916-22
[119] Cahangirov S, Topsakal M, Akturk E, Sahin H and Ciraci S 2009 Two- and One-Dimensional Honeycomb Structures of Silicon and Germanium *Phys Rev Lett* **102** 236804
[120] Sahin H, Cahangirov S, Topsakal M, Bekaroglu E, Akturk E, Senger R T and Ciraci S 2009 Monolayer honeycomb structures of group-IV elements and III-V binary compounds: First-principles calculations *Physical Review B* **80** 155453
[121] Kara A, Enriquez H, Seitsonen A P, Voon L C L Y, Vizzini S, Aufray B and Oughaddou H 2012 A review on silicene - New candidate for electronics *Surf Sci Rep* **67** 1-18
[122] Lalmi B, Oughaddou H, Enriquez H, Kara A, Vizzini S, Ealet B and Aufray B 2010 Epitaxial growth of a silicene sheet *Appl Phys Lett* **97** 223109
[123] Bianco E, Butler S, Jiang S S, Restrepo O D, Windl W and Goldberger J E 2013 Stability and Exfoliation of Germanane: A Germanium Graphane Analogue *Acs Nano* **7** 4414-21
[124] Koski K J and Cui Y 2013 The New Skinny in Two-Dimensional Nanomaterials *Acs Nano* **7** 3739-43
[125] Quhe R G, Fei R X, Liu Q H, Zheng J X, Li H, Xu C Y, Ni Z Y, Wang Y Y, Yu D P, Gao Z X and Lu J 2012 Tunable and sizable band gap in silicene by surface adsorption *Sci Rep-Uk* **2** 853
[126] Li H, Wang L, Liu Q H, Zheng J X, Mei W N, Gao Z X, Shi J J and Lu J 2012 High performance silicene nanoribbon field effect transistors with current saturation *Eur Phys J B* **85** 274
[127] Wang Y Y, Zheng J X, Ni Z Y, Fei R X, Liu Q H, Quhe R G, Xu C Y, Zhou J, Gao Z X and Lu J 2012 Half-Metallic Silicene and Germanene Nanoribbons: Towards High-Performance Spintronics Device *Nano* **7** 1250037
[128] Ma Y D, Dai Y, Niu C W and Huang B B 2012 Halogenated two-dimensional germanium: candidate materials for being of Quantum Spin Hall state *J Mater Chem* **22** 12587-91
[129] Tahir M and Schwingenschlogl U 2013 Valley polarized quantum Hall effect and topological insulator phase transitions in silicene *Sci Rep-Uk* **3** 1075

[130] Liu C C, Feng W X and Yao Y G 2011 Quantum Spin Hall Effect in Silicene and Two-Dimensional Germanium *Phys Rev Lett* **107** 076802
[131] Tao L, Cinquanta E, Chiappe D, Grazianetti C, Fanciulli M, Dubey M, Molle A and Akinwande D 2015 Silicene field-effect transistors operating at room temperature *Nat Nano* **10** 227-31
[132] Xu C Y, Luo G F, Liu Q H, Zheng J X, Zhang Z M, Nagase S, Gao Z X and Lu J 2012 Giant magnetoresistance in silicene nanoribbons *Nanoscale* **4** 3111-7
[133] Guzman-Verri G G and Voon L C L Y 2007 Electronic structure of silicon-based nanostructures *Physical Review B* **76** 075131
[134] Min H, Hill J E, Sinitsyn N A, Sahu B R, Kleinman L and MacDonald A H 2006 Intrinsic and Rashba spin-orbit interactions in graphene sheets *Physical Review B* **74** 165310
[135] Drummond N D, Zolyomi V and Fal'ko V I 2012 Electrically tunable band gap in silicene *Physical Review B* **85** 075423
[136] Ni Z Y, Liu Q H, Tang K C, Zheng J X, Zhou J, Qin R, Gao Z X, Yu D P and Lu J 2012 Tunable Bandgap in Silicene and Germanene *Nano Letters* **12** 113-8
[137] Wang Y Y, Zheng J X, Ni Z Y, Fei R X, Liu Q H, Quhe R G, Xu C Y, Zhou J, Gao Z X and Lu J 2012 Half-Metallic Silicene and Germanene Nanoribbons: Towards High-Performance Spintronics Device *Nano* **7**
[138] Zeng M G and Liang G C 2012 Spin filtering and spin separating effects in U-shaped topological insulator devices *J Appl Phys* **112** 073707
[139] Neto A H C and Guinea F 2009 Impurity-Induced Spin-Orbit Coupling in Graphene *Phys Rev Lett* **103** 026804
[140] Xu Y, Yan B, Zhang H-J, Wang J, Xu G, Tang P, Duan W and Zhang S-C 2013 Large-Gap Quantum Spin Hall Insulators in Tin Films *Phys Rev Lett* **111** 136804
[141] Ohtsubo Y, Le Fèvre P, Bertran F and Taleb-Ibrahimi A 2013 Dirac Cone with Helical Spin Polarization in Ultrathin α-Sn(001) Films *Phys Rev Lett* **111** 216401
[142] Gupta G, Jalil M B, Yu B and Liang G C 2012 Performance evaluation of electro-optic effect based graphene transistors *Nanoscale* **4** 6365-73
[143] Yang H, Heo J, Park S, Song H J, Seo D H, Byun K-E, Kim P, Yoo I, Chung H-J and Kim K 2012 Graphene Barristor, a Triode Device with a Gate-Controlled Schottky Barrier *Science* **336** 1140-3
[144] Zeng M G, Feng Y P and Liang G C 2011 Graphene-based Spin Caloritronics *Nano Letters* **11** 1369-73
[145] Kan E-J, Li Z, Yang J and Hou J G 2007 Will zigzag graphene nanoribbon turn to half metal under electric field? *Appl Phys Lett* **91** 243116
[146] Yazyev O V 2010 Emergence of magnetism in graphene materials and nanostructures *Reports on Progress in Physics* **73** 056501
[147] Nair R R, Sepioni M, Tsai I L, Lehtinen O, Keinonen J, Krasheninnikov A V, Thomson T, Geim A K and Grigorieva I V 2012 Spin-half paramagnetism in graphene induced by point defects *Nat Phys* **8** 199-202
[148] Chen L, Liu C-C, Feng B, He X, Cheng P, Ding Z, Meng S, Yao Y and Wu K 2012 Evidence for Dirac Fermions in a Honeycomb Lattice Based on Silicon *Phys Rev Lett* **109** 056804
[149] Vogt P, De Padova P, Quaresima C, Avila J, Frantzeskakis E, Asensio M C, Resta A, Ealet B and Le Lay G 2012 Silicene: Compelling Experimental Evidence for Graphenelike Two-Dimensional Silicon *Physical Review Letters* **108** 155501
[150] Dávila M E, Xian L, Cahangirov S, Rubio A and Lay G L 2014 Germanene: a novel two-dimensional germanium allotrope akin to graphene and silicene *New J Phys* **16** 095002
[151] Ye X-S, Shao Z-G, Zhao H, Yang L and Wang C-L 2014 Intrinsic carrier mobility of germanene is larger than graphene's: first-principle calculations *RSC Advances* **4** 21216-20
[152] Bishnoi B and Ghosh B 2013 Spin transport in silicene and germanene *Rsc Adv* **3** 26153-9

[153] Bishnoi B and Ghosh B 2014 Spin transport in N-armchair-edge silicene nanoribbons *J Comput Electron* **13** 186-91
[154] Zhang S L, Collins-Mcintyre L J, Zhang J Y, Wang S G, Yu G H and Hesjedal T 2013 Nonvolatile Full Adder based on a Single Mutlivalued Hall Junction *SPIN* **03** 1350008
[155] Miao M S, Yan Q, Van de Walle C G, Lou W K, Li L L and Chang K 2012 Polarization-Driven Topological Insulator Transition in a GaN/InN/GaN Quantum Well *Phys Rev Lett* **109** 186803
[156] Zhang D, Lou W, Miao M, Zhang S-c and Chang K 2013 Interface-Induced Topological Insulator Transition in GaAs/Ge/GaAs Quantum Wells *Phys Rev Lett* **111** 156402
[157] Ezawa M 2012 A topological insulator and helical zero mode in silicene under an inhomogeneous electric field *New J Phys* **14** 033003
[158] Ezawa M 2012 Valley-Polarized Metals and Quantum Anomalous Hall Effect in Silicene *Phys Rev Lett* **109** 055502
[159] Ezawa M 2013 Photoinduced Topological Phase Transition and a Single Dirac-Cone State in Silicene *Phys Rev Lett* **110** 026603
[160] Soodchomshom B 2014 Perfect spin-valley filter controlled by electric field in ferromagnetic silicene *J Appl Phys* **115** 023706
[161] Žutić I, Fabian J and Das Sarma S 2004 Spintronics: Fundamentals and applications *Rev Mod Phys* **76** 323-410
[162] Miroshnichenko A E, Flach S and Kivshar Y S 2010 Fano resonances in nanoscale structures *Rev Mod Phys* **82** 2257-98
[163] Abbas A N, Liu G, Liu B, Zhang L, Liu H, Ohlberg D, Wu W and Zhou C 2014 Patterning, Characterization, and Chemical Sensing Applications of Graphene Nanoribbon Arrays Down to 5 nm Using Helium Ion Beam Lithography *Acs Nano* **8** 1538-46
[164] Ma Y, Dai Y, Guo M, Niu C and Huang B 2012 Intriguing Behavior of Halogenated Two-Dimensional Tin *The Journal of Physical Chemistry C* **116** 12977-81
[165] Moore J E 2010 The birth of topological insulators *Nature* **464** 194-8
[166] Hasan M Z and Kane C L 2010 Colloquium: Topological insulators *Rev Mod Phys* **82** 3045-67
[167] Hsieh D, Qian D, Wray L, Xia Y, Hor Y S, Cava R J and Hasan M Z 2008 A topological Dirac insulator in a quantum spin Hall phase *Nature* **452** 970-U5
[168] Gupta G, Jalil M B A and Liang G 2014 Effect of Band-Alignment Operation on Carrier Transport in Bi2Se3 Topological Insulator *Sci. Rep.* **4** 6220
[169] Wang Y H, Hsieh D, Pilon D, Fu L, Gardner D R, Lee Y S and Gedik N 2011 Observation of a Warped Helical Spin Texture in Bi2Se3 from Circular Dichroism Angle-Resolved Photoemission Spectroscopy *Phys Rev Lett* **107** 207602
[170] Hong S S, Zhang Y, Cha J J, Qi X-L and Cui Y 2014 One-Dimensional Helical Transport in Topological Insulator Nanowire Interferometers *Nano Letters* **14** 2815-21
[171] Jozwiak C, Park C-H, Gotlieb K, Hwang C, Lee D-H, Louie S G, Denlinger J D, Rotundu C R, Birgeneau R J, Hussain Z and Lanzara A 2013 Photoelectron spin-flipping and texture manipulation in a topological insulator *Nat Phys* **9** 293-8
[172] Kong D, Chen Y, Cha J J, Zhang Q, Analytis J G, Lai K, Liu Z, Hong S S, Koski K J, Mo S-K, Hussain Z, Fisher I R, Shen Z-X and Cui Y 2011 Ambipolar field effect in the ternary topological insulator (BixSb1-x)2Te3 by composition tuning *Nat Nano* **6** 705-9
[173] Hong S S, Cha J J, Kong D S and Cui Y 2012 Ultra-low carrier concentration and surface-dominant transport in antimony-doped Bi2Se3 topological insulator nanoribbons *Nat Commun* **3** 757
[174] Ren Z, Taskin A A, Sasaki S, Segawa K and Ando Y 2011 Observations of two-dimensional quantum oscillations and ambipolar transport in the topological insulator Bi2Se3 achieved by Cd doping *Physical Review B* **84** 075316

[175] Checkelsky J G, Hor Y S, Cava R J and Ong N P 2011 Bulk Band Gap and Surface State Conduction Observed in Voltage-Tuned Crystals of the Topological Insulator Bi2Se3 *Phys Rev Lett* **106** 196801
[176] Skinner B, Chen T R and Shklovskii B I 2012 Why Is the Bulk Resistivity of Topological Insulators So Small? *Phys Rev Lett* **109** 176801
[177] Cho S J, Butch N P, Paglione J and Fuhrer M S 2011 Insulating Behavior in Ultrathin Bismuth Selenide Field Effect Transistors *Nano Letters* **11** 1925-7
[178] Kim Y S, Brahlek M, Bansal N, Edrey E, Kapilevich G A, Iida K, Tanimura M, Horibe Y, Cheong S W and Oh S 2011 Thickness-dependent bulk properties and weak antilocalization effect in topological insulator Bi2Se3 *Physical Review B* **84** 073109
[179] Bansal N, Kim Y S, Brahlek M, Edrey E and Oh S 2012 Thickness-Independent Transport Channels in Topological Insulator Bi2Se3 Thin Films *Phys Rev Lett* **109** 116804
[180] Chi H, Liu W, Sun K, Su X, Wang G, Lošťák P, Kucek V, Drašar Č and Uher C 2013 Low-temperature transport properties of Tl-doped Bi2Te3 single crystals *Physical Review B* **88** 045202
[181] Yang F, Taskin A A, Sasaki S, Segawa K, Ohno Y, Matsumoto K and Ando Y 2014 Top gating of epitaxial (Bi1−xSbx)2Te3 topological insulator thin films *Appl Phys Lett* **104** 161614
[182] Zhu X T, Santos L, Howard C, Sankar R, Chou F C, Chamon C and El-Batanouny M 2012 Electron-Phonon Coupling on the Surface of the Topological Insulator Bi2Se3 Determined from Surface-Phonon Dispersion Measurements *Phys Rev Lett* **108** 185501
[183] Park S R, Jung W S, Han G R, Kim Y K, Kim C, Song D J, Koh Y Y, Kimura S, Lee K D, Hur N, Kim J Y, Cho B K, Kim J H, Kwon Y S, Han J H and Kim C 2011 Intrinsic quasi-particle dynamics of topological metallic states *New Journal of Physics* **13** 013008
[184] Thalmeier P 2011 Surface phonon propagation in topological insulators *Physical Review B* **83** 125314
[185] Barreto L, Bianchi M, Guan D, Hatch R, Mi J, Iversen B B and Hofmann P 2012 Electron–phonon coupling in the two-dimensional electron gas on Bi2Se3 *physica status solidi (RRL) – Rapid Research Letters* **7** 136–8
[186] Luo C W, Wang H J, Ku S A, Chen H J, Yeh T T, Lin J Y, Wu K H, Juang J Y, Young B L, Kobayashi T, Cheng C M, Chen C H, Tsuei K D, Sankar R, Chou F C, Kokh K A, Tereshchenko O E, Chulkov E V, Andreev Y M and Gu G D 2013 Snapshots of Dirac Fermions near the Dirac Point in Topological Insulators *Nano Letters* **13** 5797-802
[187] Gupta G, Jalil M B A and Liang G 2015 Contact Effects in thin 3D-Topological Insulators: How does the current flow? *Sci. Rep.* **5** 9479
[188] Device was simulated only up to 250K as similar physics seems to be at play from experimental studies between K to 300K. Also, simulating higher temperatures, becomes increasing more compute-intensive, requiring long time for the self-energy in NEGF to converge.
[189] Costache M V, Neumann I, Sierra J F, Marinova V, Gospodinov M M, Roche S and Valenzuela S O 2014 Fingerprints of Inelastic Transport at the Surface of the Topological Insulator Bi2Se3: Role of Electron-Phonon Coupling *Phys Rev Lett* **112** 086601
[190] Buttiker M 1992 Scattering-Theory of Current and Intensity Noise Correlations in Conductors and Wave Guides *Physical Review B* **46** 12485-507
[191] Venugopal R, Paulsson M, Goasguen S, Datta S and Lundstrom M S 2003 A simple quantum mechanical treatment of scattering in nanoscale transistors *J Appl Phys* **93** 5613-25

[192] Note that interlayer scattering due to Van der Waal's forces is weaker than in-plane scattering. Therefore, using same λ for inter-layer scattering might lead to a marginal over-estimation of the net effect of scattering between the layers.
[193] Butch N P, Kirshenbaum K, Syers P, Sushkov A B, Jenkins G S, Drew H D and Paglione J 2010 Strong surface scattering in ultrahigh-mobility Bi2Se3 topological insulator crystals *Physical Review B* **81** 241301(R)
[194] Park S R, Jung W S, Kim C, Song D J, Kim C, Kimura S, Lee K D and Hur N 2010 Quasiparticle scattering and the protected nature of the topological states in a parent topological insulator Bi2Se3 *Physical Review B* **81** 041405
[195] Asonen H, Lindroos M, Pessa M, Prasad R, Rao R S and Bansil A 1982 Angle-resolved photoemission study of (100), (110), and (111) surfaces of Cu0.9Al0.1: Bulk and surface electronic structure of the alloy *Physical Review B* **25** 7075-85
[196] Huisman L, Nicholson D, Schwartz L and Bansil A 1981 Effective-medium theory of electronic states in structurally disordered metals: Application to liquid Cu *Physical Review B* **24** 1824-34
[197] For example, disorder scattering effectively broadens energy levels in alloys, see Refs. A. Bansil, Phys. Rev. B 20, 4025(1979); A. Bansil, Phys. Rev. B 20, 4035 (1979); A. Bansil, Zeitschrift Naturforschung A 48, 165 (93).
[198] We emphasize that this approach only qualitatively characterizes the temperature dependency of relative decrease in the surface current, i.e. as the Fermi-level moves away from the Dirac-point, the differences in slopes expected for greatly differing strengths of the electron-phonon coupling. The measured magnitudes of the variation will depend on the sample quality, bias, dimensions (length and sample thickness) and specific values of λ.
[199] Gupta G, Lin H, Bansil A, Jalil M B A and Liang G 2015 Carrier transport in Bi2Se3 topological insulator slab *Physica E: Low-dimensional Systems and Nanostructures* **74** 10-9
[200] Gupta G, Lin H, Bansil A, Jalil M B A and Liang G 2014 Role of acoustic phonons in Bi2Se3 topological insulator slabs: A quantum transport investigation *Physical Review B* **89** 245419
[201] Li Q, Rossi E and Das Sarma S 2012 Two-dimensional electronic transport on the surface of three-dimensional topological insulators *Physical Review B* **86** 235443
[202] Roushan P, Seo J, Parker C V, Hor Y S, Hsieh D, Qian D, Richardella A, Hasan M Z, Cava R J and Yazdani A 2009 Topological surface states protected from backscattering by chiral spin texture *Nature* **460** 1106-9
[203] Akhmerov A R, Nilsson J and Beenakker C W J 2009 Electrically Detected Interferometry of Majorana Fermions in a Topological Insulator *Phys Rev Lett* **102** 216404
[204] Li C H, van /`t Erve O M J, Robinson J T, LiuY, LiL and Jonker B T 2014 Electrical detection of charge-current-induced spin polarization due to spin-momentum locking in Bi2Se3 *Nat Nanotechnol* **9** 218-24
[205] Hong S, Diep V, Datta S and Chen Y P 2012 Modeling potentiometric measurements in topological insulators including parallel channels *Physical Review B* **86** 085131
[206] Xia B, Ren P, Sulaev A, Li Z P, Liu P, Dong Z L and Wang L 2012 Anisotropic magnetoresistance in topological insulator Bi1.5Sb0.5Te1.8Se1.2/CoFe heterostructures *AIP Advances* **2** 042171
[207] Kramers H A 1930 General theory of the paramagnetic rotation in crystals *P K Akad Wet-Amsterd* **33** 959-72
[208] Bardarson J H 2008 A proof of the Kramers degeneracy of transmission eigenvalues from antisymmetry of the scattering matrix *J Phys a-Math Theor* **41** 405203
[209] Kim D, Cho S, Butch N P, Syers P, Kirshenbaum K, Adam S, Paglione J and Fuhrer M S 2012 Surface conduction of topological Dirac electrons in bulk insulating Bi2Se3 *Nat Phys* **8** 458-62

[210] Xiu F X, Meyer N, Kou X F, He L, Lang M R, Wang Y, Yu X X, Fedorov A V, Zou J and Wang K L 2012 Quantum Capacitance in Topological Insulators *Sci Rep-Uk* **2** 669
[211] Hsieh D, Xia Y, Qian D, Wray L, Dil J H, Meier F, Osterwalder J, Patthey L, Checkelsky J G, Ong N P, Fedorov A V, Lin H, Bansil A, Grauer D, Hor Y S, Cava R J and Hasan M Z 2009 A tunable topological insulator in the spin helical Dirac transport regime *Nature* **460** 1101-5
[212] Liu X and Sinova J 2013 Reading Charge Transport from the Spin Dynamics on the Surface of a Topological Insulator *Phys Rev Lett* **111** 166801
[213] Burkov A A and Hawthorn D G 2010 Spin and Charge Transport on the Surface of a Topological Insulator *Phys Rev Lett* **105** 066802
[214] Zhang P and Wu M W 2013 Hot-carrier transport and spin relaxation on the surface of topological insulator *Physical Review B* **87** 085319
[215] Taguchi K, Yokoyama T and Tanaka Y 2014 Giant magnetoresistance in the junction of two ferromagnets on the surface of diffusive topological insulators *Physical Review B* **89** 085407
[216] Lang M, He L, Kou X, Upadhyaya P, Fan Y, Chu H, Jiang Y, Bardarson J H, Jiang W, Choi E S, Wang Y, Yeh N-C, Moore J and Wang K L 2012 Competing Weak Localization and Weak Antilocalization in Ultrathin Topological Insulators *Nano Letters* **13** 48-53
[217] Datta D, Behin-Aein B, Datta S and Salahuddin S 2012 Voltage Asymmetry of Spin-Transfer Torques *Ieee T Nanotechnol* **11** 261-72
[218] Zhang K H, Wang Z C, Zheng Q R and Su G 2012 Gate-voltage controlled electronic transport through a ferromagnet/normal/ferromagnet junction on the surface of a topological insulator *Physical Review B* **86** 174416
[219] Park C H and Louie S G 2012 Spin Polarization of Photoelectrons from Topological Insulators *Phys Rev Lett* **109** 097601
[220] Gupta G, Jalil M B A and Liang G 2014 Evaluation of mobility in thin Bi2Se3 Topological Insulator for prospects of Local Electrical Interconnects *Sci. Rep.* **4** 6838
[221] Hsieh T H, Lin H, Liu J, Duan W, Bansil A and Fu L 2012 Topological crystalline insulators in the SnTe material class *Nat Commun* **3** 982
[222] Wang Y J, Tsai W-F, Lin H, Xu S-Y, Neupane M, Hasan M Z and Bansil A 2013 Nontrivial spin texture of the coaxial Dirac cones on the surface of topological crystalline insulator SnTe *Physical Review B* **87** 235317
[223] Zhang D, Baek H, Ha J, Zhang T, Wyrick J, Davydov A V, Kuk Y and Stroscio J A 2014 Quasiparticle scattering from topological crystalline insulator SnTe (001) surface states *Physical Review B* **89** 245445
[224] McIver J W, Hsieh D, Steinberg H, Jarillo-Herrero P and Gedik N 2012 Control over topological insulator photocurrents with light polarization *Nat Nanotechnol* **7** 96-100
[225] Hsieh D, Mahmood F, McIver J W, Gardner D R, Lee Y S and Gedik N 2011 Selective Probing of Photoinduced Charge and Spin Dynamics in the Bulk and Surface of a Topological Insulator *Phys Rev Lett* **107** 077401
[226] Nowack K C, Spanton E M, Baenninger M, König M, Kirtley J R, Kalisky B, Ames C, Leubner P, Brüne C, Buhmann H, Molenkamp L W, Goldhaber-Gordon D and Moler K A 2013 Imaging currents in HgTe quantum wells in the quantum spin Hall regime *Nat Mater* **12** 787-91
[227] Yan Y, Liao Z-M, Ke X, Van Tendeloo G, Wang Q, Sun D, Yao W, Zhou S, Zhang L, Wu H-C and Yu D-P 2014 Topological Surface State Enhanced Photothermoelectric Effect in Bi2Se3 Nanoribbons *Nano Letters* **14** 4389-94
[228] *The International Technology Roadmap for Semiconductors (ITRS), Interconnects, 2011*, http://www.itrs.net/
[229] Qiao Z, Tse W-K, Jiang H, Yao Y and Niu Q 2011 Two-Dimensional Topological Insulator State and Topological Phase Transition in Bilayer Graphene *Phys Rev Lett* **107** 256801

[230] Knez I, Du R-R and Sullivan G 2011 Evidence for Helical Edge Modes in Inverted InAs/GaSb Quantum Wells *Phys Rev Lett* **107** 136603
[231] Zuan-Yi L, Kai-Tak L and Liang G 2009 Device Performance of Graphene Nanoribbon Field Effect Transistors with Edge Roughness Effects: A Computational Study. In: *Computational Electronics, 2009. IWCE '09. 13th International Workshop on*, pp 1-4
[232] Martinez A, Barker J R, Asenov A, Svizhenko A and Anantram M P 2007 Developing a full 3D NEGF simulator with random dopant and interface roughness *J Comput Electron* **6** 215-8
[233] Martinez A, Brown A R and Asenov A 2010 Full-band NEGF simulations of surface roughness in Si nanowires *Journal of Physics: Conference Series* **242** 012016
[234] Martinez A, Svizhenko A, Anantram M P, Barker J R and Asenov A 2006 A NEGF study of the effect of surface roughness on CMOS nanotransistors *Journal of Physics: Conference Series* **35** 269
[235] Hsieh D, Xia Y, Wray L, Qian D, Pal A, Dil J H, Osterwalder J, Meier F, Bihlmayer G, Kane C L, Hor Y S, Cava R J and Hasan M Z 2009 Observation of Unconventional Quantum Spin Textures in Topological Insulators *Science* **323** 919-22
[236] Ran Y, Zhang Y and Vishwanath A 2009 One-dimensional topologically protected modes in topological insulators with lattice dislocations *Nat Phys* **5** 298-303
[237] Shan W Y, Lu J, Lu H Z and Shen S Q 2011 Vacancy-induced bound states in topological insulators *Physical Review B* **84** 035307
[238] Chan C and Ng T K 2012 Impurity scattering in the bulk of topological insulators *Physical Review B* **85** 115207
[239] Teague M L, Chu H, Xiu F X, He L, Wang K L and Yeh N C 2012 Observation of Fermi-energy dependent unitary impurity resonances in a strong topological insulator Bi2Se3 with scanning tunneling spectroscopy *Solid State Commun* **152** 747-51
[240] Black-Schaffer A M and Balatsky A V 2012 Subsurface impurities and vacancies in a three-dimensional topological insulator *Physical Review B* **86** 115433
[241] Alpichshev Z, Biswas R R, Balatsky A V, Analytis J G, Chu J H, Fisher I R and Kapitulnik A 2012 STM Imaging of Impurity Resonances on Bi2Se3 *Phys Rev Lett* **108** 206402
[242] Zhang T, Cheng P, Chen X, Jia J F, Ma X C, He K, Wang L L, Zhang H J, Dai X, Fang Z, Xie X C and Xue Q K 2009 Experimental Demonstration of Topological Surface States Protected by Time-Reversal Symmetry *Phys Rev Lett* **103** 266803
[243] Culcer D, Hwang E H, Stanescu T D and Das Sarma S 2010 Two-dimensional surface charge transport in topological insulators *Physical Review B* **82** 155457
[244] Wu L, Brahlek M, Valdes Aguilar R, Stier A V, Morris C M, Lubashevsky Y, Bilbro L S, Bansal N, Oh S and Armitage N P 2013 A sudden collapse in the transport lifetime across the topological phase transition in (Bi1-xInx)2Se3 *Nat Phys* **9** 410-4
[245] Wei P, Wang Z Y, Liu X F, Aji V and Shi J 2012 Field-effect mobility enhanced by tuning the Fermi level into the band gap of Bi2Se3 *Physical Review B* **85** 201402(R)
[246] Suri R, Thakoor A P and Chopra K L 1975 Electron-Transport Properties of Thin Copper-Films .1. *J Appl Phys* **46** 2574-82
[247] Cao H L, Xu S Y, Miotkowski I, Tian J F, Pandey D, Hasan M Z and Chen Y P 2013 Structural and electronic properties of highly doped topological insulator Bi2Se3 crystals *Phys Status Solidi-R* **7** 133-5
[248] Kim D, Syers P, Butch N P, Paglione J and Fuhrer M S 2013 Coherent topological transport on the surface of Bi2Se3 *Nat Commun* **4** 2040
[249] Hor Y S, Richardella A, Roushan P, Xia Y, Checkelsky J G, Yazdani A, Hasan M Z, Ong N P and Cava R J 2009 p-type Bi2Se3 for topological insulator and low-temperature thermoelectric applications *Physical Review B* **79** 195208
[250] Niquet Y-M, Nguyen V-H, Triozon F, Duchemin I, Nier O and Rideau D 2014 Quantum calculations of the carrier mobility: Methodology, Matthiessen's rule, and comparison with semi-classical approaches *J Appl Phys* **115** 054512

[251] Zhu H, Richter C A, Zhao E H, Bonevich J E, Kimes W A, Jang H J, Yuan H, Li H T, Arab A, Kirillov O, Maslar J E, Ioannou D E and Li Q L 2013 Topological Insulator Bi2Se3 Nanowire High Performance Field-Effect Transistors *Sci Rep-Uk* **3** 1757
[252] Le P H, Wu K H, Luo C W and Leu J 2013 Growth and characterization of topological insulator Bi2Se3 thin films on SrTiO3 using pulsed laser deposition *Thin Solid Films* **534** 659-65
[253] Behnam A, Lyons A S, Bae M H, Chow E K, Islam S, Neumann C M and Pop E 2012 Transport in Nanoribbon Interconnects Obtained from Graphene Grown by Chemical Vapor Deposition *Nano Letters* **12** 4424-30
[254] Balandin A A, Ghosh S, Bao W Z, Calizo I, Teweldebrhan D, Miao F and Lau C N 2008 Superior thermal conductivity of single-layer graphene *Nano Letters* **8** 902-7
[255] Naeemi A and Meindl J D 2007 Conductance modeling for graphene nanoribbon (GNR) interconnects *Ieee Electr Device L* **28** 428-31
[256] Xu C A, Li H and Banerjee K 2009 Modeling, Analysis, and Design of Graphene Nano-Ribbon Interconnects *Ieee T Electron Dev* **56** 1567-78
[257] Kureshi A K and Hasan M 2009 Analysis of CNT Bundle and Its Comparison with Copper Interconnect for CMOS and CNFET Drivers *J Nanomater* **2009** 486979
[258] Rakheja S, Kumar V and Naeemi A 2013 Evaluation of the Potential Performance of Graphene Nanoribbons as On-Chip Interconnects *P Ieee* **101** 1740-65
[259] Tanaka Y, Ren Z, Sato T, Nakayama K, Souma S, Takahashi T, Segawa K and Ando Y 2012 Experimental realization of a topological crystalline insulator in SnTe *Nat Phys* **8** 800-3
[260] Yan Y, Wang L-X, Ke X, Van Tendeloo G, Wu X-S, Yu D-P and Liao Z-M 2014 High-Mobility Bi2Se3 Nanoplates Manifesting Quantum Oscillations of Surface States in the Sidewalls *Sci. Rep.* **4** 3817
[261] Pierce D G and Brusius P G 1997 Electromigration: A review *Microelectron Reliab* **37** 1053-72
[262] Ceric H and Selberherr S 2011 Electromigration in submicron interconnect features of integrated circuits *Mat Sci Eng R* **71** 53-86
[263] Tan C M and Roy A 2007 Electromigration in ULSI interconnects *Materials Science and Engineering: R: Reports* **58** 1-75
[264] Hai-Bao C, Tan S X D, Xin H and Sukharev V 2015 New electromigration modeling and analysis considering time-varying temperature and current densities. In: *Design Automation Conference (ASP-DAC), 2015 20th Asia and South Pacific*, pp 352-7
[265] Sukharev V, Xin H, Hai-Bao C and Tan S X D 2014 IR-drop based electromigration assessment: Parametric failure chip-scale analysis. In: *Computer-Aided Design (ICCAD), 2014 IEEE/ACM International Conference on*, pp 428-33
[266] Hau-Riege C S 2004 An introduction to Cu electromigration *Microelectron Reliab* **44** 195-205
[267] Li B, Sullivan T D, Lee T C and Badami D 2004 Reliability challenges for copper interconnects *Microelectron Reliab* **44** 365-80
[268] Hu C K, Gignac L and Rosenberg R 2006 Electromigration of Cu/low dielectric constant interconnects *Microelectron Reliab* **46** 213-31
[269] Hu C K, Canaperi D, Chen S T, Gignac L M, Kaldor S, Krishnan M, Malhotra S G, Liniger E, Lloyd J R, Rath D L, Restaino D, Rosenberg R, Rubino J, Seo S C, Simon A, Smith S and Tseng W T 2006 Electromigration Cu mass flow in Cu interconnections *Thin Solid Films* **504** 274-8
[270] Changsup R, Kee-Won K, Loke A L S, Lee H, Nogami T, Dubin V M, Kavari R A, Ray G W and Wong S S 1999 Microstructure and reliability of copper interconnects *Electron Devices, IEEE Transactions on* **46** 1113-20
[271] Korhonen M A, Borgesen P and Li C-Y 1992 Electromigration in Aluminum Based Interconnects of VLSI-Microcircuits, with and without Preceding Stress-Migration Damage *Thin films : stresses and mechanical properties III : symposium held December 2-5, 1991, Boston, Massachusetts, USA* **Materials Research Society symposium proceedings** 695-700

[272] Doan J C, Bravman J C, Flinn P A and Marieb T N 2000 The evolution of the resistance of aluminum interconnects during electromigration *Microelectron Reliab* **40** 981-90
[273] Blech I A 1976 Electromigration in thin aluminum films on titanium nitride *J Appl Phys* **47** 1203-8
[274] D'heurle F M 1971 The effect of copper additions on electromigration in aluminum thin films *MT* **2** 683-9
[275] Setlik B J 2002 Electromigration characterization of aluminum -copper alloy interconnects *Dissertations and Master's Theses (The University of Rhode Island)*
[276] Shine M C and d'Heurle F M 1971 Activation Energy for Electromigration in Aluminum Films Alloyed with Copper *IBM Journal of Research and Development* **15** 378-83
[277] Black J R 1969 Electromigration failure modes in aluminum metallization for semiconductor devices *P Ieee* **57** 1587-94
[278] Chien P Y, Yeh C H, Hsu H H and Wu A 2014 Polarity Effect in a Sn3Ag0.5Cu/Bismuth Telluride Thermoelectric System *Journal of Elec Materi* **43** 284-9
[279] Priemuth A 1981 Electromigration of Cu in V2VI3 compounds *physica status solidi (a)* **67** 505-10
[280] Siu Z B, Jalil M B A and Tan S G 2012 Magnetoresistance in Ferromagnetically Coupled Three-Dimensional Topological Insulator Strips *Magnetics, IEEE Transactions on* **48** 4250-2
[281] Bala Kumar S, Jalil M B A and Tan S G 2013 Klein tunneling in graphene systems under the influence of magnetic field *J Appl Phys* **114** 084314
[282] Wu Z, Peeters F M and Chang K 2011 Spin and momentum filtering of electrons on the surface of a topological insulator *Appl Phys Lett* **98** 162101
[283] Zhang L B, Kai C, Xie X C, Buhmann H and Molenkamp L W 2010 Quantum tunneling through planar p–n junctions in HgTe quantum wells *New J Phys* **12** 083058
[284] Pei Z, Feenstra R M, Gong G and Jena D 2013 SymFET: A Proposed Symmetric Graphene Tunneling Field-Effect Transistor *Electron Devices, IEEE Transactions on* **60** 951-7
[285] Atulasimha J and Bandyopadhyay S 2012 Hybrid spintronic/straintronics: A super energy efficient computing scheme based on interacting multiferroic nanomagnets. In: *Nanotechnology (IEEE-NANO), 2012 12th IEEE Conference on*, pp 1-2
[286] Feenstra R M, Jena D and Gu G 2012 Single-particle tunneling in doped graphene-insulator-graphene junctions *J Appl Phys* **111** 043711
[287] Masao N, Hiroki H, Hiroyuki K and Hiroshi Y 2013 Graphene-Based Nano-Electro-Mechanical Switch with High On/Off Ratio *Appl Phys Express* **6** 055101
[288] Britnell L, Gorbachev R V, Jalil R, Belle B D, Schedin F, Mishchenko A, Georgiou T, Katsnelson M I, Eaves L, Morozov S V, Peres N M R, Leist J, Geim A K, Novoselov K S and Ponomarenko L A 2012 Field-Effect Tunneling Transistor Based on Vertical Graphene Heterostructures *Science* **335** 947-50
[289] Liang G C, Ghosh A W, Paulsson M and Datta S 2004 Electrostatic potential profiles of molecular conductors *Physical Review B* **69** 115302
[290] Liang G C and Ghosh A W 2005 Identifying Contact Effects in Electronic Conduction through C60 on Silicon *Phys Rev Lett* **95** 076403
[291] Chu R-L, Shi J and Shen S-Q 2011 Surface edge state and half-quantized Hall conductance in topological insulators *Physical Review B* **84** 085312
[292] He H T, Liu H C, Li B K, Guo X, Xu Z J, Xie M H and Wang J N 2013 Disorder-induced linear magnetoresistance in (221) topological insulator Bi2Se3 films *Appl Phys Lett* **103** 031606
[293] Rycerz A, Tworzydlo J and Beenakker C W J 2007 Valley filter and valley valve in graphene *Nat Phys* **3** 172-5

[294] Nakabayashi J, Yamamoto D and Kurihara S 2009 Band-Selective Filter in a Zigzag Graphene Nanoribbon *Phys Rev Lett* **102** 066803
[295] Kim S, Ye M, Kuroda K, Yamada Y, Krasovskii E E, Chulkov E V, Miyamoto K, Nakatake M, Okuda T, Ueda Y, Shimada K, Namatame H, Taniguchi M and Kimura A 2011 Surface Scattering via Bulk Continuum States in the 3D Topological Insulator Bi2Se3 *Phys Rev Lett* **107** 056803
[296] Schwaha P, Querlioz D, Dollfus P, Saint-Martin J, Nedjalkov M and Selberherr S 2013 Decoherence effects in the Wigner function formalism *J Comput Electron* **12** 388-96
[297] Nedjalkov M and Vasileska D 2008 Semi-discrete 2D Wigner-particle approach *J Comput Electron* **7** 222-5
[298] Lou P and Xiang T 2005 Spin Hall current and two-dimensional magnetic monopole in a Corbino disk *arXiv:cond-mat/0501307v1*
[299] Yan J and Fuhrer M S 2010 Charge Transport in Dual Gated Bilayer Graphene with Corbino Geometry *Nano Letters* **10** 4521-5
[300] Bahamon D A, Castro Neto A H and Pereira V M 2013 Effective contact model for geometry-independent conductance calculations in graphene *Physical Review B* **88** 235433
[301] Young S M, Chowdhury S, Walter E J, Mele E J, Kane C L and Rappe A M 2011 Theoretical investigation of the evolution of the topological phase of Bi2Se3 under mechanical strain *Physical Review B* **84** 085106
[302] Liu Y, Li Y Y, Rajput S, Gilks D, Lari L, Galindo P L, Weinert M, Lazarov V K and Li L 2014 Tuning Dirac states by strain in the topological insulator Bi2Se3 *Nat Phys* **10** 294-9
[303] Chadov S, Qi X L, Kubler J, Fecher G H, Felser C and Zhang S C 2010 Tunable multifunctional topological insulators in ternary Heusler compounds *Nat Mater* **9** 541-5
[304] Zhao L, Liu J W, Tang P Z and Duan W H 2012 Design of strain-engineered quantum tunneling devices for topological surface states *Appl Phys Lett* **100** 131602
[305] Tahir M and Schwingenschlogl U 2012 Quantum capacitance in topological insulators under strain in a tilted magnetic field *Appl Phys Lett* **101** 231609
[306] Wakabayashi K 2001 Electronic transport properties of nanographite ribbon junctions *Physical Review B* **64** 125428
[307] Avishai Y, Bessis D, Giraud B G and Mantica G 1991 Quantum Bound-States in Open Geometries *Physical Review B* **44** 8028-34
[308] Exner P, Seba P and Stovicek P 1990 Semiconductor Edges Can Bind Electrons *Phys Lett A* **150** 179-82
[309] Schult R L, Ravenhall D G and Wyld H W 1989 Quantum Bound-States in a Classically Unbound System of Crossed Wires *Physical Review B* **39** 5476-9
[310] Datta S 1989 Quantum devices *Superlattices and Microstructures* **6** 83-93
[311] Gupta G, Jalil M B A and Liang G 2013 Is sub-10nm thick 3D-topological insulator good for the local electrical interconnects? In: *Electron Devices Meeting (IEDM), 2013 IEEE International*, (Washington, DC: IEEE) pp 32.5.1-.5.4
[312] Nguyen V H, Bournel A, Chassat C and Dollfus P 2010 Quantum transport of Dirac fermions in graphene field effect transistors. In: *Simulation of Semiconductor Processes and Devices (SISPAD), 2010 International Conference on*, pp 9-12